Université catholique de Louvain
Ecole polytechnique de Louvain
Institute of Mechanics, Materials and Civil Engineering

Numerical Modelling and Experimental Characterization of Submarine Slide-induced Debris Flows transitioning to Turbidity Currents

Thesis presented for the degree of Doctor in Engineering Sciences by

Mariangela Sfouni-Grigoriadou

August 2018

Members of the Jury
Dr. Benoit Spinewine, Université catholique de Louvain, supervisor
Prof. Sandra Soares-Frazão, Université catholique de Louvain, co-supervisor
Prof. Athanassios Dimas, University of Patras
Prof. Miltiadis Papalexandris, Université catholique de Louvain
Dr. Octavio Sequeiros, Shell Global
Prof. Hervé Jeanmart, Université catholique de Louvain, president

Abstract

The growth of the offshore renewable energy industry as well as the rapid technological advances in oil and gas production have forced the industry to access and mitigate geohazards in deep water environments and areas of steep seabed gradients susceptible to potential mass movement events such as debris flows and turbidity currents. The risks of such events may be ascertained using numerical models that predict their dynamic evolution from inception to runout. In the present work, a two-layer model is introduced to study the dynamics of a slide-induced debris flow gradually transforming into a turbidity current through sediment mixing and detrainment. It considers a dense viscoplastic debris flow layer at the bottom and a dilute turbidity current layer of variable density but Newtonian rheology at the top. The model proposes interfacial mass and momentum exchange mechanisms to account for friction and mixing between the debris layer, the turbid layer and the ambient, and handles emerging, vanishing or detaching layers. The generation and co-evolution of a turbidity current on top of a parent debris flow is investigated on an idealized slope-break bathymetry as well as on real bathymetry data. Two experimental campaigns have been performed to complement the study of the transition and co-existence of a debris flow and a turbidity current layer. Experimental results are compared with the numerical results of the introduced numerical model and provide a valuable database for future research.

Keywords: two-layer model, submarine landslides, debris flow, turbidity current, geohazards

To my mother Nena
To Venetia and Paris

Acknowledgements

The adventure of accomplishing a PhD demands hard work, personal devotion and lots of patience. During this process, I realized that nothing could be done without my interaction with people that provided me with their expertise, guidance and support, and gave me motivation to be a better engineer.

I first wish to thank the supervisor of this work, Dr. Benoit Spinewine, for his expertise, his guidance and his trust in me, but most importantly for being an engineer and a person who I deeply respect and admire. Working with him made me want to continually improve my knowledge and performance. His support in my difficult times was crucial for continuing my work and is more than appreciated.

I would also like to thank my co-supervisor, Professor Sandra Soares-Frazão for always being kind and supportive to me. Her comments and suggestions always helped me improve the quality of this work. Special thanks to Professor Miltiadis Papalexandris, for his valuable advices that helped me accomplish this work and it was an honour having him in my jury; Dr. Octavio Sequeiros for his comments that gave a different perspective in my work; Professor Hervé Jeanmart whose presidency in the thesis jury is greatly acknowledged. I would like to deeply thank Professor Athanassios Dimas, my mentor, in who I owe all my academic career so far.

My ‘home’ during this work was FUGRO. All my colleagues supported me and broadened my knowledge and perception in different fields of engineering. I would especially like to thank Dr. Sébastien Blaise whose expertise helped me improve my numerical modelling skills and with his guidance upgraded the performance of the introduced model; my dear friends Mario Martin Santana and Nicolas Jeannelle who made every day more fun in the office; Riika Lempiainen and Nicholas Vanmol who helped me solve all my routine issues; Dr. Jean-Francois Vanden Berghe that believed in me and in my work.

My experimental work could not be made without the help of Dr. Carmelo Juez at EPFL and Samuel Laurent at UCL. Their experience helped me significantly improve my experimental skills.

Special thanks to Pierre Delnooz and Matthieu Guilmot for our collaboration at the very beginning of this work.

I am thankful to all the people that crossed my path during this period and I tried to draw knowledge from each one of them; professors, professionals, students, engineers, technicians, coming from different cultures and backgrounds.

Funding support of this research from the People Programme (Marie Curie Actions) of the European Union's Seventh Framework Programme FP7/2007-2013/ under REA grant agreement n° 607394-SEDITRANS, is gratefully acknowledged.

I could have never completed this PhD study without my friends. The most valuable gift that Brussels gave me was my two friends for life, Katerina and Vasilis, always being there to support and care for me. Orestis and Panagiota that offered me their friendship and support since day one in Belgium. My favorite Dionysis and my partner in crime Ilaria. David, Evangelia, Elli, Sofia, Stratos and Vasilis for having a great time in Brussels.

I would like to thank all the people that even though were far, were always there for me; my ‘soul-sister’ Maria for being my 24/7 support line, and my best friend-manager-maid of honour Dr. Tina Katicca; my friends Angeliki, Eleftheria, Vasilis, Lefteris, Iro, Errikos, Miss Litsa; Alekos for his support and his excellent proofreading skills.

Finally, this thesis is dedicated to my family; to my father who instilled in me the love for reading and knowledge; to the smartest and coolest guy in my world, my brother Alexandros for his endless love and support in every step of my life; to the strongest and most caring woman, my superhero-mother Nena to whom I owe everything I am and all I have achieved; to my beloved grandparents, Venetia and Paris, who left while I was away but they will always be my motivation for being a better person.

Table of Contents

Chapter 1 Introduction

1.1 Background

The offshore industry is gradually moving to deeper-water environments, to tap into frontier oil and gas resources, to install vast networks of telecommunications and power cable interconnectors, and to install anchored floating wind turbines in areas of stronger winds and lesser visual impact. These new working areas bring up new technical challenges, as their proximity with the continental slope and the occurrence of steep seabed gradients make them susceptible to mass gravity flows (Zakeri *et al*., 2008; Spinewine, 2013). The risk assessment to subsea infrastructure becomes critically important as mass gravity flows constitute a major geohazard, which can cause the transport of vast quantities of soil at significant velocities down channels and escarpments.

Subaqueous mass movements, including debris flows and turbidity currents, have had catastrophic impacts such as the destruction of seabed infrastructure, the collapse of coastal areas into the sea and in some cases the generation of tsunamis. The new surveying techniques brought to light many large debris flow and turbidity current deposits that indicate the occurrence of important submarine landslide events that took place in the past.

The Storegga slide off the west coast of Norway had displaced a sediment volume of about 3100 km^3 that travelled a distance of 400 km after the major event and was followed by a series of shorter landslides (Bryn *et al*., 2005; Haflidason *et al*., 2008). In 1979, a part of the Nice new harbour extension slumped into the sea during landfilling operations. A submarine slide with initial volume close to seashore of about 10 million m^3, was followed by a tsunami with an estimated maximum height of 3.5 m and with maximum effects observed 10 km from the slide location (Assier-Rzadkiewicz *et al*., 2000) that caused the death of 8 people. More recently, it was reported that eleven submarine cables across the Kaoping canyon and Manila trench were broken in sequence from 1500 to 4000 m deep, as a consequence of submarine landslides and turbidity currents associated with the 2006 Pingtung earthquakes offshore southwest Taiwan. This event caused major failures in international telecommunication affecting not only Taiwan but all the Southeast and East Asia countries alike (Hsu *et al*., 2008).

The above are only few of the incidents related with submarine mass gravity flows. Figure 1.1 shows the global occurrence of submarine slides reported in literature during recent decades.

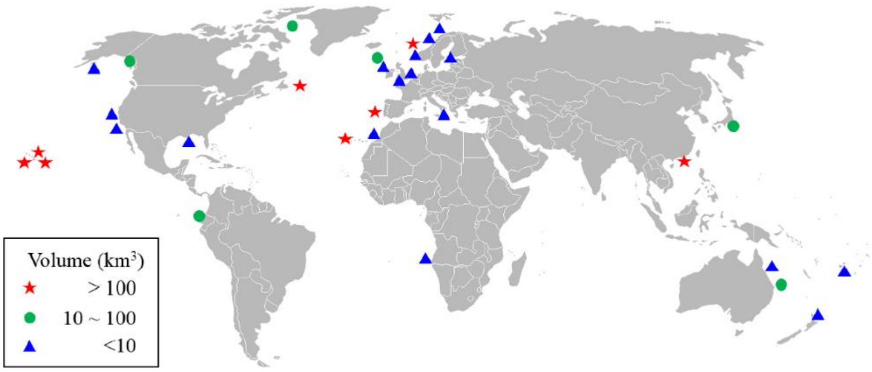

Figure 1.1. Map showing examples (locations) of submarine landslides (after Shanmugam, 2000; Dong, 2017)

The understanding of how this type of submarine flows evolve is a significant problem, as it is extremely difficult to monitor them. They take place in very deep waters where it is very difficult and expensive to approach. The frequency of occurrence of such events is relatively low to allow time predictions. Additionally, the high sediment concentration and velocity develop high forces that are able to destroy the equipment used for their observation.

The analysis of flow deposits can be a useful tool for the back calculation of the initial failure volume and runout distances as well as the type of the mass gravity flow (Bradford and Katopodes, 1999), but remains a demanding and expensive procedure.

Laboratory experiments are considered as an important tool for the understanding of the physical processes that take place during the evolution of a submarine landslide.

They provide clear-cut situations and allow to investigate mass and momentum exchanges and the rheological behaviour that characterise debris flows and turbidity currents during their development or coexistence in transient conditions.

The development of theoretical models comes to complement the physical modelling and field observations. Numerical simulations allow further investigation of the flow behaviour without the scaling limitations of experiments and the unpredictability and high expenses of field observations (Bradford and Katopodes, 1999). Numerical modelling could prove to be a significant tool for the prediction of their dynamic behaviour from inception to runout, after being carefully calibrated using field and experimental data.

1.2 Objective of the thesis

The process of a submarine slide can be divided into three main stages: slope failure of intact soil, transformation of the released material to a viscoplastic fluid that develops a debris flow and the generation of a turbidity current due to the shear stress on top of the debris flow producing a cloud of suspended matter. The term ‘debris flows’ represents a laminar and cohesive flow composed of sediments, and ‘turbidity current’ is a flow with sediment grains suspended in fluid turbulence. Due to the water entrainment and strength degradation of the sliding material, debris flows’s strength decreases gradually and various morphology patterns are shaped within its mass. Although various conceptual runout mechanisms have been reported, the understanding of transformation processes and deposits remains an open scientific issue. The role of the initial volume of the sediments, the seabed slope, the shear strength of the slide-seabed interface and the intact and remoulded shear strength of the sliding material are still far from well-studied.

The aim of this thesis is to present a framework which reproduces submarine landslides and investigates the case of the evolution of a dense debris flow to a dilute turbidity current. This is accomplished in two main parts, the numerical and the experimental study.

The numerical study introduces a two layer framework that describes the coexistence and transition from a basal debris flow to an upper turbidity current layer. A non-Newtonian Herschel-Bulkley rheology is adopted for the lower layer which is assumed to retain a constant density, while the upper layer is endowed with a variable density, depending on the rate of sediment transferred from the parent debris flow and the amount of ambient seawater entrained through mixing. Equations for the conservation of mass and momentum of both layers are expressed in a depth-integrated framework. Exchange mechanisms of mass and momentum between the two layers are proposed to account for the formation of a turbidity cloud and the gradual transition to a fully-developed turbidity current. The model is robust to the emergence or disappearance of any of the two layers by vanishing thickness, and downgrades to known solutions for pure debris flows or turbidity currents when any of the two layers vanishes. Strength degradation of the parent material is included as an option in the model. Simulations at both idealised and real bathymetries are also included in the scope.

The experimental study consists of two experimental campaigns.

The first one focuses on reproducing small scale sediment density flows in a laboratory flume at the Department of Civil Engineering of EPFL. Dense mixtures of plastic sediment of variable grain size (thermoplastic polyurethane) and water were fed into the water-filled flume by gravity from a supply tank. The effects of sediment size and bed slope on the propagation and the internal stratification of such flows are investigated. The runout distance and flow thickness are used to highlight the differences in the dynamic behaviour of the flow for each test case.

The second part includes dam-break type experiments that were conducted at the laboratory of the Civil Engineering department of UCL. Mixtures of plastic sediment and water are examined in a sudden lock-exchange release for different combinations to highlight the effect of sediment volumetric concentration. Image analysis and UVP (Ultrasonic Velocity Profile) allowed the observation of velocity fields, runout distance, flow thickness and internal stratification. A second set of experiments using kaolin clay slurries tested in the same set-up will provide information for opening a discussion about the performance of different sediment types in such experiments.

The observations from the data gathered from the experiments, are aimed to provide a validation database for the two layer depth-integrated model of subaqueous landslides presented in this study but also for different modelling approaches. The obtained dataset may also serve as a basis for the improvement of the parametrization of the relations that govern the transition between different phases of the flows.

1.3 Thesis organization

This thesis comprises eight chapters. The seven chapters following the introductory chapter are arranged as follows.

Chapter 2 reviews state-of-the-art research on submarine landslides, covering both experimental and numerical studies. The rheological models that characterise the flow behaviour and the mechanisms that govern the development of a dilute layer on top of the parent flow, are also reviewed.

Chapter 3 introduces the numerical formulation and development of the two-dimensional two-layer model SWBI2D. The constitutive equations and the numerical schemes are described in detail. The numerical solution is tested for a dam-break problem for a case involving two layers of identical density and for a case involving two layers of different densities with known analytical solutions.

Chapter 4 investigates the model's behaviour on a hypothetical 1-D slope break bathymetry. Runout distance, flow thickness, velocity and sediment concentration are presented for a main parameter's sensitivity analysis.

Chapter 5 reports on the experimental study which focuses on reproducing small scale sediment density flows in a laboratory flume. The effects of sediment size and bed slope on the propagation and the internal stratification of such flows are investigated. The coexistence of two superposed layers is justified.

Chapter 6 presents the experimental campaign on lock-exchange set-up which investigates the evolution of a density-laden flow that can be interpreted in various ways depending on the initial sediment concentration of the upstream reservoir. It involves the reproduction from debris flows for high concentration to hybrid flows for low concentrations. Results produced after image processing procedure and UVP measurements are used to prove the effect of different initial sediment concentration. Results are compared with those of the numerical simulation of the problem using the introduced two-layer model SWBI2D.

Chapter 7 presents a simulation of a large scale event. Real bathymetry data have been used to test the model's behaviour on a 2-D case.

Chapter 8 summarises the key conclusions from this research and provides further recommendations for future studies.

Chapter 2 Literature Review

2.1 Introduction

This chapter presents a state-of-the-art review of submarine landslide research focusing on the transformation of a debris flow to a turbidity current. The discussion covers experimental and numerical modelling techniques of the runout and transition process, flow behaviour characterised by rheological models and interaction mechanisms that govern the development of a debris flow layer on top of a parent debris flow layer. A brief introduction to the strain softening phenomenon is also included.

2.2 Submarine gravity flows

Submarine landslides constitute a widespread phenomenon in submarine environments. The classification of a submarine gravity flow into rigidly defined categories is not clear, as there is no wholly accepted definition for these flows, nor is there a quantitative way of determining whether a flow is a debris flow, a turbidity current or some other type of gravity flow. The basic categories are turbidity currents, debris (and mudflows), and grain flows. Gani (2004) recognizes that these flows are distinguished by four characteristics: sediment concentration, sediment-support mechanism, flow rate, and rheology. Among these, rheology can be mostly used as diagnostic tool. Despite the different modes of mudflows, all initiate when the down-slope component of shear stress exceeds the shear strength (Hampton *et al*., 1996; Iverson *et al*., 1997). This work is focused on the study of subaqueous debris flows and turbidity currents.

Subaqueous debris flows are dense, viscous sediment-water mixtures that move downslope linearly as an agglomeration of particles held together by a thick sediment matrix. They are mainly composed of silt, clay and water and show cohesive behavior (Middleton and Hampton, 1976; Elverhoi *et al*., 2000). This cohesion gives the matrix a shear strength. Shear stresses in the bottom of the flow generated by its movement exceed the matrix shear strength and cause the flow to shear. This shearing decreases upward through the flow as stresses drop and velocity increases (Pratson *et al*., 2000). At the height that the shear stress becomes less than the matrix shear strength, shearing stops and the flow moves as a plug with uniform velocity. Thus a debris flow can be subdivided into a shear layer overlain by a plug layer (Lin and Leblond, 1993). According to laboratory experiments conducted by Mohrig *et al*. (1998, 1999), subaqueous debris flows cause negligible sea-floor erosion and water entrainment. The hydroplaning of the head of the flow, as also the cohesive mud matrix of a debris flow inhibits the exchange of water and sediment across its surface (Pratson *et al.*, 2000). As a consequence, the volume of sediment and water in a subaqueous debris flow does not change significantly between when it starts and ends.

Turbidity currents are particle-laden, gravity-driven underflows in which the particles are largely or wholly suspended by fluid turbulence. Turbidity currents are considered as non-conservative, in the sense that they may exchange particles with a loose lower boundary (i.e., a sediment bed) by deposition or suspension, and may exchange fluid with the ambient by entrainment or detrainment (Middleton and Hampton, 1976; Meiburg and Kneller, 2010). Such flows dissipate mainly through the deposition of the particles. Particle volumetric concentrations are between 0.1 to 7% so that particle-particle interactions play a negligible role in maintaining in suspension (Bagnold, 1954). Nevertheless it should be noted that higher concentration turbidity currents have been proposed by Lowe (1982). Turbulence keeps the sediment in suspension and acts to entrain new material from the bed as other grains settle out (Garcia and Parker, 1991).

2.3 Stages of submarine mass movements

The initiation of a subaqueous landslide can originate from a hyperconcentrated flow, a single failure event or smaller failures that merge into a larger one (Locat and Lee, 2005). Main triggering mechanisms are the increase of the gravitational forces and the decrease of the material’s strength. Possible triggers are earthquakes (Hampton, 1996), sediment accumulation

(Christian, 1994), erosion (Lee, 2004), gas hydrates (Bryn *et al*., 2005), groundwater seepage (Hampton, 2002) and human activity (Seed, 1988).

Depending on the nature of the material that forms the slide, the triggering mechanism and the available energy, the initial mass can form a debris flow with specific flow properties. As it runs down the slopes and interacts with the sea floor and ambient sea water, this mass movement event may evolve from a dense, debris flow to a dilute, turbidity current.

According to Locat and Lee (2005), the release and development of a slide can be divided into three main phases: (i) the initial failure and break-up of blocks and slumps, (ii) the transformation of the released material to a viscoplastic fluid and the development of a debris flow and (iii) the generation of the turbidity current due to the shear stress on top of the debris flow producing a cloud of suspended matter. Figure 2.1 gives a schematic diagram of key characteristics of a submarine landslide.

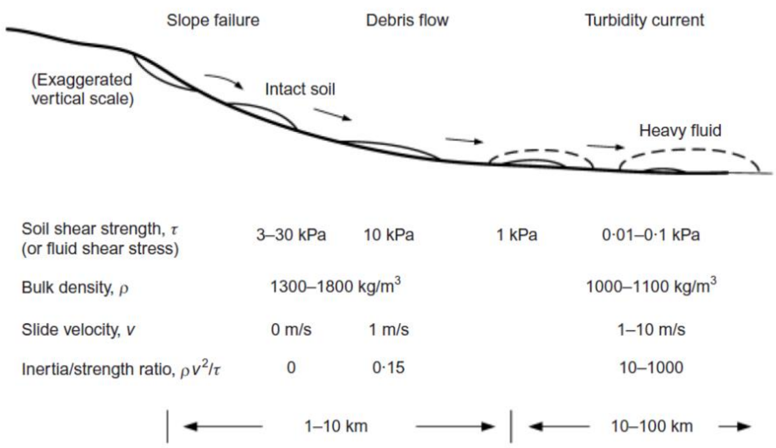

Figure 2.1. Schematic diagram of key submarine slide characteristics (after Boukpeti, 2012).

2.4 Rheological models

The study of the strain rate within the deforming material of a subaqueous mass plays a major role for the description of the evolution process from an intact seabed material to a debris flow and then to a turbidity current. Turbidity currents and debris flows are described by different flow models.

The most common fluid flow model is Newton's law of viscosity, which relates the shear stress in the fluid to the shear strain rate by means of a constant proportionality called the dynamic viscosity. Viscosity is generally referred to the slope of the shear stress–strain rate curve. A turbidity current is characterized by very low volumetric particle concentration (<10%) that leads to a very small to negligible interaction between particles. Therefore, it can be considered as a Newtonian fluid, with the shear stress τ described by the following relationship

$$\tau = \mu\dot{\gamma} = \mu\left(\frac{du}{dz}\right) \tag{2.1}$$

where μ is the dynamic viscosity, $\dot{\gamma}$ is the shear rate, u the horizontal velocity and z is the vertical coordinate.

Conversely, the fluids like debris flows that contain a certain sediment concentration are considered as non-Newtonians, as they exhibit a minimum stress below which the strain rates are very small and no movement can occur. This minimum stress is called yield stress τ_y.

The models used to describe debris flow based on the rheology are classified into viscous models (Johnson, 1970; Jiang and LeBlond, 1992), viscoplastic models (Edgers and Karlsrud, 1981) and frictional models (Locat and Demers, 1988). Among them, the Bingham viscoplastic fluid (Bingham, 1922) has been commonly used due to its simplicity and its ability to reproduce dynamic behaviors of the flow such as stoppage and formation of plugs (Pastor, 2004). However, Bingham model may overestimate the yield stress significantly due to the shear thinning at low shear rates (Wan, 1982; O'Brien and Julien, 1988) in the cases of clay-rich slurries mudflows. Huang and Garcia (1998) suggested that the nonlinear viscoplastic Herschel-Bulkley model (Coussot, 1997) is more appropriate in depicting the shear thinning behavior of debris flows and fits rheological data very well in a wider range of shear rates (Niedorodo 2006, Elverhoi, 2005).

The relationship between shear stress τ and the rate of strain $\dot{\gamma} = \dot{\partial u}/\partial z$ for a viscoplastic fluid following the Bignham rheology can be expressed as

$$\tau = \mu\dot{\gamma} = \begin{cases} 0 & if \quad |\tau| < \tau_y \\ \tau - \tau_y \operatorname{sgn}(\dot{\gamma}) & if \quad |\tau| \geq \tau_y \end{cases} \tag{2.2}$$

where τ_y is the yield strength and μ is the dynamic viscosity.

The non-linear Hershel-Bulkley rheological model can be expressed as:

$$\tau = K|\dot{\gamma}|^n \operatorname{sgn}(\dot{\gamma}) = \begin{cases} 0 & if \quad |\tau| < \tau_y \\ \tau - \tau_y \operatorname{sgn}(\dot{\gamma}) & if \quad |\tau| \geq \tau_y \end{cases} \tag{2.3}$$

where K is the consistency coefficient determined from rheological tests and n is the flow behavior index usually ranging between 0 and 1. The model is reduced to the Bingham rheological model for the case of $n = 1$ and $K = \mu$, with μ the dynamic viscosity.

All the above mentioned rheological models that are commonly used to describe subaqueous mass flows are depicted in Figure 2.2.

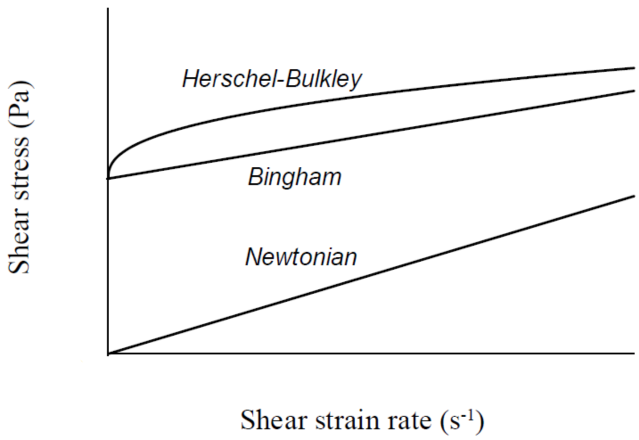

Figure 2.2. Rheological models.

2.5 Laboratory experiments

For many decades following the pioneering papers by (Kuenen, 1937; Kuenen and Migliorini, 1950; Heezen and Ewing, 1954), turbidity currents have been at the focus of geologists' research on large-scale sediment transport in the oceans. The experimental work of (Hampton, 1970-1972) showed convincingly that submarine debris flows have the potential for transporting large sediment masses over considerable distances and play a more important role in generating turbidity currents than had hitherto been recognized.

No exact concentration and viscosity limits were given by Kuenen for the different flow categories, but these were presented later by Dangeard (1965) for flows with different clay types of different concentrations. The importance of composition was also observed in the experiments of Buffington (1961) who generated turbidity currents using a lock box on the ocean floor in which sea floor sediment was used to start a dense flow.

Experiments on subaqueous sediment failures starting from an intact bed have been described in several studies (Rettger, 1935; Einsele, 1974; Schwartz, 1982; Zreik, 1994; Zreik et al., 1995; Ancey and Cochard, 2009; Cochard and Ancey, 2009). These experiments induce failure by tilting a tabular sediment bed until failure occurs or with a ‘dam-break’ release method in which a vertical wall is suddenly released in front of an inclined tabular bed (Ancey and Cochard, 2009).

Dangeard *et al.* (1965) observed the formation of a dilute cloud on top of a dense underflow if the velocity was high enough and the viscosity of the underflow not too high. This dilute flow on top continued moving as an independent turbidity current even after the dense underflow had stopped.

Hampton (1972) observed in laboratory experiments of very dense initial flows that this dilute cloud formed mainly due to erosion of material from the head of the flow, whereas not much material was eroded from the top of the main body of the flow.

The experiments of Mohrig *et al.* (1998) with clay-rich slurries reveal high mobility of the frontal part due to the formation of a lubricating water layer, a process called hydroplaning, that leads to higher velocities and shear and therefore more erosion from the head in its interface with ambient fluid. Mohrig *et al.* (1998) demonstrated that the initiation of hydroplaning is governed by a threshold densimetric Froude number. They report calculations that indicate that hydroplaning of field scale subaqueous debris flows should be relatively common, and offer it as one mechanism for the relatively long runout on very low slopes often inferred from submarine deposits. All of the experimental slurries of Mohrig (1998) consisted of mixtures of water, silt, and sand.

Mohrig *et al.* (1999) showed that the debris flow needs to accelerate to the speed which satisfies the threshold Froude number and additionally needs to be clay-rich so that it remains a coherent fluid mass as it flows. Elverhøi *et al*. (2005) define a clay-rich mudflow as more than 25 percent clay. They found that weakly coherent "sandy" debris flows have less than 10 percent clay and moderately coherent flows have 10-20 percent clay. Ilstad (2004) point out that sandy debris flows lack the coherence needed to hydroplane. Instead, when they accelerate, the heads tend to take on ambient water, expand and become turbulent. This is a direct transition to a turbidity current.

Using data and equations from many laboratory experiments, Talling *et al.* (2002) quantitatively show that shear mixing at the head and upper surface of a debris flow can be an efficient transformation to a turbidity current if the parent flow is large and has high enough velocity.

Mohrig and Marr (2003) performed laboratory experiments to examine the processes controlling the transfer of sediment from a relatively dense submarine debris flow or slide to a relatively dilute turbidity current, as a function of the original composition of the dense parent phase and the transport velocity of the dense parent flow. It was concluded that the sediment erosion from the head of the parent flows is relatively inefficient production mechanism of turbidity current, while turbulent mixing is much more efficient but not quantified mechanism. It was also noted that less than 1% of the debris flow material gets incorporated into the turbidity current, the amount does increase with decreasing coherence of the debris flow.

Laboratory experiments were undertaken by Felix and Peakall (2006) to investigate the transformation mechanisms of debris flows into turbidity currents. The transformation includes multiple processes like erosion off the dense mass, breaking apart of the dense underflow, breaking of internal waves and turbulent mixing. Some of these processes take place simultaneously in a flow event, while other at different places and positions. It was observed that more transformation to a turbidity current layer occurs for less-cohesive debris flows (Felix and Peakal, 2006).

Elverhio *et al.* (2010) tested subaqueous debris flows of varying sand-to-clay ratio. If the sand-content is increased, the flow becomes less cohesive and that leads to internal particle segregation and a bipartite flow with an upper clayey and silty low-density layer and a lower sandy granular high-density layer. The experimental program of Zakeri (2010) studied subaqueous gravity flows of different clay-rich slurries. The thickness of the slurry flows, the generated turbidity currents, as also of their deposits were measured. It was reported that the increase of the clay content tends to decrease the thickness of the slurry head and increase the thickness of the overriding turbidity currents and the deposited layers.

2.6 Numerical models

As the direct observation of the initiation and flow of submarine landslides is almost impossible, main information is given by the analysis of landslide deposits. Laboratory experiments and study of the historical data form empirical relationships and approximated numerical methods are used to predict runout distance, flow thickness, velocity and deposits' volume. Numerical models are developed to simulate submarine sediment-laden flows taking into account rheology, topography and complexity.

Most of the models introduce 1-D and 2-D depth-averaged single layer frameworks (Edgers and Karlsrud, 1981; Bradford and Katopodes, 1999; Imran, 2001). The loss of information about the vertical profiles of velocity and density is usually insignificant for large scale events (Masson, 2006), therefore shallow water equations (depth-integrated Navier-Stokes equations) are usually used. The depth-averaged formulation consists of a hyperbolic system of partial differential equations derived by Parker (1986). Godunov-type schemes like HLL and HLLC Rieman solvers are typically used to treat the discontinuities of hyperbolic equations (Toro and Spruce, 1994; Fracarollo *et al.*, 2003).

Huang and Garcia (1998) presented a viscoplastic model to describe the propagation and deposition of a 2-D unsteady laminar mud flow that can be adapted to both subaerial and submarine environment. The results achieved good agreement with experimental and measured data.

Pratson *et al.* (2000) presented a debris flow model based on the 1-D depth averaged flow equations as proposed by Lin and Leblond (1993) and a turbidity current model described by the depth averaged flow and concentration equations as proposed by Parker *et al.* (1986). The numerical models were used for the comparison of the dynamic behavior and deposits of these sediment-laden flows.

Imran *et al.* (2001) presented a 1-D model to simulate the dynamics of a finite-source subaqueous debris flow incorporating the Herschel-Bulkley and bilinear rheologies of viscoplastic fluids. It is a layer-integrated model in a Langrangian framework, using explicit finite difference schemes. It was used by Marr *et al.* (2002) to evaluate the sensitivity of the run-out distances to the fall height, volume and fluid parameters for the real cases of the Isfjorden Fan and Bear Island debris flows.

Drago (2001) presented two models, one suitable for debris flows and the other for turbidity currents. The two models have been coupled imposing the results of the debris flow model as bottom boundary condition of the turbidity current generated on top.

Niederoda *et al.* (2003) developed a debris flow model that operates in Eulerian framework based on the assumption that the flow thickness is relative to its length and its rheology can be represented as a Bingham fluid.

More recently, two-layer models have been introduced in which the two layers, except from their distinct densities and velocities, retain their rheological properties (Castro *et al.* 2001; Capart and Young 2002). In the two-layer models, each flow zone is characterized by specific concentration and velocity profiles, but sediments in each layer are assumed to be transported at the same velocity as water, forming a unique phase. They are based on the continuity and momentum balance equations evaluated on a specific control volume for each layer. Interactions between the two layers will include both pressure and shear stresses along the interface, under the assumption that no mass transfer takes place (Chen and Peng, 2006).

A two layer framework for dam break induced sheet flows was studied by Spinewine (2005), where a dense basal layer of mixed water and sediment is created below the clear water layer. Chen and Peng (2006) presented a 1-D model imposing two superposed layers with different velocity, density and rheology and using a finite volume method to solve 2-D shallow water equations. A similar model was implemented in breach flow cases with a mud-flow layer and a clear water layer (Chen *et al*, 2007). Benkhaldoun *et al.* (2014) proposed a solver of multi-layer shallow water equations for density-driven flows over flat or non-flat topography. The method consists of two steps in which the hydraulic variables of the flow equations are coupled with the concentration variables of the sediment transport equations.

2.7 Interactions between layers

2.7.1 Sediment erosion/deposition

One of the main tasks of the study of subaqueous sediment-laden flows is the understanding and the parametrisation of the processes that define their interaction with the surrounding environment. Their influence on the sea bed morphology by depositing, eroding or dispersing large quantities of sediments, the mechanism that governs the development of a turbidity current on top of a debris flow and the entrainment of ambient water that causes the dissipation of such flows have been studied. Some of the attempts for the quantification of such processes are discussed below.

According to laboratory experiments conducted by Mohrig (1998, 1999), subaqueous debris flows cause negligible sea-floor erosion and water entrainment. The hydroplaning of the head of the flow, as well as the cohesive mud matrix of a debris flow inhibits the exchange of water and sediment across its surface (Pratson *et al.*, 2000).

On the contrary, during the propagation of a turbidity current, deposition and erosion of the sea bed takes place as well as the incorporation of ambient water in the flow through mixing in the head and their interface.

The volumetric rate of total (sediment and water) deposition D_t is given by

$$D_t = \frac{w_s r_0 C}{1-\varepsilon} \tag{2.4}$$

where w_s is the sediment settling velocity, r_0 is the ratio between the sediment concentration at the bed c_b to the concentration averaged through the thickness of the turbidity current layer C and ε is the bed porosity.

Parker (1982) suggested the following formula for the calculation of the ratio r_0

$$r_0 = 1 + 31.4\left(\frac{u_*}{w_s}\right)^{-1.46} \tag{2.5}$$

where $u_* = (\tau_b/\rho)^{0.5}$ is the bed shear velocity, τ_b is the bed shear stress and w_s is the settling velocity.

Garcia (1985) tested the formula for laboratory experiments and achieved good agreement for $5 < u_*/w_s < 50$. A constant value of r_0 equal to 1.6 has been found that it approximates well the data (Parker *et al.*, 1986).

The settling velocity w_s is calculated by the empirical relationship developed by Dietrich (1982)

$$w_s = \sqrt[3]{w_* R g \nu} \tag{2.6}$$

where w_* is the dimensionless settling velocity that can be calculated by the following approximation based on data from arbitrarily shaped natural particles

$$\log w_* = -3.76715 + 1.92944(\log D_*) - 0.09815(\log D_*)^2 - 0.00575(\log D_*)^3 + 0.00056(\log D_*)^4$$

with D_* the effective diameter

$$D_* = D_s\left(\frac{Rg}{\nu^2}\right)^{1/3}$$

$R = (\rho_{sed} - \rho_w)/\rho_w$ is the submerged specific gravity of the sediments, ρ_{sed} is the density of the sediments, ρ_w is the density of ambient fluid (most cases water), g is the gravitational acceleration, D_s the sediment particle diameter and ν is the kinematic viscosity of the ambient fluid.

During the propagation of the turbidity current on the seabed, partial erosion of the seabed may be observed. Experimental studies (Akiyama and Fukushima, 1984; Garcia, 1985; Parker *et al.*, 1986) suggested that bed sediment entrainment to the turbidity current can be influenced by its velocity, sediment size, sediment and fluid density, fluid viscosity and particle settling velocity. The volumetric rate of sediment erosion is represented as

$$E_{sed} = E_s w_s \tag{2.7}$$

where E_s is the bed sediment entrainment coefficient and w_s is the sediment settling velocity.

Akiyama and Fukushima (1984) based on field and lab data for open channel flow suspensions, proposed the following relationship for bed sediment entrainment coefficient

$$E_s = \begin{cases} 0.3 & for \quad Z > 13.2 \\ 3 \cdot 10^{-12} Z^{10} \left(1 - \frac{5}{Z}\right) & for \quad 5 > Z > 13.2 \\ 0 & for \quad Z < 5 \end{cases} \tag{2.8}$$

where

$$Z = \frac{u_*}{w_s} R_p^{\,0.5}$$

with u_* the bed shear velocity, w_s the sediment settling velocity and $R_p = (RgD_s)^{0.5} D_s / v$ the particle Reynolds number, D_s the sediment particle diameter and v the kinematic viscosity of water.

Garcia and Parker (1993) developed another empirical relationship for sediment entrainment coefficient

$$E_s = \frac{1.3 \cdot 10^{-7} Z^5}{1 + \frac{1.3 \cdot 10^{-7} Z^5}{0.5}} \tag{2.9}$$

where

$$Z = \alpha_1 u_* R_p^{\,\alpha_2}$$

with u_* the bed shear velocity, R_p the particle Reynolds number and α_1 and α_2 given by

$$\alpha_1 = \begin{cases} 1 & for \quad R_p > 2.36 \\ 0.586 & for \quad R_p \le 2.36 \end{cases}$$

$$\alpha_2 = \begin{cases} 0.6 & for \quad R_p > 2.36 \\ 1.23 & for \quad R_p \le 2.36 \end{cases}$$

as suggested by Imran *et al.* (1998).

The volumetric rate of total erosion E_t is given by

$$E_t = \frac{w_s E_s}{1-\varepsilon} \tag{2.10}$$

where w_s is the sediment settling velocity, E_s is the bed sediment entrainment coefficient and ε is the bed porosity.

2.7.2 Water entrainment

Entrainment of ambient water into the current reduces the density of the turbidity current and the component of the gravitational force acting in the downslope direction. This fact causes the reduction of the velocity of the current and leads to the drop of its sediment load that eventually leads to its dissipation.

Experimental work of Ellison and Turner (1958), Fukushima (1981) and Parker *et al.*(1986) connected entrainment with turbidity current's velocity, the relative density difference between the turbidity current and the ambient fluid, and the dimension of the turbidity current. The entrainment velocity w_e is represented as

$$w_e = e_w U \tag{2.11}$$

where e_w is the dimensionless entrainment coefficient and U is the cross-sectional averaged velocity of the turbidity current layer.

Ellison and Turner (1959) suggested a relationship that connects the detrainment coefficient to the Richardson number Ri

$$e_w = f(Ri) \tag{2.12}$$

with $$Ri = \frac{RCgh_{TC}}{U^2}$$

where R is the submerged specific gravity, C is the layer-averaged current concentration, g is the gravitational constant and U is the layer-averaged current velocity. Egashira (1977), Fukushima (1981) and Garcia (1986) proposed variations on this relationship given below

(i) Ellison and Turner (1959)

$$e_w = \frac{0.08 - 0.1Ri}{1 + 5Ri} \qquad for \quad Ri < 0.8 \tag{2.13}$$

(ii) Ashida and Egashira (1977)

$$e_w = \frac{0.0015}{Ri} \tag{2.14}$$

(iii) Fukushima *et al.* (1985) for large Richardson values

$$e_w = \frac{0.00153}{0.0204 + Ri} \tag{2.15}$$

(iv) Garcia (1985)

$$e_w = \frac{0.075}{(1 + 718Ri^{2.4})^{0.5}} \tag{2.16}$$

The empirical relation proposed by Garcia (1985) has been used in the work of Fukushima *et al*. (1985), Parker (1987), Bradford and Katopodes (1999) and others.

2.7.3 Sediment detrainment

Along the top surface of the debris flow layer, sediment material is detached and incorporated into the turbidity current region. The detrainment of the debris flow layer has been suggested as the main mechanism of the generation of the turbidity current layer by many studies (Hampton, 1972; Beghin, 1981; Dai and Garcia, 1998, Mohrig and Marr, 2003; Elverhoi, 2010).

The quantification of the detrainment process remains a challenging area for research and little progress has been done.

Dai and Garcia (2010) adopted thermal theory to investigate the influence of detrainment on a gravity current and to quantify the effect of detrainment. For semi-elliptical gravity current of cross section area A, the rate of detrainment is given by

$$\delta = \kappa S \sqrt{A} U \tag{2.17}$$

where κ is the detrainment coefficient, S is a shape factor equal to circumference/$\sqrt{A}$ for a semi-ellipse and U is the mass-center velocity. Values between 0 and 0.1 were proposed for the detrainment coefficient, based on the available data on the velocity of the thermal in the deceleration phase. The factors that influence the detrainment coefficient are worthwhile of further investigation.

2.7.4 Interfacial friction

After the creation of a turbidity current on top of the parent debris flow, the two layers coexist and propagate simultaneously. Due to the different densities and velocities of the layers, shear stresses are developed at their interface.

Chen (2006) proposed that the upper turbidity current layer can be assumed fluid-like under shear while the lower debris flow layer behaves as a solid-like and responses passively to the shear stress imposed by the upper layer. The basal debris flow layer behaves as a rigid plug with a shear layer developed only close to bed. The interface shear stress τ_{int} between debris flows and turbidity current layers, is ascribed to turbulence and can be expressed by the following Chezy-type relation

$$\tau_{\text{int}} = \rho_{TC} C_f \left| U_r \right| U_r \qquad (2.18)$$

where ρ_{TC} is the turbidity current density, C_f is the Chezy friction coefficient and $U_r = U_{TC} - U_{DF}$ is the relative velocity between the two layers. The Chezy friction coefficient C_f can be calculated by empirical formulas.

2.8 Strain Softening

Slope failures initiate the movement of material downslope in the front of mass gravity flows. Material involved in a slide originates as a solid material and gradually transforms towards a fluid state as it remoulds and softens during its propagation entraining additional water (Randolph, 2011). At failure, the slide material is characterized by geotechnical properties defining stress-strain characteristics. During runout, the slide material undergoes remoulding and softening and transforms into a debris flows with viscoplastic material properties. With further progress the flow transforms into a heavy liquid best described by fluid properties, like a turbidity current. (Randolph *et al.*, 2011).

During the transitional stage as the soil mass accelerates and remoulds, its internal particle-to-particle structure is deranged and its strength drops.

Strength decreases by factors of two to three are common (Locat and Lee 2002) and in extreme cases may be an order of magnitude or more (Locat and Demers 1988). Behavior during the different flow stages largely depends on the composition of a debris flow. This is determined by the relative amount of cohesive clay and granular particles, the size of the grains and clasts, the clay mineralogy and the water content (Middleton & Hampton, 1973; Marr, 2002; Ilstad, 2004c; Elverhøi, 2005). In coarse-grained debris flows where the clay content is relatively low, the flow is characterized by both an internal shearing and grain-to-grain dispersive pressures (Huang and García, 1998).

This gradual reduction of their resistance to shearing, is referred as strain degradation or strain softening, which may result from distinct processes such as water entrainment or shear strain accumulation. The influence of strain softening is important as it will alter the dynamics of the debris flow even for the study of past landslides with matched runout distances.

Randolph *et al.* (2011) suggested that any of the various models that are used to describe debris flows need to be coupled with strain softening and remoulding models to cover soil behaviour during the different transformation stages.

2.8.1 Numerical models

Jiang and LeBlond (1993) developed the BING model using finite difference method with a fixed grid to solve the layer averaged governing equations which uses a two-layer non-steady deformable body to represent debris flows comprising a lower shear layer and an upper plug layer. Imran (2001) implemented Herschel-Bulkley and bilinear rheology to the model. De Blasio *et al.* (2004) and Elverhoi *et al.* (2005) used BING model to back-calculate part of the historic Storegga slide in Norway.

Hu and Randolph (1998a, 1998b) developed a numerical method for two-dimensional large deformation problems in soils based on conventional small strain finite element formulation, involving updating of coordinates, re-meshing and interpolation of mesh and stress parameters.

De Blasio *et al*. (2003) modelled the Storegga debris flow and found that the Bingham yield stress probably decreased with distance travelled because no single value would produce the correct thicknesses over the whole length of the resulting deposit.

Randolph (2004) introduced a numerical model to represent the soil strength degradation from intact to remolded strength due to the accumulated shear strains using an exponential decay law.

Moresi *et al.* (2003) and O'Neill *et al.* (2006) developed a particle-in-cell finite element method, specifically targeted at problems involving large deformation of visco-elastic/plastic material with history-dependent material properties.

2.9 Summary

This chapter has provided a detailed literature review of submarine landslide research. Submarine landslides can be proven as a major geohazard for subsea infrastructure and the understanding of the dynamic processes that govern their initiation and transformation are of high interest for industry. Both experimental and numerical studies are focused on reproducing the behaviour of such flows and estimate runout distances, velocities and potential impact forces on subaqueous infrastructures. The different stages of the evolution process from a dense debris flow to a dilute turbidity current are described by different rheological models. The present research would not exist without the knowledge of the past.

Chapter 3 A two layer framework for the modelling of submarine slide-induced debris flows transitioning to turbidity currents

3.1 Introduction

The present study introduces a two layer framework that describes the coexistence and transition from a basal debris flow layer to an upper turbidity current layer. It considers a dense basal layer with high density that is characterized by a non-Newtonian rheology, and a dilute upper layer of variable density constituting a turbulent turbidity current with Newtonian rheology. Equations for the conservation of mass and momentum of both layers are expressed in a depth-integrated framework. Finite volume method is implemented using HLL schemes for the computation of the fluxes. Exchange mechanisms of mass and momentum between the two layers account for the formation of a turbidity cloud and the gradual transition to a fully-developed turbidity current. The model manages zeroing layer thickness well, and downgrades to known solutions for debris flows and turbidity currents when one layer vanishes.

Since the definition of debris flows and turbidity currents are not strictly quantified, in this study the characterization of the dense basal layer as a debris flows and of the generated dilute layer as a turbidity current constitute an assumption. This assumption is secured by the fact that each layer follows the characteristics and behaviour that are fully established. In the following sections, the debris flow layer refers to the parent dense flow and the turbidity current layer to the upper dilute layer.

3.2 Two-layer model SWBI2D

3.2.1 Formulation of the equations

A two-layer flow submerged into an ambient fluid as shown in Figure 3.1 is adopted. The basal layer of the debris flow is characterized by a height h_{DF}, the depth-averaged velocities $U_{DF,x}$ and $U_{DF,y}$ in the x and y direction respectively and a constant density ρ_{DF}. The upper layer of the turbidity current is characterized by a height h_{tc}, the depth-averaged velocities $U_{TC,x}$ and $U_{TC,y}$ in the x and y direction respectively and a variable density $\rho_{TC} < \rho_{DF}$. The flow takes places into an ambient fluid of constant density ρ_w. The lower rigid boundary of the flow is at level z_b, the interface of the two layers is at level $z_{DF} = z_b + h_{DF}$ and the interface of the upper layer with the ambient fluid is at level $z_{TC} = z_{DF} + h_{TC}$.

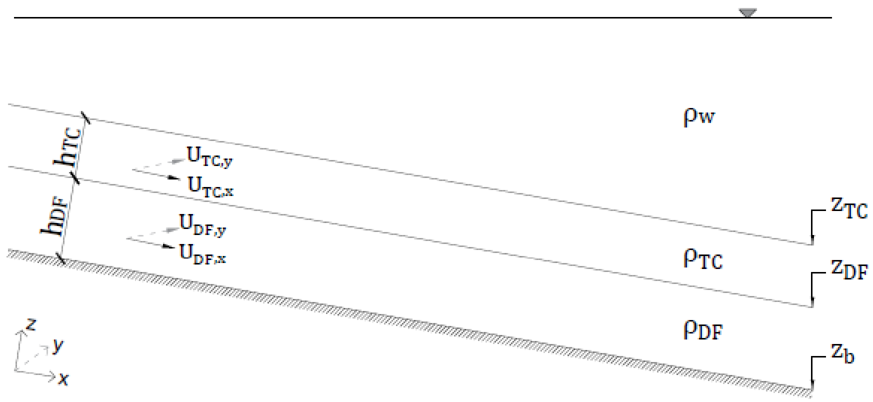

Figure 3.1. Definition sketch of a two-layer shallow-water flow over a mild sloped bed.

If the sediment volumetric concentration is denoted as C, the density of the turbidity layer can be expressed as

$$\rho_{TC} = \rho_{sed} C + \rho_w (1 - C) \tag{3.1}$$

where ρ_{sed} is the sediment density and ρ_w is the ambient fluid (water) density.

If the submerged specific density of the sediments $R = (\rho_{sed} - \rho_w)/\rho_w$ is considered, Equation (3.1) becomes

$$\rho_{TC} = \rho_w (1 + RC) \tag{3.2}$$

The depth-averaged framework is adopted for each layer assuming that the horizontal length is much larger compared to the vertical dimensions, the slopes of the interfaces between the layers are relatively small and that the pressure is considered as hydrostatic. The depth-averaged velocities in the streamwise and spanwise direction are expressed as

$$U_{k,i} = \frac{1}{h_k} \int_0^{h_k} u_{k,i} dh_k \tag{3.3}$$

where the subscript $i = x, y$ denotes the streamwise direction x and the spanwise direction y respectively, the subscript $k = DF, TC$ denotes the lower, debris flow layer and the upper, turbidity current layer and h is the height of each layer.

The mass conservation law and the momentum conservation law in the longitudinal and transverse direction are applied to each layer separately.

Mass conservation for Debris flow layer

The Reynolds transport theorem is applied to a generic mobile control volume CV for each layer separately to express the variation of mass m_k

$$\frac{Dm_k}{Dt} = \underbrace{\frac{\partial}{\partial t} \int_{CV} \rho_k dV}_{\text{I}} + \underbrace{\oint_{CS} \rho_k \overrightarrow{u_{rel}} \cdot d\vec{S}}_{\text{II}} = 0 \tag{3.4}$$

where ρ is the mass density with the subscript $k = DF, TC$ to denote the lower, debris flow layer or the upper, turbidity current layer respectively, CS is the control surface surrounding the CV, $\vec{n}$ is the outward pointing unit vector normal to CS, $d\vec{S} = \vec{n} dS$ is a vector parallel to the $\vec{n}$ with modulus equal to dS and

$$\overrightarrow{u_{rel}} = \overrightarrow{u_k} - \overrightarrow{u_{cs}}$$

is the relative velocity of the fluid with respect to the mobile control surface velocity $\overrightarrow{u_{cs}}$.

The mobile control surface velocity $\overrightarrow{u_{cs}}$ correspond to the normal velocity of each surface S_{num} that surrounds the control volume CV, where num denotes each surface number as depicted in Figure 3.2.

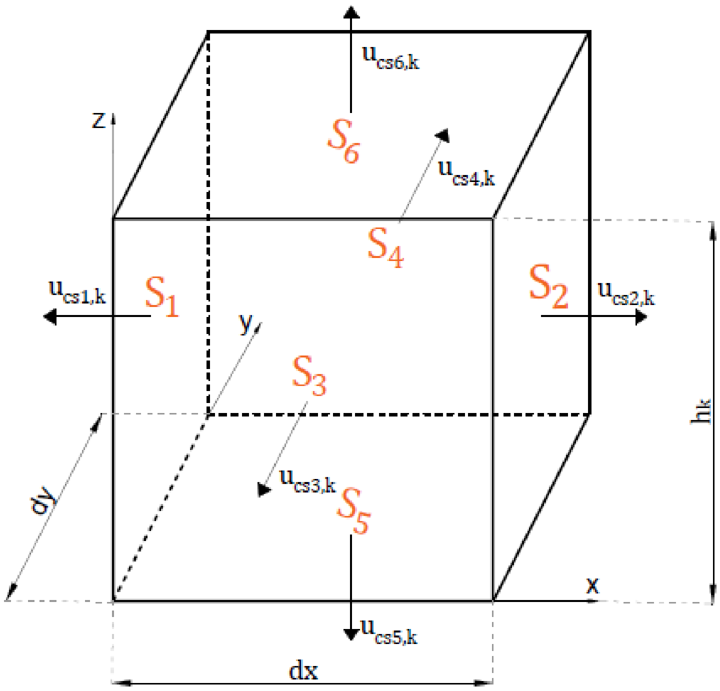

Figure 3.2. Sketch of the control surfaces S_{num} for a control volume CV ($dx \times dy \times h_k$).

Figure 3.3 shows the mass fluxes through control surfaces of the chosen control volume for the debris flow layer. The integral over the control volume of the Equation (3.4) can be expressed as

$$\int_{CV} \rho_{DF} dV = \int_{z_b}^{z_b+h_{DF}} \int_{y}^{y+dy} \int_{x}^{x+dx} \rho_{DF} dxdydz = \rho_{DF} h_{DF} dxdy \tag{3.5}$$

since the distances dx and dy are considered infinitesimal and points x and y are considered fixed. The flow thickness h_{DF} is considered constant between points x and $x + dx$ and points y and $y + dy$, as dx and dy are infinitesimal. Using the Equation (3.5), the term I of Equation (3.4) can be written as

$$\frac{d}{dt}\int_{CV} \rho_{DF} dV = \frac{\partial(\rho_{DF} h_{DF})}{\partial t} dxdy \tag{3.6}$$

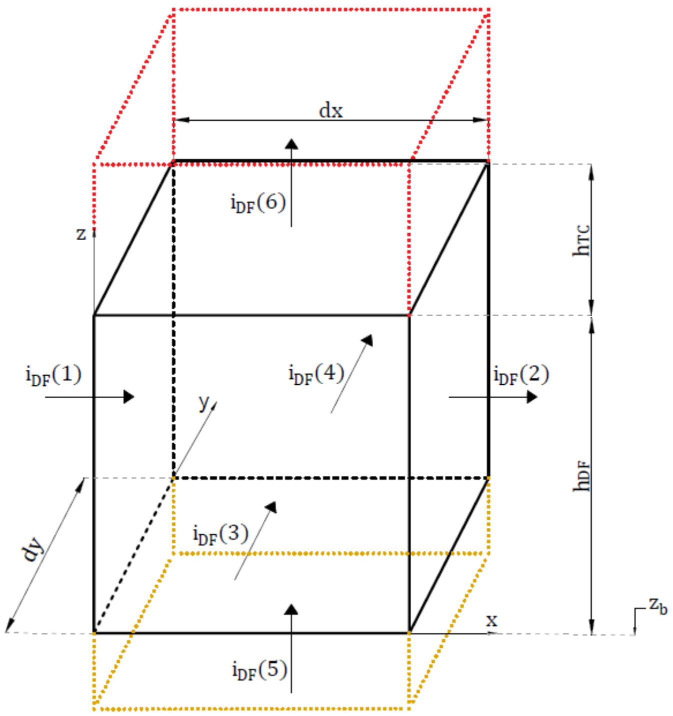

Figure 3.3. The differential control volume CV of the debris flow layer and the mass fluxes through its control surfaces CS.

The control surface CS is composed by six segments (see Figure 3.3).The term II of Equation (3.4) can be written as

$$\begin{aligned}&\oint_{CS} \rho_{DF} \overrightarrow{u_{rel}} \cdot d\vec{S} = \\ &\underbrace{\oint_{S_1} \rho_{DF} \overrightarrow{u_{rel,1}} \cdot d\vec{S_1}}_{i(1)} + \underbrace{\oint_{S_2} \rho_{DF} \overrightarrow{u_{rel,2}} \cdot d\vec{S_2}}_{i(2)} + \underbrace{\oint_{S_3} \rho_{DF} \overrightarrow{u_{rel,3}} \cdot d\vec{S_3}}_{i(3)} + \\ &\underbrace{\oint_{S_4} \rho_{DF} \overrightarrow{u_{rel,4}} \cdot d\vec{S_4}}_{i(4)} + \underbrace{\oint_{S_5} \rho_{DF} \overrightarrow{u_{rel,5}} \cdot d\vec{S_5}}_{i(5)} + \underbrace{\oint_{S_6} \rho_{DF} \overrightarrow{u_{rel,6}} \cdot d\vec{S_6}}_{i(6)}\end{aligned} \tag{3.7}$$

where $i_{DF}(num)$ is the mass flux for control surface num.

According to Taylor's theorem, if a function is continuous and differentiable in an interval $[x, x + dx]$, it can be written

$$f(x+dx)=f(x)+dx\cdot f'(x)+\frac{dx^2}{2}\cdot f''(x)+...$$

The mass fluxes along the x and y direction are calculated taking into account that the intervals $[x, x+dx]$ and $[y, y+dy]$ are so small such that the integrals in the x and y direction are equal to the integrated value times the infinitesimal dx and dy respectively. The control surfaces do not move in the x and y direction, therefore the velocity of the control surfaces S_1, S_2, S_3 and S_4, are equal to zero. As dx and dy are too small, only the first two terms of Taylor's expansion are used for the calculation of $i_{DF}(2)$ and $i_{DF}(4)$.

The absolute values of the mass fluxes along the x direction are calculated as

$$\begin{aligned}&\left|i_{DF}(1)\right|=\left|i_{DF}(x)\right|=\\&\left|\int_{z_b}^{z_b+h_{DF}}\int_{y}^{y+dy}\rho_{DF}(U_{DF,x}-0)dydz\right|=\rho_{DF}U_{DF,x}h_{DF}dy\end{aligned}\tag{3.8}$$

$$\begin{aligned}&\left|i_{DF}(2)\right|=\left|i_{DF}(x+dx)\right|=\left|i_{DF}(1)\right|+dx\cdot\left|i_{DF}(1)\right|^2=\\&\rho_{DF}U_{DF,x}h_{DF}dy+dx\frac{\partial}{\partial x}(\rho_{DF}U_{DF,x}h_{DF}dy)\end{aligned}\tag{3.9}$$

The absolute values of the mass fluxes along the y direction are calculated as

$$\begin{aligned}&\left|i_{DF}(3)\right|=\left|i_{DF}(y)\right|=\\&\left|\int_{z_b}^{z_b+h_{DF}}\int_{x}^{x+dx}\rho_{DF}(U_{DF,y}-0)dxdz\right|=\rho_{DF}U_{DF,y}h_{DF}dx\end{aligned}\tag{3.10}$$

$$\begin{aligned}&\left|i_{DF}(4)\right|=\left|i_{DF}(y+dy)\right|=\left|i_{DF}(3)\right|+dy\cdot\left|i_{DF}(4)\right|^2=\\&\rho_{DF}U_{DF,x}h_{DF}dx+dy\frac{\partial}{\partial y}(\rho_{DF}U_{DF,y}h_{DF}dx)\end{aligned}\tag{3.11}$$

The mass flux $i_{DF}(5)$ corresponds to the flux through the bed level where both the fluid and the control volume velocities are null as it is considered impermeable boundary for the case in which the lower layer is a debris flow where no erosion-deposition with the seabed takes place and the no-slip condition is applied. Consequently, there is no mass flux from the bed to the debris flow layer.

The mass flux $i_{DF}(6)$ is only directed from the debris flow layer to the turbidity current layer, as mass flux with the opposite direction is not considered in this model. The turbidity current can just detrain the debris flow layer and not to deposit on top of it. The $U_{rel,z}$ can be translated as the velocity at which the detrainment takes place. Dai and Garcia (2010) (see Section 2.7) proposed the following relation for the detrainment rate

$$\frac{dA}{dt} = \kappa S \sqrt{A} U \tag{3.12}$$

where A is the cross-sectional area, κ is the detrainment coefficient, S is a shape factor equal to circumference/$\sqrt{A}$ for a semi ellipse and U is the mass-center velocity of the layer.

For this study the above relationship is modified for a two-dimensional and two-layer flow. The total relative velocity of the two layers will be used

$$U_{rel} = \sqrt{(U_{TC,x} - U_{DF,x})^2 + (U_{TC,y} - U_{DF,y})^2} \tag{3.13}$$

The shape factor S is written as

$$S = \frac{A}{\sqrt{Ah_{DF}}}$$

as the height of the flow should be taken into account and the detrainment rate of the debris flow can be written as

$$\frac{d(Ah_{DF})}{dt} = \kappa \frac{A}{\sqrt{Ah_{DF}}} \sqrt{Ah_{DF}} U_{rel,\mathrm{int}} \Rightarrow \frac{dh_{DF}}{dt} = \kappa U_{rel} \tag{3.14}$$

So mass flux $i_{DF}(6)$ that is identical with the detrainment process, can be expressed as

$$\left| i_{DF}(6) \right| = \left| \int_y^{y+dy} \int_x^{x+dx} \rho_{DF} U_{rel,z} dxdy \right| = \rho_{DF} e_d U_{rel} dxdy \tag{3.15}$$

where κ is written as e_d for this two-layer model.

After substituting Equation (3.8) – (3.14), Equation (3.7) becomes

$$\begin{aligned}&\oint_{CS}\rho_{DF}\overrightarrow{u_{rel}}\cdot d\vec{S}=\\&-i_{DF}(1)+i_{DF}(2)-i_{DF}(3)+i_{DF}(4)-i_{DF}(5)+i_{DF}(6)=\\&\rho_{DF}dxdy\frac{\partial(U_{DF,x}h_{DF})}{\partial x}+\rho_{DF}dxdy\frac{\partial(U_{DF,y}h_{DF})}{\partial y}+\rho_{DF}dxdye_dU_{rel}\end{aligned} \tag{3.16}$$

After invoking Equations (3.6) and (3.16) divided by ρ_{DF}dxdy that are independent of position and time, the mass conservation Equation (3.4) becomes

$$\frac{\partial h_{DF}}{\partial t}+\frac{\partial(U_{DF,x}h_{DF})}{\partial x}+\frac{\partial(U_{DF,y}h_{DF})}{\partial y}=-e_dU_{rel} \tag{3.17}$$

Mass conservation for Turbidity current layer

Figure 3.4 shows the mass fluxes through the control surface of the chosen control volume for the turbidity current layer. The integral over the control volume of Equation (3.4) can be expressed as

$$\int_{CV}\rho_{TC}dV=\int_{z_b+h_{DF}}^{z_b+h_{DF}+h_{TC}}\int_y^{y+dy}\int_x^{x+dx}\rho_{TC}dxdydz=\rho_{TC}h_{TC}dxdy \tag{3.18}$$

and the term I of Equation (3.4) becomes

$$\frac{d}{dt}\int_{CV}\rho_{TC}dV=\frac{\partial(\rho_{TC}h_{TC})}{\partial t}dxdy \tag{3.19}$$

The control surface CS is composed by six segments (see Figure 3.4). The term II of Equation (3.4) can be written as

$$\begin{aligned}&\oint_{CS}\rho_{TC}\overrightarrow{u_{rel}}\cdot d\vec{S}=\underbrace{\oint_{S_1}\rho_{TC}\overrightarrow{u_{rel,1}}\cdot d\overrightarrow{S_1}}_{i(1)}+\underbrace{\oint_{S_2}\rho_{TC}\overrightarrow{u_{rel,2}}\cdot d\overrightarrow{S_2}}_{i(2)}+\\&\underbrace{\oint_{S_3}\rho_{TC}\overrightarrow{u_{rel,3}}\cdot d\overrightarrow{S_3}}_{i(3)}+\underbrace{\oint_{S_4}\rho_{TC}\overrightarrow{u_{rel,4}}\cdot d\overrightarrow{S_4}}_{i(4)}+\underbrace{\oint_{S_5}\rho_{TC}\overrightarrow{u_{rel,5}}\cdot d\overrightarrow{S_5}}_{i(5)}+\\&\underbrace{\oint_{S_6}\rho_{TC}\overrightarrow{u_{rel,6}}\cdot d\overrightarrow{S_6}}_{i(6)}\end{aligned} \tag{3.20}$$

where $i_{TC}(num)$ is the mass flux for control surface num.

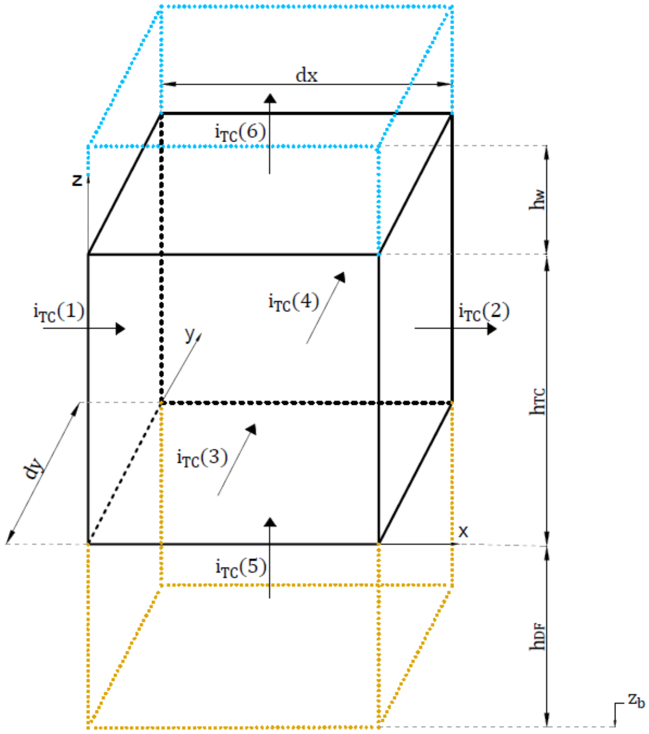

Figure 3.4. The differential control volume CV of the turbidity current layer and the mass fluxes through its control surfaces CS.

Following the same procedure as the one for the debris flows layer and using the Taylor's expansion and the hypotheses that control surfaces do not move along x and y direction, the absolute values of the mass fluxes in the x direction are

$$\left|i_{TC}(1)\right| = \left|i_{TC}(x)\right| = \left|\int_{z_b+h_{DF}}^{z_b+h_{DF}+h_{TC}} \int_{y}^{y+dy} \rho_{TC}(U_{TC,x} - 0)dydz\right| = \rho_{TC} U_{TC,x} h_{TC} dy \tag{3.21}$$

$$\left|i_{TC}(2)\right| = \left|i_{TC}(x+dx)\right| = \left|i_{TC}(1)\right| + dx \cdot \left|i_{TC}(1)\right|^2 = \rho_{TC} U_{TC,x} h_{TC} dy + dx \frac{\partial}{\partial x}(\rho_{TC} U_{TC,x} h_{TC} dy) \tag{3.22}$$

and in the y direction are

$$\left|i_{TC}(3)\right| = \left|i_{TC}(y)\right| = \left|\int_{z_b+h_{DF}}^{z_b+h_{DF}+h_{TC}} \int_x^{x+dx} \rho_{TC}(U_{TC,y} - 0)dxdz\right| = \rho_{TC} U_{TC,y} h_{TC} dx \tag{3.23}$$

$$\left|i_{TC}(4)\right| = \left|i_{TC}(y+dy)\right| = \left|i_{TC}(3)\right| + dy \cdot \left|i_{TC}(4)\right|^2 = \rho_{TC} U_{TC,x} h_{TC} dx + dy \frac{\partial}{\partial y}(\rho_{TC} U_{TC,y} h_{TC} dx) \tag{3.24}$$

The mass flux $i_{TC}(5)$ corresponds to the interface of the two layers. Mass flux occurs only from the basal layer to the turbidity current layer, as in this model deposition of the turbidity current on top of the debris flow is not considered

$$\left|i_{TC}(5)\right| = \left|i_{DF}(5)\right| = \left|\int_y^{y+dy} \int_x^{x+dx} \rho_{DF} U_{rel,z} dxdy\right| = \rho_{DF} U_{rel} dxdy \tag{3.25}$$

The mass flux $i_{TC}(6)$ corresponds to the interface of the turbidity current and the ambient fluid layer. Mass flux $i_{TC}(6)$ refers to the entrainment of the ambient fluid into the turbidity current layer. As discussed in Section 2.7, the entrainment rate is equal to $e_w U_{rel}$ which can represent the relative motion of the interface to the flow velocity. The velocity of the interface between the turbidity current layer and the ambient water layer for the two dimensional flow is

$$U_{rel,TCw} = \sqrt{(U_{TC,x} - U_{w,x})^2 + (U_{TC,y} - U_{w,y})^2} \tag{3.26}$$

and as the ambient fluid layer is at rest $U_{w,x} = U_{w,y} = 0$, Equation (3.26) becomes

$$U_{TC,xy} = U_{rel,TCw} = \sqrt{(U_{TC,x})^2 + (U_{TC,y})^2} \tag{3.27}$$

Using this definition, the mass flux $i(6)$ is calculated as

$$\left|i_{TC}(6)\right| = \left|\int_y^{y+dy} \int_x^{x+dx} \rho_{TC} U_{rel,z} dxdy\right| = \rho_{TC} e_w U_{TC,xy} dxdy \tag{3.28}$$

After substituting Equations (3.21) – (3.28), the Equation (3.20) becomes

$$\begin{aligned}
&\oint_{CS} \rho_{TC} \overrightarrow{u_{rel}} \cdot d\vec{S} = \\
&-i_{TC}(1) + i_{TC}(2) - i_{TC}(3) + i_{TC}(4) - i_{TC}(5) - i_{TC}(6) = \\
&\rho_{TC} dxdy \frac{\partial (U_{TC,x} h_{TC})}{\partial x} + \rho_{TC} dxdy \frac{\partial (U_{TC,y} h_{TC})}{\partial y} + \\
&\rho_{TC} e_w U_{TC,xy} dxdy + \rho_{DF} dxdy e_d U_{rel}
\end{aligned} \tag{3.29}$$

After invoking Equation (3.19) and (3.29) divided by $\rho_{TC} dxdy$ that are independent of position and time, the mass conservation Equation (3.4) for the turbidity current layer becomes

$$\frac{\partial h_{TC}}{\partial t} + \frac{\partial (U_{TC,x} h_{TC})}{\partial x} + \frac{\partial (U_{TC,y} h_{TC})}{\partial y} = \frac{\rho_d}{\rho_{TC}} e_d U_{rel} + e_w U_{TC,xy} \tag{3.30}$$

Sediment mass conservation for Turbidity current layer

The turbidity layer has variable density that depends on the sediment concentration. The sediment mass of the turbidity current can be expressed as

$$m_{sed} = \rho_{sed} V_{sed} = \rho_{sed} C V_{TC} = \rho_{sed} C V_{TC} = \frac{\rho_{sed}}{\rho_{TC}} C m_{TC} \tag{3.31}$$

where V corresponds to volume and the Reynold's theorem can be applied for its conservation

$$\frac{Dm_{sed}}{Dt} = \underbrace{\frac{\partial}{\partial t} \int_{CV} \rho_{TC} \frac{\rho_{sed}}{\rho_{TC}} C dV}_{\mathrm{I}} + \underbrace{\oint_{CS} \rho_{TC} \frac{\rho_{sed}}{\rho_{TC}} C \overrightarrow{u_{rel}} \cdot d\vec{S}}_{\mathrm{II}} = 0 \tag{3.32}$$

The sediment mass fluxes through control surface of the chosen control volume for the turbidity current layer can be shown in Figure 3.4. The integral over the control volume of the Equation (3.32) can be expressed a

$$\int_{CV} \rho_{sed} C dV = \int_{z_b + h_{DF}}^{z_b + h_{DF} + h_{TC}} \int_{y}^{y+dy} \int_{x}^{x+dx} \rho_{sed} C dx dy dz = \rho_{sed} C h_{TC} dx dy \tag{3.33}$$

and the term I of Equation (3.32) becomes

$$\frac{d}{dt} \int_{CV} \rho_{TC} dV = \frac{\partial (\rho_{sed} C h_{TC})}{\partial t} dx dy \tag{3.34}$$

Following the same procedure and hypotheses as for the total mass conservation of the turbidity current, the absolute values of the mass fluxes in the x direction are

$$\begin{aligned}&\left|i_C(1)\right| = \left|i_C(x)\right| = \\ &\left|\int_{z_b+h_{DF}}^{z_b+h_{DF}+h_{TC}} \int_{y}^{y+dy} \rho_{sed} C(U_{TC,x} - 0) dydz\right| = \rho_{sed} C U_{TC,x} h_{TC} dy\end{aligned} \tag{3.35}$$

$$\begin{aligned}&\left|i_C(2)\right| = \left|i_C(x+dx)\right| = \left|i_C(1)\right| + dx \cdot \left|i_C(1)\right|^2 = \\ &\rho_{sed} C U_{TC,x} h_{TC} dy + dx \frac{\partial}{\partial x}(\rho_{sed} C U_{TC,x} h_{TC} dy)\end{aligned} \tag{3.36}$$

and in the y direction are

$$\begin{aligned}&\left|i_C(3)\right| = \left|i_C(x)\right| = \\ &\left|\int_{z_b+h_{DF}}^{z_b+h_{DF}+h_{TC}} \int_{x}^{x+dx} \rho_{sed} C(U_{TC,y} - 0) dxdz\right| = \rho_{sed} C U_{TC,y} h_{TC} dx\end{aligned} \tag{3.37}$$

$$\begin{aligned}&\left|i_C(4)\right| = \left|i_C(y+dy)\right| = \left|i_C(3)\right| + dy \cdot \left|i_C(4)\right|^2 = \\ &\rho_{sed} C U_{TC,x} h_{TC} dx + dy \frac{\partial}{\partial y}(\rho_{sed} C U_{TC,y} h_{TC} dx)\end{aligned} \tag{3.38}$$

There is no sediment flux from or to the ambient fluid layer which is considered to be at rest, therefore $i_{num}(5) = 0$.

The sediment mass flux $i(6)$ enters the control volume coming from the debris flow layer (see Equation (3.15))

$$\left|i_{TC}(6)\right| = \left|\int_{y}^{y+dy} \int_{x}^{x+dx} \rho_{DF} C_{DF} U_{rel,z} dxdy\right| = \rho_{sed} C_{DF} e_d U_{rel} dxdy \tag{3.39}$$

where C_{DF} the sediment concentration that corresponds to the density ρ_{DF} of the debris flow and is calculated as

$$C_{DF} = \frac{\rho_{DF} - \rho_w}{\rho_{sed} - \rho_w}$$

After Equations (3.35) - (3.39), the term II of Equation (3.32) becomes

$$\oint_{CS} \rho_{sed} C\overrightarrow{u_{rel}} \cdot d\vec{S} = -i(1) + i(2) - i(3) + i(4) - i(5) - i(6) =$$
$$\rho_{sed} dxdy \frac{\partial (CU_{TC,x} h_{TC})}{\partial x} + \rho_{sed} dxdy \frac{\partial (CU_{TC,y} h_{TC})}{\partial y} - \tag{3.40}$$
$$\rho_{sed} C_{DF} e_d U_{rel} dxdy$$

After invoking (3.34) and (3.40*)* divided by $\rho_{sed} dxdy$ that are independent of position and time, the sediment mass conservation Equation (3.32) becomes

$$\frac{\partial (Ch_{TC})}{\partial t} + \frac{\partial (CU_{TC,x} h_{TC})}{\partial x} + \frac{\partial (CU_{TC,y} h_{TC})}{\partial y} = C_{DF} e_d U_{rel} \tag{3.41}$$

Momentum conservation for Debris flow layer

The Reynolds transport theorem is now applied to the momentum conservation on an arbitrary control volume Ω for each layer separately

$$\frac{Dm_k U_{k,i}}{Dt} = \underbrace{\frac{\partial}{\partial t} \int_{CV} \rho_k U_{k,i} dV}_{I} + \underbrace{\oint_{CS} \rho_k U_{k,i} \vec{u}_{rel} \cdot d\vec{S}}_{II} = \underbrace{\sum_{num} \vec{F}_{k,i,num}}_{III} \tag{3.42}$$

where ρ is the mass density with the subscript $k = DF, TC$ to denote the lower, debris flow layer or the upper, turbidity current layer respectively, CS is the control surface surrounding the CV, n is the outward pointing unit vector normal to CS, $d\vec{S} = \vec{n} dS$ is a vector parallel to the n with modulus equal to dS and

$$\overrightarrow{u_{rel}} = \overrightarrow{u_k} - \overrightarrow{u_{cs}}$$

is the relative velocity of the fluid with respect to the mobile control surface velocity $\overrightarrow{u_{cs}}$ and $\sum_n \vec{F}_{k,i,n}$ is the sum of the num forces F exerted on the k layer in the i direction.

To derive the linear momentum equations for each layer the following assumptions should be adopted:

(i) the vertical direction and the normal to the bed are essentially parallel vectors so that the following relation is valid

$$-\frac{\partial z_b}{\partial x} = i_f \tag{3.43}$$

where z_b is the bed level and i_f is the bed slope

(i) as the shallow water approximation is adopted
- (a) velocity normal to the bed is negligible
- (b) acceleration in z direction is negligible
- (c) the pressure distribution along the vertical direction is hydrostatic
- (d) shear stresses along the vertical axis are negligible

(ii) shear stresses in free surface are null

An infinitesimal control volume CV and the forces applied of the debris flow layer is depicted in Figure 3.5.

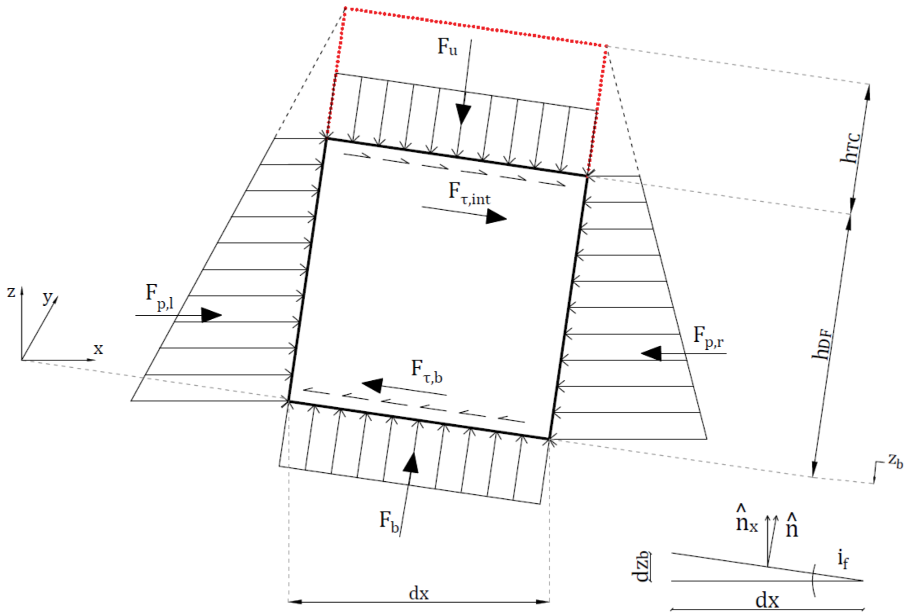

Figure 3.5. The differential control volume CV of the debris flow layer and the forces applied to its control surfaces CS for the x-direction.

The term I of Equation (3.42) can be written for the case of linear momentum balance of the debris flow layer in x direction, as

$$\begin{aligned}&\frac{\partial}{\partial t}\int_{CV}\rho_{DF}U_{DF,dir}dV=\\&\frac{\partial}{\partial t}\int_{z_b}^{z_b+h_{DF}}\int_{y}^{y+dy}\int_{x}^{x+dx}\rho_{DF}U_{DF,dir}dxdydz=\frac{\partial(\rho_{DF}U_{DF,dir}h_{DF})}{\partial t}dxdy\end{aligned}\tag{3.44}$$

since the distances dx and dy are considered infinitesimal and points x and y are considered fixed. The subscript $dir = x, y$ denotes the streamwise and the spanwise direction.

Term II of Equation (3.42) is analytically written for the debris flow layer

$$\begin{aligned}&\oint_{CS}\rho_{DF}U_{DF,dir}\overrightarrow{u_{rel}}\cdot d\vec{S}=\underbrace{\oint_{S_1}\rho_{DF}U_{DF,dir}\overrightarrow{u_{rel,1}}\cdot d\overrightarrow{S_1}}_{j_{DF,dir}(1)}+\\&\underbrace{\oint_{S_2}\rho_{DF}U_{DF,dir}\overrightarrow{u_{rel,2}}\cdot d\overrightarrow{S_2}}_{j_{DF,dir}(2)}+\underbrace{\oint_{S_3}\rho_{DF}U_{DF,dir}\overrightarrow{u_{rel,3}}\cdot d\overrightarrow{S_3}}_{j_{DF,dir}(3)}+\\&\underbrace{\oint_{S_4}\rho_{DF}U_{DF,dir}\overrightarrow{u_{rel,4}}\cdot d\overrightarrow{S_4}}_{j_{DF,dir}(4)}+\underbrace{\oint_{S_5}\rho_{DF}U_{DF,dir}\overrightarrow{u_{rel,5}}\cdot d\overrightarrow{S_5}}_{j_{DF,dir}(5)}+\\&\underbrace{\oint_{S_6}\rho_{DF}U_{DF,dir}\overrightarrow{u_{rel,6}}\cdot d\overrightarrow{S_6}}_{j_{DF,dir}(6)}\end{aligned}\tag{3.45}$$

where subscript $dir = x, y$ denotes the streamwise and the spanwise direction.

Momentum fluxes are obtained in a similar way to the mass fluxes considering Taylor's expansion and control surfaces fixed in x and y direction. If the subscript $dir = x, y$ denotes the streamwise and the spanwise direction, the momentum fluxes j of the debris flow layer are for the x direction

$$\begin{aligned}&\left|j_{DF,dir}(1)\right|=\left|j_{DF,dir}(x)\right|=\\&\left|\int_{z_b}^{z_b+h_{DF}}\int_{y}^{y+dy}\rho_{DF}U_{DF,dir}(U_{DF,x}-0)dydz\right|=\rho_{DF}U_{DF,dir}U_{DF,x}h_{DF}dy\end{aligned}\tag{3.46}$$

$$\begin{aligned}&\left|j_{DF,dir}(2)\right|=\left|j_{DF,dir}(x+dx)\right|=\left|j_{DF,dir}(1)\right|+dx\cdot\left|j_{DF,dir}(1)\right|^2=\\&\rho_{DF}U_{DF,dir}U_{DF,x}h_{DF}dy+dx\frac{\partial}{\partial x}(\rho_{DF}U_{DF,dir}U_{DF,x}h_{DF}dy)\end{aligned}\tag{3.47}$$

and for the y direction

$$\left|j_{DF,dir}(3)\right| = \left|j_{DF,dir}(y)\right| = \\ \left|\int_{z_b}^{z_b+h_{DF}}\int_{x}^{x+dx}\rho_{DF}U_{DF,dir}(U_{DF,y}-0)dxdz\right| = \rho_{DF}U_{DF,dir}U_{DF,y}h_{DF}\,dx \qquad (3.48)$$

$$\left|j_{DF,dir}(4)\right| = \left|j_{DF,dir}(y+dy)\right| = \left|j_{DF,dir}(3)\right| + dy\cdot\left|j_{DF,dir}(4)\right|^2 = \\ \rho_{DF}U_{DF,dir}U_{DF,x}h_{DF}\,dx + dy\frac{\partial}{\partial y}(\rho_{DF}U_{DF,dir}U_{DF,y}h_{DF}\,dx) \qquad (3.49)$$

The momentum flux $j(5)$ corresponds to the bed level where both the fluid and the control volume velocities are null. Consequently, there is no momentum flux through surface S_5.

The detrained mass flux of the debris flow exits the control volume through surface S_6 with velocity $U_{rel,z}$ and after its multiplication with the velocity of the fluid $U_{DF,dir}$ in the examined direction it gives the momentum flux through surface S_6

$$\left|j_{DF,dir}(6)\right| = \\ \left|\int_{y}^{y+dy}\int_{x}^{x+dx}\rho_{DF}U_{DF,dir}U_{rel,z}dxdy\right| = \rho_{DF}U_{DF,dir}e_dU_{rel}dxdy \qquad (3.50)$$

Term II of Equation (3.42) is re-written considering that the positive direction is pointing outwards the control volume

$$\oint_{CS}\rho_kU_{k,i}\vec{u}_{rel}\cdot d\vec{S} = -j_{DF,dir}(1) + j_{DF,dir}(2) - j_{DF,dir}(3) + \\ j_{DF,dir}(4) - j_{DF,dir}(5) + j_{DF,dir}(6) \qquad (3.51)$$

The left-hand side of the momentum conservation equation after dividing by $\rho_{DF}dxdy$ that are independent of position and time, can be written as

$$\frac{\partial}{\partial t}\int_{CV}\rho_kU_{i,k}dV + \oint_{CS}\rho_kU_{k,i}\vec{u}_{rel}\cdot d\vec{S} = \frac{\partial(U_{DF,dir}h_{DF})}{\partial t} + \\ dx\frac{\partial(U_{DF,dir}U_{DF,x}h_{DF})}{\partial x} + \frac{\partial(U_{DF,dir}U_{DF,y}h_{DF})}{\partial y} + U_{DF,dir}e_dU_{rel} \qquad (3.52)$$

The right-hand part corresponds to the sum of the forces exerted on to the control volume as shown in Figure 3.5.

The exerted forces are the following

1. The resultants of the pressure distribution caused by sediment on the vertical surfaces. The ambient fluid layer is not taken into account and all densities are considered submerged. Force induced by hydrostatic pressure, applied on surface S_1 is

$$F_{p,l} = \{(\rho_{TC} - \rho_w) g h_{TC} + [(\rho_{TC} - \rho_w) g h_{TC} + (\rho_{DF} - \rho_w) g h_{DF}]\} h_{DF} dy / 2 \quad (3.53)$$

Exploiting the fact that the control volume is infinitesimal, the Taylor's series can be used to calculate the thrust term

$$F_{p,r} = -F_{p,l} - dx \frac{\partial F_{p,l}}{\partial x} \quad (3.54)$$

2. The resultant of the pressure distribution exerted by the bed on the control volume

$$\vec{F}_b = [(\rho_{TC} - \rho_w) g h_{TC} + (\rho_{DF} - \rho_w) g h_{DF}] dy \vec{n_3} ds \quad (3.55)$$

where $\vec{n_3}$ is the unit vector normal to the bed and $ds = dx/cos\varphi$ if φ is the bed slope. The component of the vector $\vec{n_3}$ that is parallel to dx, is equal to $sin\varphi$. The Equation *(3.55)* can be written as

$$F_b = [(\rho_{TC} - \rho_w) g h_{TC} + (\rho_{DF} - \rho_w) g h_{DF}] dy \tan\varphi dx \quad (3.56)$$

According to relation (3.43) bed slope i_f is equal to $-\partial z_b/\partial x$ and as $i_f = tan\varphi$, the Equation (3.56) is expressed as

$$F_b = -[(\rho_{TC} - \rho_w) g h_{TC} + (\rho_{DF} - \rho_w) g h_{DF}] \frac{\partial z_b}{\partial x} dx dy \quad (3.57)$$

3. The resultant of the pressure distribution exerted by the turbidity current layer

$$\vec{F}_u = [(\rho_{TC} - \rho_w) g h_{TC}] dx dy \vec{n_4} ds_u \quad (3.58)$$

where $\overrightarrow{n_4}$ is the unit vector normal to the upper surface of the debris flow layer and $ds_u = dx/cos\beta$ if β is slope of the upper surface of the layer. The streamwise component of the vector $\overrightarrow{n_4}$ is equal to $sin\beta$ and Equation (3.58) is transformed to

$$F_u = -[(\rho_{TC} - \rho_w)gh_{TC}]\frac{\partial z_{DF}}{\partial x}dxdy \qquad (3.59)$$

with $z_{DF} = z_b + h_{DF}$

4. Bed shear stresses result to a force applied parallel to bed

$$\vec{F}_\tau = -\tau_{b,x}dxdy\vec{t_3}ds \qquad (3.60)$$

where $\overrightarrow{t_3}$ is the unit vector parallel to bed. The component of the vector $\overrightarrow{t_3}$ that is parallel to dx, is equal to $cos\varphi$ and $ds = dx/cos\varphi$, so that Equation (3.60) becomes

$$F_{\tau.b} = -\tau_{b,x}dy\cos\phi\frac{dx}{\cos\varphi} = -\tau_{b,x}dxdy \qquad (3.61)$$

5. As discussed in Section 2.7, shear stresses are developed on the interface of the two layers following the direction of the flow

$$F_{\tau,\text{int}} = \tau_{\text{int}}dy\cos\varphi\frac{dx}{\cos\varphi} = \tau_{\text{int}}dxdy \qquad (3.62)$$

The sum of the relations (3.53) to (3.62), forms the right-hand part of the linear momentum conservation Equation (3.42) for the debris flow layer in x direction

$$\begin{aligned}&\sum F_{DF,x} = F_p + F_b - F_u + F_{\tau,b} + F_{\tau,\text{int}} = \\ &-\frac{\partial}{\partial x}[(\rho_{DF} - \rho_w)g\frac{h_{DF}^{\ 2}}{2}] - h_{DF}\frac{\partial}{\partial x}[(\rho_{TC} - \rho_w)gh_{TC}] - \\ &(\rho_{DF} - \rho_w)gh_{DF}\frac{\partial z_b}{\partial x} + (\tau_{\text{int}} - \tau_b)\end{aligned} \qquad (3.63)$$

As the submerged densities have used for the calculation of the forces applied on the control volume, the submerged density can be introduced for the debris flow layer

$$g' = g\frac{\rho_{DF} - \rho_w}{\rho_{DF}}$$

and for the turbidity current layer if the submerged specific gravity $R = (\rho_{sed} - \rho_w)/\rho_w$ is introduced, its density can be written as

$$\rho_{TC} = \rho_w(1 + RC)$$

If Equation (3.63) is divided by ρ_{DF}, it takes the following form

$$\sum F_{DF,x} = -\frac{\partial}{\partial x}\left(g'\frac{{h_{DF}}^2}{2}\right) - h_{DF}\frac{\partial}{\partial x}\left(\frac{\rho_w}{\rho_{DF}}RCgh_{TC}\right) - g'h_{DF}\frac{\partial z_b}{\partial x} + \frac{(\tau_{\text{int},x} - \tau_{b,x})}{\rho_{DF}} \tag{3.64}$$

If the left-hand side of (3.52) and the right-hand side of (3.64) are substituted into Equation (3.42), the linear momentum equation in x direction for the bottom debris flow layer is

$$\frac{\partial(U_{DF,x}h_{DF})}{\partial t} + \frac{\partial}{\partial x}\left(U_{DF,x}^2 h_{DF} + g'\frac{{h_{DF}}^2}{2}\right) + h_{DF}\frac{\rho_w}{\rho_{DF}}g\frac{\partial}{\partial x}\left(RCh_{TC}\right) + g'h_{DF}\frac{\partial z_b}{\partial x} + \frac{\partial(U_{DF,x}U_{DF,y}h_{DF})}{\partial y} = \frac{(\tau_{\text{int},x} - \tau_{b,x})}{\rho_{DF}} - U_{DF,x}e_d U_{rel} \tag{3.65}$$

The exerted forces in the y direction are calculated taking the y-components of the forces calculated for the x direction. If the $\sum F_{DF,y}$ is substituted in relation (3.42), the linear momentum equation in y direction for the bottom debris flow layer is

$$\frac{\partial(U_{DF,y}h_{DF})}{\partial t} + \frac{\partial(U_{DF,x}U_{DF,y}h_{DF})}{\partial x} + \frac{\partial}{\partial y}\left(U_{DF,y}^2 h_{DF} + g'\frac{{h_{DF}}^2}{2}\right) + h_{DF}\frac{\rho_w}{\rho_{DF}}g\frac{\partial}{\partial y}\left(RCh_{TC}\right) + g'h_{DF}\frac{\partial z_b}{\partial y} = \frac{(\tau_{\text{int},y} - \tau_{b,y})}{\rho_{DF}} - U_{DF,y}e_d U_{rel} \tag{3.66}$$

Momentum conservation for the Turbidity flow layer

The term I of Equation (3.42) can be written for the case of linear momentum balance of the turbidity current layer in x direction, as

$$\frac{\partial}{\partial t}\int_{CV}\rho_{TC}U_{TC,dir}dV = \frac{\partial}{\partial t}\int_{z_b}^{z_b+h_{DF}}\int_{y}^{y+dy}\int_{x}^{x+dx}\rho_{TC}U_{TC,dir}dxdydz = \frac{\partial(\rho_{TC}U_{TC,dir}h_{TC})}{\partial t}dxdy \tag{3.67}$$

since the distances dx and dy are considered infinitesimal and points x and y are considered fixed. The subscript $dir = x, y$ denotes the streamwise and the spanwise direction

The momentum fluxes of term II of Equation (3.42) for the turbidity current layer are calculated with the same way as for the debris flow layer and the left-hand side of the momentum conservation equation after dividing by $\rho_{TC}dxdy$ that are independent of position and time, can be written as

$$\frac{\partial}{\partial t}\int_{CV}\rho_k U_{i,k}dV + \oint_{CS}\rho_k U_{k,i}\vec{u}_{rel}\cdot d\vec{S} = \frac{\partial(U_{TC,dir}h_{TC})}{\partial t} + \frac{\partial(U_{TC,dir}U_{TC,x}h_{TC})}{\partial x} + \frac{\partial(U_{TC,dir}U_{TC,y}h_{TC})}{\partial y} + U_{DF,dir}\frac{\rho_{DF}}{\rho_{TC}}e_d U_{rel} \tag{3.68}$$

Figure 3.6 shows all the forces that act on a generic infinitesimal control volume of the turbidity current layer.

The exerted forces are the following:

1. The resultants of the pressure distribution caused by sediment on the vertical surfaces. As mentioned, the ambient fluid layer is not taken into account and all densities are considered. Force induced by hydrostatic pressure, applied on surface S_1 is

$$F_{p,l} = [(\rho_{TC} - \rho_w)gh_{TC}]h_{TC}dy/2 \tag{3.69}$$

Using Taylor's theorem, the on surface S_2

$$F_{p,r} = -F_{p,l} - dx\frac{\partial F_{p,l}}{\partial x} \tag{3.70}$$

2. The resultant of the pressure distribution exerted by the debris flow layer

$$\vec{F}_u = [(\rho_{TC} - \rho_w) g h_{TC}] dxdy \vec{n}_4 ds_u \tag{3.71}$$

where n_4 is the unit vector normal to the upper surface of the debris flow layer and $ds_u = dx/cos\beta$ if β is slope of the upper surface of the layer. The streamwise component of the vector n_4 is equal to $sin\beta$ and Equation (3.70) is transformed to

$$F_u = -[(\rho_{TC} - \rho_w) g h_{TC}] \frac{\partial z_{DF}}{\partial x} dxdy \tag{3.72}$$

with $z_{DF} = z_b + h_{DF}$

3. As discussed in Section 2.7, shear stresses are developed on the interface of the two layers following the direction of the flow

$$F_{\tau,\text{int}} = \tau_{\text{int}} dy \cos\varphi \frac{dx}{\cos\varphi} = \tau_{\text{int}} dxdy \tag{3.73}$$

The ambient fluid layer is considered as it is at rest and shear stresses in the interface with the turbidity current are negligible as they are much smaller than stresses developed at the interface of the two layers.

The sum of the relations (3.67) to (3.71) divided by $\rho_{TC} dxdy$, forms the right-hand part of the linear momentum conservation Equation (3.42) of the turbidity current in x direction of the turbidity current

$$\sum F_{TC,x} = F_p + F_b - F_u + F_{\tau,b} + F_{\tau,\text{int}} =$$
$$-\frac{\partial}{\partial x}\left(\frac{\rho_w}{\rho_{TC}} RCg \frac{h_{TC}^{\ 2}}{2}\right) - \frac{\rho_w}{\rho_{TC}} RCg h_{TC} \frac{\partial z_{DF}}{\partial x} - \frac{\tau_{\text{int},x}}{\rho_{TC}} \tag{3.74}$$

if the submerged specific gravity $R = (\rho_{sed} - \rho_w)/\rho_w$ is introduced.

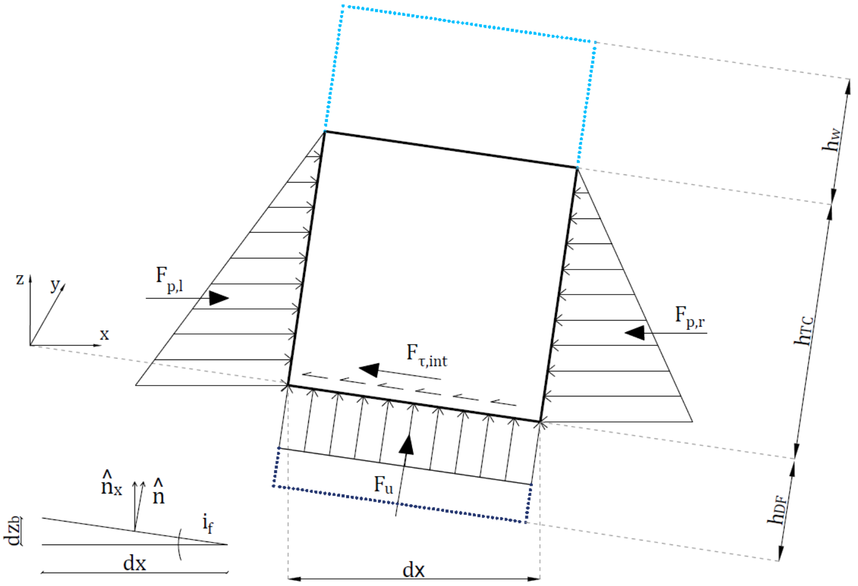

Figure 3.6. The differential control volume CV of the turbidity current layer and the forces applied to its control surfaces CS for the x-direction.

Substituting relations (3.68) and (3.74) in Equation (3.42) and using Boussinesq approximation ($\rho_w/\rho_{TC} = 1$), the linear momentum equation for the turbidity current layer in the x direction

$$\frac{\partial(U_{TC,x}h_{TC})}{\partial t}+\frac{\partial}{\partial x}\left(U^2_{TC,x}h_{TC}+RCg\frac{{h_{TC}}^2}{2}\right)+ \\ RCgh_{TC}\frac{\partial z_{DF}}{\partial x}+\frac{\partial(U_{TC,x}U_{TC,y}h_{TC})}{\partial y}+ \\ =-\frac{\tau_{\text{int},x}}{\rho_{TC}}+U_{DF,x}\frac{\rho_{DF}}{\rho_{TC}}e_dU_{rel} \tag{3.75}$$

After the calculation of the y-components of the forces calculated for the x direction, the linear momentum equation in y direction for the turbidity current layer is formed as

$$\frac{\partial(U_{TC,y}h_{TC})}{\partial t}+\frac{\partial(U_{TC,x}U_{TC,y}h_{TC})}{\partial x}+$$
$$\frac{\partial}{\partial y}\left(U_{TC,y}^{2}h_{TC}+RCg\frac{h_{TC}{}^{2}}{2}\right)+RCgh_{TC}\frac{\partial z_{DF}}{\partial y}= \tag{3.76}$$
$$-\frac{\tau_{\text{int},y}}{\rho_{TC}}+U_{DF,y}\frac{\rho_{DF}}{\rho_{TC}}e_dU_{rel}$$

The complete set of equations is summarized below:

- Mass conservation equation for the debris flow layer $\frac{\partial h_{DF}}{\partial t}+\frac{\partial}{\partial x}(h_{DF}U_{DF,x})+\frac{\partial}{\partial y}(h_{DF}U_{DF,y})=-e_dU_{rel}$
- Mass conservation equation for the turbidity current layer

$$\frac{\partial h_{TC}}{\partial t}+\frac{\partial}{\partial x}(h_{TC}U_{TC,x})+\frac{\partial}{\partial y}(h_{TC}U_{TC,y})=e_wU_{TC,xy}+\frac{\rho_{DF}}{\rho_{TC}}e_dU_{rel}$$

- Sediment mass conservation equation for the turbidity current layer

$$\frac{\partial}{\partial t}(Ch_{TC})+\frac{\partial}{\partial x}(Ch_{TC}U_{TC,x})+\frac{\partial}{\partial y}(Ch_{TC}U_{TC.y})=C_de_dU_{rel}$$

- Linear momentum conservation equation for the debris flow layer

$$\frac{\partial}{\partial t}(h_{DF}U_{DF,i})+\frac{\partial}{\partial x_i}(h_{DF}U_{DF,i}{}^{2}+g'\frac{h_{DF}{}^{2}}{2})+g'h_{DF}\frac{\partial z_b}{\partial x_i}+\frac{\rho_w}{\rho_{DF}}gh_{DF}\frac{\partial}{\partial x_i}(RCh_{TC})$$
$$+\frac{\partial}{\partial x_j}(h_{DF}U_{DF,i}U_{DF,j})=\frac{(\tau_{\text{int},i}-\tau_{b,i})}{\rho_{DF}}-U_{DF,i}e_dU_{rel}$$

- Linear momentum conservation equation for the debris flow layer

$$\frac{\partial}{\partial t}(h_{TC}U_{TC,i})+\frac{\partial}{\partial x_i}(h_{TC}U_{TC,i}{}^{2}+RCg\frac{h_{TC}{}^{2}}{2})+(RCgh_{TC})\frac{\partial z_{DF}}{\partial x_i}+$$
$$+\frac{\partial}{\partial x_j}(h_{TC}U_{DF,i}U_{DF,j})=-\frac{\tau_{\text{int},i}}{\rho_{TC}}+\frac{\rho_{DF}}{\rho_{TC}}U_{DF,i}e_dU_{rel}$$

where the subscript $i,j=1,2$ denotes the streamwise direction x and the spanwise direction y, z_b is the seabed level, $g'=[(\rho_{DF}-\rho_w)/\rho_{DF}]g$ is the debris flow submerged gravity, R is the submerged specific density, C is the sediment concentration and $z_{DF}=z_b+h_{DF}$.

3.3 Numerical method

3.3.1 Numerical scheme

The Equations of the previous section can be written in vector form

$$\frac{\partial U}{\partial t}+\frac{\partial F}{\partial x}+\frac{\partial G}{\partial y}=S \tag{3.77}$$

where $\boldsymbol{U}$ is the conserved variables vector, $\boldsymbol{F}$ is the flux vector along the streamwise direction x, $\boldsymbol{G}$ is the flux vector along the spanwise direction y and $\boldsymbol{S}$ is the source terms vector, as given below

$$U=\begin{bmatrix} h_{DF} \\ h_{TC} \\ h_{DF}U_{DF,x} \\ h_{TC}U_{TC,x} \\ h_{DF}U_{DF,y} \\ h_{TC}U_{TC,y} \\ Ch_{TC} \end{bmatrix} \quad F=\begin{bmatrix} h_{DF}U_{DF,x} \\ h_{TC}U_{TC,x} \\ h_{DF}U_{DF,x}{}^{2}+g'\dfrac{h_{DF}{}^{2}}{2} \\ h_{TC}U_{TC,x}{}^{2}+RCg\dfrac{h_{TC}{}^{2}}{2} \\ h_{DF}U_{DF,x}U_{DF,y} \\ h_{TC}U_{TC,x}U_{TC,y} \\ Ch_{TC}U_{TC,x} \end{bmatrix}, G=\begin{bmatrix} h_{DF}U_{DF,y} \\ h_{TC}U_{TC,y} \\ h_{DF}U_{DF,y}{}^{2}+g'\dfrac{h_{DF}{}^{2}}{2} \\ h_{TC}U_{TC,y}{}^{2}+RCg\dfrac{h_{TC}{}^{2}}{2} \\ h_{DF}U_{DF,y}U_{DF,x} \\ h_{TC}U_{TC,y}U_{TC,x} \\ Ch_{TC}U_{TC,y} \end{bmatrix}$$

$$S=\begin{bmatrix} -e_{d}U_{rel} \\ e_{w}U_{TC,xy}+\dfrac{\rho_{DF}}{\rho_{TC}}e_{d}U_{rel} \\ \dfrac{\tau_{\text{int},x}-\tau_{b,x}}{\rho_{DF}}-e_{d}U_{DF,x}U_{rel} \\ -\dfrac{\tau_{\text{int},x}}{\rho_{TC}}+\dfrac{\rho_{DF}}{\rho_{TC}}e_{d}U_{DF,x}U_{rel} \\ \dfrac{\tau_{\text{int},y}-\tau_{b,y}}{\rho_{DF}}-e_{d}U_{DF,y}U_{rel} \\ -\dfrac{\tau_{\text{int},y}}{\rho_{TC}}+\dfrac{\rho_{DF}}{\rho_{TC}}e_{d}U_{DF,y}U_{rel} \\ C_{d}e_{d}U_{rel} \end{bmatrix}$$

The momentum equations for both layers include non-conservative terms that are not treated in the initial calculation of mass fluxes. A computation scheme is used for the correction of the mass fluxes in which the non-conservative terms are added. The terms that are not included in the initial flux vectors are for the debris flow layer

$$g' h_{DF} \frac{\partial z_b}{\partial x_i} + \frac{\rho_w}{\rho_{DF}} g h_{DF} \frac{\partial}{\partial x_i}(RCh_{TC}) \tag{3.78}$$

and for the turbidity current layer

$$RCgh_{TC} \frac{\partial z_{DF}}{\partial x_i} \tag{3.79}$$

where the subscript i = 1, 2 denotes the streamwise direction x and the spanwise direction y.

The finite volume method (FVM) is used for the discretization of Equation (3.77*)*. FVM uses a volume integral formulation of the problem with a finite partitioning set of volumes to discretize the equations. In the finite volume approach, the hydraulic variables are calculated at discrete volumes (cells) on a meshed geometry for each timestep t.

The homogenous form of Equation (3.77) is integrated in a control volume V

$$\frac{d}{dt}\iiint_V U dV + \iiint_V \left(\frac{\partial F(U)}{\partial x} + \frac{\partial G(U)}{\partial y} \right) dV = 0 \tag{3.80}$$

After applying divergence theorem in the second term, Equation (3.80) becomes

$$\frac{d}{dt}\iiint_V U dV + \iint_\Omega (F(U) \cdot n_x + G(U) \cdot n_y) d\Omega = 0 \tag{3.81}$$

where Ω is the control volume boundary and $\vec{n} = (n_x, n_y)$ is the outward unit vector normal to the surface Ω.

The first term of Equation (3.81) for a two-dimensional depth-integrated flow is written as

$$\frac{d}{dt}\iiint_V U dV = \frac{d}{dt}(US_i) = S_i \frac{dU}{dt} \tag{3.82}$$

where S_i is the cell surface.

The second term of Equation (3.81) for a cell composed by N interfaces can be written as

$$\iint_\Omega (F(U)\cdot n_x + G(U)\cdot n_y) d\Omega = \sum_{j=1}^{N}\int_{A_j}^{A_{j+1}} (F(U_i)\cdot n_x + G(U_i)\cdot n_y) dA \tag{3.83}$$

where N are the cell interfaces each of them is determined by nodes A_j and A_{j+1} and has length of L_j and S_i is the cell surface. The term in the parenthesis is the flux with direction normal to the cell interface. A triangular shaped cell is used (Figure 3.7) and N is equal to 3.The variable U is defined in the center of each cell i.

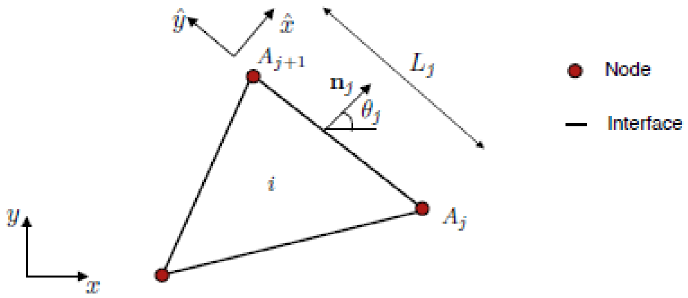

Figure 3.7. Triangular cell.

If the flux vectors are defined in the local coordinates system $(\hat{x}, \hat{y})$ of each interface j of the cell and ϑ_j is the angle formed by the outward unit vector n_j normal to the surface L_j and the streamwise direction x, Equation (3.83) becomes

$$F(U_i)\cdot n_x + G(U_i)\cdot n_y = T_j^{-1}\overbrace{F(\underbrace{T_j U}_{\hat{U}})}^{\hat{F}} \tag{3.84}$$

where T_j is the rotation matrix and T_j^{-1} is the inverse rotation matrix for each interface j.

After invoking Equation (3.84), Equation (3.81) becomes

$$\frac{dU_i}{dt} = -\frac{1}{S_i}\sum_{j=1}^{N} L_j T_j^{-1}\hat{F}_i$$

and the temporal discretization scheme takes the following form

$$U_i^{n+1} = U_i^n - \frac{\Delta t}{S_i}\sum_{j=1}^{N} L_j T_j^{-1}\hat{F}_i \tag{3.85}$$

with

$$F(U_i)\cdot\cos\theta_j + G(U_i)\cdot\sin\theta_j = T_j^{-1}F(T_jU_i) = T_j^{-1}\hat{F}_i$$

Riemann problem-Godunov's method

The computation of the flux vector $\hat{F}$ $(F(U_i), G(U_i))$ at each cell interface is based on the Godunov's method (1959) who proposed a constant value in each computational cell, which lead to discontinuities at the interfaces.

Each cell interface can be treated as a Riemann problem. The Riemann problem consists of a conservation law together with piecewise constant data having a single discontinuity. The initial state refers to the initial value problem when the initial data consists of two constant states U_L and U_R separated by a jump discontinuity at x = 0 and is expressed as

$$U(x,t=0) = \begin{cases} U_L & for \quad x \le 0 \\ U_R & for \quad x \ge 0 \end{cases} \tag{3.86}$$

Godunov (1959) introduced the utilisation of the solution of the local Riemann problem at each cell interface as the basis for determining the fluxes of the left and right side of a discontinuity. The numerical value of the solution U_i^n is considered to be the cell averages of the analytical solution at time level n

$$U_i^n = \frac{1}{\Delta x}\int_{x_{i-1/2}}^{x_{i+1/2}} U(x, n\Delta t)dx \tag{3.87}$$

for a regular grid. At each cell boundary, the resulting Riemann problem is then solved and the union of all Riemann solutions averaged over each cell gives the updated numerical solution values.

The equation of the system of hyperbolic conservation laws can be written as

$$U_t + F(U)_x = 0 \tag{3.88}$$

and by integrating the above equation over the cell $[x_{i-1/2}, x_{i+1/2}] \times [n\Delta t, (n+1)\Delta t]$ (**Error! Reference source not found.** and Figure 3.9).

$$\int_{t^n}^{t^{n+1}} \int_{x_{i-1/2}}^{x_{i+1/2}} U_t(x,t)dxdt = -\int_{t^n}^{t^{n+1}} \int_{x_{i-1/2}}^{x_{i+1/2}} F_x(U(x,t))dxdt$$

$$\int_{x_{i-1/2}}^{x_{i+1/2}} (U_t(x,t^{n+1}) - U_t(x,t^n))dx = -\int_{t^n}^{t^{n+1}} (F(U(x_{i+1/2},t)) - F(U(x_{i+1/2},t)))dt$$

$$\Delta x(U_t^{\,n+1} - U_t^{\,n}) = -\Delta t\left(\frac{1}{\Delta t}\int_{t^n}^{t^{n+1}} F(U(x_{i+1/2},t))dt - \frac{1}{\Delta t}\int_{t^n}^{t^{n+1}} F(U(x_{i-1/2},t))dt\right)$$

If a numerical flux is defined as

$$F_{i-1/2}^n = \frac{1}{\Delta t}\int_{t^n}^{t^{n+1}} F(U(x_{i-1/2},t))dt \tag{3.89}$$

then Godunov's method in conservation form is written as

$$U_i^{n+1} = U_i^n - \frac{\Delta x}{\Delta t}(F_{i+1/2}^n - F_{i-1/2}^n) \tag{3.90}$$

At this stage, the key remaining difficulty is the calculation of the fluxes $F_{i-1/2}^n$ and $F_{i+1/2}^n$. As the exact Riemann solution is costly involving iteration methods, approximate Riemann solvers are commonly used. One possible method that can be used is the HLL (Harten, Lax and van Leer) method, introduced in the next section.

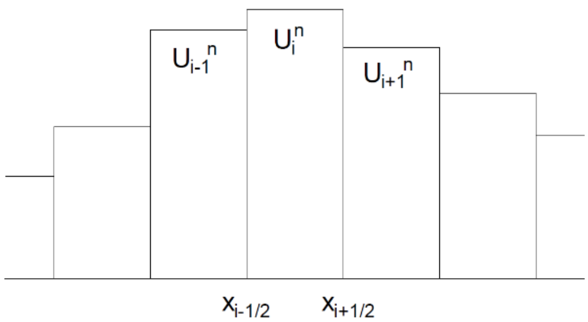

Figure 3.8. The piecewise constant data representation.

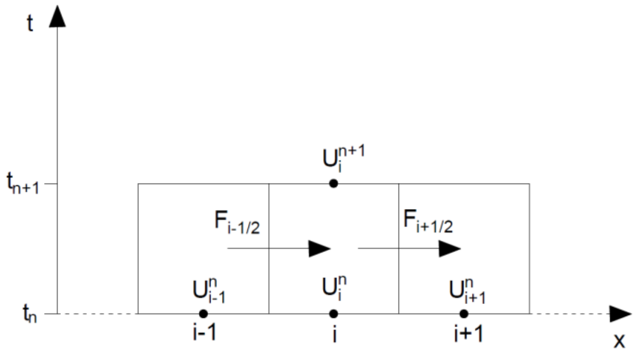

Figure 3.9. Integral averages give piece-wise data for Godunov's method for a hyperbolic system.

HLL (Harten, Lax & Leer) solver

Harten, Lax and van Leer (1983) proposed an approximation for the fluxes which assumes a Riemann solver consisting of two waves separating three constant states. If ${s_{i-1/2}}^R$ and ${s_{i-1/2}}^L$ are upper and lower bounds, respectively, for the largest and smallest signal velocities resulting from the solution of the Riemann problem is centred at $x_{i-1/2}$, then the approximate solution is

$$\tilde{U} = \begin{cases} U_{i-1} & if \quad x/t \le s_{i-1/2}^L \\ U_{i-1/2}^{HLL} & if \quad s_{i-1/2}^L \le x/t \le s_{i-1/2}^R \\ U_i & if \quad s_{i-1/2}^R \le x/t \end{cases} \tag{3.91}$$

where the intermediate state is obtained from conservation to be

$$U_{i-1/2}^{HLL} = \frac{s_{i-1/2}^R U_i - s_{i-1/2}^L U_{i-1}}{s_{i-1/2}^R - s_{i-1/2}^L} - \frac{F_i - F_{i-1}}{s_{i-1/2}^R - s_{i-1/2}^L} \tag{3.92}$$

Integrating this solution substituted into the conservation law over the half cell $[x_{i-1/2}, x_i] \times [t^n, t^{n+1}]$ results the HLL flux

$$F_{i-1/2} = \begin{cases} F_{i-1} & if \quad x/t \le s_{i-1/2}^{L} \\ F_{i-1/2}^{HLL} & if \quad s_{i-1/2}^{L} \le x/t \le s_{i-1/2}^{R} \\ F_{i} & if \quad s_{i-1/2}^{R} \le x/t \end{cases} \tag{3.93}$$

where

$$F_{i-1/2}^{HLL} = \frac{s_{i-1/2}^{R} F_{i-1} - s_{i-1/2}^{L} F_{i} + s_{i-1/2}^{R} s_{i-1/2}^{L} (U_{i} - U_{i-1})}{s_{i-1/2}^{R} - s_{i-1/2}^{L}} \tag{3.94}$$

The intermediate state is a mean value of the exact Riemann solution. The two states U_{i-1} and U_i can be connected by a shock of the first or n^{th} order, then the correct shock speed is obtained and the solution is exact (Figure 3.10). The upper and lower bounds $s_{i-1/2}{}^{R}$ and $s_{i-1/2}{}^{L}$ can be calculated as the maximum eigenvalue at the right state and the minimum eigenvalue at the left state respectively, or as the maximum of the largest eigenvalue at either state and the minimum of the smallest as suggested by Davis (1988).

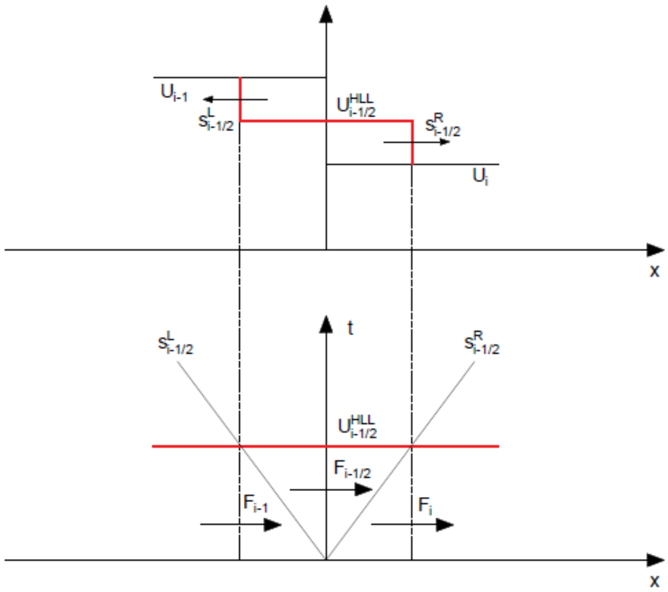

Figure 3.10. HLL method.

One major flaw of the HLL scheme, which is a two-wave model, is exposed by contact discontinuities, shear waves and material interfaces, or any type of intermediate waves.

HLLC solver

The HLLC approximate Riemann solver (Toro, 1994) is a modification of the basic HLL scheme to account for the presence of intermediate waves in the structure of the solution of Riemann problem.

If ${s_{i-1/2}}^R$ and ${s_{i-1/2}}^L$ are upper and lower bounds, respectively, for the largest and smallest signal velocities resulting from the solution of the Riemman problem centred at $x_{i-1/2}$, and ${s_{i-1/2}}^{HLLC}$ is the intermediate wave speed (Figure 3.11), the numerical fluxes are

$$\tilde{U} = \begin{cases} U_{i-1} & if \quad x/t \le s_{i-1/2}^{L} \\ U_{i-1/2}^{HLLC,L} & if \quad s_{i-1/2}^{L} \le x/t \le s_{i-1/2}^{HLLC} \\ U_{i-1/2}^{HLLC,R} & if \quad s_{i-1/2}^{HLLC} \le x/t \le s_{i-1/2}^{R} \\ U_{i} & if \quad s_{i-1/2}^{R} \le x/t \end{cases} \tag{3.95}$$

By integrating this solution substituted into the conservation law over the half cell $\left[x_{i-1/2}, x_i\right] \times [t^n, t^{n+1}]$ results the HLLC flux is calculated as

$$F_{i-1/2}^{HLLC} = \begin{cases} F_{i-1} & if \quad x/t \le s_{i-1/2}^{L} \\ F_{i-1/2}^{HLLC,L} & if \quad s_{i-1/2}^{L} \le x/t \le s_{i-1/2}^{HLLC} \\ F_{i-1/2}^{HLLC,R} & if \quad s_{i-1/2}^{HLLC} \le x/t \le s_{i-1/2}^{R} \\ F_{i} & if \quad s_{i-1/2}^{R} \le x/t \end{cases} \tag{3.96}$$

and the following relationships are obtained

$$F_{i-1/2}^{HLLC,L} = F_{i-1} + s_{i-1/2}^{L}(U_{i-1/2}^{HLLC,L} - U_{i-1}) \tag{3.97}$$

$$F_{i-1/2}^{HLLC,R} = F_{i-1/2}^{HLLC,L} + s_{i-1/2}^{HLLC}(U_{i-1/2}^{HLLC,R} - U_{i-1/2}^{HLLC,L}) \tag{3.98}$$

$$F_{i-1/2}^{HLLC,R} = F_{i} + s_{i-1/2}^{R}(U_{i-1/2}^{HLLC,R} - U_{i}) \tag{3.99}$$

Equations (3.97)-(3.99*)* have four unknown vectors $F_{i-1/2}^{HLLC,L}$, $U_{i-1/2}^{HLLC,L}$, $F_{i-1/2}^{HLLC,R}$ and $U_{i-1/2}^{HLLC,R}$. There are more unknowns than equations and the following extra conditions need to be imposed, in order to solve the algebraic problem

- for pressure: $p_{i-1/2}^{HLLC,L} = p_{i-1/2}^{HLLC,R} = p_{i-1/2}^{HLLC}$
- for normal velocity: $U_{i-1/2}^{HLLC,L} = U_{i-1/2}^{HLLC,R} = U_{i-1/2}^{HLLC}$
- for tangential velocities: $V_{i-1/2}^{HLLC,L} = V_{i-1/2}^{HLLC,R} = V_{i-1/2}^{HLLC}$ and $W_{i-1/2}^{HLLC,L} = W_{i-1/2}^{HLLC,R} = W_{i-1/2}^{HLLC}$

and additionally

$$S_{i-1/2}^{HLLC} = U_{i-1/2}^{HLLC}$$

The fluxes are completely determined and the HLLC flux for the Godunov method can be written a

$$F_{i-1/2}^{HLLC} = \begin{cases} F_{i-1} & if \quad 0 \le s_{i-1/2}^{L} \\ F_{i-1/2}^{HLLC,L} = F_{i-1} + s_{i-1/2}^{L}(U_{i-1/2}^{HLLC,L} - U_{i-1}) & if \quad s_{i-1/2}^{L} \le 0 \le s_{i-1/2}^{HLLC} \\ F_{i-1/2}^{HLLC,R} = F_{i-1} + s_{i-1/2}^{R}(U_{i-1/2}^{HLLC,R} - U_{i}) & if \quad s_{i-1/2}^{HLLC} \le 0 \le s_{i-1/2}^{R} \\ F_{i} & if \quad s_{i-1/2}^{R} \le 0 \end{cases} \quad (3.100)$$

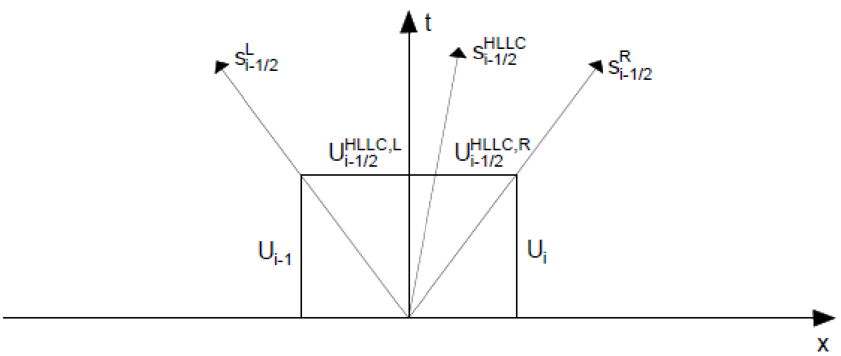

Figure 3.11. Assumed wave pattern for the HLLC Riemann solver

LHLL solver

The LHLL scheme was developed by Fraccarollo (2003) to account robustly for the non-conservative terms associated with bottom slope. It accounts for non-conservative products as lateralised corrections to the standard HLL fluxes. The lateralized momentum fluxes are given by

$$\sigma_{i-1/2}^{LHLL,L} = \sigma_{i-1/2}^{HLL} - \frac{s_{i-1/2}^{L}}{s_{i-1/2}^{R} - s_{i-1/2}^{L}} \frac{g}{2} (h_{term,i-1} + h_{term,i})(z_{b,i} - z_{b,i-1}) \tag{3.101}$$

$$\sigma_{i-1/2}^{LHLL,R} = \sigma_{i-1/2}^{HLL} - \frac{s_{i-1/2}^{R}}{s_{i-1/2}^{R} - s_{i-1/2}^{L}} \frac{g}{2} (h_{term,i-1} + h_{term,i})(z_{b,i} - z_{b,i-1}) \tag{3.102}$$

where h_{term} is the term associated with the flow thickness.

Mass flux calculation

The flux vector $\hat{F}$ at each cell interface is computed by HLL (Harten, Lax, van Leer, 1983) solvers. These numerical schemes do not require the full eigenstructure system to be explicitly known. In this study, outer real bounds are used for the computations as proposed by Spinewine (2005).

If $i-1/2$ corresponds to each cell interface and the Riemann problem is centred at $x_{i-1/2}$, then the following notations can be used for simplification purposes

$$(i-1) \rightarrow L \qquad (i) \rightarrow R \qquad (i-1/2) \rightarrow *$$

If the mass flux is denoted by $p = h_k U_{k,j}$, the mass flux of the debris flow layer after treatment with the HLL scheme (Equation (3.94)) is

$$p_{DF}^{*} = \frac{S_R}{S_R - S_L} p_{L,DF}^{n} - \frac{S_L}{S_R - S_L} p_{R,DF}^{n} + \frac{S_R S_L}{S_R - S_L} (z_{R,DF}^{n} - z_{L,DF}^{n}) \tag{3.103}$$

with $z_{DF} = z_b + h_{DF}$.

The mass flux of the turbidity current layer is calculated as

$$p_{TC}^{*} = p_{tot}^{*} - p_{DF}^{*} \tag{3.104}$$

where p_{dt}^{*} is the total mass flux for both layers

$$\begin{aligned} p_{tot}^{*} = {} & \frac{S_R}{S_R - S_L} (p_{L,DF}^{n} + p_{L,TC}^{n}) - \frac{S_L}{S_R - S_L} (p_{R,DF}^{n} + p_{R,TC}^{n}) \\ & + \frac{S_R S_L}{S_R - S_L} [(z_{R,DF}^{n} + z_{R,TC}^{n}) - (z_{L,DF}^{n} + z_{L,TC}^{n})] \end{aligned} \tag{3.105}$$

with $z_{TC} = z_b + h_{DF} + h_{TC}$

The definitions for the celerities S_L and S_R proposed by Chen (2007), after modification for the debris flow-turbidity current layer model, are

$$\begin{cases} S_L = \min(S_{\min,L}, S_{\min,R}, 0) \\ S_R = \max(S_{\max,L}, S_{\max,R}, 0) \end{cases} \tag{3.106}$$

with

$$\begin{cases} S_{\min} = \min(U_{TC}, U_{DF}) - \sqrt{RCgh_{TC} + h_{DF}} \\ S_{\max} = \max(U_{TC}, U_{DF}) + \sqrt{RCgh_{TC} + h_{DF}} \end{cases} \tag{3.107}$$

For the case that one of the two layers becomes zero, the celerities are computed with the single layer expression t

$$\begin{aligned} S_{DF} &= U_{DF} \pm \sqrt{gh_{DF}} \\ S_{TC} &= U_{TC} \pm \sqrt{gh_{TC}} \end{aligned} \tag{3.108}$$

Momentum flux calculation

The momentum fluxes are solved using LHLL scheme to include the non-conservative product related to the pressure interaction (topographic terms) that are not used in the mass flux calculation.

In order to include the topographic term

$$g' h_{DF} \frac{\partial z_b}{\partial x_i} + \frac{\rho_w}{\rho_{DF}} g h_{DF} \frac{\partial}{\partial x_i}(RCh_{TC}) = g' h_{DF} \frac{\partial}{\partial x_i}(z_b + RCh_{TC}\rho_w / (\rho_w - \rho_{DF}))$$

the momentum flux for the debris flow layer in the x direction, σ, is calculated using the LHLL solver (Equations (3.101)-(3.102)), as following

$$\begin{cases} \sigma^*_{L,DF} = \sigma^*_{DF} - \dfrac{S_L}{S_R - S_L} \dfrac{1}{2} g' (h^n_{L,DF} + h^n_{R,DF})(Z^n_{R,DF} - Z^n_{L,DF}) \\ \sigma^*_{R,DF} = \sigma^*_{DF} - \dfrac{S_R}{S_R - S_L} \dfrac{1}{2} g' (h^n_{L,DF} + h^n_{R,DF})(Z^n_{R,DF} - Z^n_{L,DF}) \end{cases} \tag{3.109}$$

with σ^*_{DF} the HLL momentum flux

$$\sigma^*_{DF} = \frac{S_R}{S_R - S_L} \sigma^n_{L,DF} - \frac{S_L}{S_R - S_L} \sigma^n_{R,DF} + \frac{S_R S_L}{S_R - S_L} (p^n_{R,DF} - p^n_{L,DF})$$

and $Z_{R-L,DF} = z_b + RCh_{TC}\rho_w/(\rho_{DF}-\rho_w)$.

In order to include the topographic term $RCgh_{TC}\frac{\partial z_{DF}}{\partial x_i}$, the momentum flux for the debris flow layer in the x direction, σ, is calculated using the LHLL solver (Equations (3.101)-(3.102)), as following

$$\begin{cases} \sigma^*_{L,TC} = \sigma^*_{TC} - \dfrac{S_L}{S_R - S_L} Rg[(Ch)^n_{L,TC} + (Ch)^n_{R,TC})(Z^n_{R,TC} - Z^n_{L,TC}) \\ \sigma^*_{R,TC} = \sigma^*_{TC} - \dfrac{S_R}{S_R - S_L} Rg((Ch)^n_{L,TC} + (Ch)^n_{R,TC})(Z^n_{R,TC} - Z^n_{L,TC}) \end{cases} \tag{3.110}$$

with σ^*_{TC} the HLL momentum flux

$$\sigma^*_{TC} = \frac{S_R}{S_R - S_L}\sigma^n_{L,TC} - \frac{S_L}{S_R - S_L}\sigma^n_{R,TC} + \frac{S_R S_L}{S_R - S_L}(p^n_{R,TC} - p^n_{L,TC})$$

and $Z_{R-L,DF} = z_b + h_{DF}$.

The HLLC scheme is used for the calculation of the momentum fluxes along the y direction μ. For the debris flow layer is written

$$\mu^*_{DF} = \begin{cases} V^n_{L,DF}\, p^*_{DF} & if \quad p^*_{DF} \geq 0 \\ V^n_{R,DF}\, p^*_{DF} & if \quad p^*_{DF} \leq 0 \end{cases} \tag{3.111}$$

where p^*_{DF} is the mass flux was calculated by the Equation (3.103) and V^{n}_{DF} is the velocity of the debris flow layer in the y direction ($U^{\mathrm{n}}_{y,DF}$),

and for the upper layer

$$\mu^*_{TC} = \begin{cases} V^n_{L,TC}\, p^*_{TC} & if \quad p^*_{TC} \geq 0 \\ V^n_{R,TC}\, p^*_{TC} & if \quad p^*_{TC} \leq 0 \end{cases} \tag{3.112}$$

where p^*_{TC} is the mass flux was calculated by the Equation (3.104) and V^{n}_{TC} is the velocity of the turbidity current layer in the y direction ($U^{\mathrm{n}}_{y,TC}$).

The sediment flux of the turbidity current is calculated with an HLLC scheme as well

$$\mu_C^* = \begin{cases} C_{L,TC}^n p_{TC}^* & if \quad p_{TC}^* \geq 0 \\ C_{R,TC}^n p_{TC}^* & if \quad p_{TC}^* \leq 0 \end{cases} \tag{3.113}$$

where p_{TC}^* is the mass flux was calculated by the Equation (3.104).

Source terms

After the computation of the fluxes with HLL solvers, the homogenous equation $\partial U/\partial t + \partial F/\partial x + \partial G/\partial x = 0$ is solved using the discretization scheme of Equation (3.75).

The source operator S is split in various components that are more easily integrated separately. To follow this approach, the computations should be carefully kept stable and it should be ensured the physical sense to each of the individual operators.

An explicit Euler scheme is used for the treatment the source terms S and constitutes the final step of the calculation of each iteration

$$\begin{aligned} & U_{i,1}^{n+1} = U_i^{n+1} + \Delta t S_1(U_i^{n+1}) \rightarrow \\ & U_{i,2}^{n+1} = U_{i,1}^{n+1} + \Delta t S_2(U_{i,1}^{n+1}) \rightarrow \ldots \rightarrow \\ & U_i^{n+1} = U_{i,st}^{n+1} \end{aligned} \tag{3.114}$$

where the subscript $st = \mathrm{N}$ indicates the number N of the successive step in which only one source term is added.

A Courant-Friedrichs-Levy condition is applied to stabilize computations

$$Cr = \frac{\max(|\lambda_{\min}|, |\lambda_{\max}|)}{\Delta x / \Delta t} \leq 1$$

and a constant Courant number $Cr = 0.5$ is used for all the computations.

3.4 Features of SWBI2D

The program SWBI2D developed for this PhD thesis, has followed the main structure of the program SFlow2D. SFlow2D was created for modelling flows solving shallow water equations with finite volume method in unstructured mesh by Professor Soares-Frazão. The present model introduces a two-layer debris flow-turbidity current flow over a two-dimensional unstructured mesh.

The SWBI2D needs as an input the initial geometry, the number and the coordinates of all cells, nodes and interfaces of the computational domain.

The way of mesh generation is chosen by the user. The free software GMSH is suggested and used for the simulations presented in this study that produces unstructured triangular mesh.

Apart from mesh information, the model needs input information about the initial condition of the layers in order to run the simulation. It can treat the cases in which there is an initial volume of a debris flow or both layers already exist. The input parameters, which need to be defined by the user, are given as a text file which is read in the beginning of each simulation (see Appendix B).

3.5 Model validation

The proposed numerical scheme consists of hyperbolic solvers that are used to solve a partially non-hyperbolic problem. This fact leads to the necessity of a detailed examination of the computational results.

The solution behaviour is tested for cases in which hyperbolicity is guaranteed and analytical solutions are available.

3.5.1 Single density validation

The model SWBI2D is tested for a dam-break problem involving two layers of identical density $\rho_1 = \rho_2$ that are initially at rest in a configuration characterized by a step as their internal interface as depicted in Figure 3.12. Fluid depths to the left and right of the dam are set equal to 10 and 1 m respectively (Wang and Shen, 1999).

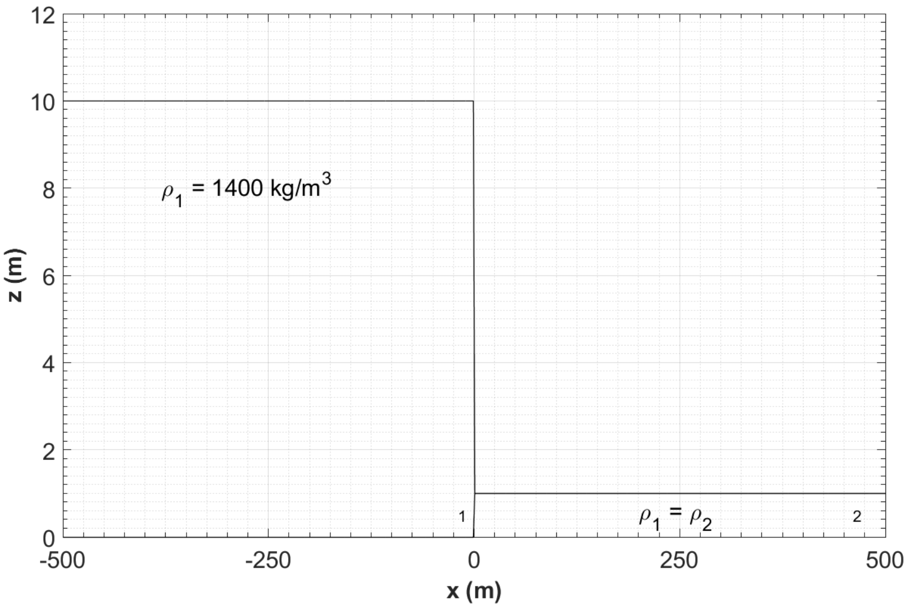

Figure 3.12. Definition sketch of a dam-break flow involving two layers of equal densities $\rho_1 = \rho_2$.

As proposed in the work of Spinewine (2011), the initial conditions are the following:

$$x<0:\begin{pmatrix} h_1 \\ h_2 \\ u_1 \\ u_2 \end{pmatrix} = \begin{pmatrix} h_{1L} \\ h_{2L} \\ u_{1L} \\ u_{2L} \end{pmatrix} = \begin{pmatrix} \frac{10}{9}H \\ 0 \\ 0 \\ 0 \end{pmatrix}, x>0:\begin{pmatrix} h_1 \\ h_2 \\ u_1 \\ u_2 \end{pmatrix} = \begin{pmatrix} h_{1R} \\ h_{2R} \\ u_{1R} \\ u_{2R} \end{pmatrix} = \begin{pmatrix} 0 \\ \frac{1}{9}H \\ 0 \\ 0 \end{pmatrix}$$

Detrainment and entrainment are not considered. The level difference $H = h_{1L} + h_{2L} - h_{1R} + h_{2R}$ between the two sides of the dam is used as basic scale for the problem (Spinewine, 2011).

For identical densities $\rho_1 = \rho_2$, the velocities of the two layers are considered the same. The problem is treated as a three degrees of freedom system and it can be described by the classical analytical solution for a single layer dam-break presented by Stoker (1957). This solution was used by Chen et al. (2007) and Spinewine (2011) to validate two-layer shallow flow computations.

The wave consists of a gradually expanding self-similar profile composed of a smooth rarefaction upstream, a central uniform region of depth h_C and velocity u_C , and a shock propagating downstream at speed v_s. In the rarefaction, the profile is given by

$$u - c = x/t$$
$$u + 2c = 2c_L \qquad where \qquad c = \sqrt{g(h_1 + h_2)}$$

and across the shock

$$h_C = \frac{1}{2} h_R \left\{ \sqrt{1 + 8v_s^2 / (gh_R)} - 1 \right\}$$

Figure 3.13 compares computed profiles for different times t with the Stoker analytical solution for the sudden breach of a dam over a horizontal frictionless bed. Both the computed and analytical profiles are plotted in dimensionless similarity coordinates z/H versus $x/t\sqrt{gH}$. It is checked that the numerical profiles converge towards the analytical solution as the ratio $t\sqrt{gH}/\Delta x$ grows that corresponds to a longer time being equivalent to a finer discretization. The HLL scheme handles adequately the transcritical transition at the location of the dam break $x = 0$.

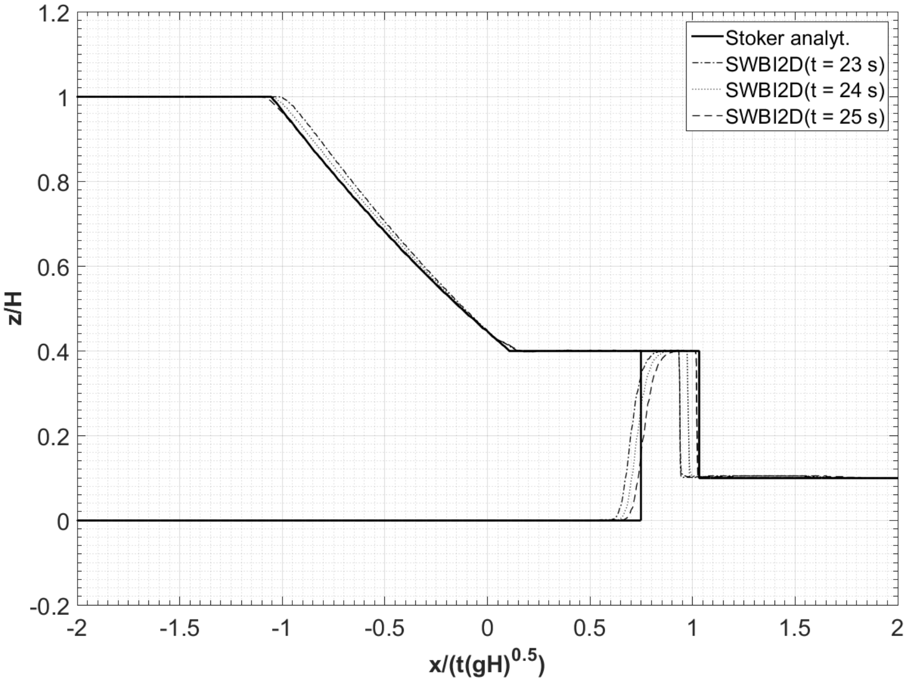

Figure 3.13. Comparison of numerical and analytical results for a dam-break problem. Non-dimensional surface profiles.

3.5.2 Dam-break flow of light fluid over dense fluid

The case of a dam-break wave involving two layers is simulated to test the numerical scheme in transient flow conditions. The two layers are initially at rest with the depth of the bottom layer to be the same on both sides $h_{2L} = h_{2R} = \eta$ and the depth of the upper layer is $h_{1L} = H$ to the left and $h_{1R} = 0$ to the right.

The initial conditions of the two-layer dam-break wave problem for which $\rho_1 \neq \rho_2$ can be written as:

$$
\left.\begin{array}{l} h_{upper} = h_{1L} = H \\ h_{bottom} = h_{2L} = \eta \end{array}\right\} for \quad x < 0
$$

$$
\left.\begin{array}{l} h_{upper} = h_{1R} = 0 \\ h_{bottom} = h_{2L} = \eta \end{array}\right\} for \quad x > 0
$$

$$
u_{upper} = u_{bottom}
$$

The configuration of the problem with $H = 1\ m$ and $\eta = 0.357\ m$ is sketched in Figure 3.14.

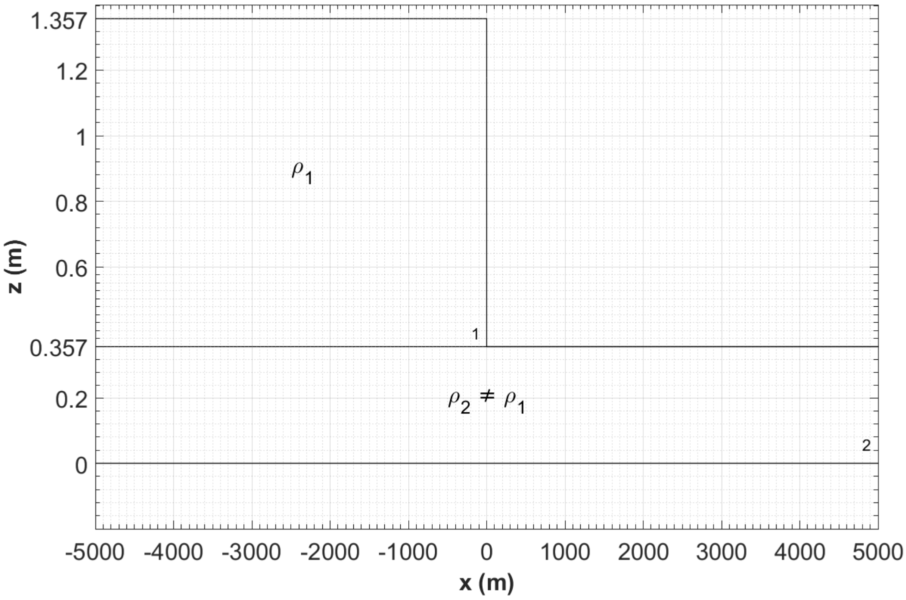

Figure 3.14. Definition sketch of a dam-break flow involving two layers of different densities ρ_1 and ρ_2.

This transient two-layer flow with density contrast $\rho_1 \neq \rho_2$, can be compared with the analytical solution for a case of a single dam-break wave propagating over an initially dry bed that was given by Ritter (1892). For the bottom layer assumed to be dry and initially at rest, the solution reads

$$h(x,t) = \frac{4H}{9}\left\{1 - \frac{x/t}{2\sqrt{gH}}\right\}^2$$

and it is defined in the interval

$$-\sqrt{gH} \le x/t \le 2\sqrt{gH}$$

Outside of this interval the layer depths and velocities are not affected by the wave and remain hence identical to the initial conditions.

Results for the numerical simulation of the dam-break flow of light fluid over dense fluid case for decreasing density ratios compared with Stoker and Ritter analytical solutions are presented from Figure 3.15 to Figure 3.20. The profiles are shown in dimensionless form of coordinates z/H versus $x/t\sqrt{gH}$. The density ratios examined are $\rho_1/\rho_2 = 1, 0.5, 0.2, 0.1, 0.02$ and 0.01.

For the case of ρ_1/ρ_2=1, the two fluids have the same density and therefore the same mobility. This case can be approximated by the analytical solution for a dam-break flow over wet bed proposed by Stoker (1922) similar to the one of the previous section. A contact discontinuity is marking the point at which the two distinct fluids are in contact with each other.

As the ratio ρ_1/ρ_2 decreases, the mobility of the lower layer decreases and the initially sharp discontinuity evolves into a smoother profile. The mixing of the two layers of different density at the front region is enhanced by the decrease of the density ratio.

For very low density ratios, the collapse of the upper layer will not be able to move the bottom layer, as its relative inertia becomes so large that it behaves as a rigid solid body. The upper layer adopts the smooth profile of the analytical solution of the Ritter case of a dam-break flow over an initially dry bed.

The lowest density ratios are explored here only for the sake of probing the asymptotic behaviour of the two-layer model, since it is clear that such ratios are not encountered for natural liquids nor granular materials (Spinewine, 2011).

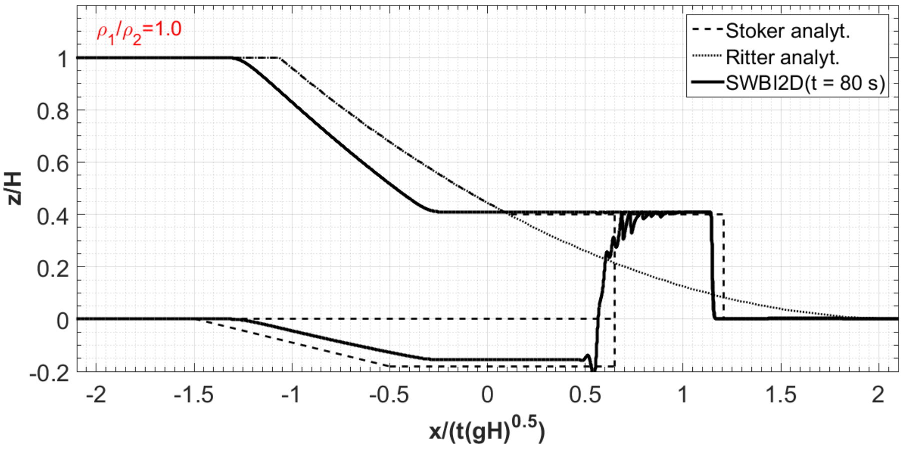

Figure 3.15. Non-dimensional surface profiles of numerical results for the dam-break of a light fluid over a heavier fluid problem for a density ratio $\rho_1/\rho_2 = 1.0$. Analytical results for the Stoker solution ($\rho_1/\rho_2 = 1.0$) in dashed line and for the Ritter solution ($\rho_1/\rho_2 \rightarrow 0$) in dotted line.

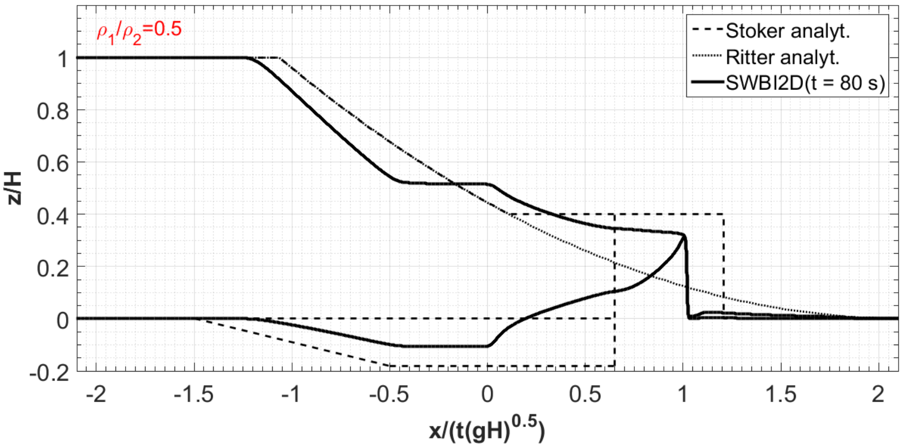

Figure 3.16. Non-dimensional surface profiles of numerical results for the dam-break of a light fluid over a heavier fluid problem for a density ratio $\rho_1/\rho_2 = 0.5$. Analytical results for the Stoker solution ($\rho_1/\rho_2 = 1.0$) in dashed line and for the Ritter solution ($\rho_1/\rho_2 \rightarrow 0$) in dotted line.

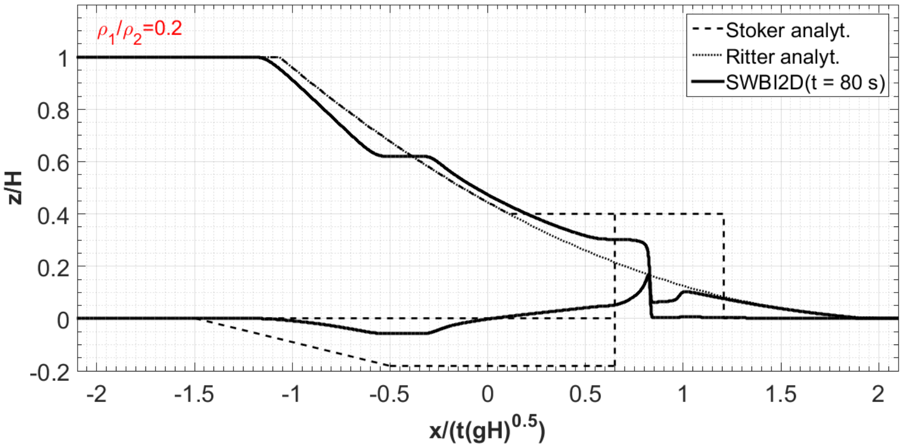

Figure 3.17. Non-dimensional surface profiles of numerical results for the dam-break of a light fluid over a heavier fluid problem for a density ratio $\rho_1/\rho_2 = 0.2$. Analytical results for the Stoker solution ($\rho_1/\rho_2 = 1.0$) in dashed line and for the Ritter solution ($\rho_1/\rho_2 \rightarrow 0$) in dotted line.

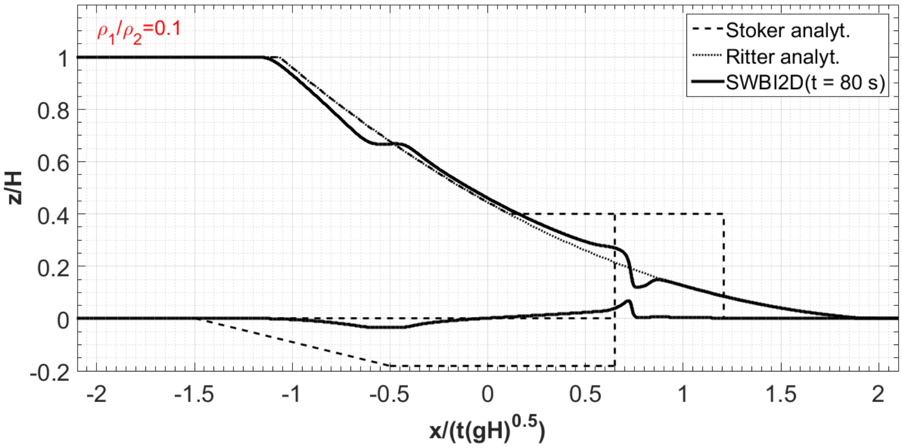

Figure 3.18. Non-dimensional surface profiles of numerical results for the dam-break of a light fluid over a heavier fluid problem for a density ratio $\rho_1/\rho_2 = 0.1$. Analytical results for the Stoker solution ($\rho_1/\rho_2 = 1.0$) in dashed line and for the Ritter solution ($\rho_1/\rho_2 \rightarrow 0$) in dotted line.

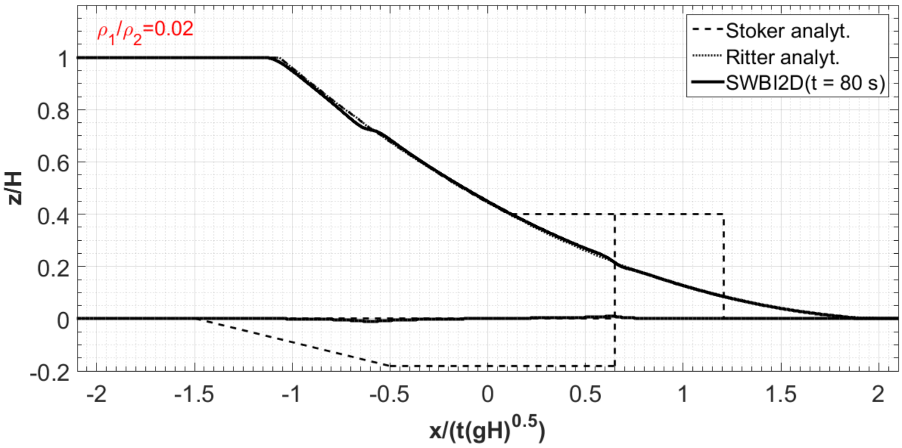

Figure 3.19. Non-dimensional surface profiles of numerical results for the dam-break of a light fluid over a heavier fluid problem for a density ratio $\rho_1/\rho_2 = 0.02$. Analytical results for the Stoker solution ($\rho_1/\rho_2 = 1.0$) in dashed line and for the Ritter solution ($\rho_1/\rho_2 \rightarrow 0$) in dotted line.

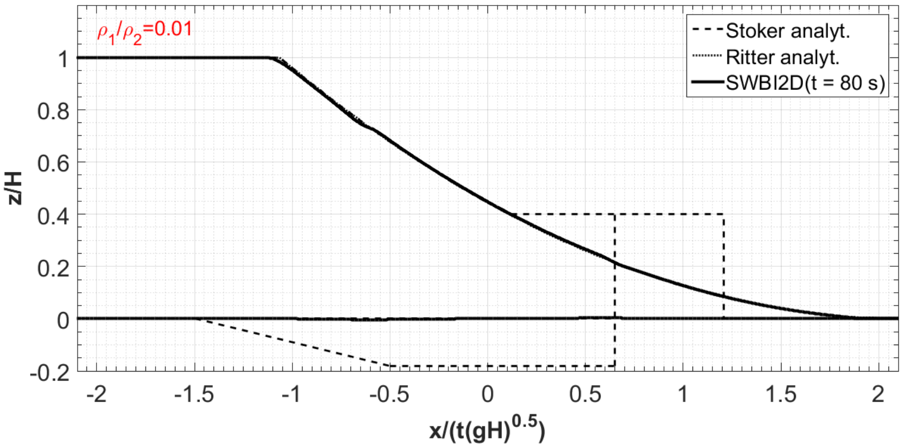

Figure 3.20. Non-dimensional surface profiles of numerical results for the dam-break of a light fluid over a heavier fluid problem for a density ratio $\rho_1/\rho_2 = 0.01$. Analytical results for the Stoker solution ($\rho_1/\rho_2 = 1.0$) in dashed line and for the Ritter solution ($\rho_1/\rho_2 \rightarrow 0$) in dotted line.

3.6 Summary

A two–layer shallow-flow model where the layers have distinct densities and are allowed to flow at distinct velocities, was introduced aiming to represent the dynamics of a submarine slide-induced debris flow transforming into a turbidity current. The resulting set of governing equations derived after applying the principles of mass and momentum conservation to each layer separately followed by the incorporation of all exchange processes that take place between the two layers and their interfaces with the surrounding environment. The non-linear Herschel-Bulkley rheological model was adopted for the debris flow layer while the turbidity layer is considered as a Newtonian fluid in consequence of its low sediment concentration. The sediment detrainment of the debris flow layer is suggested as the generation mechanism of the turbidity current. Interfacial friction and water entrainment complement the exchange mechanisms. The model is robust to the emergence or disappearance of any of the two layers by vanishing thickness, and downgrades to known solutions for pure debris flows or turbidity currents when any of the two layers vanishes.

Numerical computations were performed, using the finite volume approach. Mass and momentum fluxes at each cell's interface have been calculated by the adequate HLL numerical solver. Source terms are treated successively with an explicit Euler scheme. Validation of the model against limiting cases with known analytical solutions, permitted to verify that the partially non-hyperbolic problem can be sufficiently treated by the proposed hyperbolic solvers, and gain insights of the behaviour of the two layers depending on the initial conditions. The next chapter of the thesis achieves a more detailed examination of the model's performance, analysing the numerical results in an idealised hypothetical bathymetry case.

Chapter 4 Runout of submarine landslide on an idealized bathymetry

4.1 Introduction

The satisfactory validation of the model against known solutions, allows to proceed to the illustration of the model in a hypothetical test case. An initial debris flow mass is released on a sloped profile that features a sudden reduction in seabed slope at some distance downstream of the initial release point. Such a bathymetry is reminiscent of a canyon-fan transition which has been investigated in several modelling and experimental setups by other authors.

Detrainment and friction terms of the obtained equations of Section 3.2.1 depend on the selection of the corresponding coefficients e_d and C_d as input parameters by the user. In order to assess the behaviour of the model, the effect of each term should be investigated. The sediment detrainment from the debris flow layer works as the production mechanism of the turbidity current layer, and the detrainment coefficient e_d becomes a determinant factor for the evolution of the two layers. The investigation of the effect of the friction coefficient C_d permits to gain insights into the influence of the interfacial friction in the velocities of the two layers and the formulation of the generated turbidity current.

The dependence of layer thickness, velocity, composition and propagation distance on the detrainment and friction coefficient, is examined for different scenarios in this chapter. While the model has been developed and implemented in two dimensions, the applications that are presented to illustrate the model behavior in this chapter, will be restricted to one-dimensional cases.

4.2 1-D Case Study: Hypothetical bathymetry

The test case adopted to illustrate the model behaviour investigates the release of an imposed debris flows mass on a hypothetical bathymetry profile that features a sudden slope break and splits the computational domain in two portions. The sloping portion of this bathymetry has a constant gradient of 8°, with a horizontal projection of 400m before flattening out and continuing for another 1000m. The initial debris flow release has a height of 4 m and a length of 90 m, placed on the top of the slope (Figure 4.1). This geometry has been chosen as the most simplified approach of a submarine canyon-fan which constitutes the most common environment of such mass flow events.

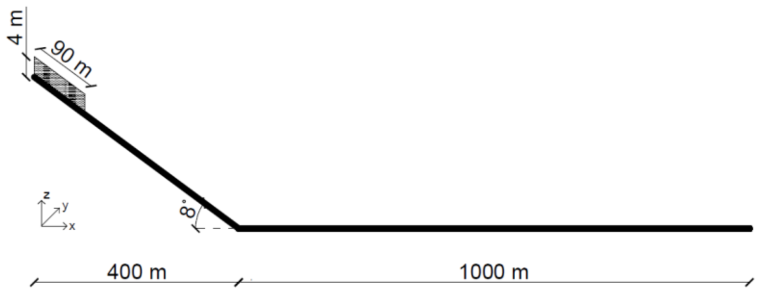

Figure 4.1. Hypothetical bathymetry with a slope break.

All model runs are conducted for a debris flow density, ρ_{DF} of 1400 kg/m^3 and an ambient fluid density ρ_w of 1025 kg/m^3. The Herchel-Bulkley rheological model is adopted for yield stress τ_y equal to 400 Pa, consistency coefficient K equal to 90 Pa·s^n and flow behaviour index n equal to 0.3.

The properties of the sediment that constitutes the solid part of the debris flow are the sediment density ρ_{sed} equal to 2650 kg/m^3 and the mean diameter of the sediment grain size is 80 μm that corresponds to fine sand (see Table 4.1).

Table 4.1. Input parameters

Input parameters	
ρ_{DF}	1400 kg/m^3
ρ_w	1025 kg/m^3
ρ_{sed}	2650 kg/m^3
d_{50}	80 μm
τ_y	400 Pa
K	90 Pa·s^n
n	0.3

The computational mesh is generated using the GMSH software (Geuzaine and Remacle, 2009). Given the initial bathymetry, an unstructured triangular grid is constructed. Triangular mesh is better suited for field application, while for a simple case as the one presented in this chapter, a 1-D mesh could also have been used. A constant cell size equal to 4.7 m is used in all the domain except the source area where there is a small refinement of the mesh. The number of cells along the y-axis is chosen to be equal to 2. The choice of two cells with a common surface located in the middle of y-axis assures the symmetry of the domain with respect to the transversal direction y which allows to consider the results as one-dimensional. Due to the refinement in the source area, there is an additional cell of smaller size with its centre to be located in the middle of y-axis, so that the domain can be identified as symmetric across the y-axis.

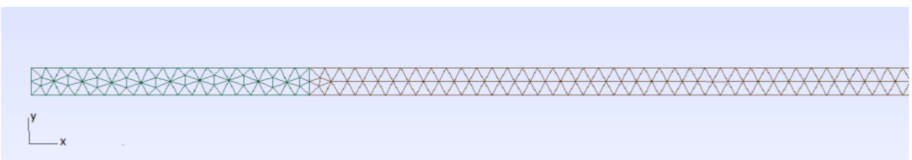

Figure 4.2. Detail of the computational mesh in the source area and part of the runout area, generated by GMSH software.

The influence of the detrainment coefficient e_d and the Chezy friction coefficient C_d on the runout distance of the debris flow and the development and propagation of the turbidity current, are examined in 8 different scenarios given in Table 4.2. All simulations were executed for a total time of 500 s.

Table 4.2. Simulation cases

Scenario	Detrainment Coef.	Friction Coef.
	e_d	C_d
A	0.001	0.005
B	0.01	0.005
C	0.05	0.005
D	0.05	0.01
E	0.001	0.001
F	0.01	0.001
G	0.01	0.01
H	0	0

Table 4.3 provides information on the behaviour of the flow for different combinations of entrainment and friction coefficients for all tested scenarios. The values of the maximum longitudinal velocity and the corresponding time of occurrence for each layer are given. The runout distance of the debris flow layer before it stops its propagation and the flow thickness of the turbidity current layer are also presented in Table 4.3.

Table 4.3. Characteristic velocity, length and flow thickness values for debris flow (DF) and turbidity current (TC) layer for all tested scenarios.

Scenario	Detraiment Coef.	Friction Coef	Max Velocity DF		Max Velocity TC		Runout distance of DF		Max thickness of TC	
	e_d	C_d	$u_{max,DF}$ [m/s]	$t_{max,DF}$ [s]	$u_{max,TC}$ [m/s]	$t_{max,TC}$ [s]	$l_{max,DF}$ [m]	$t_{lmax,DF}$ [s]	$h_{max,TC}$ [m]	$t_{max,TC}$ [s]
A	0.001	0.005	8.62	45.01	2.69	46.00	517.5	75.13	6.28	416.12
B	0.01	0.005	8.42	40.00	4.72	45.06	500.0	77.06	6.65	438.16
C	0.05	0.005	8.44	41.09	5.56	40.00	497.5	75.09	6.72	431.35
D	0.05	0.01	8.22	41.05	5.36	41.05	497.5	76.00	7.84	500.32
E	0.001	0.001	9.46	48.03	2.42	44.06	545.0	75.15	4.51	316.01
F	0.01	0.001	8.59	39.02	4.87	44.04	490.0	74.05	4.82	400.22
G	0.01	0.01	8.12	41.00	4.47	45.03	500.0	78.02	8.20	500.23
H	0	0	9.80	48.01	-	-	570.0	78.00	-	

4.2.1 Effect of the detrainment coefficient e_d

The detrainment coefficient e_d constitutes the single mechanism that governs the generation of the turbidity current layer from the initial debris flow layer in this model. In this section, the effects of e_d on the runout distance, the thickness of the two layers, the propagation velocity, the sediment concentration of the turbidity current and on the general behaviour of the flow, are investigated for the different scenarios, A, B and C.

In Figure 4.3 and Figure 4.4, the evolution of the flow as also the sediment concentration of the turbidity current are presented. It should be reminded that the debris flow density is considered constant and in Figure 4.3-Figure 4.4 is represented by the dark red colour. In each Figure, the left side corresponds to the Scenario A with e_d equal to 0.001 and the right side corresponds to the Scenario B with e_d equal to 0.01. The friction coefficient C_d is equal to 0.005 for both scenarios. All flow heights are exaggerated 5 times for illustrative purposes.

The first seconds after the start of the simulation and the release of the imposed volume, the effect of the detrainment coefficient is not significant as the runout distance for the two cases is quite similar (Figure 4.3). After t = 30 s, the difference in the formation of the turbidity current layer is more apparent. For Scenario A, limited detrainment has occurred coming from the main body of the debris flow, while for Scenario B the detrainment process has been fully activated along the whole length of the parent debris flow. The sediment concentration of the turbidity current is higher for the case of higher e_d (Figure 4.3). As the flow for Scenario B reaches the slope break at $t =$ 50 s, the head of the flow for Scenario A has travelled 20 m more with double the thickness than the other. At t = 70 s, the debris flow continues its propagation with a relatively dilute turbidity current on top for the case of low e_d, while for the higher e_d the created turbidity current propagates downstream with high concentration (Figure 4.3). In Figure 4.4, the initial debris flow layer has completely transformed into a turbidity current that is characterised by a denser main body and a more dilute tail that continues its propagation as a single layer for Scenario B, while the detrainment processes continues much slower for the Scenario A.

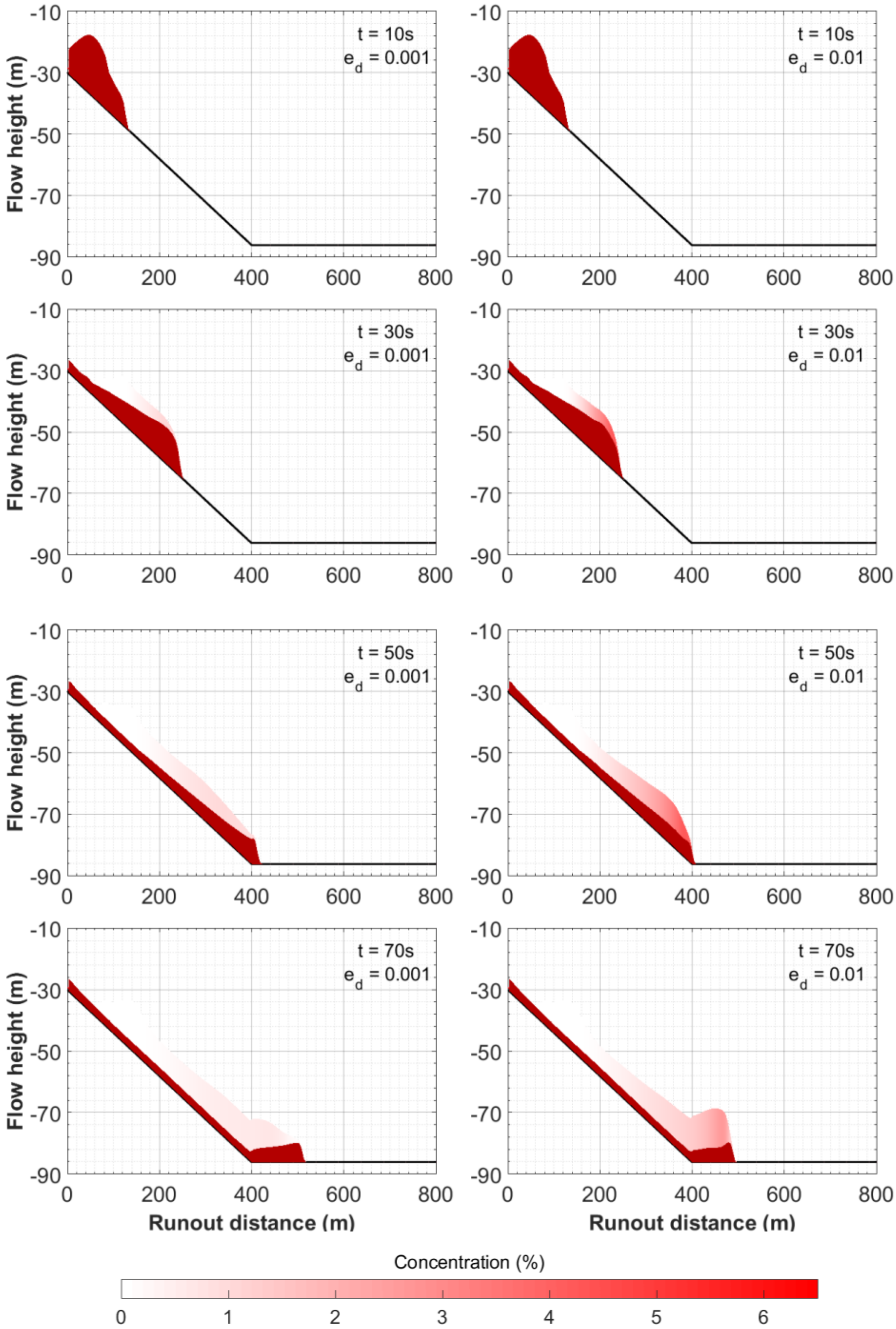

Figure 4.3. Simulations with detrainment coefficient e_d = 0.001 (left) and e_d = 0.01 (right) at various time instances. Flow height is exaggerated 5 times.

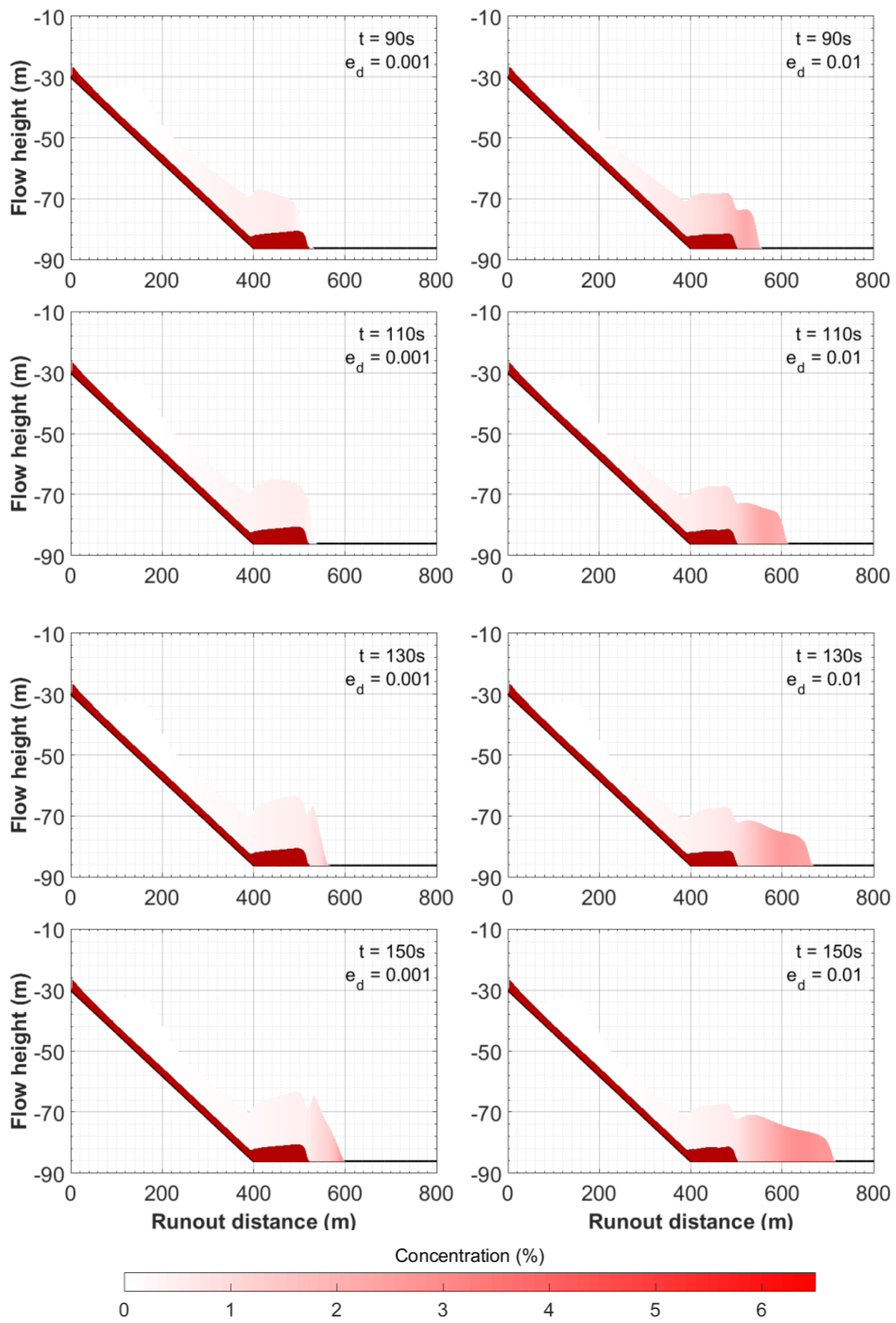

Figure 4.4. Simulations with detrainment coefficient e_d = 0.001 (left) and e_d = 0.01 (right) at various time instances. Flow height is exaggerated 5 times.

Figure 4.5 to Figure 4.12 illustrate the flow thickness of the two layers and the corresponding longitudinal velocity at the same time instance. Solid lines correspond to the debris flow while dotted line correspond to the turbidity current. Figures on the left correspond to Scenario A for $e_d = 0.001$ and figures on the right correspond to Scenario B for $e_d = 0.01$. It should be noted that the velocities are averaged over the layer thickness and flow thickness is 5 times exaggerated for illustrative purposes.

Ten seconds after the release of the volume, no significant difference is observed between the two cases (Figure 4.5). At t = 30 s, the velocity of the front of the turbidity current is almost the double for the smaller value of e_d, while the debris flow layer velocities for both cases are of the same order. The difference of the flow thickness of the turbidity current layer in the region following the front, starts to be noticeable (Figure 4.6).

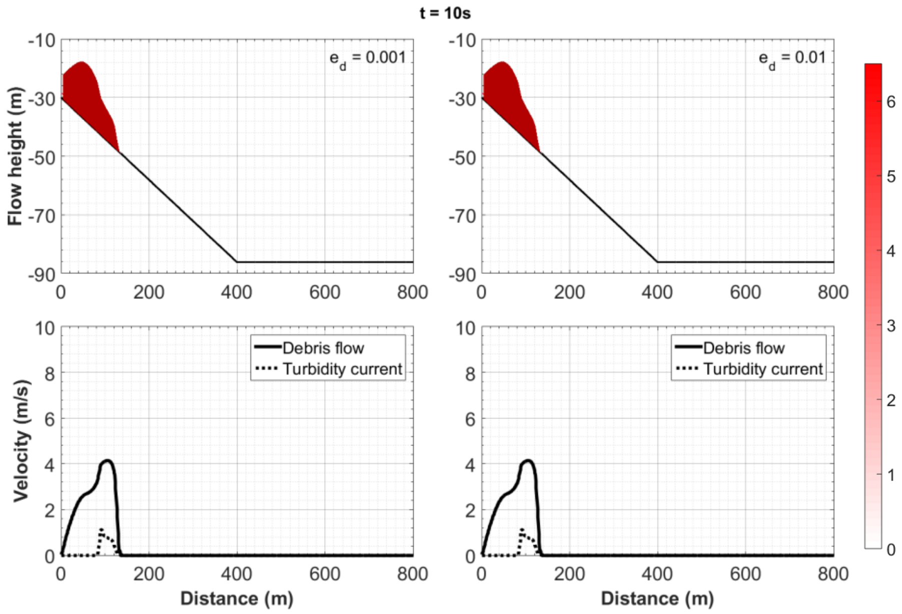

Figure 4.5. Flow height (exaggerated x5) and the corresponding longitudinal velocity of the debris flow and turbidity current layer for e_d = 0.001 (left) layer and e_d = 0.01 (right) at t = 10 s. Colorbar refers to sediment concentration (%).

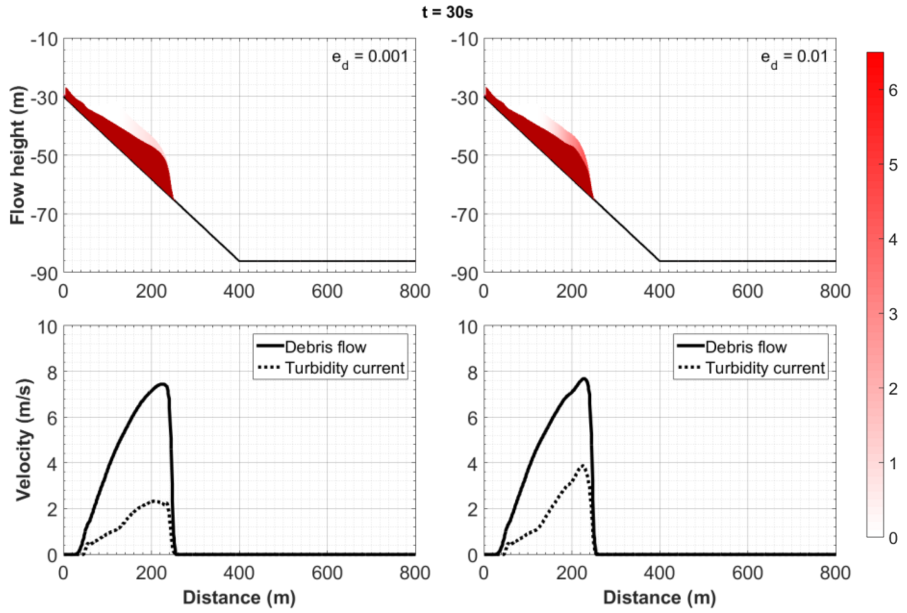

Figure 4.6. Flow height (exaggerated x5) and the corresponding longitudinal velocity of the debris flow and turbidity current layer for e_d = 0.001 (left) layer and e_d = 0.01 (right) at t = 30 s. Colorbar refers to sediment concentration (%).

At t = 50 s when the front of the flow has reached the slope break, it is observed that for the case with e_d equal to 0.001, the debris flow has maintained the thickness of its head with the detrainment process to be more intense behind it. At the same time instance for e_d equal to 0.01, the detrainment takes place uniformly along the debris flow layer and the front of the generated turbidity current propagates with the double velocity.

Figure 4.8 shows the flow height along the runout distance when the flow has reached the horizontal part of the bathymetry for both cases. Instantaneous peaks observed in the debris flow velocity that had already stopped, can be explained by the remobilization of its deposits, caused by the propagation of the turbidity current on the top of them. The remobilisation of some parts of the deposits is a result of the applied shear stress on them by the propagating turbidity current layer.

The velocity of the debris flow layer for both cases, is increasing until the flow reaches the slope break without significant differences in their values. For a ten times larger e_d, the velocity of the corresponding turbidity current layer is double. The debris flow velocity reaches its maximum value 5 sec earlier for e_d = 0.01 than for e_d = 0.001 (see Table 4.3). After that point the debris flow starts to decelerate while the turbidity current velocity decreases.

Looking at Figure 4.9 to Figure 4.12, it can be observed that the debris flow has stopped propagating and been deposited for both cases. The total runout distance of the debris flow layer is 17.5 m longer for $e_d = 0.001$ than for $e_d = 0.01$. It is worth mentioning that the turbidity current continues its propagation for e_d = 0.01, while for e_d = 0.001 the turbidity current has the resemblance of a very dilute cloud that is suspended on top of the debris flow deposits. The turbidity current is too weak to be able to detrain the remaining deposits of the debris flow for both cases.

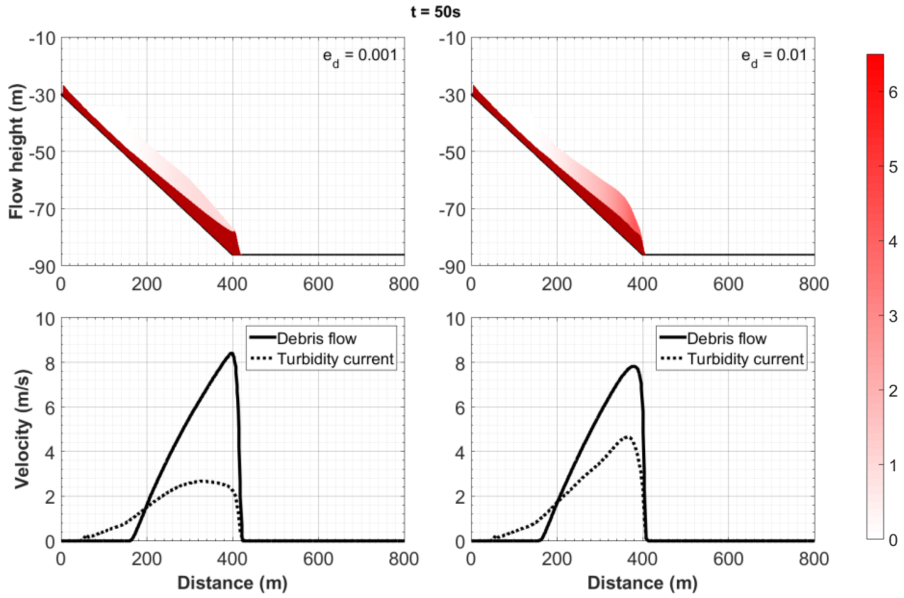

Figure 4.7. Flow height (exaggerated x5) and the corresponding longitudinal velocity of the debris flow and turbidity current layer for e_d = 0.001 (left) layer and e_d = 0.01 (right) at t = 50 s. Colorbar refers to sediment concentration (%).

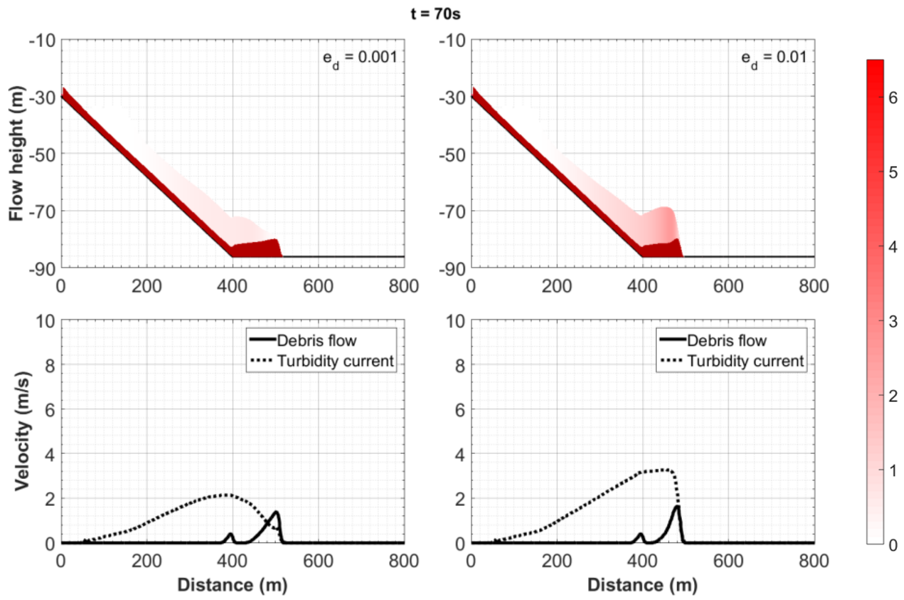

Figure 4.8. Flow height (exaggerated x5) and the corresponding longitudinal velocity of the debris flow and turbidity current layer for e_d = 0.001 (left) layer and e_d = 0.01 (right) at t = 70 s. Colorbar refers to sediment concentration (%).

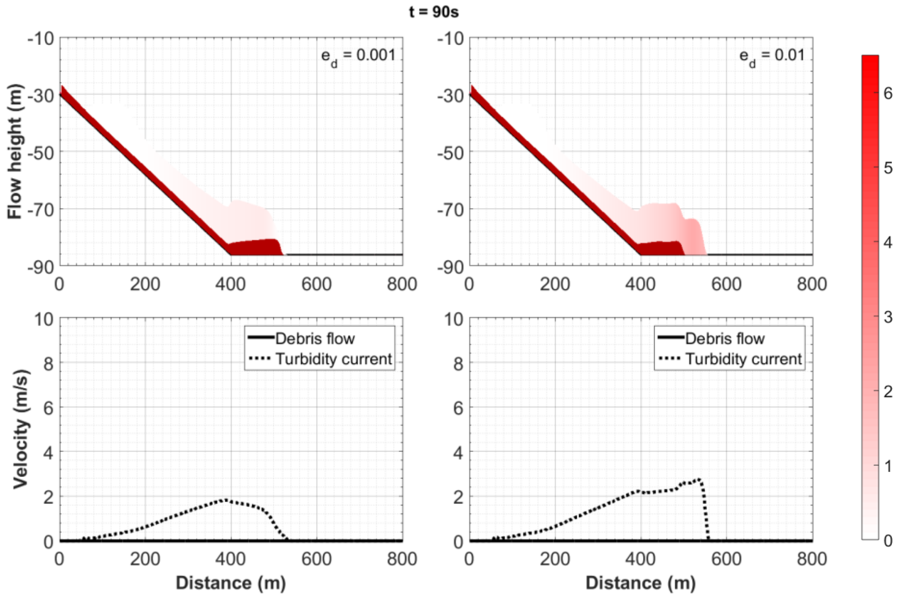

Figure 4.9. Flow height (exaggerated x5) and the corresponding longitudinal velocity of the debris flow and turbidity current layer for e_d = 0.001 (left) layer and e_d = 0.01 (right) at t = 90 s. Colorbar refers to sediment concentration (%).

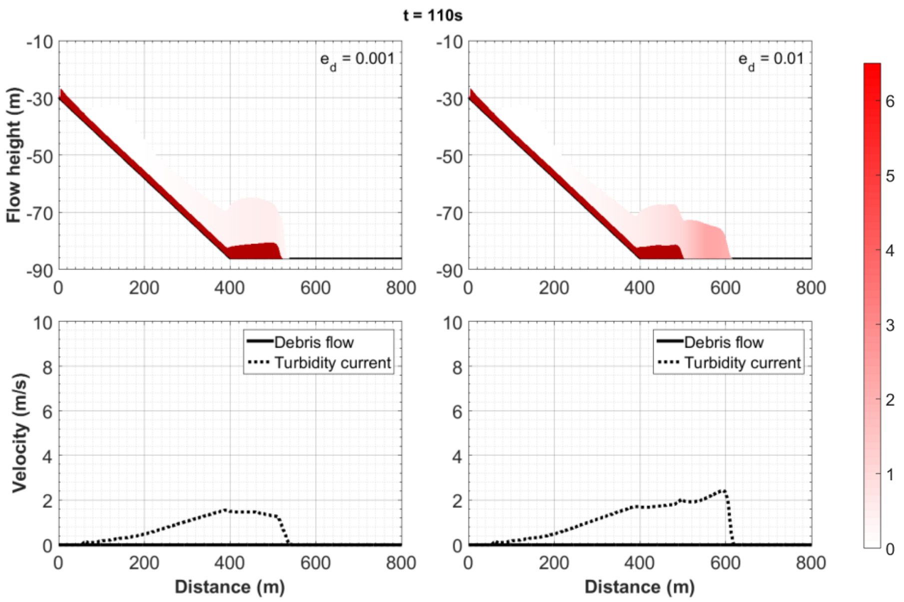

Figure 4.10. Flow height (exaggerated x5) and the corresponding longitudinal velocity of the debris flow and turbidity current layer for e_d = 0.001 (left) layer and e_d = 0.01 (right) at t = 110 s. Colorbar refers to sediment concentration (%).

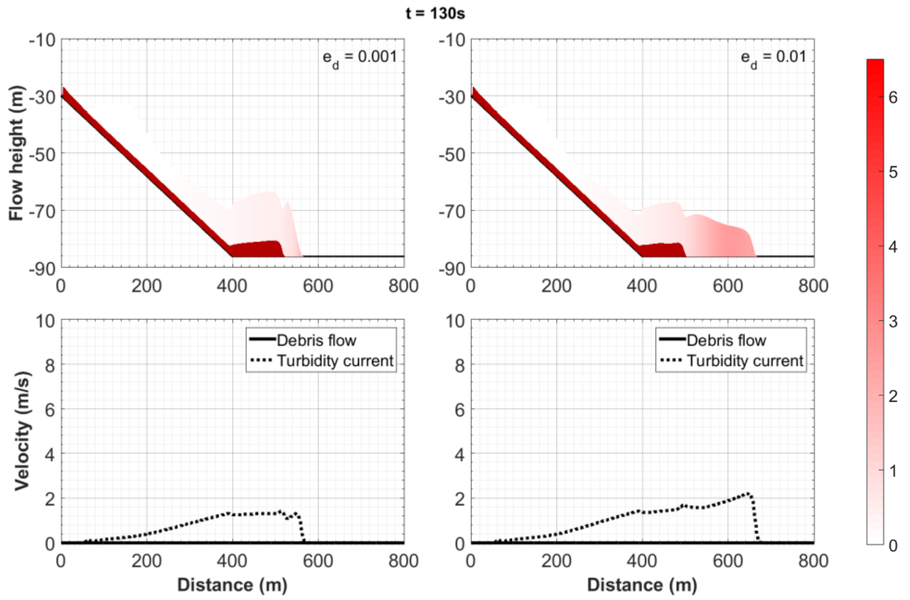

Figure 4.11. Flow height (exaggerated x5) and the corresponding longitudinal velocity of the debris flow and turbidity current layer for e_d = 0.001 (left) layer and e_d = 0.01 (right) at t = 130 s. Colorbar refers to sediment concentration (%).

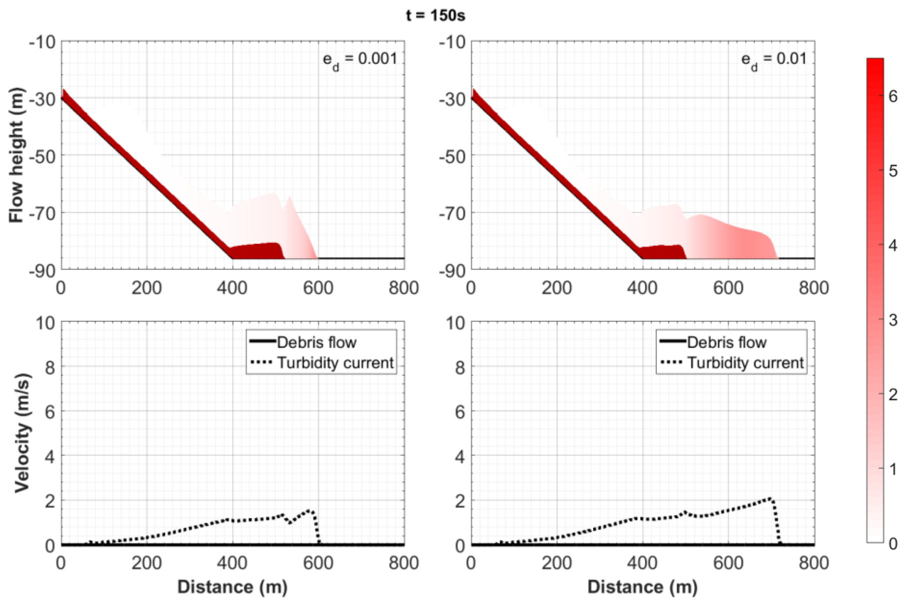

Figure 4.12. Flow height (exaggerated x5) and the corresponding longitudinal velocity of the debris flow and turbidity current layer for e_d = 0.001 (left) layer and e_d = 0.01 (right) at t = 150 s. Colorbar refers to sediment concentration (%).

Figure 4.13 presents the evolution of the sediment concentration of the generated turbidity current for the cases of different detrainment coefficient, A and B, with a timestep of 20 s. Sediment concentration for $e_d = 0.01$ has a maximum value of 8 % while for $e_d = 0.001$ is equal to 2%, when the flow reaches the slope break ($t = 50\ s$). At $t = 90\ s$, the maximum sediment concentration is decreased by half for both cases which follows the halt of the debris flow layer (see Table 4.3). After $t = 110\ s$, the sediment concentration starts to increase again, reaching approximately the same maximum value for both detrainment coefficients (around 6%).

The main difference is found in the sediment concentration distribution along the total length of the turbidity current layer, which reaches a sharp peak indicating that most of the sediment concentration is confined to the head area for $e_d = 0.001$, while for $e_d = 0.01$ is more uniformly distributed. It is also observed that the generated turbidity current for the case of higher e_d, has larger total length.

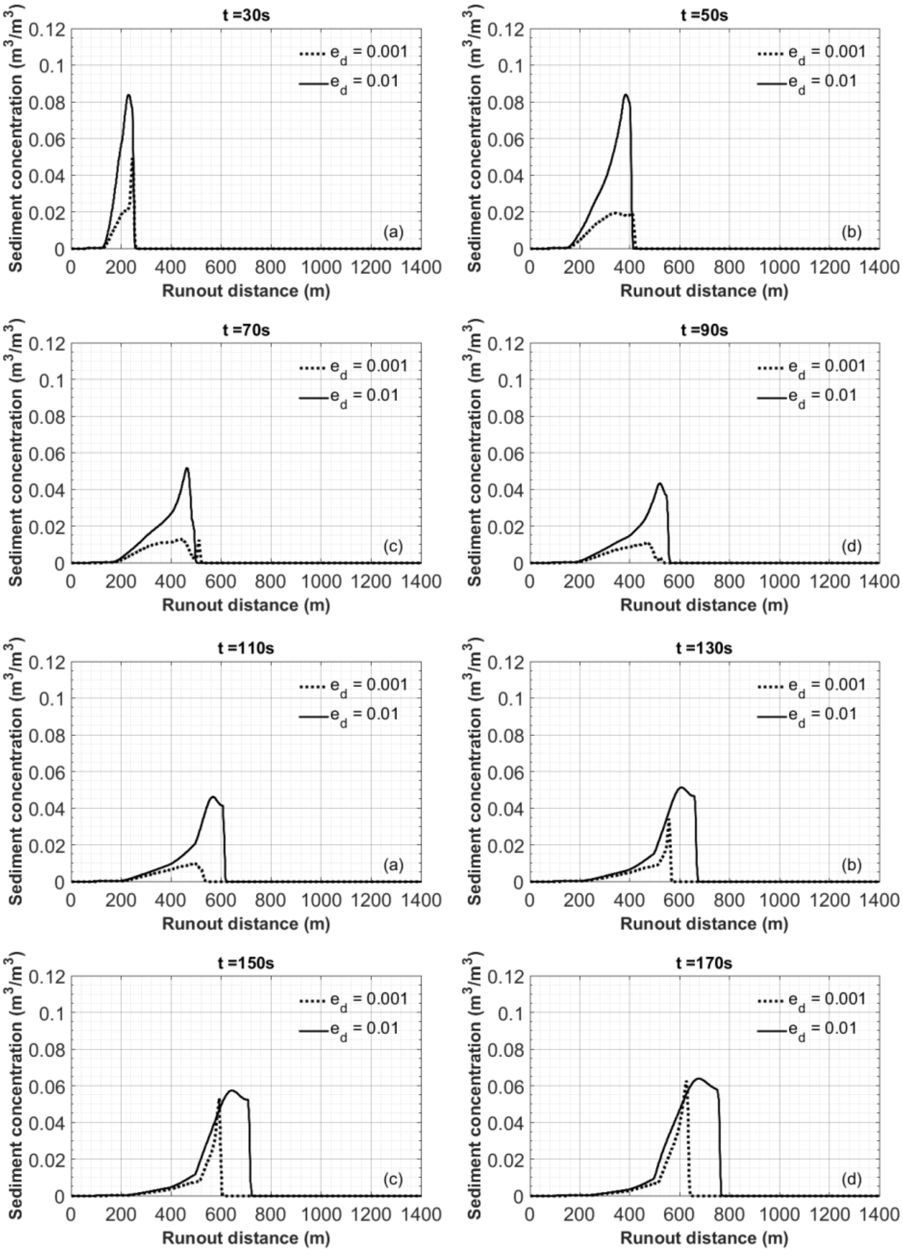

Figure 4.13. Sediment concentration of the turbidity current layer.

Scenario C investigates the behaviour of the model for a detrainment coefficient $e_d = 0.05$, keeping constant the friction coefficient C_d to 0.005 as in Scenarios A and B. Figure 4.14 presents the time evolution of the longitudinal velocity of the debris flow layer for the three different values of e_d. No significant difference is noticed for the three scenarios at the initiation of the flow. After $t = 30\ s$ until the halt of the debris flow layer, the most worth-noticed observations are that the velocity for the two larger values of e_d reaches its maximum earlier than for the smaller e_d and the difference in values is ranging between 0.1 to 0.6 m/s. At $t = 60\ s$, the front velocity for $e_d\ = 0.01$ and 0.05 are identical. For all cases, debris flow layer has stopped propagating before $t = 80\ s$.

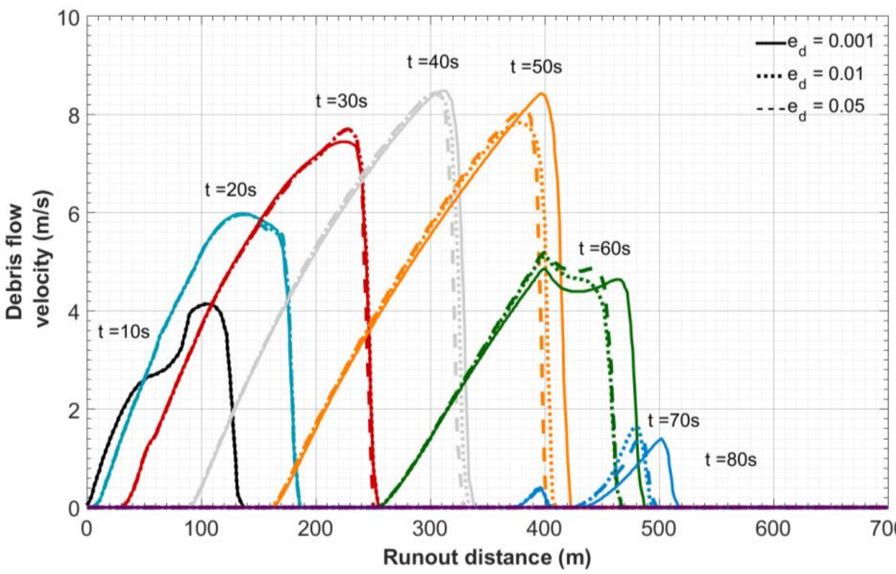

Figure 4.14. Longitudinal velocity evolution of the debris flow layer for detrainment coefficient e_d =0.001 (scenario A-solid line), e_d =0.01 (scenario B-dotted line) and e_d =0.05 (scenario C-dashed line). Black colour corresponds to t = 10 s, cyan to t = 20 s, red to t = 30 s, grey to t = 40 s, orange to t = 50 s, green to t = 60 s, blue to t = 70 s and purple to t = 80 s.

In Figure 4.15 which presents the longitudinal velocity of the turbidity current layer, the effect of the detrainment coefficient is more pronounced. The larger the detrainment coefficient is, the larger the velocity of the generated turbidity current. Going from $e_d = 0.001$ to a ten-time larger value, results in a 75%

increase of the maximum longitudinal velocity while the increase from $e_d = 0.01$ to $e_d = 0.05$ causes 15% increase of the maximum turbidity current velocity (see Table 4.3 and Figure 4.15). From $t = 70\,s$ to $t = 80\,s$, the deceleration rate is three times larger for Scenario A with $e_d = 0.001$, than for Scenarios B and C.

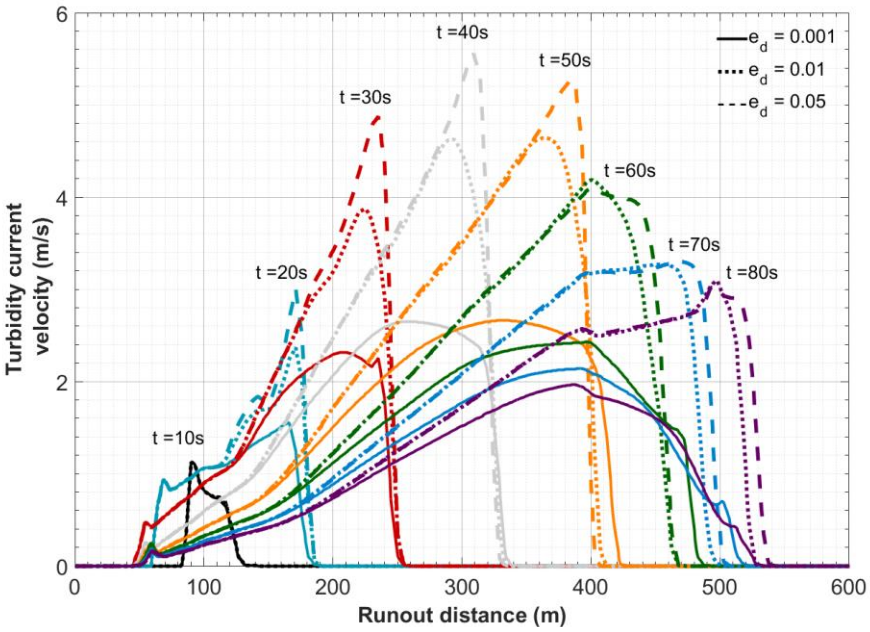

Figure 4.15. Longitudinal velocity evolution of the turbidity current layer for detrainment coefficient e_d =0.001 (scenario A-solid line), e_d =0.01 (scenario B-dotted line) and e_d =0.05 (scenario C-dashed line). Black colour corresponds to t = 10 s, cyan to t = 20 s, red to t = 30 s, grey to t = 40 s, orange to t = 50 s, green to t = 60 s, blue to t = 70 s and purple to t = 80 s.

4.2.2 Effect of the friction coefficient C_d

The friction coefficient C_f governs the friction developed at the interface between the debris flow and turbidity current layers. As previously mentioned, the debris flow layer is assumed to be solid-like and responds passively to the shear stress imposed by the turbidity current that behaves as a fluid, under shear layer. A higher C_d leads to the generation of a turbidity layer with higher thickness but more dilute and slower propagation compared to the case with a lower C_d.

Figure 4.16 and Figure 4.17 show the flow thickness of both layers as well as the sediment concentration of the turbidity current layer during its propagation along the slope break bathymetry. The debris flow density is considered constant and is represented by the dark red colour. In each Figure, the left side corresponds to the Scenario F with C_d equal to 0.001 and the right side corresponds to the Scenario G with C_d equal to 0.01. The detrainment coefficient e_d is equal to 0.01 for both scenarios. All flow heights are exaggerated 5 times for illustrative purposes.

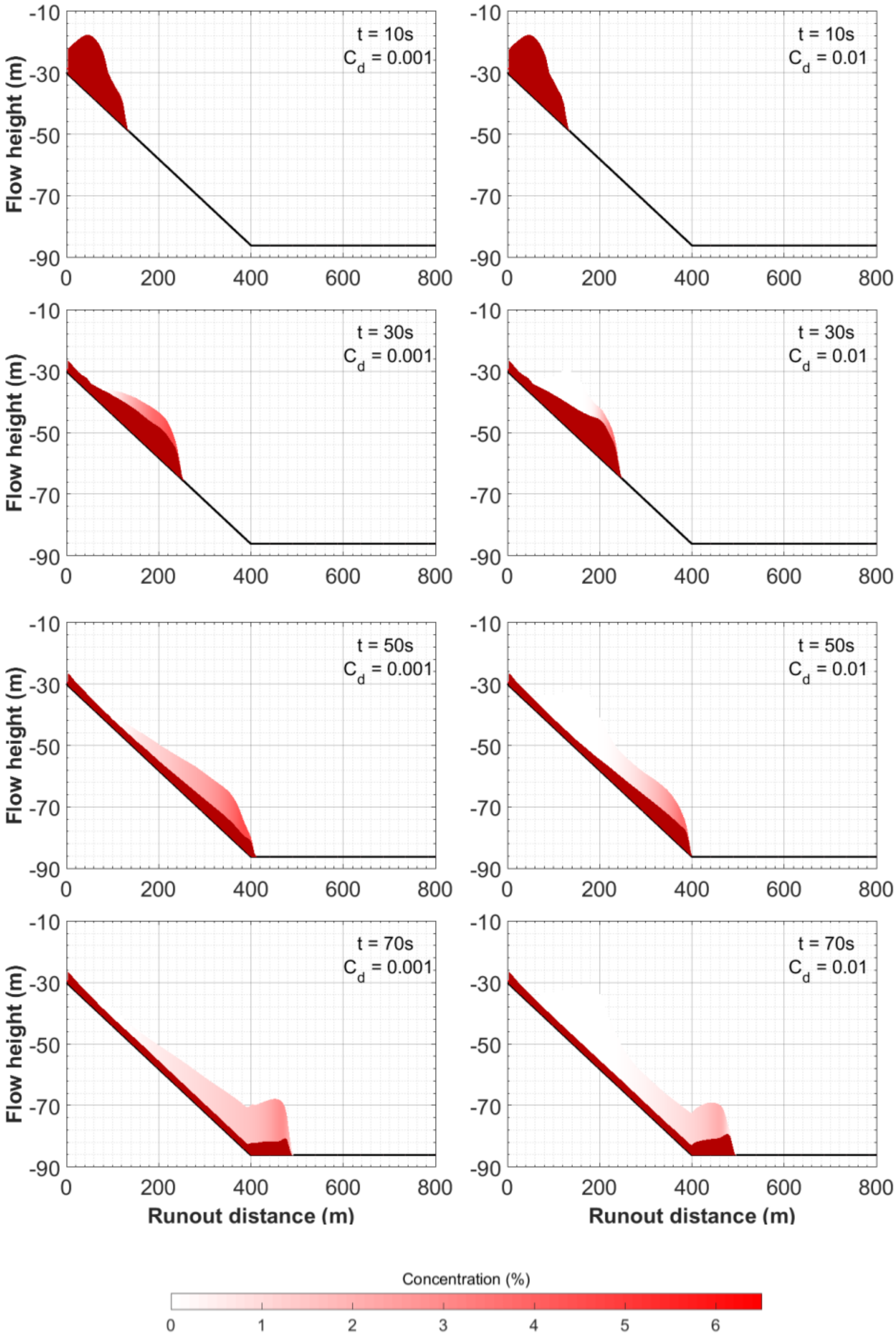

Figure 4.16. Simulations with friction coefficient C_d = 0.001 (left) and C_d = 0.01 (right) at various time instances. Flow height is exaggerated 5 times.

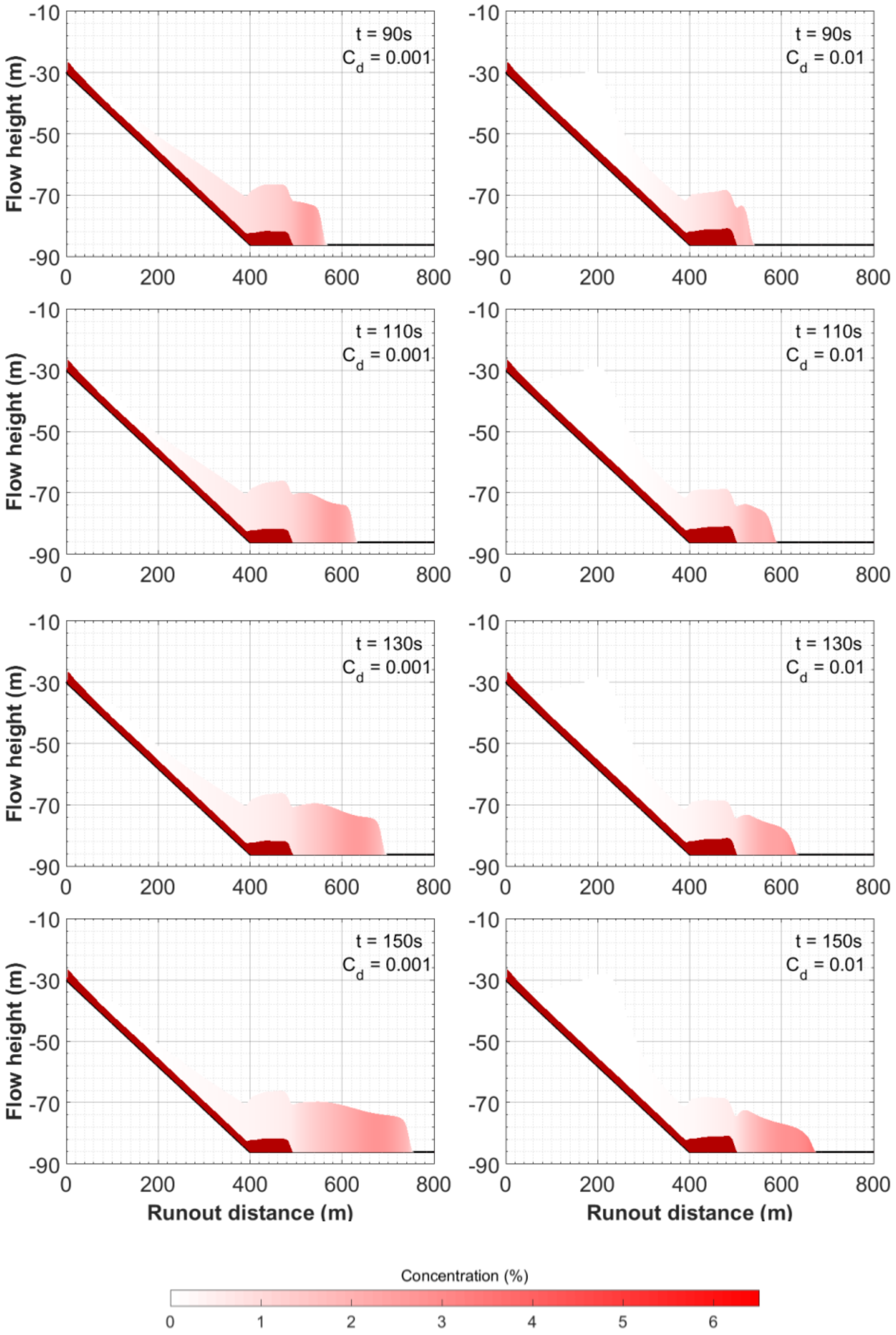

Figure 4.17. Simulations with friction coefficient C_d = 0.001 (left) and C_d = 0.01 (right) at various time instances. Flow height is exaggerated 5 times.

From Figure 4.18 to Figure 4.21, the velocity in the x direction of each layer is given in relation with the height and the runout distance of the flow for various time instances. The left part of the Figures corresponds to Scenario F for $C_d = 0.001$ and the right part corresponds to Scenario G for $C_d = 0.01$. It should be noted that the velocities are averaged over the layer thickness and flow thickness is 5 times exaggerated for illustrative purposes. Solid lines correspond to the debris flow while dotted line correspond to the turbidity current.

The velocity profiles for both scenarios show quite similar longitudinal velocity profiles. The main difference is that for higher friction coefficient the main body of the flow stays more attached to the basal flow while the larger velocities are developed in the front area. The turbidity current that was created when higher friction is applied between the two layers, develops a high thickness in the back which can be more described as a layer of suspended material on top of the basal layer with velocities less than 1 m/s and very low sediment concentration.

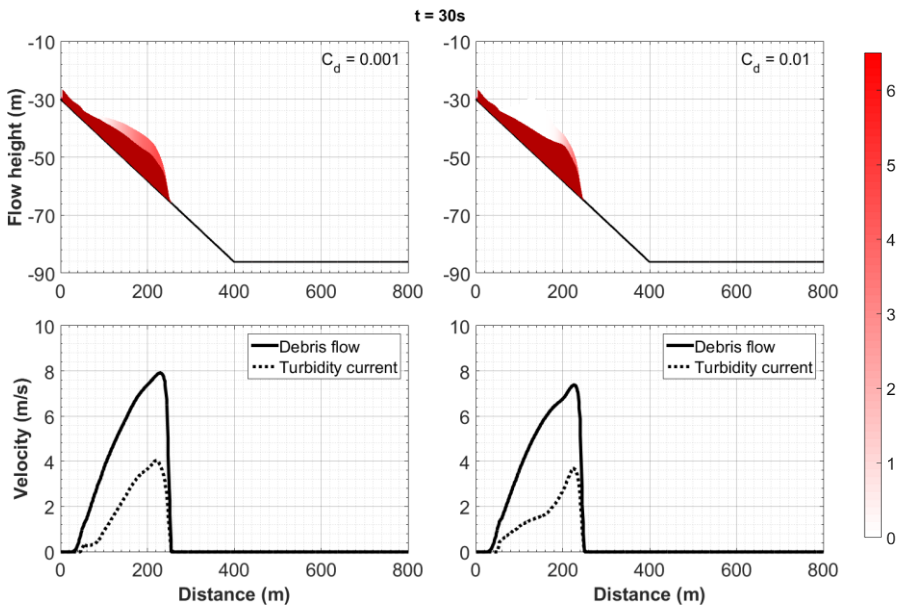

Figure 4.18. Flow height (exaggerated x5) and the corresponding longitudinal velocity of the debris flow and turbidity current layer for $C_d = 0.001$ (left) and for $C_d = 0.01$ (right) at $t = 30$ s. Colorbar refers to sediment concentration (%).

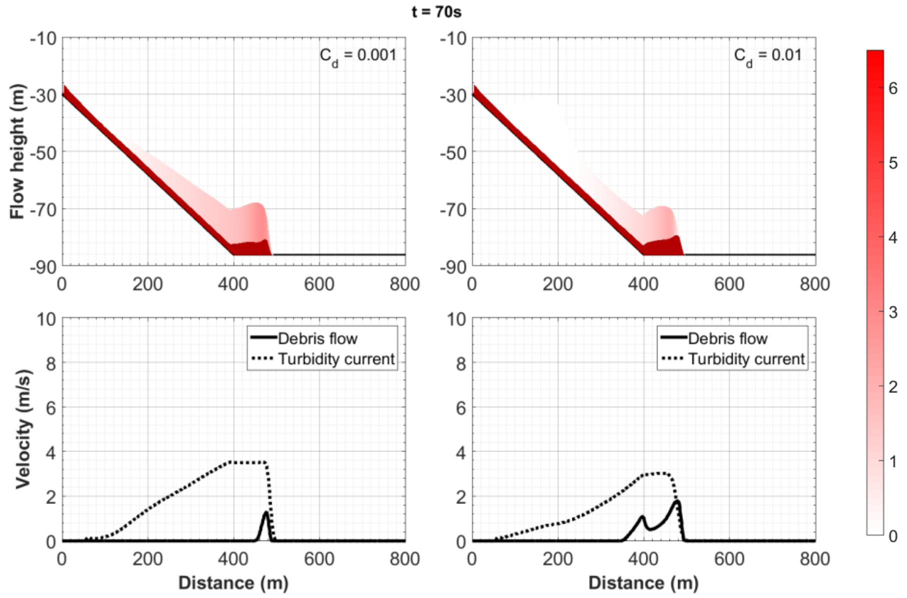

Figure 4.19. Flow height (exaggerated x5) and the corresponding longitudinal velocity of the debris flow and turbidity current layer for C_d =0.001 (left) and for C_d =0.01 (right) at t = 70 s. Colorbar refers to sediment concentration (%).

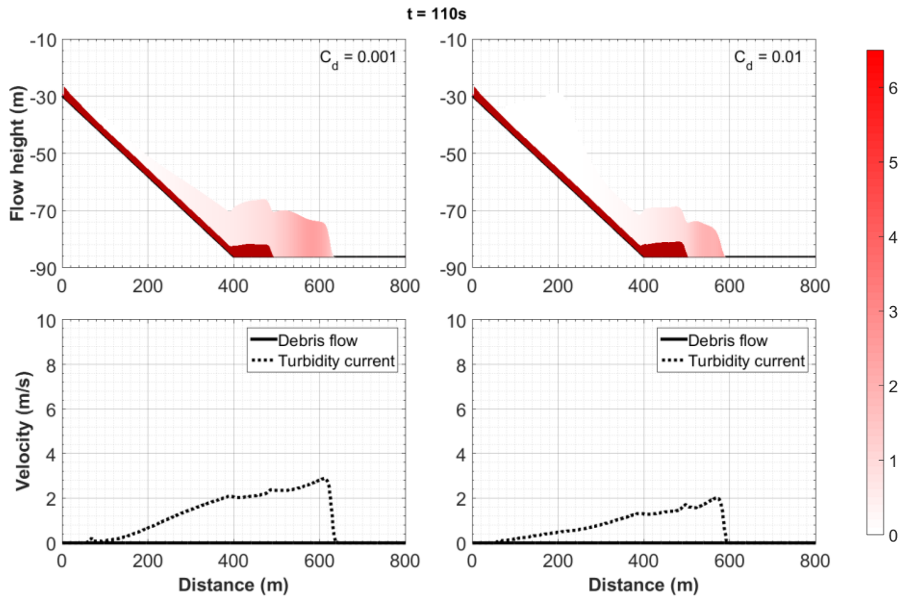

Figure 4.20. Flow height (exaggerated x5) and the corresponding longitudinal velocity of the debris flow and turbidity current layer for C_d = 0.001 (left) and for C_d = 0.01 (right) at t = 110 s. Colorbar refers to sediment concentration (%).

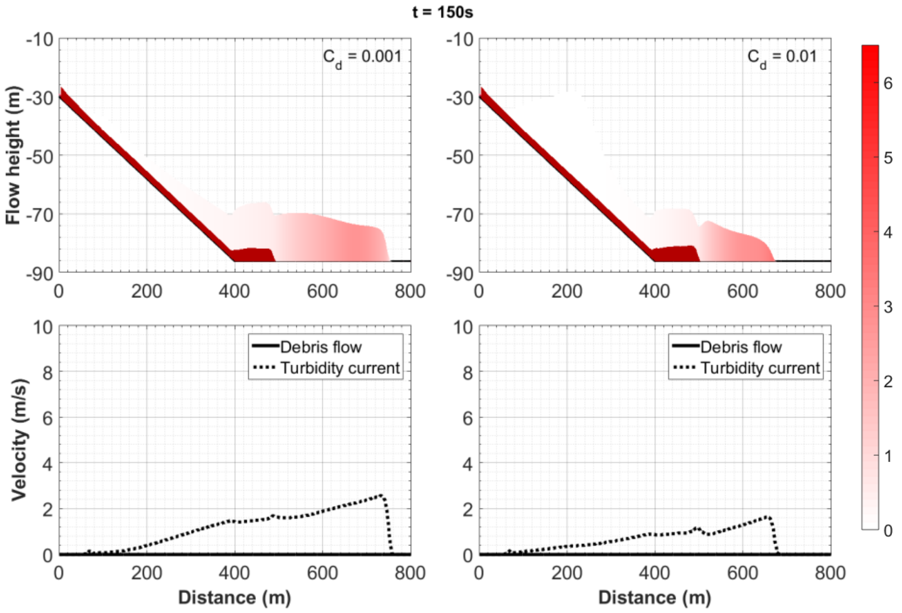

Figure 4.21. Flow height (exaggerated x5) and the corresponding longitudinal velocity of the debris flow and turbidity current layer for C_d = 0.001 (left) and for C_d = 0.01 (right) at t = 150 s. Colorbar refers to sediment concentration (%).

Figure 4.22 presents the evolution of the sediment concentration of the generated turbidity current for the cases of different detrainment coefficient C_d, F and G, with a timestep of 20 s. The lower value of C_d allows the generation of a turbidity current of higher concentration along the whole length of the basal layer. On the contrary, higher value of C_d that corresponds to higher friction between the two layers, limits the generation of the turbidity current in the front area. Until t = 70s, this condition can be clearly shown in Figure 4.22. After t = 70s when the debris flow layer has stopped for both scenarios, sediment concentration of the turbidity shows the same behaviour for the different values of C_d. After t = 130 s, the turbidity current created by lower friction coefficient is more dilute but propagates with higher velocity.

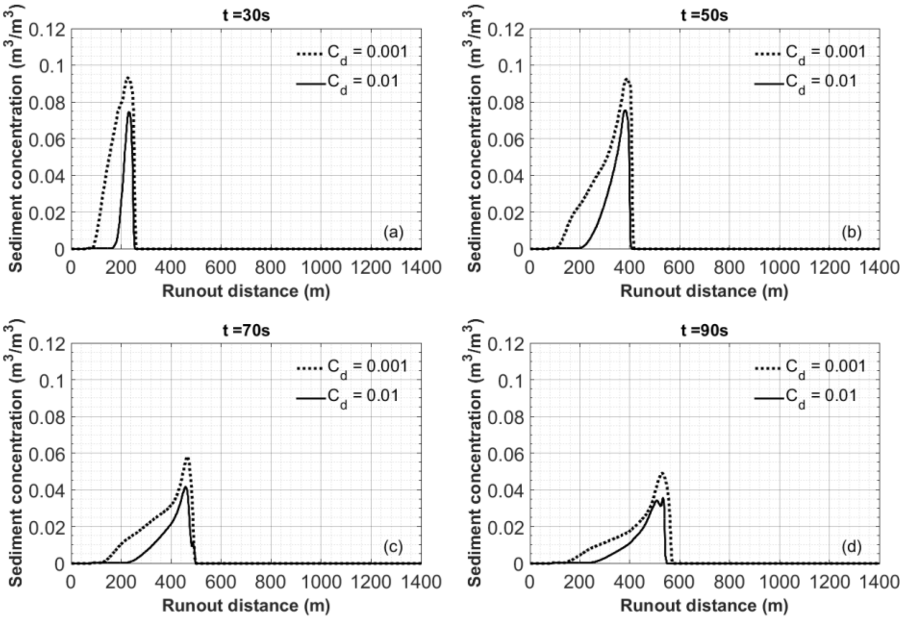

33

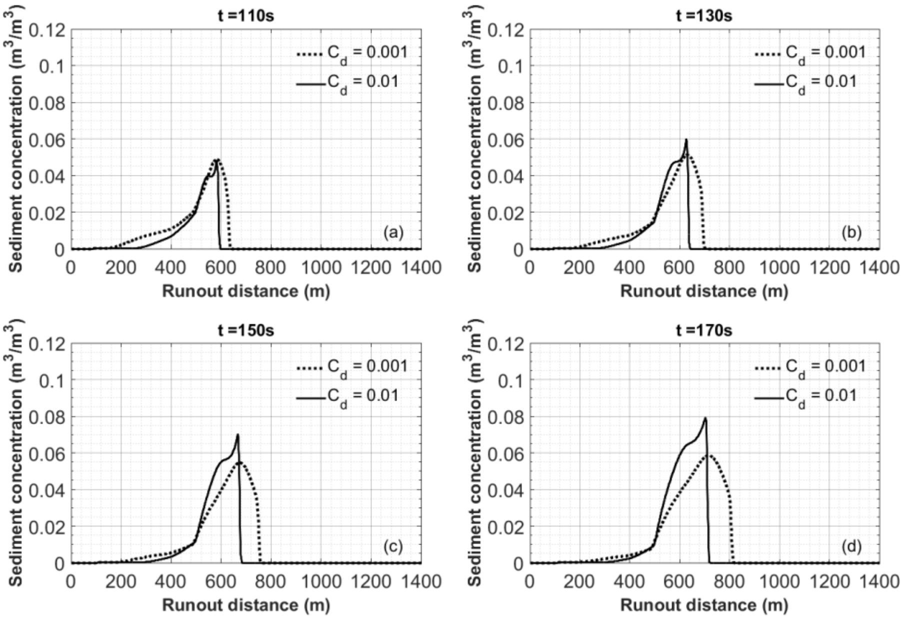

Figure 4.22. Sediment concentration of the turbidity current layer for friction coefficient C_d =0.001 and 0.01.

Scenario B investigates the behaviour of the model for a friction coefficient $C_d = 0.005$, keeping constant the detrainment coefficient e_d to 0.001 as in Scenarios F and G.

Figure 4.23 presents the time evolution of the longitudinal velocity of the debris flow layer for the three different values of C_d. No significant difference is noticed for the three scenarios at the initiation of the flow. The debris flow layer in which lower friction is applied from the developed top layer, develops a higher longitudinal velocity after the initiation of the landslide. As the flow arrives in the slope break, the velocity profiles are very similar for all the values of C_d. In the horizontal part, the debris flow with higher friction coefficient manages to maintain high velocity while for the two smaller values, is decreasing faster. At t = 70 s, the spikes in the velocity for $C_d = 0.005$ and 0.01, reveals that the turbidity current layer with higher friction was able to remobilize part of the debris flow that has been deposited close to the slope break.

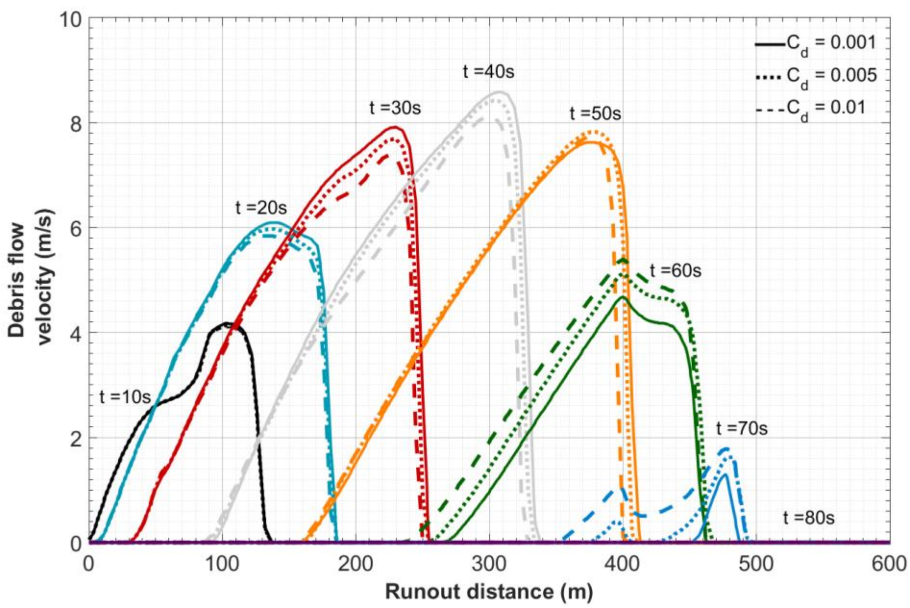

Figure 4.23. Longitudinal velocity evolution of the debris flow layer for friction coefficient C_d =0.001 (scenario F-solid line), C_d =0.01 (scenario G-dotted line) and C_d =0.05 (scenario B-dashed line). Black colour corresponds to t = 10 s, cyan to t = 20 s, red to t = 30 s, grey to t = 40 s, orange to t = 50 s, green to t = 60 s, blue to t = 70 s and purple to t = 80 s.

Figure 4.24 presents the longitudinal velocity of the generated turbidity current layer. Lower friction coefficient C_d results to a turbidity current that propagates with higher velocity. It is observed that for all scenarios, the front of the flow propagates with relatively similar velocity and the main differences occur in the main body of the turbidity current. After t = 80 s, the front for the case of $C_d = 0.01$ starts to decelerate more in comparison to the one of $C_d = 0.001$. The effect of C_d is more pronounced in the maximum thickness of the turbidity current. Going from $C_d = 0.001$ to a five-time larger value, results in a 38% increase of the maximum thickness while the increase from $C_d = 0.005$ to $C_d = 0.01$ results in a 23% increase of the maximum thickness (see Table 4.3).

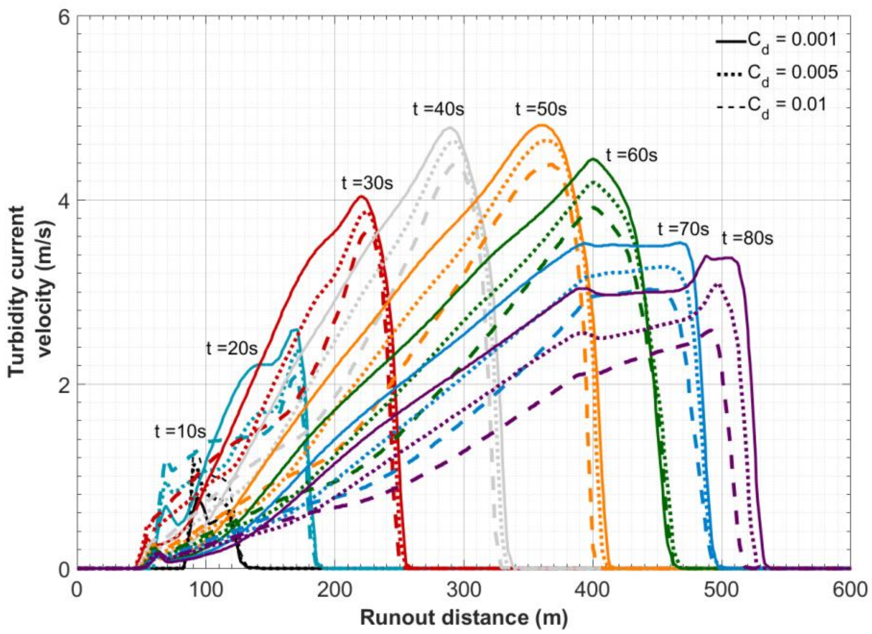

Figure 4.24. Longitudinal velocity evolution of the turbidity current layer for friction coefficient C_d =0.001 (scenario F-dashed line), C_d =0.01 (scenario G-dotted line) and C_d =0.05 (scenario B-dashed line). Black colour corresponds to *t* = 10 s, cyan to *t* = 20 s, red to *t* = 30 s, grey to *t* = 40 s, orange to *t* = 50 s, green to *t* = 60 s, blue to *t* = 70 s and purple to *t* = 80 s.

4.3 Summary

The SWBI2D numerical model has been tested in a hypothetical case of a slope break bathymetry. An imposed initial volume with rheological properties that could correspond to a potential debris flow, was released from the top of the sloped part of the bathymetry. Simulations were carried out for different scenarios aiming to investigate the influence of the sediment detrainment and interfacial friction on the behavior of the two layers during the transition process. The increase of detrainment coefficient of the debris flow is connected with the development of a turbidity current which propagates faster and has higher sediment concentration than it does in cases with low detrainment, and is able to remobilize or eliminate the debris flow deposits. The high friction at the interface of the two layers leads to a behavior where the two layers propagate with almost the same velocity as single mass but for shorter runout distances and the generated turbidity current is much weaker in comparison with low friction coefficient cases where the turbidity current is quickly detached and continues its propagation as a single layer.

Following the testing of the 2-D model on a simple 1-D case that provided reasonable results, the following chapters will exploit the validity of the model compared with experimental results as well as its performance on a 2-D case using real bathymetry data to simulate the event of a large-scale submarine landslide.

Chapter 5 Laboratory experiments on sediment flows

5.1 Introduction

An experimental study which focuses on reproducing small scale sediment density flows in a laboratory flume and was conducted at the Hydraulic Constructions Laboratory of the École Polytechnique Fédérale de Lausanne, is presented. The observations are aimed at improving the parametrization of the relations that govern the transition between different phases of the flows. Dense mixtures of plastic sediment of variable grain size (thermoplastic polyurethane) and water were fed into the water-filled flume by gravity from a supply tank. Different grain-size and slope combinations were examined and the resulting velocity fields were obtained using UVP (Ultrasonic Velocity Profile) at various points along the channel. The flow was imaged through the transparent sidewall to track the velocity of the flow head for each test case. Image analysis also allowed a qualitative characterization of the vertical density stratification and water entrainment during runout. The runout distance and flow thickness are used to highlight the differences in the dynamic behavior of the flow for each test case. Data gathered from the experiments will be exploited in the further development of predictive numerical models for slide-induced debris flows transitioning to turbidity currents.

The transition from a dense debris flow to a dilute turbidity current, as a result of downslope propagation and interaction with the sea floor and ambient sea water, can be divided into three main phases: (i) the initial failure and break-up of blocks and slumps, (ii) the transformation of the released material to a viscoplastic fluid and the development of a debris flow and (iii) the generation of a turbidity current due to friction and mixing at the top interface of the debris flow producing a cloud of dilute suspended matter (Locat and Lee, 2005).

A predictive model of turbidity current generation from submarine debris flows was presented by Mohrig and Marr (2003). Their laboratory experiments confirmed that the influence of the dynamic stresses, developed at the very fronts of the parent debris flows, on the turbidity current development depends on their magnitude relative to an effective yield strength for the parent mixture of sediment and water (Mohrig and Marr, 2003).

Felix and Peakall (2006) studied the generation of turbidity currents from debris flows. The transformation of debris flows occurs through multiple processes like erosion off the dense mass, breaking apart of the dense underflow, breaking of internal waves and turbulent mixing. Some of these processes take place simultaneously in a flow event, while others occur at different phases and positions. It was observed that a more efficient transformation to a turbidity current layer occurs for less-cohesive debris flows (Felix and Peakal, 2006).

Zakeri et al. (2010) studied the process in which a submarine debris flow and the overriding turbidity form the seabed deposits and how the deposits relate to the parent flow. In a series of flume experiments, slurries with different clay content were tested.

The details of the experimental set-up are presented in Section 5.2 Section 5.3 focuses on the instrumentation and processing of acquired images. Section 5.4 details the experimental procedure, and results are presented in Section 5.5.

5.2 Experimental set-up

The experiments were conducted in a flume with a variable bottom slope at the Hydraulic Constructions Laboratory of the École Polytechnique Fédérale de Lausanne. The flume has a total length of 3.5 m, a width of 0.14 m and a height of 0.21 m. One of the sidewalls is made of transparent glass, while the other is plastic. Both ends (the upstream and downstream reaches) are closed with plastic surfaces. The flume can be emptied by adjustable pipes located at the bottom of the flume which are controlled by valves. It can be tilted using adjustable supports at slopes ranging from 0% to 4.4%.

The length of the flume was shortened for the purposes of the presented experimental campaign. A vertical and a tilted plastic plate are placed in such way that they limit the total runout distance to 2.7 m. A head tank with a capacity of 8 l, is placed at a height of 0.46 m from the top of the flume. It is used to convey the mixtures through a plastic tube ending in a perforated screen to the bottom of the flume.

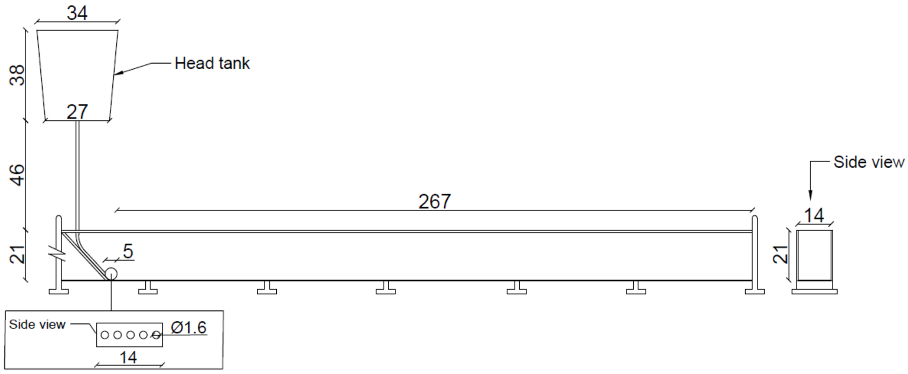

Figure 5.1. Sketch of the experimental set-up. All dimensions are in centimeters.

Figure 5.2. Picture of the experimental set up (LCH, EPFL, 2016).

5.3 Test conditions

5.3.1 Material properties

The material used in the present work is SCHAETTI FIX 6511, which is a high performance thermoplastic polyurethane. Three different grades of sediment were used to investigate the effect of the sediment size on the behaviour of submarine density flow. Their characteristics are given in Table 5.1. The density of the material for all sizes is ρ_{sed} = 1.16 g/cm^3.

Table 5.1. Characteristics of the sediments.

Sediment Type	**Mean Diameters**		
	$D_{v0.1}$ (μm)	$D_{v0.5}$(μm)	$D_{v0.9}$(μm)
S	30.60	83.73	159.52
M	59.14	132.80	214.93
L	95.20	169.77	264.10

Figure 5.3 - Figure 5.5 present the particle size distribution for the three sediment types.

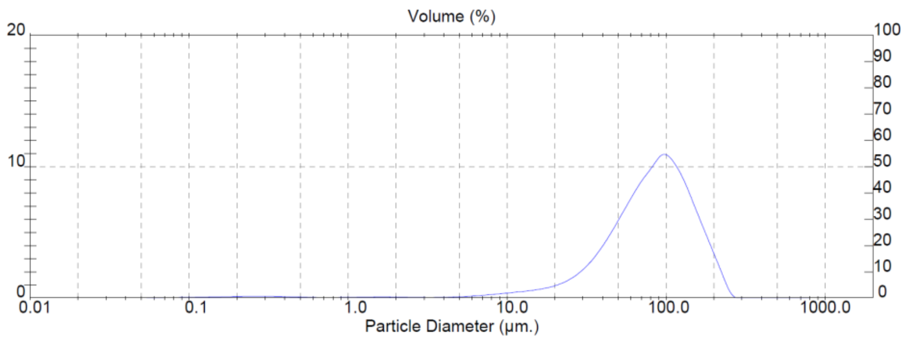

Figure 5.3. Particle size distribution for the sediment type S (taken from the analysis report provided by Malvern Instruments Ltd.).

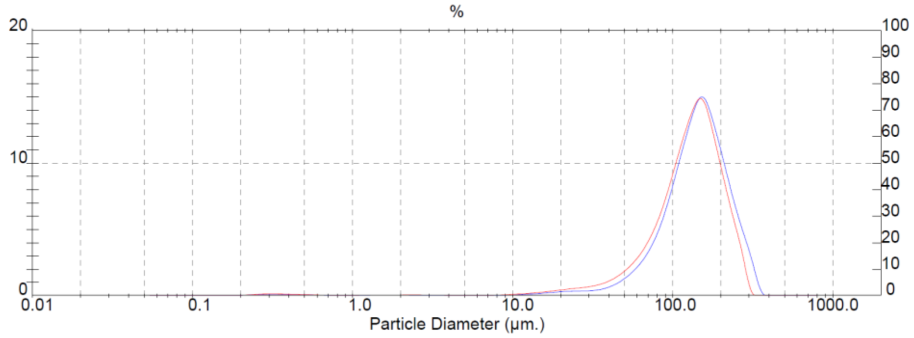

Figure 5.4. Particle size distribution for the sediment type M (taken from the analysis report provided by Malvern Instruments Ltd.).

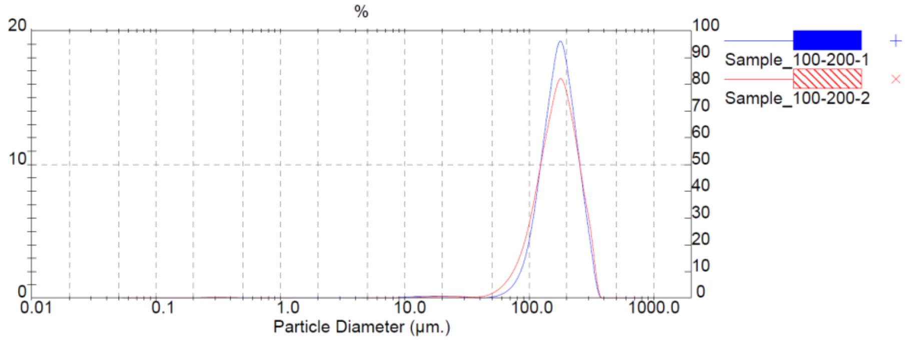

Figure 5.5. Particle size distribution for the sediment type L (taken from the analysis report provided by Malvern Instruments Ltd.).

5.3.2 Initial conditions

This experimental campaign is targeted to investigate the effect of the sediment size and bed slope on the behavior of subaqueous sediment density flows such as debris flows and turbidity currents. Mixtures of different sizes of the plastic sediments (thermoplastic polyurethane) and water were fed into the flume from the 8-litre head tank through a plastic tube ending in a perforated screen, to ensure uniform release of the material across the flume width. For each experiment, a mixture of different sediment size or combination of different sizes is prepared. For each sediment grain size, three different channel slopes were investigated. The sediment mass concentration in the head tank was set equal to 30% for most experiments. This percentage indicates a high density flow that could potentially reproduce the behavior of a debris flow. A few experiments were performed with a reduced initial sediment mass concentration equal to 8%.

Overall, the combinations of channel slope, sediment mixture and initial sediment concentration, resulted in a total of 15 individual experiments, as detailed in Table 5.2.

Table 5.2. List of experiments.

Experiment name	SEDIMENT TYPE	SLOPE (%)	MASS CONCENTRATION (%)
S1	S	0	30
M1	M	0	30
L1	L	0	30
MIX1	50%S + 50%L	0	30
TC1	M	0	8
S2	S	2.2	30
M2	M	2.2	30
L2	L	2.2	30
MIX2	50%S + 50%L	2.2	30
TC2	M	2.2	8
S3	S	4.4	30
M3	M	4.4	30
L3	L	4.4	30
MIX3	50%S + 50%L	4.4	30
TC3	M	4.4	8

From the above list, experiments S1, MIX1 and S2 failed, as an important amount of the released material remained in the region just after the release point without being incorporated in the developed current. As a result the total mass of the current could not be considered equal to the one of the other experiments and could not be used for comparison. This behaviour is attributed to the failure of small sediments to be properly mixed and to avoid high surface tension. Also TC2 is not presented in the results, as the data after propagation time of 68 s were not obtained.

5.4 Instrumentation

5.4.1 Velocity measurements

Velocity profiles were measured using an Ultrasonic Doppler Velocity Profiler (Met-Flow, UVP). The UVP (Ultrasound Velocity Profile) represents both a method and a device for measuring an instantaneous velocity profile in liquid flow along the ultrasonic beam axis by detecting the Doppler shift frequency of echoed ultrasound as a function of time.

Each ultrasonic transducer transmits short ultrasonic (US) pulses along transducer axis. Part of the US energy is reflected from minuscule particles scattered in flowing water and returned back to the transducer, which also acts as US receiver. The reflected signal is Doppler-shifted, and comes back to transducer with certain delay. Doppler shift frequency is proportional to particle (and liquid) velocity, and the delay is proportional to particle position in the time of pulse reflection. By space separation of many measurement points UVP Monitor is capable of evaluation of a complete velocity profile in the flowing liquid. Since each UVP transducer can measure one projection of a complete flow field, simultaneous measurement with several transducers makes complete measurement of the flow field possible.

The functional principles of UVP operation can be described on an example of a flow with free surface (Figure 5.6). An ultrasonic transducer transmits a short emission of ultrasound (US), which travels along the measurement axis Lm, and then switches over to receiving ('listening'). When the US pulse hits a small particle in the liquid, part of the US energy scatters on the particle and echoes back. The echo reaches the transducer after a time delay

$$t = \frac{2x}{c}$$

where t is the time delay between transmitted and received signal (s), x is the distance of scattering particle from transducer (m) and c is the speed of sound in the liquid (m/s). If the scattering particle is moving with non-zero velocity component into the acoustic axis L_m of the transducer, Doppler shift of echoed frequency takes place, and received signal frequency becomes 'Doppler-shifted':

$$\frac{v}{c} = \frac{f_d}{2f_0}$$

where v is the velocity component into transducer axis (m/s), c is the sound velocity in liquid (m/s), f_d is the Doppler shift (Hz) and f_0 is the transmitting frequency (Hz).

From the equation above, v can be expressed as

$$v = \frac{f_d}{\frac{2f_0}{c}} = f_d \cdot \frac{\lambda}{2}$$

where $\lambda = c/f_0$ is the wavelength of ultrasound in medium (m).

If UVP succeeds to measure the delay t and Doppler shift f_d it is then possible to calculate both the position and the velocity of a particle. Since we presume that scattering particles are small enough to follow the liquid flow, we can also presume that UVP Monitor has established the fluid flow component in the given space point. The basic feature of UVP Monitor is the ability to establish the velocity in many separate space points along measurement axis.

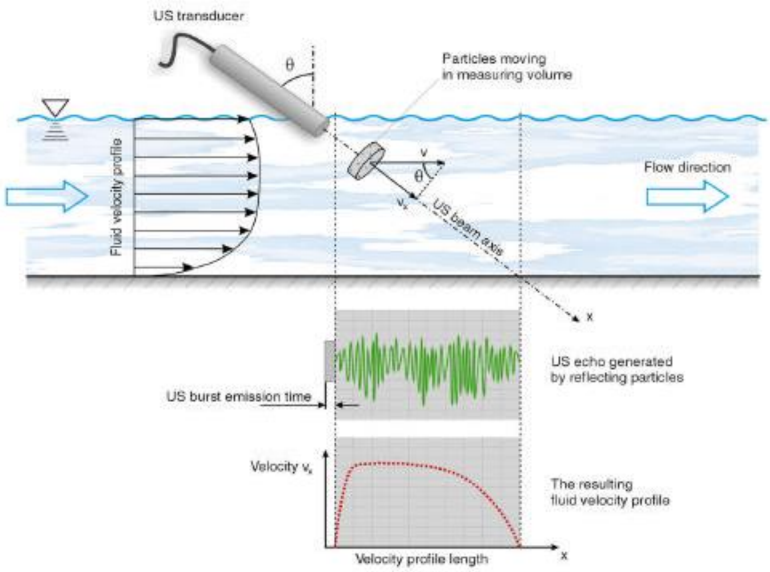

Figure 5.6. Schematic picture of UVP velocity profile measurement on a flow with free surface (taken by UVP-DUO User's Guide R5.2).

The UVP (Ultrasonic Doppler Velocity Profiler)–DUO by Met-Flow has been used for the present experiments (Figure 5.7).

Figure 5.7. UVP-DUO Monitor ((taken by UVP-DUO User's Guide R5.2).

Three ultrasonic transducers with working frequency 4 MHz, external diameter 8mm and transducer active diameter 5 mm were used for the measurements. They have been placed near water surface and the axis of probe was at an angle of 25° to the normal of the flume bottom, with the first transducer looking down the main flow and point to the same position as the second that is looking against the main flow located in a distance of 62 cm from the release of the flow and the third one looking down the main flow and located after 104 cm from the release point. The position of the transducers is illustrated in Figure 5.8.

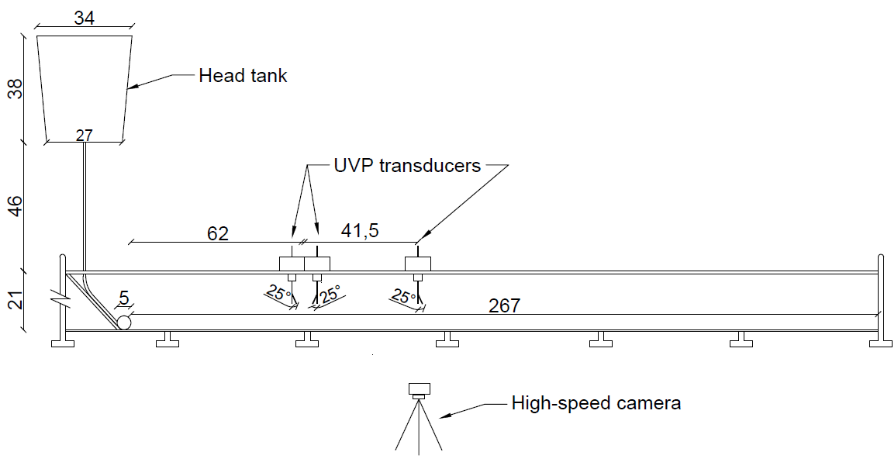

Figure 5.8. Sketch of the experimental set-up. All dimensions are in centimetres.

Figure 5.9. Picture of an ultrasound transducers.

The velocity resolution of UVP DUO was set at 0.764 mm/s and its spatial resolution was set at 0.74 mm. A fixed number of 128 points were measured in each profile and the sampling period was equal to 0.161 s. The measurements gave the projected vertical profiles in the middle of the width of the flume. Each of the three UVPs was interrogated in sequence with a multiplexer throughout the duration of the experiment, and the time interval between successive measurements at a given transducer is in the order of 2.3 s.

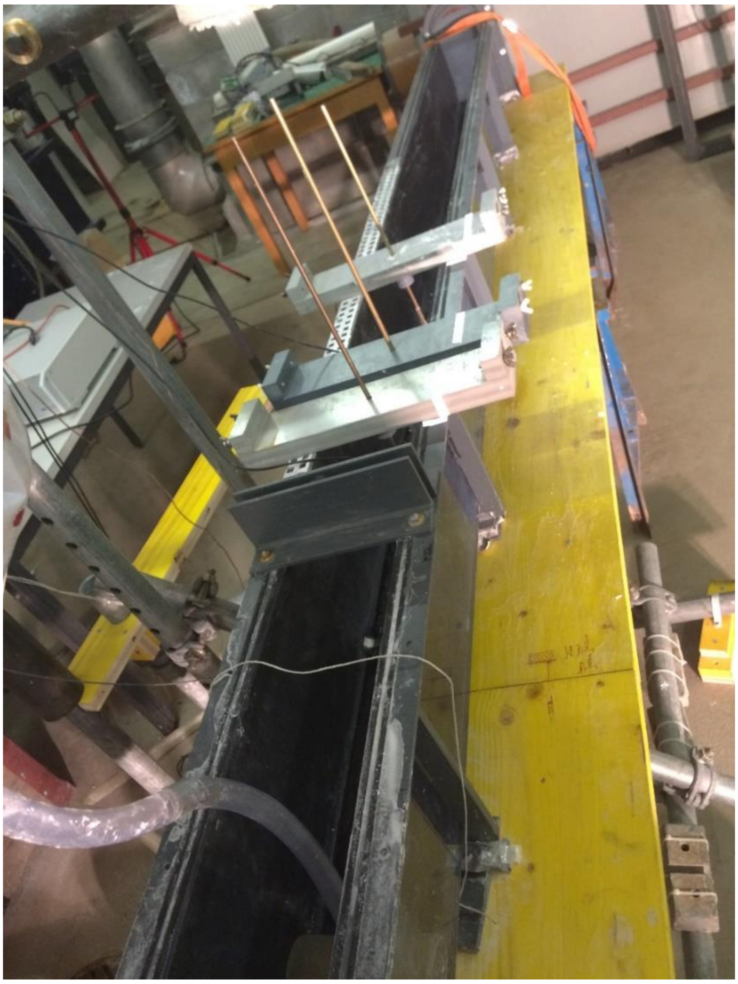

Figure 5.10. Pictures of the transducers placed in the flume.

5.4.2 Flow imaging and image processing

Detailed sidewall measurements are acquired by filming the flow through the transparent side wall of the flume using a video camera. A SMX-160 camera with acquisition frequency of 10 frames per second was used to obtain grey scale digital images with a resolution of 2208 by 400 pixels. The position of the camera is illustrated in Figure 5.8 and it was fixed for all experiments. On average 350 frames were taken for each experiment.

Lighting is provided by two projectors, properly positioned to guarantee the most possible better uniform illumination of the flume and avoid reflections of light towards the cameras. The plastic back sidewall ensures a uniform background.

Four steps of image processing are applied to the raw images.

- First, the images are ortho-rectified using a number of reference points with known coordinates to correct image distortion, and the resulting ortho-rectified image is resampled at a resolution of 1 pixel per mm, with the x-axis being defined as streamwise, tilted along-slope direction, and the y-axis orthogonally upwards.

- Second, a correction is applied to account for uneven illumination of the flow from the single light source used. A bell-shaped brightness correction factor is applied, which is calibrated on the basis of the observed illumination of a reference plate along the bottom of the flume sidewall.

- Third, the image background is removed by subtracting the initial image, prior to flow initiation, from the entire image sequence. Due to the bright color of the plastic sediment used, the current appears on the resulting image sequence as variable shades of grey on a perfectly black background, and the local brightness of the flow is, to a good approximation, a direct proxy for the local sediment concentration at that location.

- Lastly, for better visualization, the grey image is transformed into a color image with a jet colormap featuring variations of blue-green-yellow-red shades that highlight regions of dense and dilute flow. The color map is altered so that image regions indiscernible of the image background (with a pixel value of 0) are painted white for better visualization of the limits of the propagating current.

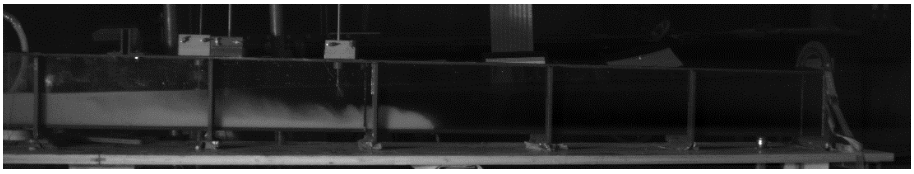

Figure 5.11. Example of a raw image.

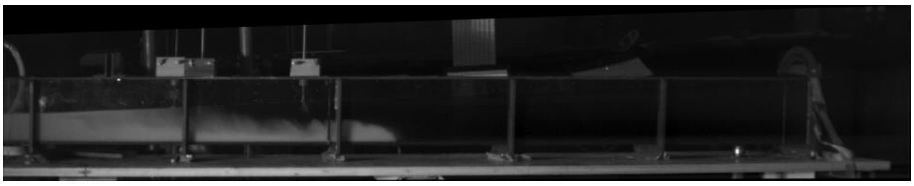

Figure 5.12. Step1: Ortho-rectified image.

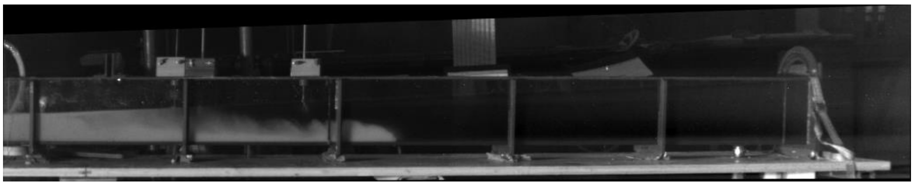

Figure 5.13. Step 2: Image after correction for even illumination.

Figure 5.14. Step 3: Image after subtraction of the background.

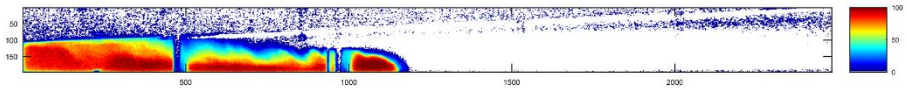

Figure 5.15. Step 4: Image after transformation into a colour image.

5.4.3 Experimental procedure

All the mixtures were prepared using a mixer device in order to ensure the uniformity of the mixture. The flume was filled with fresh water. The flume water and tank mixtures had approximately the same temperature, therefore temperature effects are considered negligible in the flow dynamics. When the mixing procedure was completed, the resulting mixture was immediately released in the head tank to avoid any settling of the sediments, and was discharged into the flume under gravity. The gradual lowering of the mixture level in the head tank was tracked with another camera, and was roughly constant for all experiments with a total emptying duration of ~25 s, which corresponds to a feeding discharge of ~1/3 l/s. The release of the mixture was synchronized with the start of the UVP measurements. Simultaneously, the recording with the digital camera was triggered. After each experiment the flume was drained out and refilled with fresh water prior to the next experiment.

5.5 Experimental observations

5.5.1 Down-channel evolution of the current

Figure 5.16 shows snapshots of the current evolution at selected instants after release for the configuration with a bed slope of 4.4%, and an initial mass concentration of sediment equal to 30% and composed solely of the larger sediment size of 200 μm. As discussed in Section 5.4.2, pixel values on the processed images are a good proxy for local sediment concentration in the current; however, in the absence of a robust calibration, the correlation cannot be precisely constrained and therefore the pixel brightness is presented in digital values rather than sediment concentration in percent. Nevertheless, what appears in shades of red color on the processed images is considered as a dense flow, while shades of yellow, green, cyan and blue correspond to gradually more dilute sediment suspensions.

The sequence of images on Figure 5.16 reveals the general down-channel propagation of the current, the preservation of a relatively dense and thick current head followed by a region where the dense basal layer is thinner, and the distinctive pattern of billows that govern the dilution of the top layer of the current and the formation of a turbidity cloud.

The current head is seen to preserve a density in the order of that in the most upstream section of the current. Mixing with the ambient fluid is initiated at the top of the head region, but the resulting turbidity is simultaneously slowed down and therefore trails behind the front, while additional dense current is fed into the frontal head from the basal layer, allowing it to remain dense. The sediment concentration in the front and dense basal layer is however not expected to be as high as 30% as in the head tank, but more possibly in the range of 10 to 15%. This is due to immediate turbulent mixing at the exit of the perforated tube ending. A more robust calibration of the brightness-to-concentration correlation is suggested for future experiments to confirm this.

Behind the front, the generation of lower density turbidity is apparent on the images, and is a result of large-scale mixing processes with the ambient water.

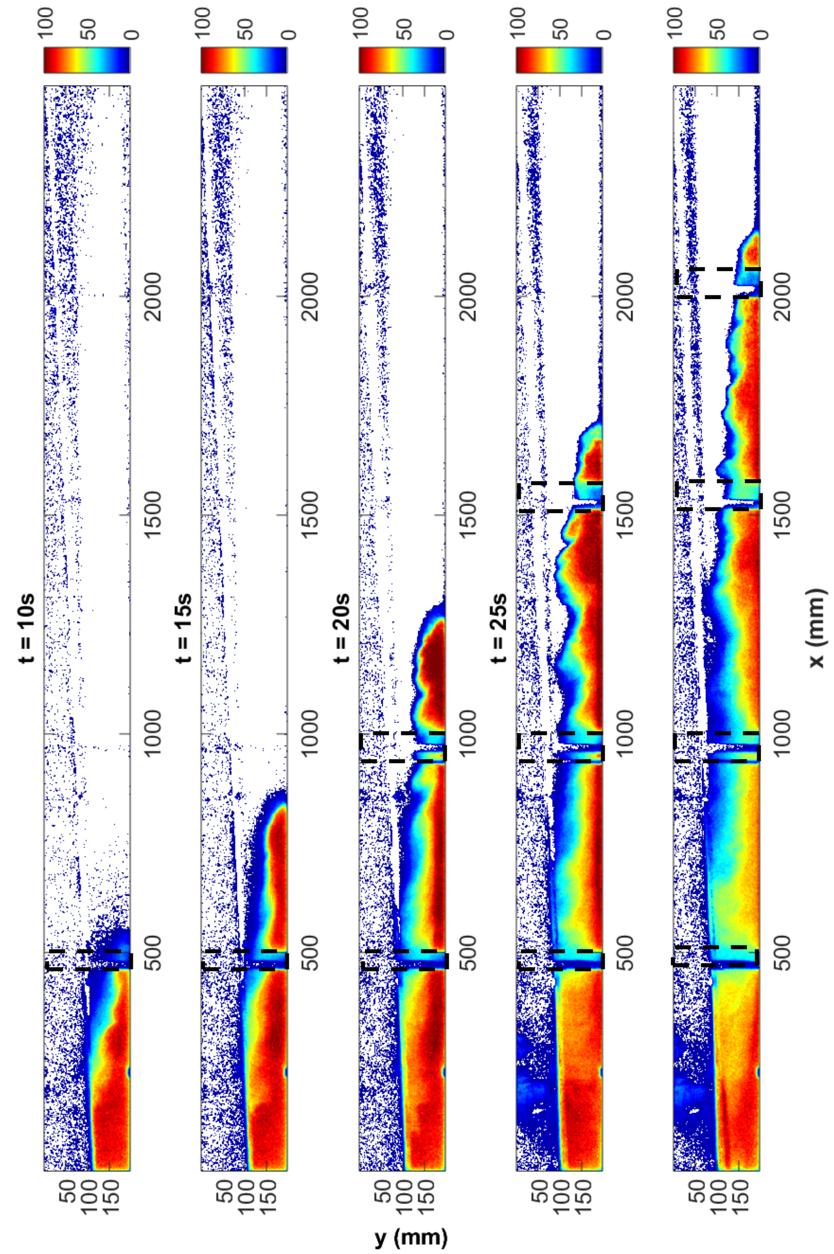

Figure 5.16. Snapshots of the flow for the test with a slope of 4.4% and 200 μm grain size. Dashed lines define regions where the existence of shadows do not allow proper illumination.

5.5.2 Frontal velocity

Visualization of the current head on the ortho-rectified images allows tracking the front position and velocity in time. The front velocity evolution for the configuration with a bed slope of 4.4%, and an initial mass concentration of sediment equal to 30% and composed by the larger sediment size of 200 μm, is presented in Figure 5.17. The top and the bottom layer are defined by chosen thresholds of brightness (see Section 5.5.3).

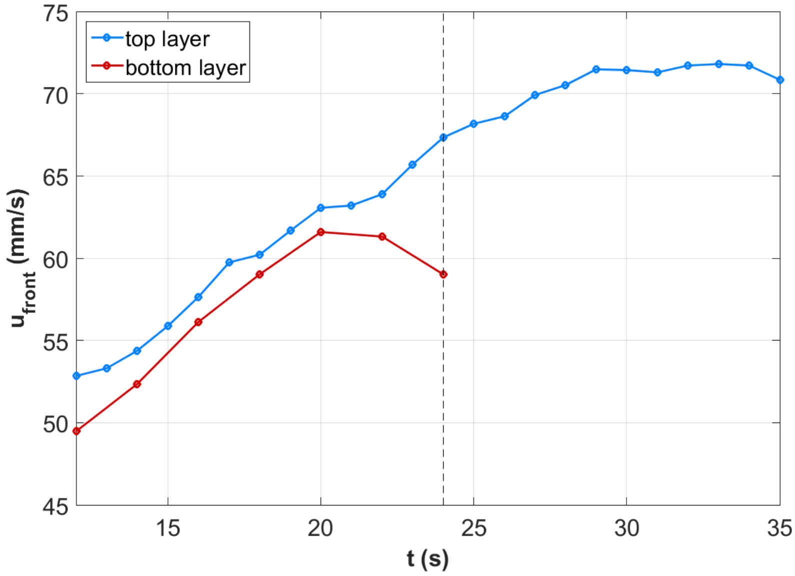

Figure 5.17. Time evolution of the front velocity for experiment L3. Blue line corresponds to the top layer and red line to the bottom layer.

The current is propagating with linearly increasing velocity for a duration of 30 s while for the last 5 s it has a constant velocity until the flow reaches the end of the flume. The maximum velocity is approximately 72 mm/s. In the head of the flow is governed by intense mixing and this explains that the denser basal layer seems to propagate following the head of the front. The dense layer has linearly increasing velocity until 20 s and then decelerates the last 4 s before it stops.

In Figure 5.19 and Figure 5.20, the time evolution of the front position and the front velocity of the current for all experiments conducted for the configuration with a bed slope of 4.4% and an initial mass concentration of sediment equal to 30%, are shown. It is observed that the current that propagates faster is the one composed by the medium grain size (experiment M3). The maximum velocity is approximately 92 mm/s and it reaches the end of the flume 7 s earlier than the current of the experiment L3. The current composed by mixed sediment sizes reaches a maximum velocity of 81 mm/s, propagating faster than both currents composed by the two grain sizes which it consists of (S and L). The front velocity increases linearly for all cases except for L3 which has constant velocity in the last 500 mm of the flume.

It can be noticed in all figures of this chapter that the readings of each experiment start at a different time instance. This can be explained by the fact that the observation of the current could only start after reaching position x = 500 mm. as the conditions did not allow the capture of the flow at the first centimetres after the release point (Figure 5.18).

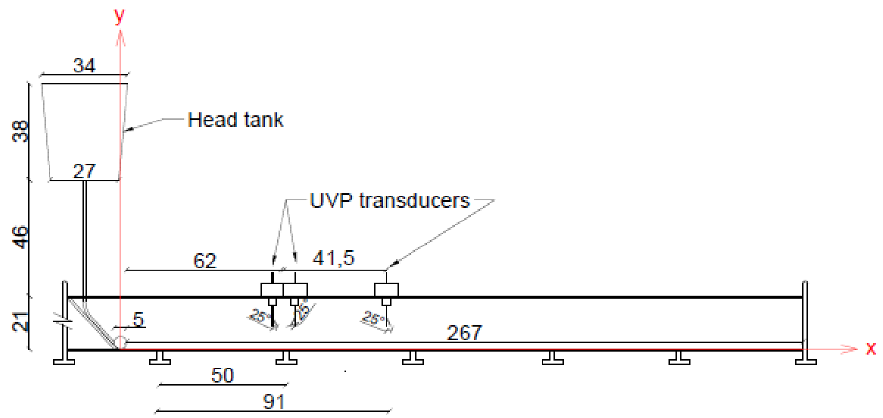

Figure 5.18. Sketch of the experimental set-up and definition axes. All dimensions are in centimetres.

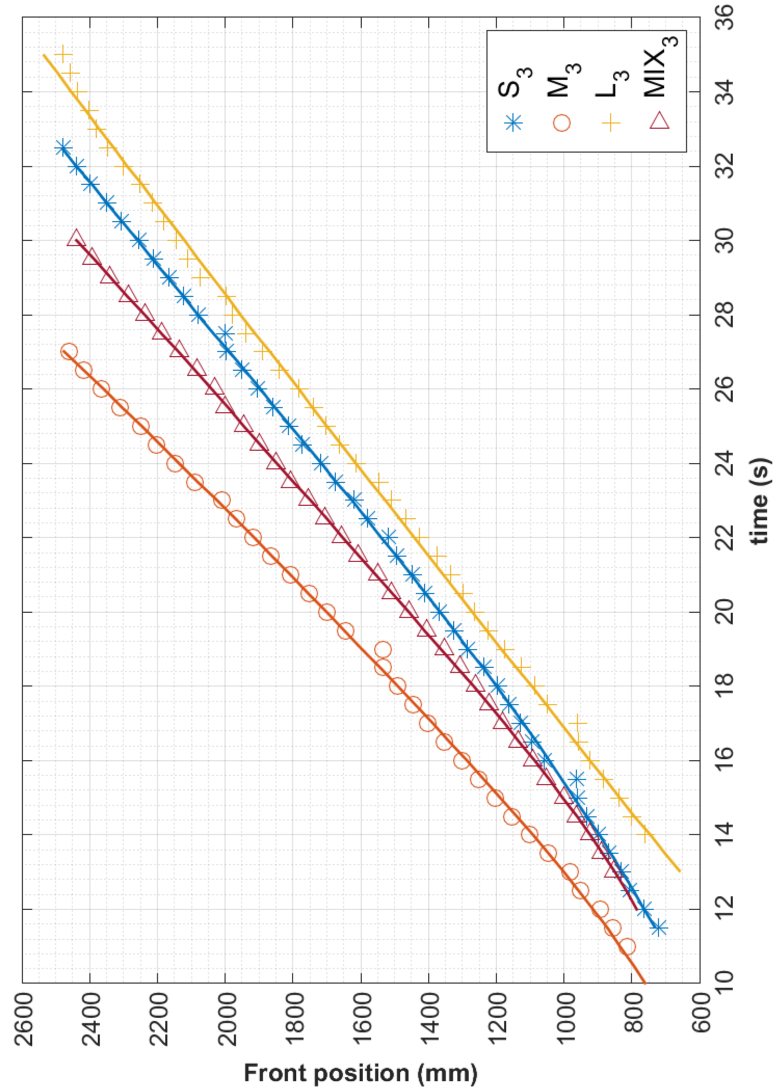

Figure 5.19. Time evolution of the front position for experiments conducted with a bed slope of 4.4% and initial mass concentration of 30%.

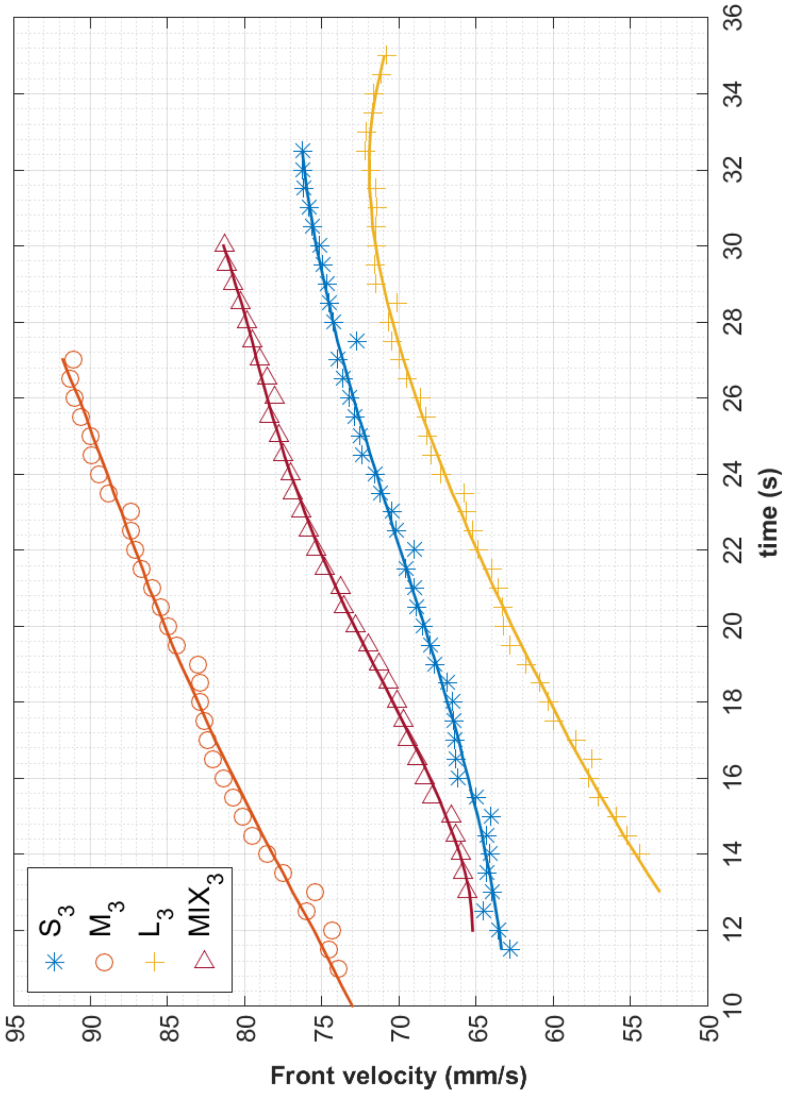

Figure 5.20. Time evolution of the front velocity for experiments conducted with a bed slope of 4.4% and initial mass concentration of 30%.

In Figure 5.21 and Figure 5.22, the time evolution of the front position and the velocity for the experiment with initial sediment mass concentration of 8%, TC3, is compared with the other experiments conducted at the same bed slope. The behavior of the dilute mixture is different as expected. The total runout time is equal to 80s and the developed velocities start from 44 mm/s (t = 20s) and decrease almost linearly to 28 mm/s.

Figure 5.23 and Figure 5.24 present the time evolution of the front velocity for the valid experiments conducted with a bed slope of 0% and 2.2%, respectively. It is observed that for experiments with sediment concentration of 30%, the sediment size does not affect the front velocity of the current for zero bed velocity. For the case with bed slope of 2.2%, the front velocity starts to depend more on the sediment size with the current of the medium grain size to propagate slightly faster than the one of the larger grain size and the current composed by mixed sediment size to develop the higher front velocity. The dependence of the front velocity on sediment size for the experiments of high density is clearly observed in experiments conducted with a bed slope of 4.4%, as it can be seen in Figure 5.22. Concerning the effect of the bed slope on the propagation of the current with a low sediment concentration of 8%, it is observed similar behavior and same propagation time for the cases with a bed slope of 0% and 4.4%.

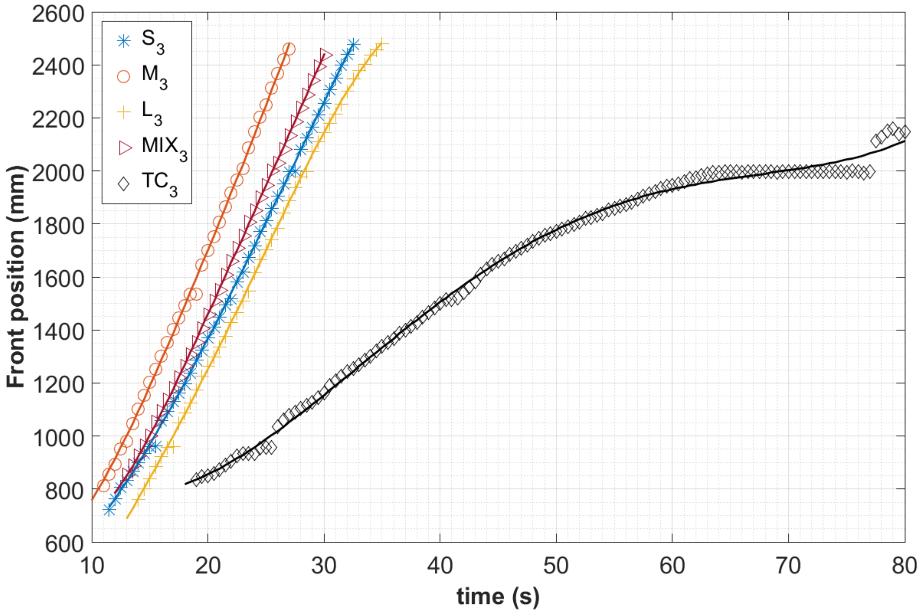

Figure 5.21. Time evolution of the front position for all experiments conducted with a bed slope of 4.4%.

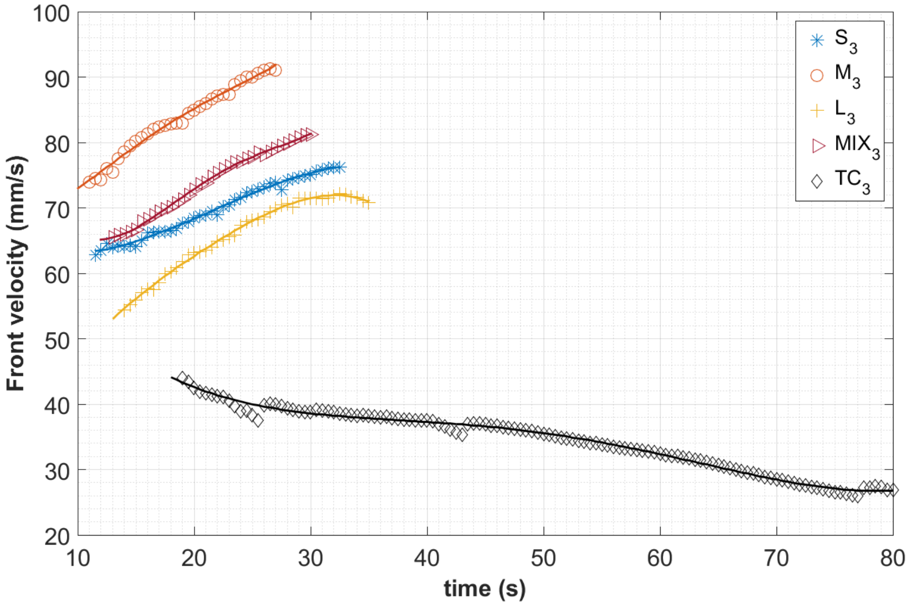

Figure 5.22. Time evolution of the front velocity for all experiments conducted with a bed slope of 4.4%.

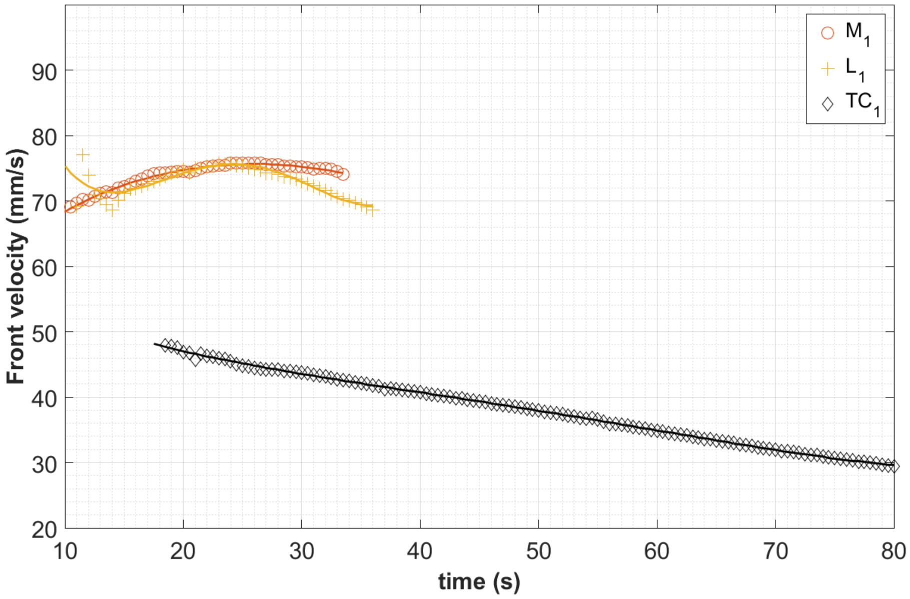

Figure 5.23. Time evolution of the front velocity for all experiments conducted with a bed slope of 0%.

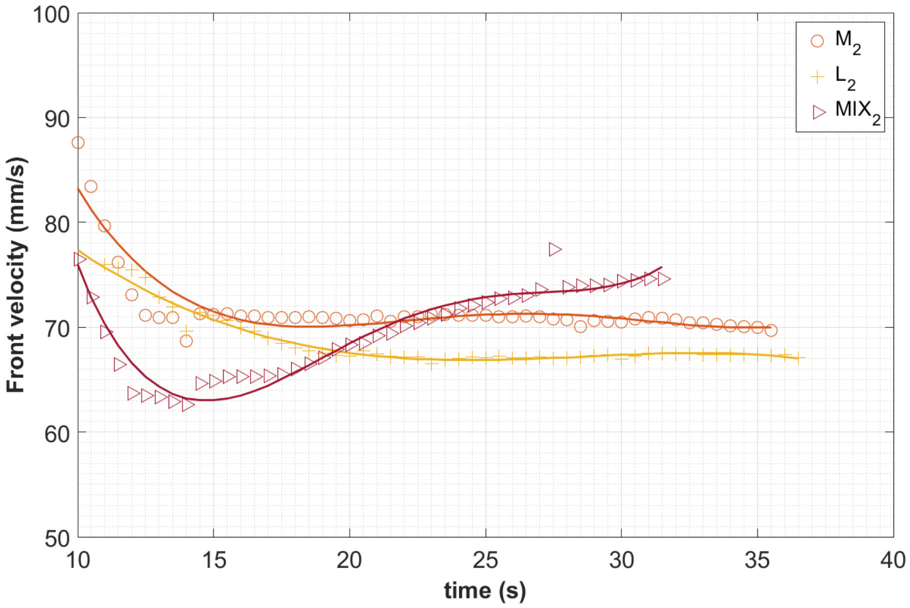

Figure 5.24. Time evolution of the front velocity for all experiments conducted with a bed slope of 2.2%.

Table 5.3. provides information about experiments composed with the same grain size but in different bed slope. The maximum velocity, the time in which is observed, and the total runout time are given. The current composed by the medium sediment size, M, is propagating much faster in an horizontal bed, while for the current composed by the large sediment size, the bed slope does not seem to play an important role on its propagation.

Table 5.3. Maximum velocities and runout time for experiments with the medium and large sediment size.

Experiment name	**Maximum Velocity (mm/s)**	**Max Velocity Time (mm/s)**	**Total Time (s)**	**Bed Slope (%)**
M1	75.8	70	70	0
M2	71.2	23.5	35.5	2.2
M3	91.3	26.5	27	4.4
L1	75.7	23	35	0
L2	67.5	31	36.5	2.2
L3	71.6	34	35	4.4

5.5.3 Velocity and density stratification

The aim of this work was to investigate the internal stratification and layering of dense subaqueous sediment flows, by simultaneously measuring velocity and density profiles. This appears possible for the present experiments by combining the UVP velocity profiles and the qualitative density information encapsulated in the brightness of the digital images, interrogated at the same position than the UVP probes.

In Figure 5.25 to Figure 5.29, the downstream velocity and the brightness profiles are presented for selected time instants at the location of the third transducer (x = 910mm) for the configuration with a bed slope of 4.4%, and an initial mass concentration of sediment equal to 30% and composed solely of the larger sediment size of 200 μm (L3). On all velocity profiles (left panels), the height corresponding to a zero streamwise velocity is highlighted by a dashed line. While the bottom layer propagates down the channel, the top portion of the current propagates in the opposite direction. This is a direct result of the fact that the current is propagating in an enclosed basin, and any current in one direction must be balanced by an opposite current in the other direction, with only minor deviations possible that result from the generation of mild free surface waves at the flume free surface. Due to the limited depth available in the flume, the backward current incorporates some of the turbidity generated at the top of the density current.

The density/brightness profiles shown on the right panels of the figures reveal a pattern of upward stratification, with the brightness decreasing to zero at the top of the current. A qualitative partition of the current in a dense basal current and a dilute top current can be made by adopting a brightness threshold of 70, which corresponds to orange color on the flow images of Figure 5.16 and is slightly smaller than the maximum observed brightness. On Figure 5.25 to Figure 5.29, it is observed that this partition based on density corresponds quite well with the partition between down-channel and reverse currents based on the velocity profiles. This suggests indeed that the flow can be abstracted into two distinct layers: a basal layer that remains dense and rapid and dictates the down-channel propagation of the density current, and a top layer, which is much more dilute as a result of mixing, and propagates at a much slower velocity – which in the present case may result in backward velocity due to the lock-exchange configuration and the finite water depth in the flume.

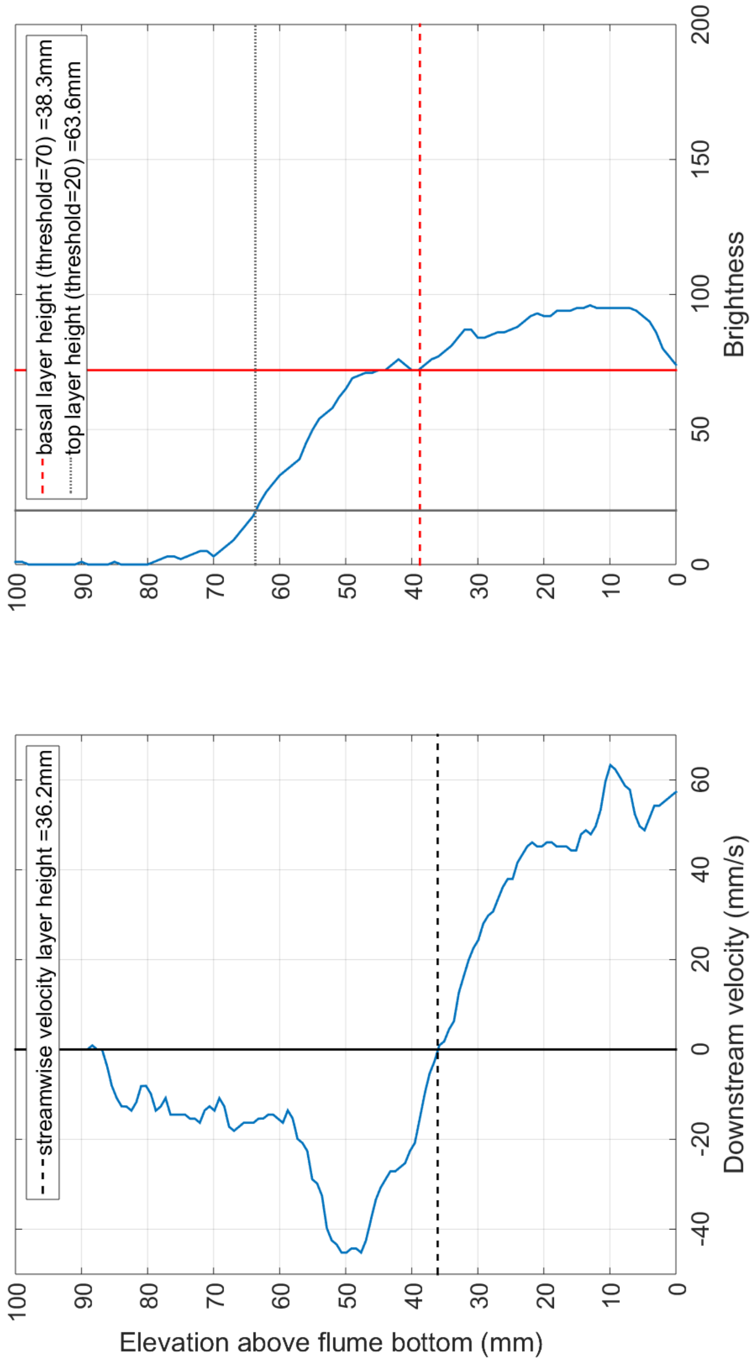

Figure 5.25. Downstream velocity and brightness profiles at position x = 910 mm and time t = 18.3 s.

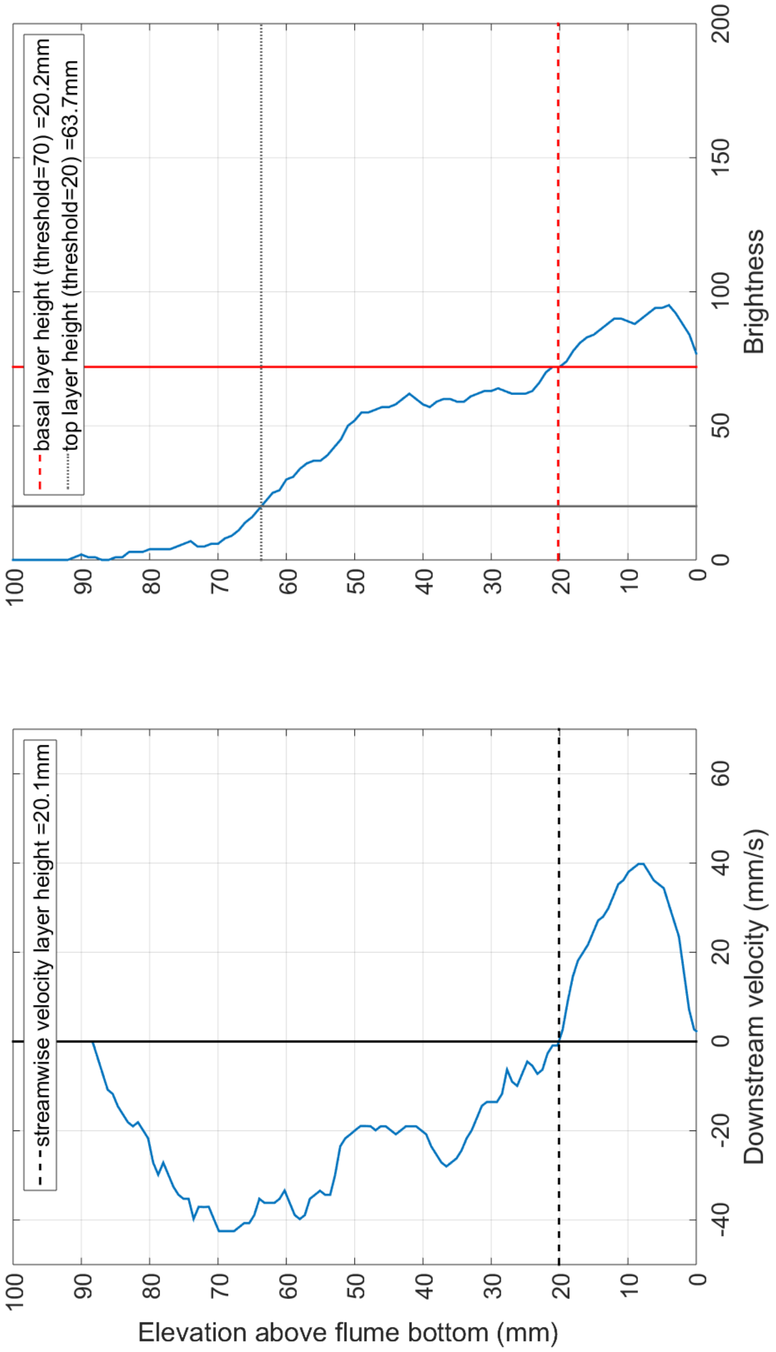

Figure 5.26. Downstream velocity and brightness profiles at position x = 910 mm and time t = 20.6 s.

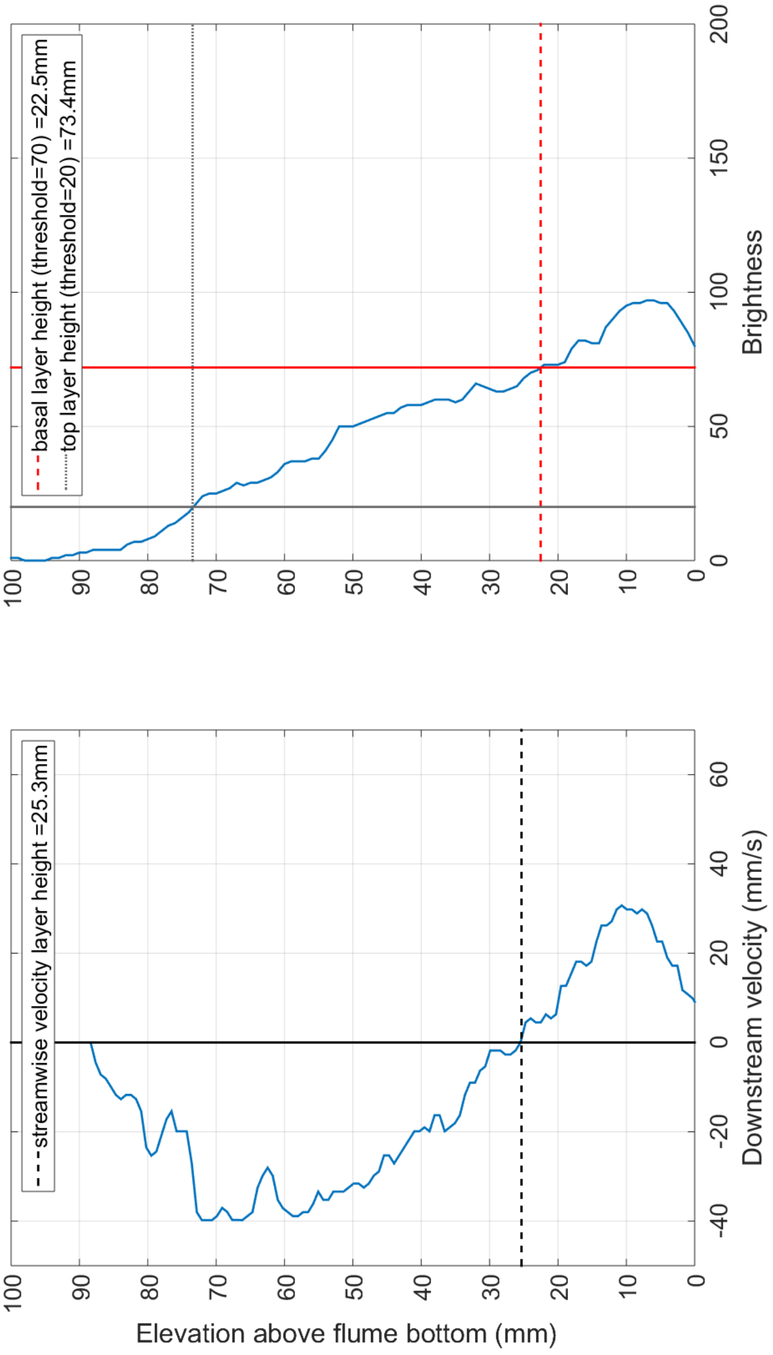

Figure 5.27. Downstream velocity and brightness profiles at position x = 910 mm and time t = 22.9 s.

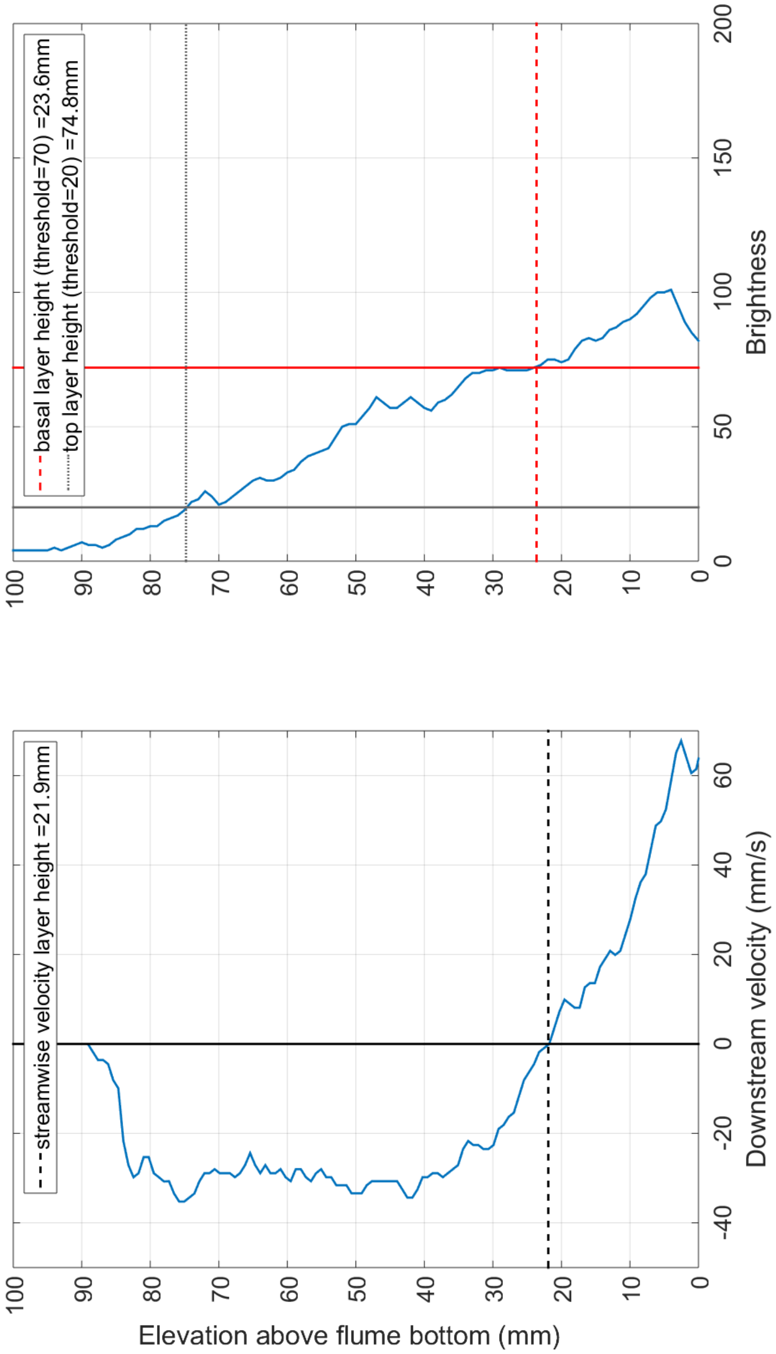

Figure 5.28. Downstream velocity and brightness profiles at position x = 910 mm and time t = 25.2 s.

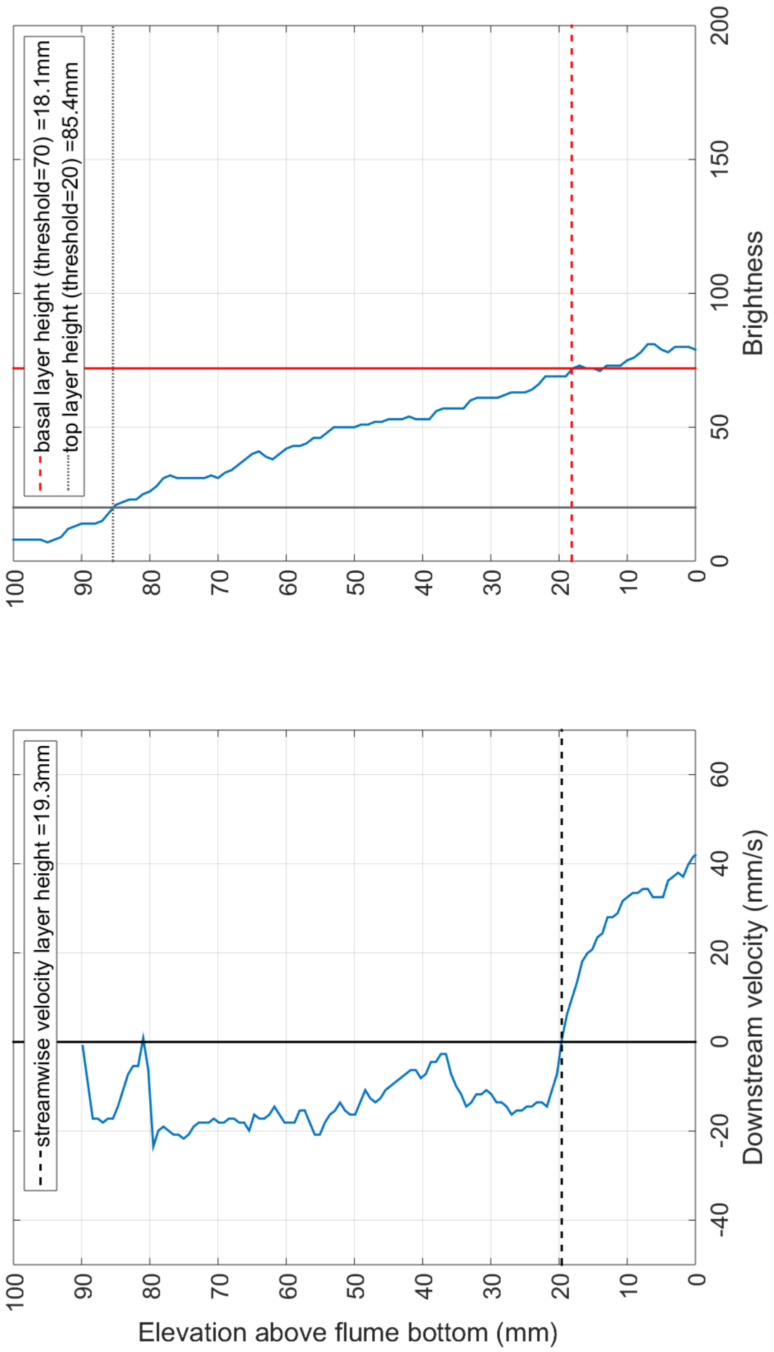

Figure 5.29. Downstream velocity and brightness profiles at position x = 910 mm and time t = 27.5 s.

Flow brightness profiles for different time instances at the same location x = 910 mm are given in Figure 5.30. At t =15 s, the flow has not reached this location yet as it is evident by the near zero values of brightness. The very front of the flow passes from the location of the transducer at t = 16 s and is characterized by the low brightness values. Immediately after, the denser part of the flow head passes, with a thickness of circa 40 mm having a brightness above the adopted threshold of 70. From time t = 18.3 to 25.2 s, the thickness of the dense layer of the flow is decreasing, while the total flow thickness is increasing due to the growth of the turbidity cloud. Passed t = 30 s, the dense layer has vanished but the total flow thickness surpasses 120 mm.

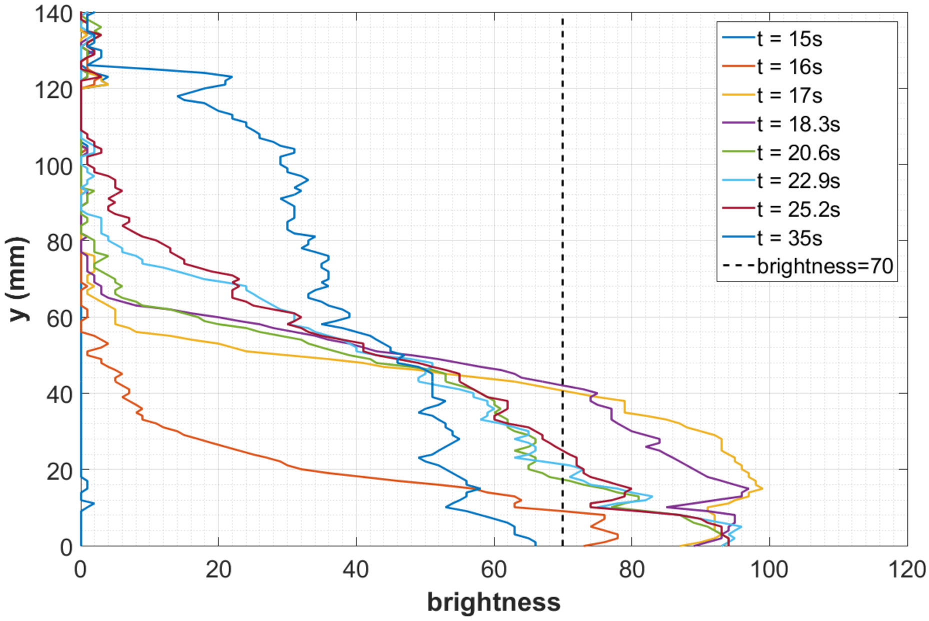

Figure 5.30. Brightness profiles for different time instances at position x = 910 mm.

A second threshold can be considered to investigate stratification, which distinguishes the dilute turbidity cloud from the background water. A brightness threshold of 20 is adopted for that purpose. The associated levels are also shown on the right panels of Figure 5.25 to Figure 5.29. By applying the same methodology to all images, on the top panel of Figure 5.31 the time evolution of the thickness of the dense and basal layers, with respective thresholds of 20 and 70, is presented, along with intermediate contours at multiples of 10. The lower panel of Figure 5.31 shows the fraction of the flow thickness that is occupied by the dense basal flow. The dense flow initially occupies roughly 90% of the flow thickness, while toward the end of the experiment it vanishes to zero as the dilute turbidity current thickens and the dense flow stops.

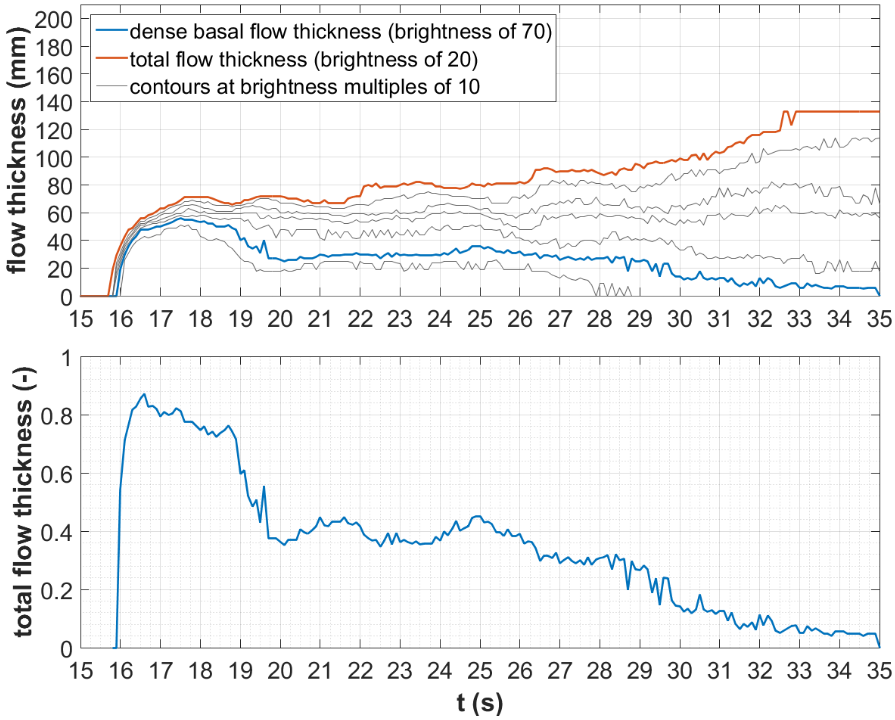

Figure 5.31. Time evolution of dense basal flow and total thickness (top) and of their ratio (bottom) at position x = 910 mm for experiment with a bed slope of 4.4% and 200 µm grain size (L3).

Figure 5.32 presents the fraction of the flow thickness that is occupied by the dense basal flow for all experiment of high initial density conducted with a flume bed slope of 4.4%. For S3, M3 and MIX3, the current reaches the end of the flume before the dense slow stops its propagation. The flow thickness decreases but does not vanishes as for the experiment L3.

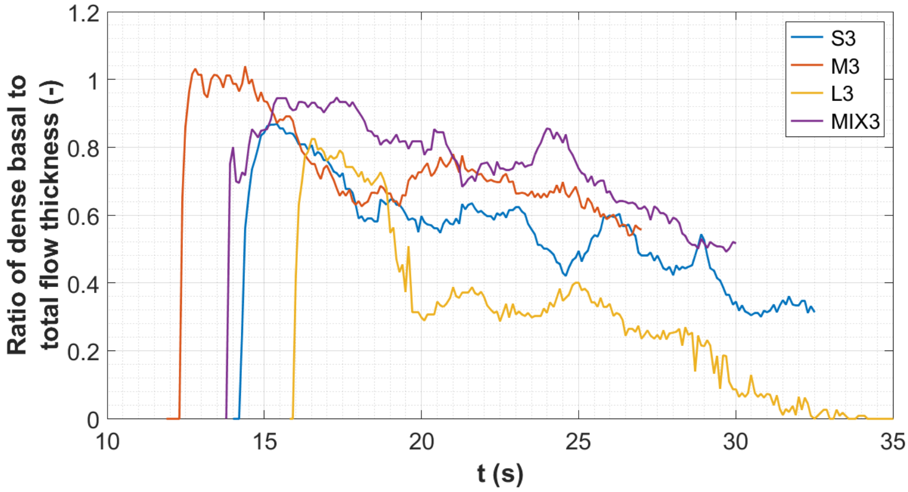

Figure 5.32. Time evolution of the ration of dense basal to total flow thickness.

Figure 5.33 present the time evolution of for the experiments conducted with a bed slope of 2.2% for the large sediment grain size (L2) at the location x = 910 mm. Based on the brightness thresholds of 20 and 70 for the total and basal layer, it is observed that the basal layer has not started to be weakened significantly and the transformation to a more dilute top layer is progressing much slower than for the case of experiment L3 presented above.

Obtaining information and correlation relations between brightness and concentration was not possible for the experiments conducted with zero bed slope. The false choice of lightning led to saturated images that did not allow image processing except the observation of the front position of the current.

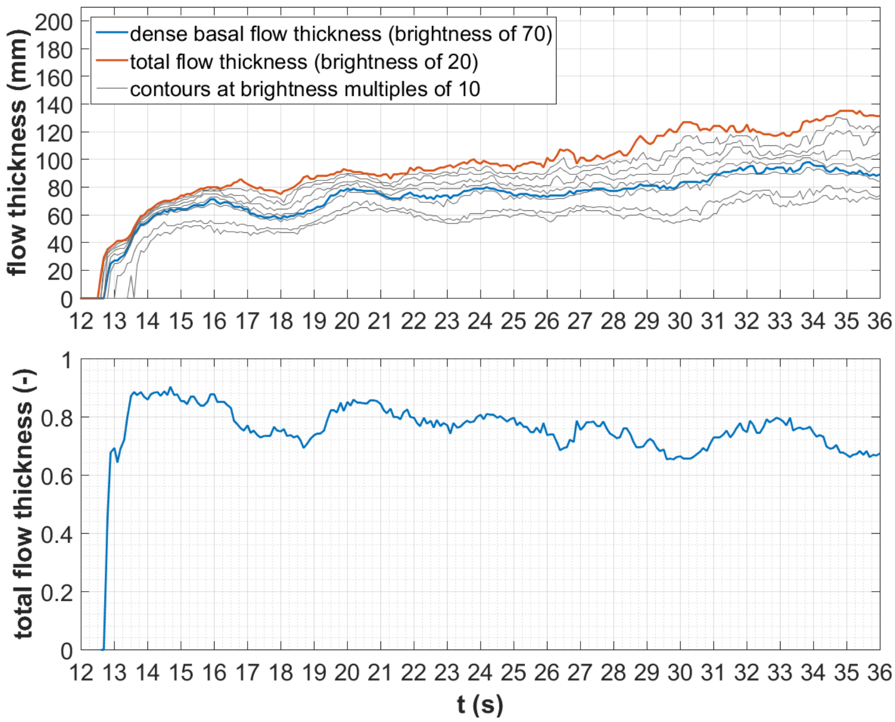

Figure 5.33. Time evolution of dense basal flow and total thickness (top) and of their ratio (bottom) for experiment with a bed slope of 2.2% and 200 μm grain size (L2).

5.5.4 Space-time evolution of depth-averaged quantities

The density flows investigated in the present experiments may be considered as shallow flows, in the sense that their development in the streamwise direction is more than an order of magnitude larger than their thickness. It is therefore of interest to derive depth-integrated quantities. Figure 5.34 and Figure 5.35 show the space-time evolution of the flow thickness and depth-averaged flow brightness, respectively. The flow thickness is here defined as the portion of the current whose brightness is larger than the previously set threshold of 20 distinguishing the turbidity cloud from the surrounding clear water. In Figure 5.34, the highest density is observed near the front of the flow. As the propagation continues, mixing starts to develop immediately behind the front and the thick mixing billows recirculate backwards, as can be seen from the curved trajectories of the regions of thick flow in Figure 5.34. The brightness is then averaged over the current thickness to yield the values reported in Figure 5.35. In that figure, the dense region of the current head and the “ejection” events associated with the formation of mixing billows are also clearly identified.

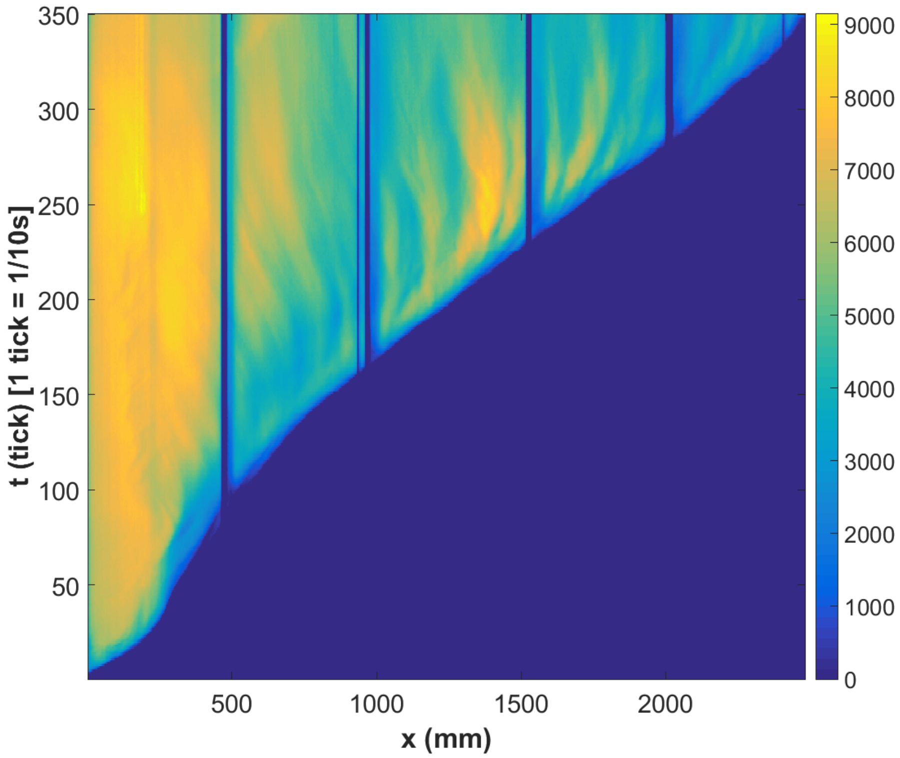

Figure 5.34. Flow thickness (defined as all pixels brighter than a set threshold of 20).

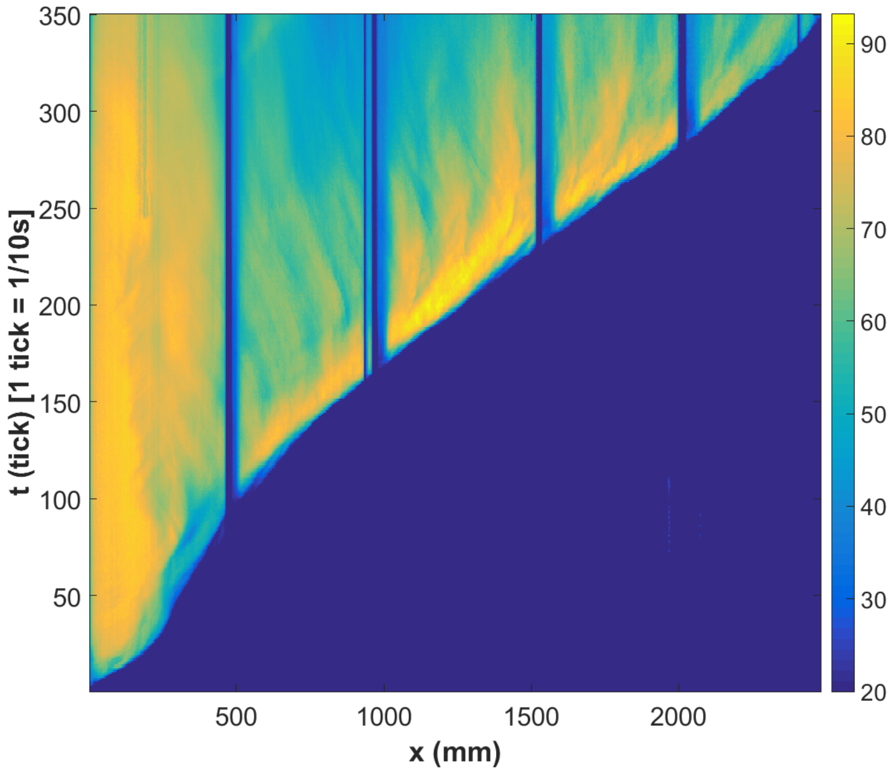

Figure 5.35. Depth-averaged flow brightness (averaged over flow thickness).

5.6 Summary

The experiments presented in Chapter 5 are focused on triggering dense subaqueous debris flows in a laboratory flume, and monitoring their propagation and associated degree of mixing and dilution. The effects of sediment size and bed slope on the propagation and the internal stratification of such flows were investigated.

After image processing analysis, the partition of the flow into a basal layer, which remains dense throughout the current propagation, and a dilute turbidity cloud resulting from mixing with ambient water at the rear of the current head are highlighted. The two layers were defined using the image brightness as an indication of concentration. The brightness profiles were correlated with the velocity profiles acquired with the UVPs and the brightness thresholds that defines each layer, were indicated. The combination of velocity and flow thickness profiles indicated rapid propagation of the dense basal layer and much slower, or even reverse, velocity for the dilute turbidity cloud.

The bed slope mostly affects the propagation of currents composed of the small and medium grain size. After the analysis of all results, the configuration with a bed slope of 4.4%, and an initial mass concentration of sediment equal to 30% and composed by the larger sediment size of 200 μm, was the most clear for the observation of the co-existence of the two layers followed by the stop of the dense basal layer and the continuation of the propagation of the dilute part of the current.

It is expected that the obtained dataset could provide a validation database for the development of a two layer depth-integrated models of subaqueous landslides. It is not used for comparison with the present model as it does consider an initial boundary condition of a continuous source. This led to the necessity to proceed into another experimental campaign which is characterized by an initial boundary condition of a sudden volume release. The lock-exchange experiments presented in Chapter 6 would prove to be a useful validation case for the introduced mod

Chapter 6 Laboratory experiments on high density subaqueous landslides

6.1 Introduction

An experimental program for investigating the initiation and propagation of a subaqueous landslide through lock-exchange type experiments is presented. In a lock exchange experiment, fluids of different densities initially at rest are separated by a vertical barrier – the lock gate – in a tank. When the gate is removed, differences in the hydrostatic pressure cause the denser fluid to flow in one direction along the bottom boundary of the tank, while the lighter fluid flows in the opposite direction along the top boundary of the tank. The initiation of many environmental flows including subaqueous landslides, debris flow or turbidity currents, is commonly connected with the collapse or sudden release of material, allowing their modelling as a lock-exchange flow. The mechanisms of sediment entrainment and movement can be thorough investigated in such intense and transient conditions as a lock-exchange.

Gravity currents have been studied extensively in the laboratory through lock-exchange experiments (Huppert and Simpson, 1980; Rottman and Simpson, 1983; Altinakar 1993; Hallworth *et al*., 1996; Zhu *et al*,. 2006). Sutherland *et al* (2002) studied gravity currents intruding into a uniformly stratified ambient in a series of finite-volume full-depth lock release laboratory experiments. Shin *et al.* (2004) provided an analysis of the motion of a gravity current produced by lock-exchange and investigated the role of dissipations in such flow conditions.

While low-density gravity flows like turbidity currents are commonly tested in lock-exchange experiments, the study of subaqueous gravity flows of very dense, viscous sediment-water mixtures like debris flows through this type of experiments is poor in the literature and is based on different types of laboratory experiments (see Section 2.5). One basic reason is the difficulty to provide the demanding initial inertia in the mixture that it will allow it to flow.

The present work suggests a series of lock-change experiments in order to reproduce small scale subaqueous landslides. Velocity, flow thickness and concentration stratification measurements are obtained using a high speed camera, a digital camera and UVP's method. Results are attained after different techniques of image processing and the UVP's results analysis. The lock-exchange problem of the experiments is numerically simulated using the SWBI2D model.

6.2 Experimental set-up

The experiments were performed in the flume illustrated in Figure 6.1 at the laboratory of the Department of Civil and Environmental Engineering, Université catholique de Louvain, Belgium. It has an overall length of 6 meters which is divided in two equal parts by a central gate simulating the idealized dam. The flume is mounted on an array of horizontal crossbeams, designed such that the deformation in the horizontal plane is less than 1 mm over the flume length. Sidewalls, with a height of 70 cm, are made by transparent glass fitted with two juxtaposed steel frames that are connected with outer support structure and ensures stiffness in the lateral direction.

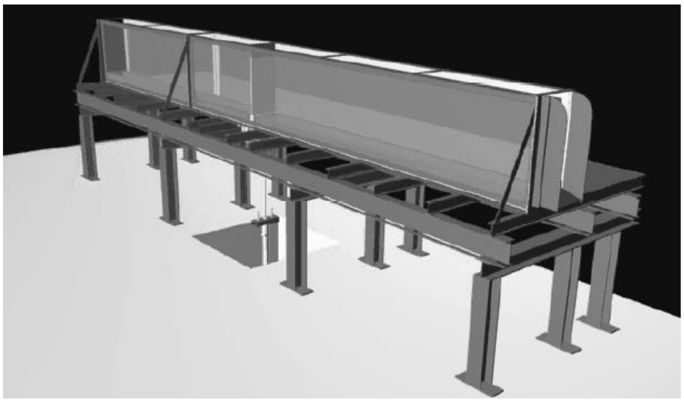

Figure 6.1. Overall view of the dam-break flume used in the present work (after Spinewine, 2005).

The cross-section of the channel is rectangular with a constant width equal to 25 cm. The bottom of the channel is a lined wood plane sealed to the transparent sidewalls. The downstream end of the channel may be sealed using an additional removable gate.

The dam-break wave is initiated by the sudden removal of a narrow vertical gate at the middle of the flume. The gate was designed to reach initial test conditions that approach as much as possible the idealization of an instantaneous dam collapse, while minimising perturbations to the sediments and water during the removal of the gate. To achieve this, the lowering of the gate was chosen instead of the most common rapid raise of the gate in dam-break experiments. The gate is aluminium with a thickness of 7 mm and is fitted on its circumference with a hollow PVC seal ensuring watertightness against the sidewalls. The downward movement of the gate is controlled by the rapid action of a pneumatic jack. When reaching its lower position, the gate is rapidly decelerated over a distance of less than two centimetres by two external hydraulic dampers and a pneumatic damper in the lower chamber of the cylinder, and does not rebound.The set-up described above was designed and firstly used in the framework of the experimental study of the doctoral thesis of Spinewine (2005).

For the purposes of the present experimental work, the length upstream the gate has been modified as illustrated in Figure 6.2. A wooden plate has been placed in order to limit the length of the upstream reservoir to 20 cm. It was stabilized using silicon that also provides water tightness. Level regulation at the downstream end is achieved by inserting a steel plate of a height of 70 cm into a slot fitted with a watertight joint around the cross-section, depending on the desired level of water in the channel. Overflow is conveyed by a gully into a settling tank.

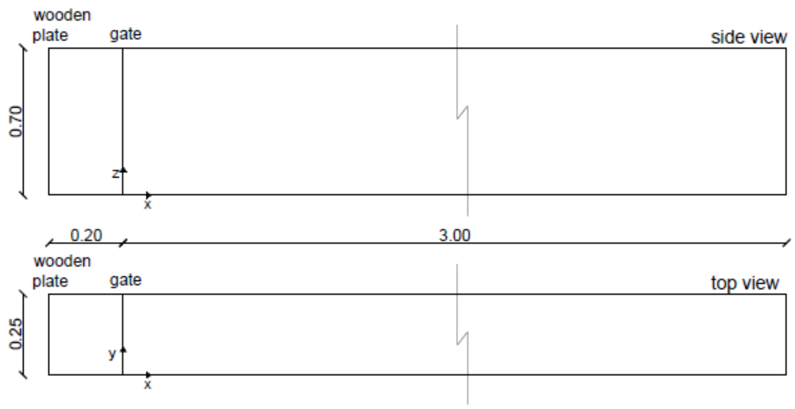

Figure 6.2. Side and top view of the used part of the flume after the modification for the present study.

6.3 Test conditions

6.3.1 Material properties

The mixture that was used to reproduce the behavior of a subaqueous high density flow, like a debris flow, is composed by water and sediments. This experimental campaign is divided in two parts, in each of those a different type of sediment is used for the composition of the input mixture. The different mixtures are tested in the exact same configuration.

One of the materials used is the high performance thermoplastic polyurethane, SCHAETTI FIX 6511. The polyurethane has a density ρ_{sed} = 1.16 g/cm^3. Two different grades with d_{50} = 84 μm and d_{50}= 169 μm, respectively, were tested. Detailed description of the material properties is given in Section 5.3.1.

The other sediment chosen for the mixtures is china clay which is typically used in laboratory experiments of high-density flows. In concentrated clay slurries, particle interactions produce a structure with some rigidity which is the source of yield stress. If a shear stress is applied below the yield stress this network or structure prevents flow. At high particle concentrations, this structure would be present throughout the suspending water medium. For shear stresses above the critical yield stress flow causes the structure to break up into smaller elements composed of flocculated particles (Michaels and Bolger, 1962). The apparent viscosity may also decreases with increasing shear rate as particle or aggregate orientation becomes more ordered (Catty et al., 2001). Many researchers have investigated the rheological behavior of kaolin clay (or china clay) slurries (Michaels and Bolger, 1962; Thomas et al., 1963; Xu et al.2003; Rossington et al., 1999). According to the study of Larsen et al. (1994), the kaolin clay slurries can exhibit a yield stress of 30 up to 300 Pa, and were fitted to either the non-Newtonian Bingham or Casson rheological models. The non-Newtonian Herschel-Bulkley model can also satisfactorily describe the non-Newtonian clay slurries (El-Nahhas et al., 2005; Vlasak and Chara, 2011).

6.3.2 Initial conditions

As mentioned above, the total length of the flume upstream the gate was shorten in order to form an initial reservoir where the mixture is placed, with a length of 20 cm, a width of 25 cm and a maximum height of 65 cm.

Different techniques were followed for the preparation of the initial mixture for the two different series of experiments based on the type of sediment used. They will be described separately and in detail in following sections of the chapter.

The configurations explored in the present work consists of the upstream side of the gate which is filled with the water-sediment mixture and the downstream side which is filled with clear water.

6.4 Instrumentation

6.4.1 Velocity measurements

Velocity profiles were measured using an Ultrasonic Doppler Velocity Profiler (Met-Flow, UVP). The UVP (Ultrasound Velocity Profile) represents both a method and a device for measuring an instantaneous velocity profile in liquid flow along the ultrasonic beam axis by detecting the Doppler shift frequency of echoed ultrasound as a function of time. The method and the device are the same used for the experimental work presented in Chapter 5 and they are described in detail in Section 5.4.1.

Three ultrasonic transducers with working frequency 4 MHz, external diameter 8mm and transducer active diameter 5 mm were used for the measurements. They have been placed near the water surface and the axis of probe was at an angle of 30° to the normal of the flume bottom looking down the main flow. The first transducer is located at a distance of 0.5 m from the gate, while the second at a distance of 1 m from the gate.

The velocity resolution of UVP DUO was set at 0.713 mm/s and its spatial resolution was set at 0.74 mm. A fixed number of 120 points were measured in each profile and the sampling period was equal to 72 ms.The measurements gave the projected vertical profiles in the middle of the width of the flume. Each of the two UVPs was interrogated in sequence with a multiplexer throughout the duration of the experiment, and the time interval between successive measurements at a given transducer is in the order of 0.4 s. Two profiles per cycle were taken for each transducer with a total number of profiles set to 800.

6.4.2 Imaging apparatus

Detailed sidewall measurements are acquired by filming the flow through the transparent side wall of the flume using two different video cameras.

A PENTAX K20D digital camera was used to acquire image sequences of the entire -used for the experiments- length of the flume at a frame rate 3 images per second and with a resolution of 4672×3104 pixels. The focal length of the lens was chosen to be 50 mm with exposure time of 1/45 sec and focal ratio of f/9.5.

A Photron FASTCAM SA3 model 120K high-speed camera was used to capture the first 1.22 m of the flume, focusing on the initiation of the flow after the lowering of the gate. The location of the camera was set in a distance of 1 m from the front sidewall of the flume. Image sequences were acquired at a frame rate of 60 images per second with a resolution of 1024×512 pixels. The images were provided with 256 grey levels. The shutter speed of the lens was 1/1000 s. A ZEISS Planar 2.4/85 mm lens has been used.

Lighting is provided by two 400 Watt halogen spot heads that were hanged in height above in order to guarantee uniform illumination of the used-part of the flume and avoid direct reflections of light towards the camera. An external black sheet was used to cover the back sidewall to provide uniform background. A ruler on the sidewall provides scaling and reference positions for the different images. The location of the two cameras is illustrated in Figure 6.3.

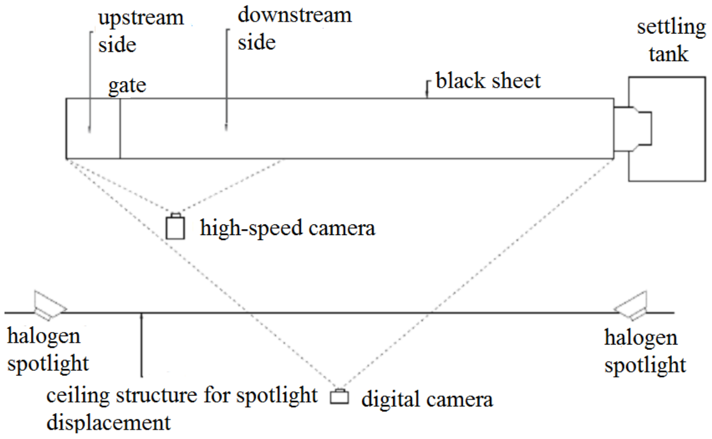

Figure 6.3. Top-view of the flume and position of imaging devices.

6.4.3 Concentration measurement

After filling the upstream reservoir with the already prepared sediment-water mixture, it was set in suspension using an electric drill and a sample was taken using a 50 ml syringe. The sample was weighted, dried in the oven and then its concentration was calculated in order to cross-check the initially imposed volumetric concentration of the mixture.

6.5 Imaging correction

A step must be preceded before the final image processing which will lead to the quantitative analysis of the results. A correction technique based on reference images is introduced in this study in order to guarantee the uniform illumination of the images and assure maximum quality.

Firstly, the downstream part of the flume was filled with water and then 5 l of milk were added. A mechanical drill was used for mixing the two fluids along the full length of the flume until complete uniformity was achieved. Milk was chosen to give to the water deposit the light white colour that facilitates the image processing, without changing dramatically its density (Figure 6.4). The milk density is 1030 kg/m^3 at 20C°. 5 l of milk were mixed with 370 l of water with density of around 1000 kg/m^3 , so the density of the resulting mixture corresponds to 1000,6 kg/m^3 that is quite close to the water density.

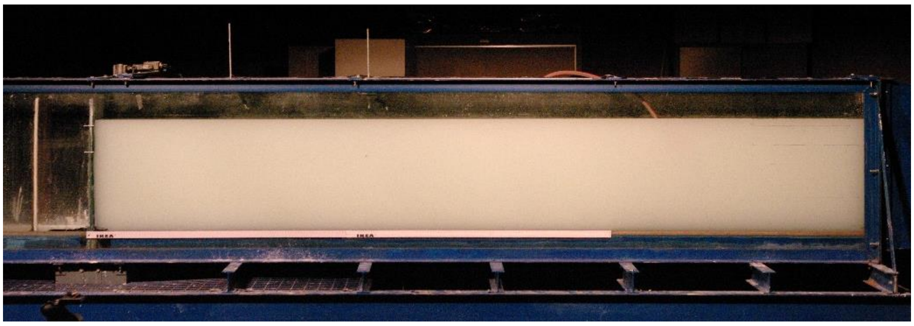

Figure 6.4. Example of reference image using water-milk mixture (captured by the digital camera).

A line along the length is selected and the matrix of the brightness of the selected points was created. Every image was then multiplied by this matrix and corrected for uneven illumination. This correction was applied for both high-speed and digital camera's images.

6.6 Experimental observations

In this section, experimental observations are presented based on the analysis of the images sequences and UVP measurements for both kaolin clay and polyurethane slurries. The behavior of the flow is investigated based on sediment type and sediment volumetric concentration of each slurry.

6.6.1 Experiments with kaolin clay slurries

The physical experiments reproducing subaqueous high-density flows were conducted in the flume presented in Section 6.2. The slurries were a mixture of kaolin clay and water. A total of 4 experiments were carried out with a clay volumetric concentration of 1%, 2%, 3% and 15%, respectively. The total volume of the slurry for each run was equal to 25 l.

Each slurry was prepared in a tank out of the flume using an electric drill. The density of the kaolin clay (china clay) used was equal to 2615 kg/m^3. Considering water density of 1000 kg/m^3, the resulted density of the slurry was 1016,15 kg/m^3 for volumetric concentration of 1%, 1032,3 kg/m^3 for volumetric concentration of 2%, 1048,45 kg/m^3 for volumetric concentration of 3% and 1242,25 kg/m^3 for volumetric concentration of 15%.

The flume was filled with water up to the level of 0.5 m and then the prepared mixture was transferred into the upstream reservoir. An electric drill used to keep the mixture in full suspension and a sample was taken using a 100 ml syringe for checking later the sediment concentration. The drill was removed just before the lowering of the gate. The gate dropped and at the same instance the high-speed camera, the digital camera and the UVP profiler start to record the flow.

General evolution of the current

First, the images were corrected to account for uneven illumination of the flow applying the technique presented in Section 6.5. In the following step, the images are ortho-rectified using a number of reference points with known coordinates to correct for image distortion, and the resulting ortho-rectified image is resampled at a resolution of 1 pixel per mm, with the x-axis being defined as streamwise and the y-axis orthogonal upwards. Finally, the image background is removed by subtracting the initial image, prior to flow initiation, from the entire image sequence. Due to the bright color of the kaolin clay slurry, the current appears on the resulting image sequence as variable shades of grey on a perfectly black background. This procedure was presented in detail in Section 5.4.2.

Figure 6.5 shows snapshots of the current evolution at selected instances after release. Pixel values on the processed images are used to define the thickness of the current that appears in red color on the processed images.

Snapshots of the current when the front reaches the position x = 500 mm and 1000m for all experiments, are given in Figure 6.6 and Figure 6.7, respectively. Processed images provide information on the position and the flow thickness at all captured time instances and can be used for the calculation of the velocity of the head of the current.

The uniformity of the slurries do not allow the estimation of the concentration distribution in each experiment, based as brightness proxy. This result prevents the quantitative analysis of layering in such flows.

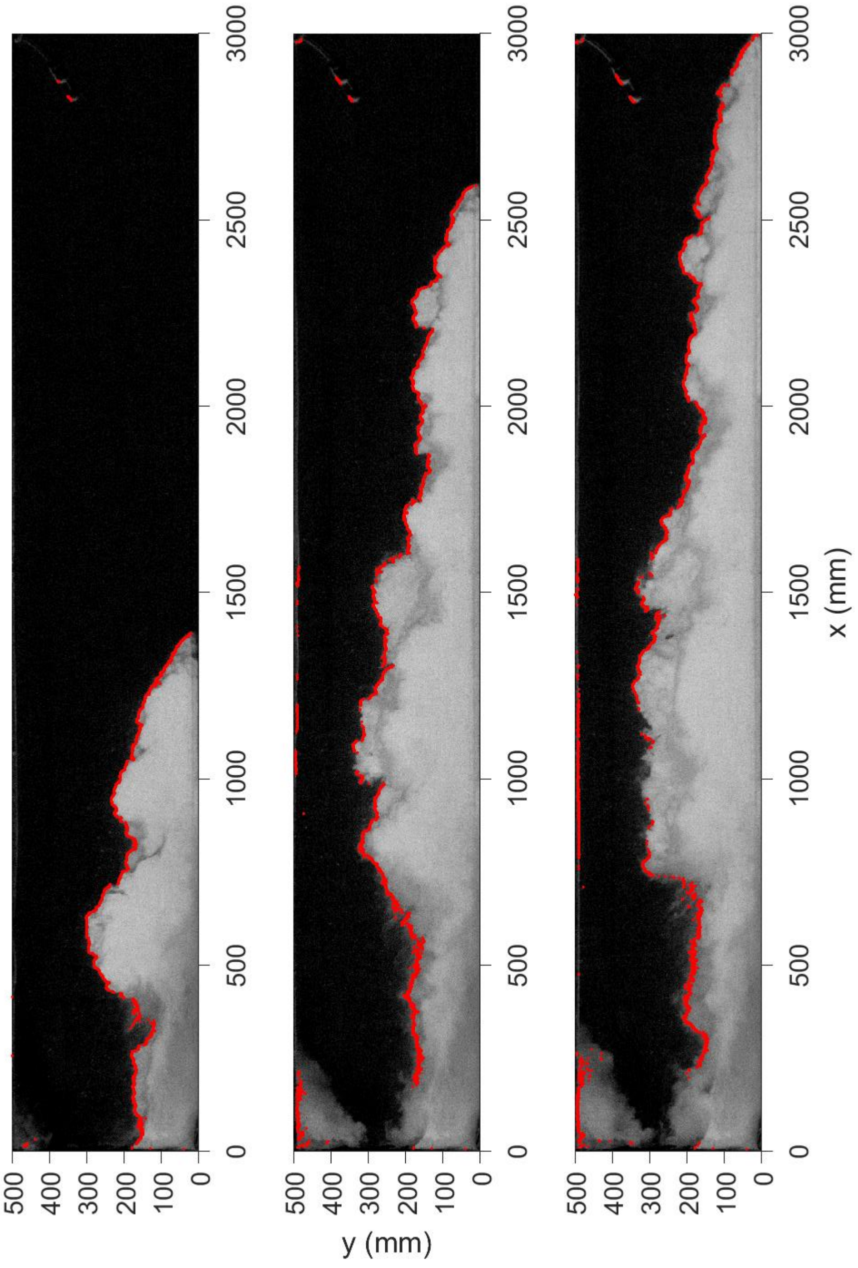

Figure 6.5. Snapshots of the flow for the experiment with kaolin clay concentration of 15% at instances *t* = 3.3, 4.2 and 5 s. Red line define the region of the current.

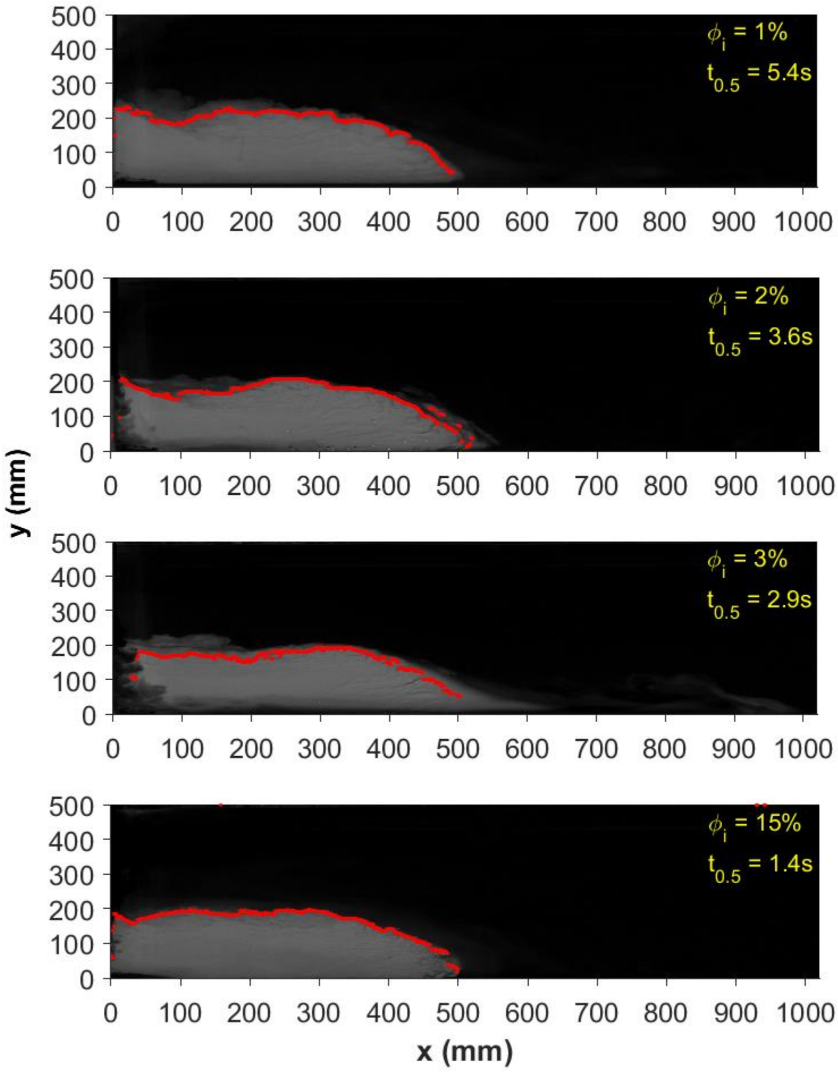

Figure 6.6. Snapshots of the flow for the experiments with kaolin clay concentration of 1, 2, 3 and 15% when the front arrives at the position x = 500 mm. Red line define the region of the current.

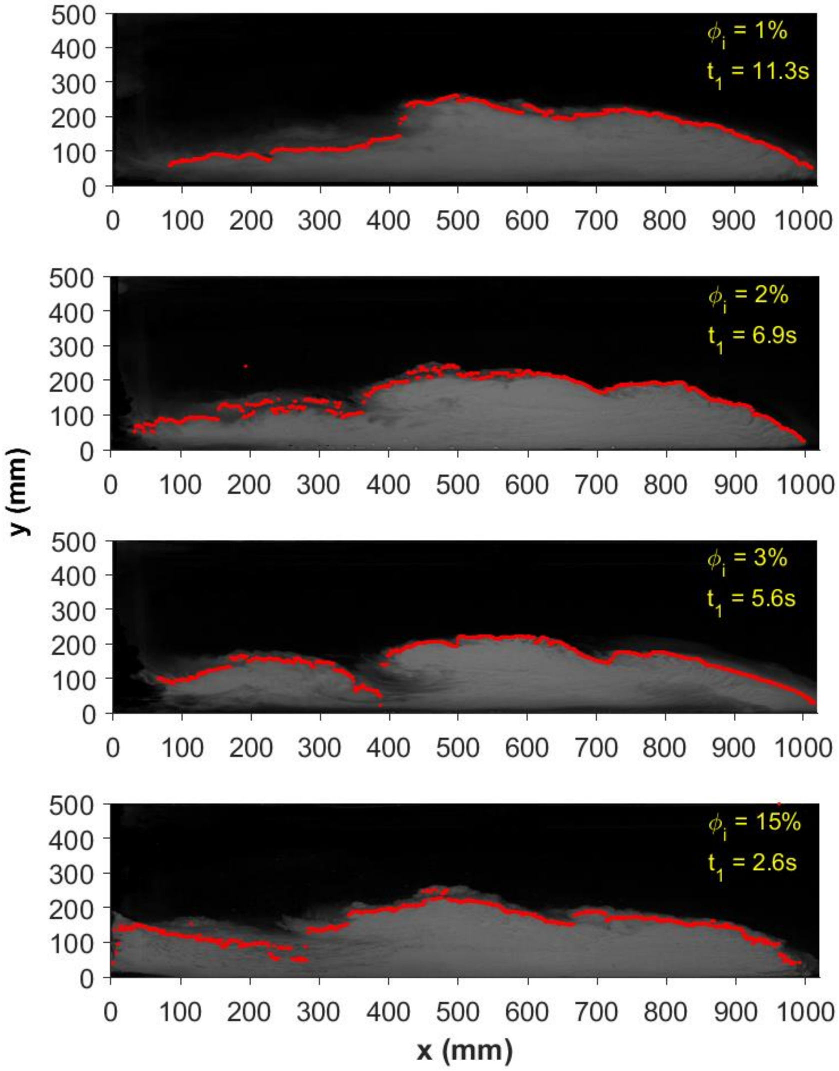

Figure 6.7. Snapshots of the flow for the experiments with kaolin clay concentration of 1, 2, 3 and 15% when the front arrives at the position x = 1000 mm. Red line define the region of the current.

Frontal Velocity

The visualization of the current head on the rectified images allowed the tracking of the front position and the front velocity. Figure 6.8 and Figure 6.9 present the time evolution of the front position and velocity based on the images shoot with the PHOTRON high speed camera. As described in Section 6.4.2, the high speed camera captures the first 1.02 m after the gate.

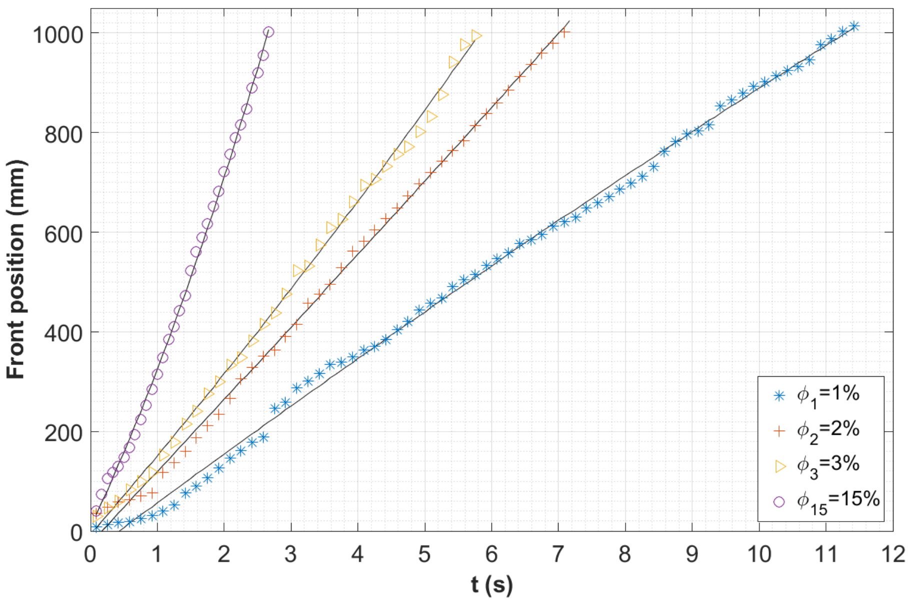

Figure 6.8. Time evolution of the front position for different volumetric concentration φ_i after processing of the images taken from the high-speed camera.

In Figure 6.9, a high velocity for fractions of a second immediately after the lowering of the gate is observed. When the current is fully formed, the velocity of the head accelerates for few centimeters and then propagates with almost constant velocity for the three case with kaolin clay volumetric concentration φ_i of 1%, 2% and 3%. With the increase of the kaolin clay content, the current head is still accelerating when it reaches the position of 1.22 m. The velocity in which the current arrives in the end of the high-speed domain (1.22 m) is 89 mm/s for φ_i of 1%, 141 mm/s for φ_i of 2%, 172 mm/s for φ_i of 3% and 375 mm/s for φ_i of 15%.

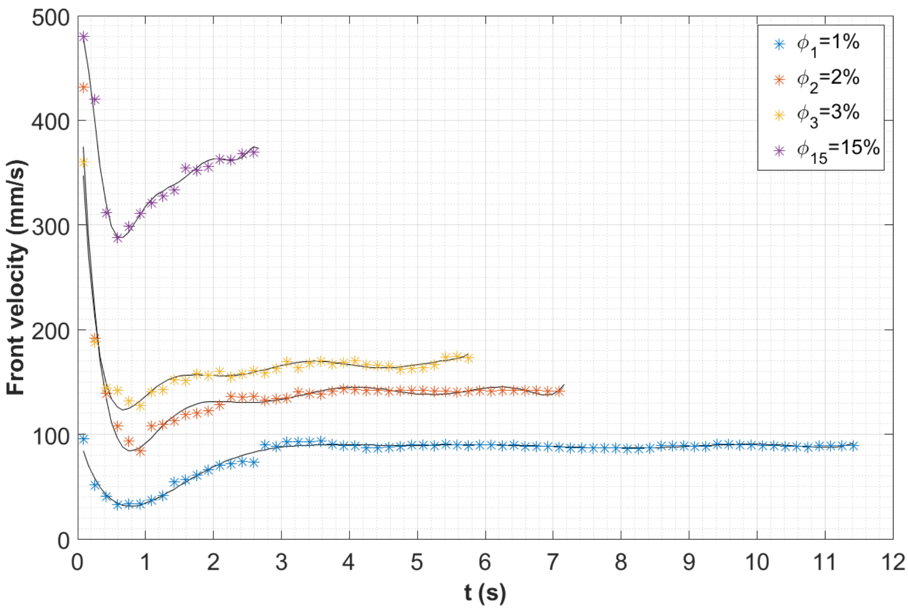

Figure 6.9. Time evolution of the front velocity for different volumetric concentration φ_i after processing of the images taken from the high-speed camera.

Starting from a slurry with sediment volumetric concentration of 1%, the addition of 1% reduced the time in which the head reaches the position of 1.22 m by 37%, while for an addition of 2% by 49%. The difference between the slurry of 1% and 15% of kaolin clay volumetric concentration reaches the 76% (see Figure 6.10).

The digital camera was located in such a position that allows the capture of the full runout domain. The drawback is that the maximum number of images that the digital camera can capture is 3 frames per second with continuous shooting. This fact limited significantly the obtained images for each experiment. In Figure 6.11, which presents the time evolution of the front position of the current for all experiments, is observed a good agreement between the data obtained from the high-speed camera and the digital camera.

Figure 6.12 shows the time evolution of the front velocity for each experiment. For the cases with low sediment volumetric concentration, the current after its full development propagates with almost constant velocity and then starts to accelerate until it reaches the end of the flume. For the experiment with sediment volumetric concentration of 15% a different behavior is observed.

The head of the current is accelerating more rapidly and the rate of acceleration keeps increasing until it reaches the end of the runout domain.

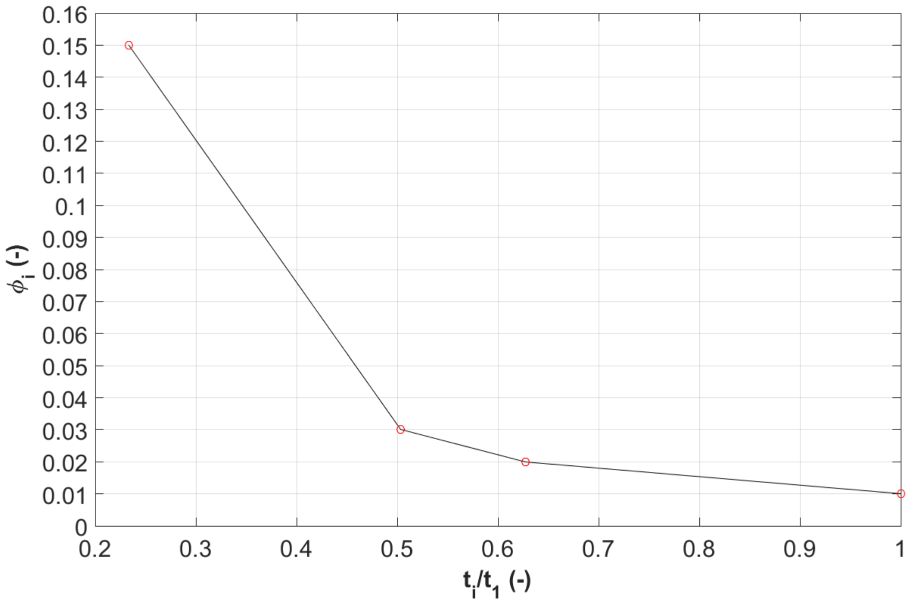

Figure 6.10. Propagation time of the current front position (divided by the propagation time t_1 of the slurry with φ_i=1%) with the volumetric concentration φ_i, after processing of the images taken from the high-speed camera.

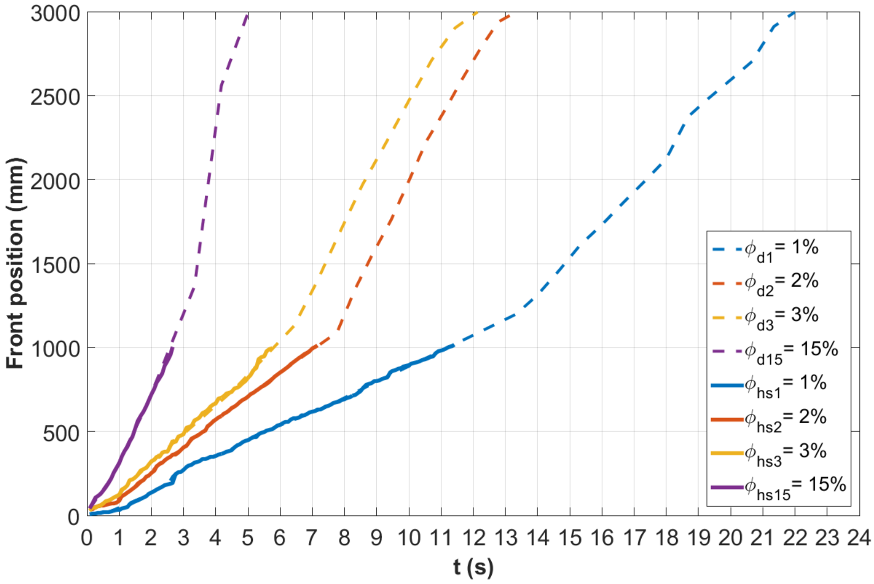

Figure 6.11. Time evolution of the front position for different volumetric concentration φ_i. Subscript d, denotes that the results obtained from the images captured by the digital camera and subscript *hs*, by the high speed camera.

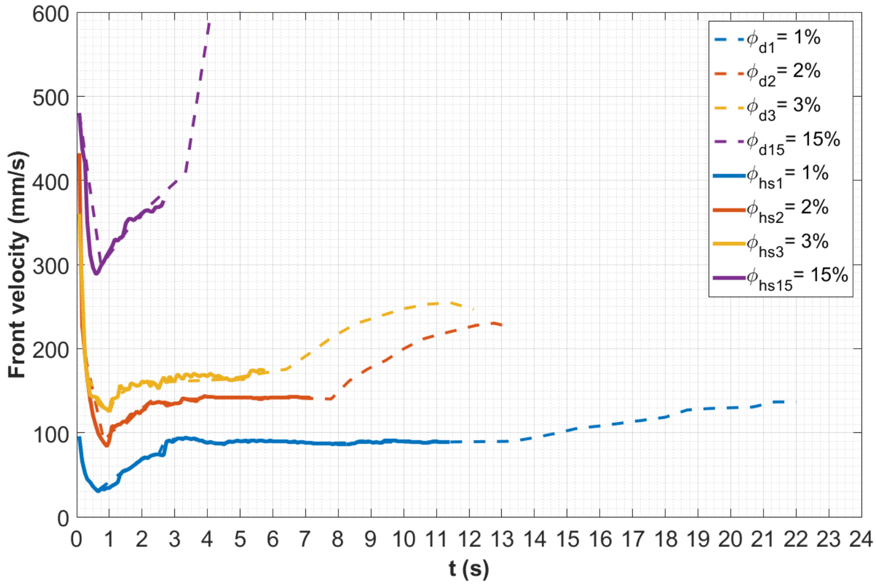

Figure 6.12. Time evolution of the front velocity for different volumetric concentration φ_i. Subscript *d*, denotes that the results obtained from the images captured by the digital camera and subscript *hs*, by the high speed camera.

Velocity measurements with UVP method

Two UVP transducers were used for the experiments with the first to be located at a distance of 0.5 m after the gate and the second one after 0.5 m from the first, in a distance of 1 m from the gate. Figure 6.13 - Figure 6.16 present the downstream velocity profile for all experiment at various time instances. At each figure the top left picture for each transducers corresponds to the time in which the current arrives. For the cases with low sediment volumetric concentration, the results are satisfying and in a good agreement with the flow thickness and front propagation time obtained from the processing of the images. For the slurry with concentration of kaolin clay equal to 15%, the UVP measurements did not match with the velocity calculated from the image processing. The flow thickness seems to be better captured, although especially the second transducer did not manage to penetrate along the total thickness of the current. Counterflow was expected as a result of the lock-exchange type of the experiments. This behavior could not be modelled by the introduced model, as it has no free surface and assumes that that the top layer is propagating in an ambient fluid of infinite thickness. In Figure 6.13Figure 6.16, the red dashed lines correspond to the successive profiles obtained by the same transducer before the next transducer start its measurement and the blue line corresponds to the average of the two successive profiles of each transducer.

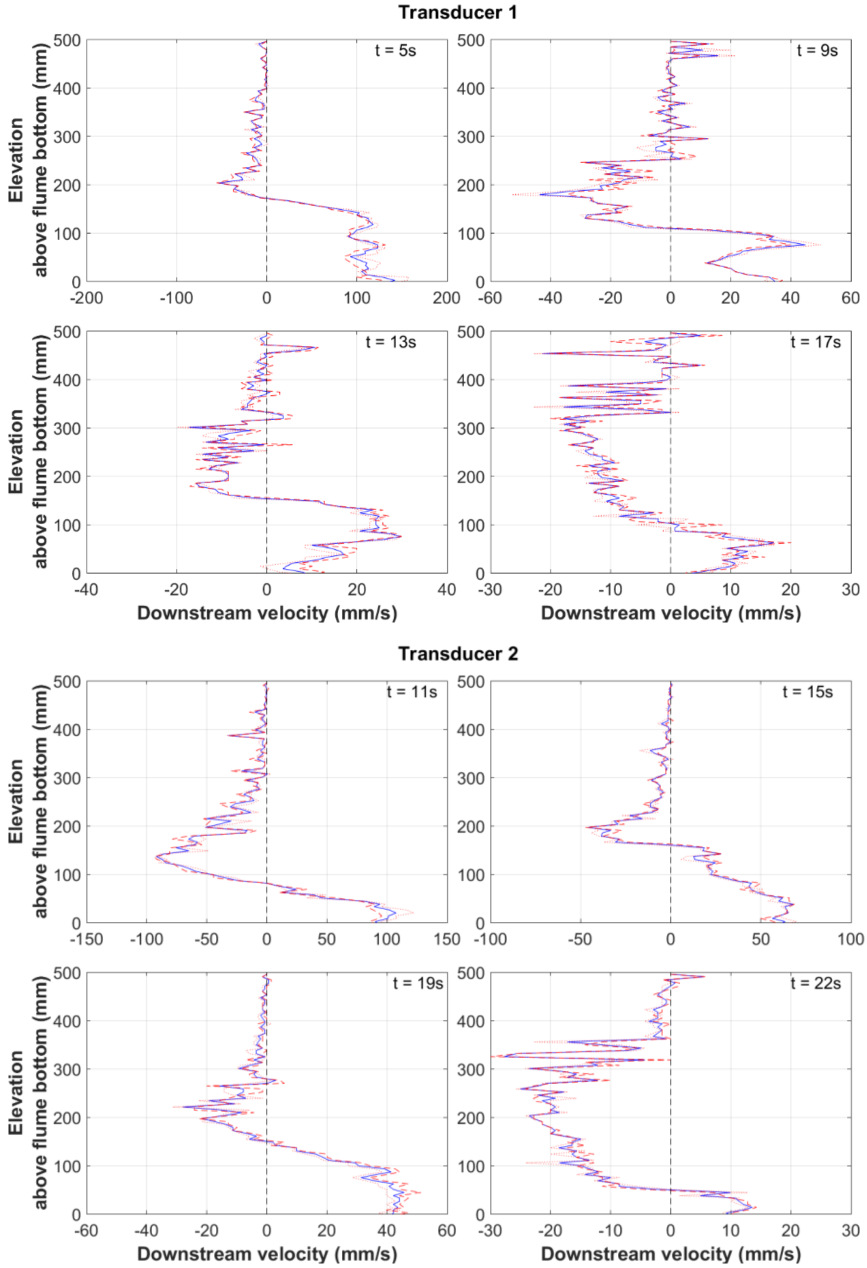

Figure 6.13. Downstream velocity profiles at selected instances for the experiment with kaolin clay volumetric concentration of 1%.

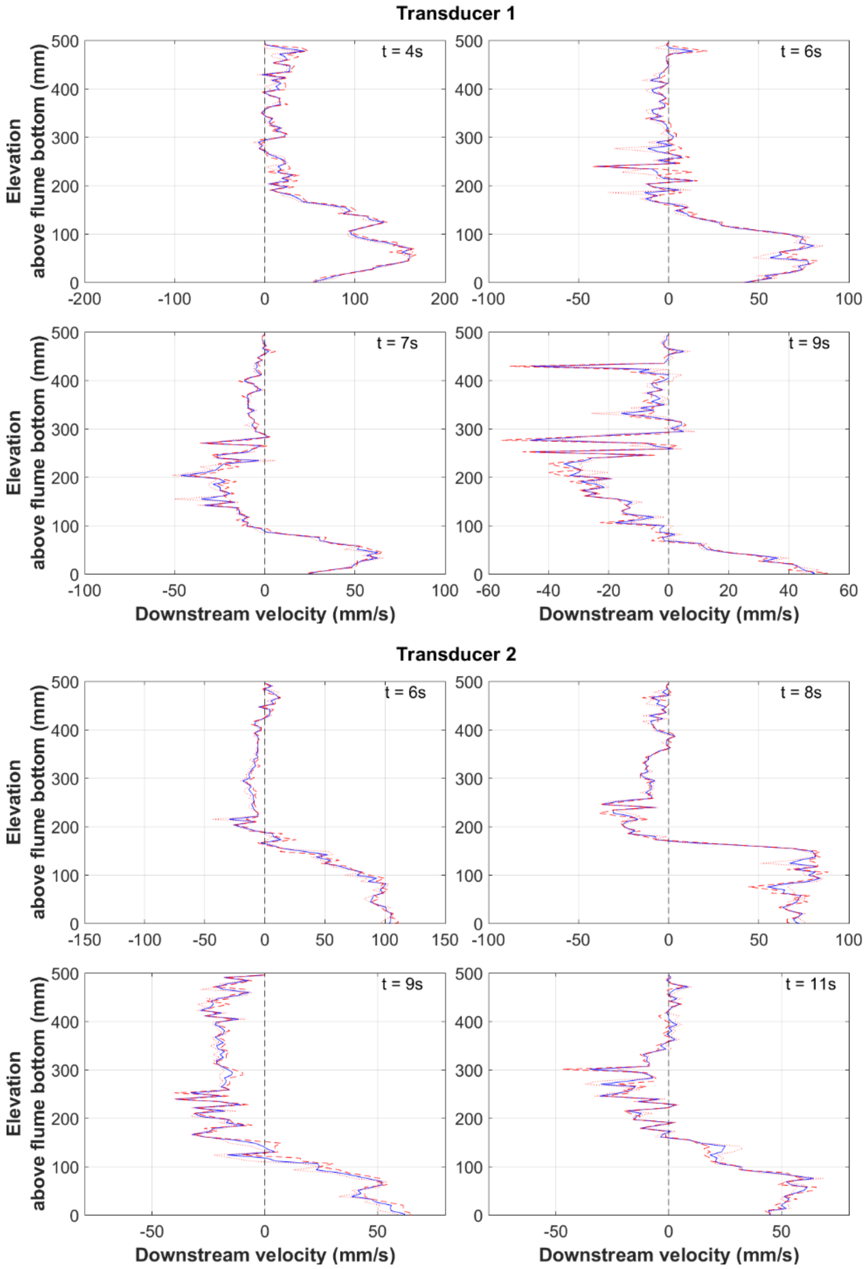

Figure 6.14. Downstream velocity profiles at selected instances for the experiment with kaolin clay volumetric concentration of 2%.

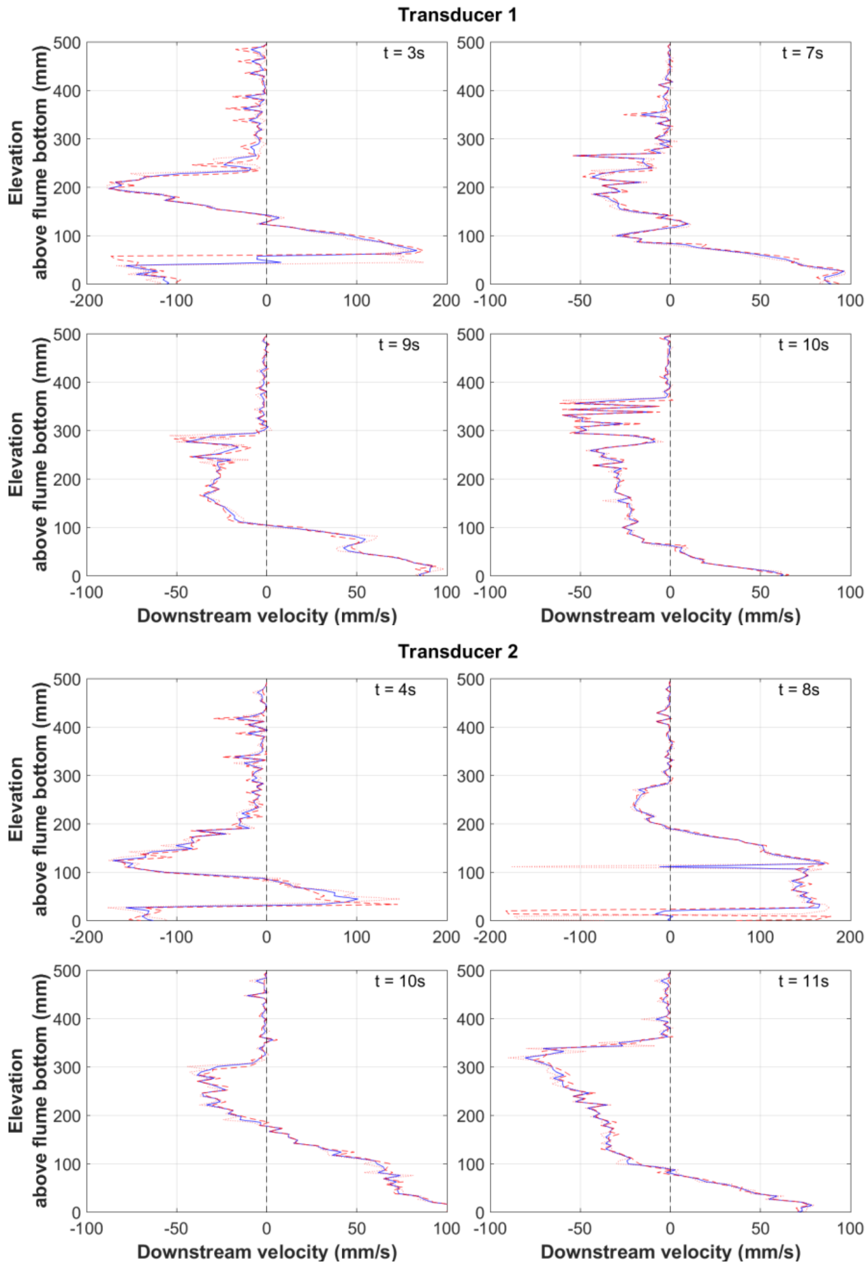

Figure 6.15. Downstream velocity profiles at selected instances for the experiment with kaolin clay volumetric concentration of 3%.

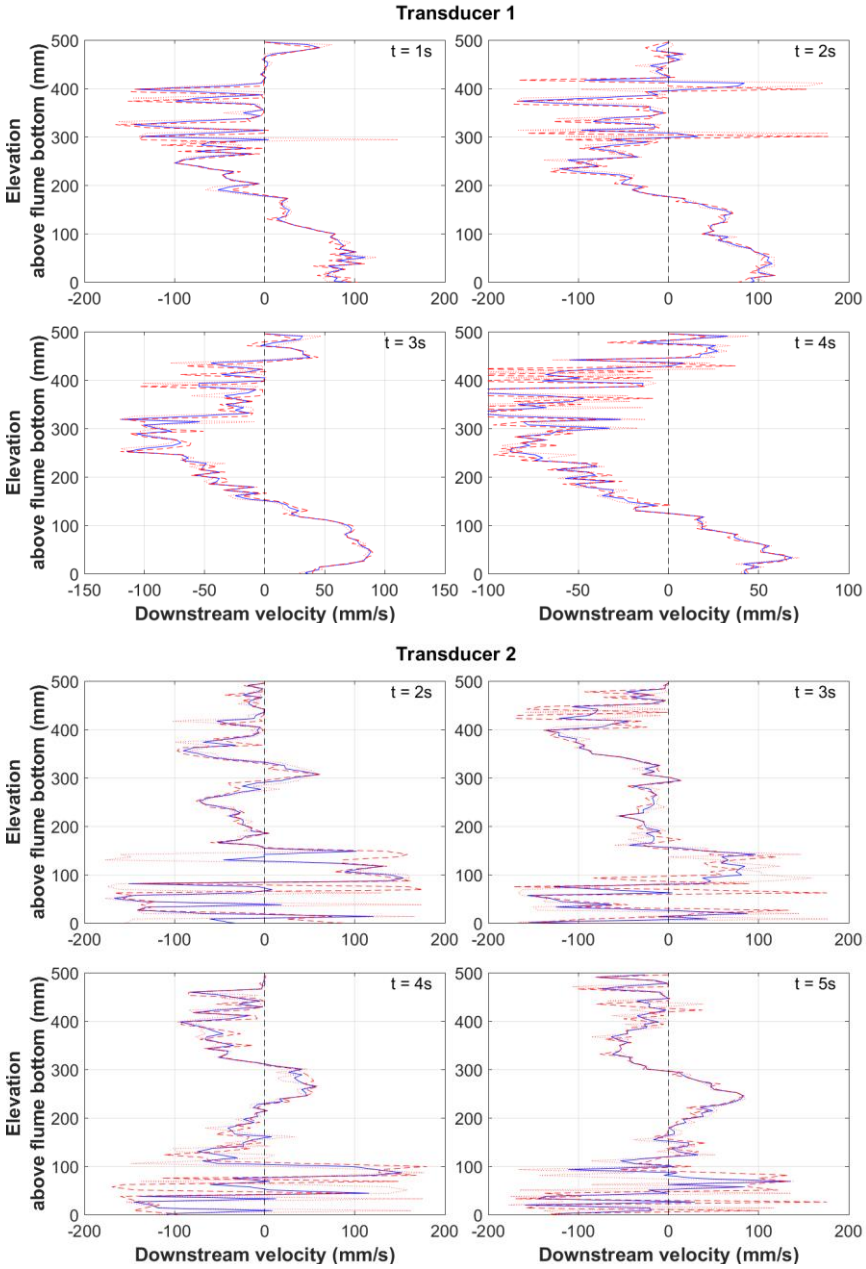

Figure 6.16. Downstream velocity profiles at selected instances for the experiment with kaolin clay volumetric concentration of 15%.

6.6.2 Experiments with polyurethane slurries

The polyurethane sediments that were used in the experimental campaign presented in Chapter 5, were tested in the lock-exchange experiments conducted in the flume at the laboratory of the Université catholique de Louvain.

Based on the information about the behavior of the material as a part of a slurry gained from the previous experimental campaign, effort has been made to achieve the maximum quality on its performance. The challenge was to reduce surface tension on the mixture. This was achieved through a delicate procedure. The total mass of the dry sediment depending on the volumetric concentration of each slurry, was divided in samples of 100 g. Each sediment sample was transferred in the proper sieve according to the particle size and then placed in the sieve shaker of the laboratory. The aim of the sieving was to dissolve as many aggregates as possible that allowed better mixing in the preparation of the final slurry. After this procedure, the sieved material was transferred into a device which removes the air using a pressurized pump. Every few minutes the sample had to be removed from the device to add few milliliters of water and mix it and then placed back to the device. This procedure lasted from 5 to 15 hours depending on the sediment concentration of each slurry.

Another difficulty observed with the treatment of this material was that the resulted mixture (sediment volumetric concentration ranging from 5% to 30%) was too dense that needed significant initial momentum in order to flow. In order to achieve this initial momentum, the slurry was placed into the upstream reservoir and was kept in suspension using an electric drill mixing with constant pace. The drill was removed few seconds before the beginning of the experiments, so that the sediment did not have the time to settle.

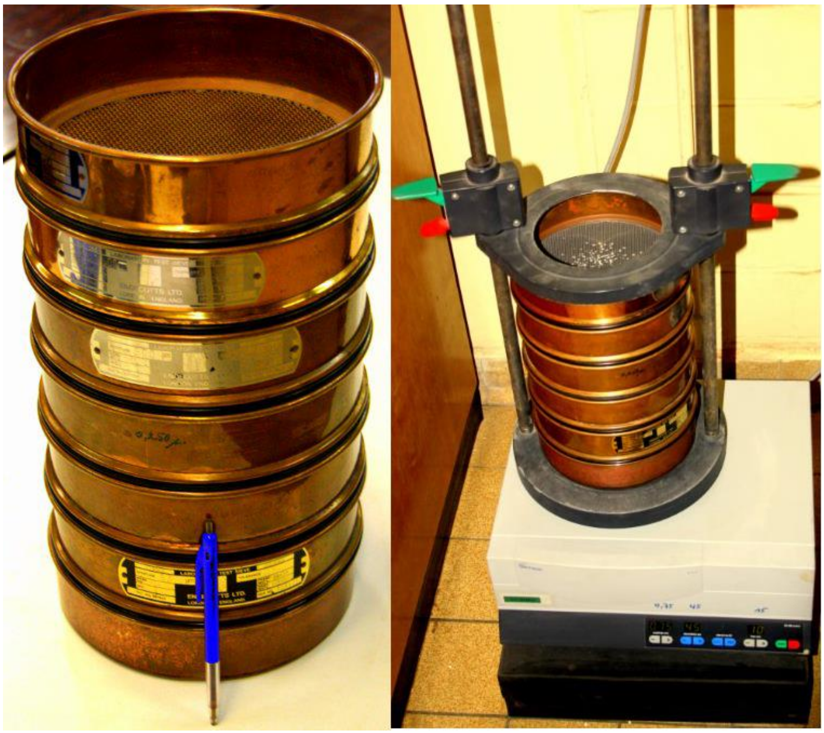

Figure 6.17. Sieves of different screen openings (left) and sieve shaker at the laboratory of the Department of Civil Engineering, UCL.

Reference images method for sediment distribution estimation

A method based on reference pictures was introduced in order to be used as a tool for the estimation of concentration distribution along the height of the current. A part of the flume was isolated and filled with slurries and polyurethane sediment with volumetric concentration of 1%, 3%, 5% and 7%. Snapshots of each slurry in situation of full suspension were taken using the high-speed camera programmed with the exact settings as used for the main experiments (Figure 6.18). The lightning was the same as well. A central portion of each image was selected in order to avoid sidewall effects. (Figure 6.19). The matrix of the brightness of the selected portion was created and the mean of each row is computed (Figure 6.20).

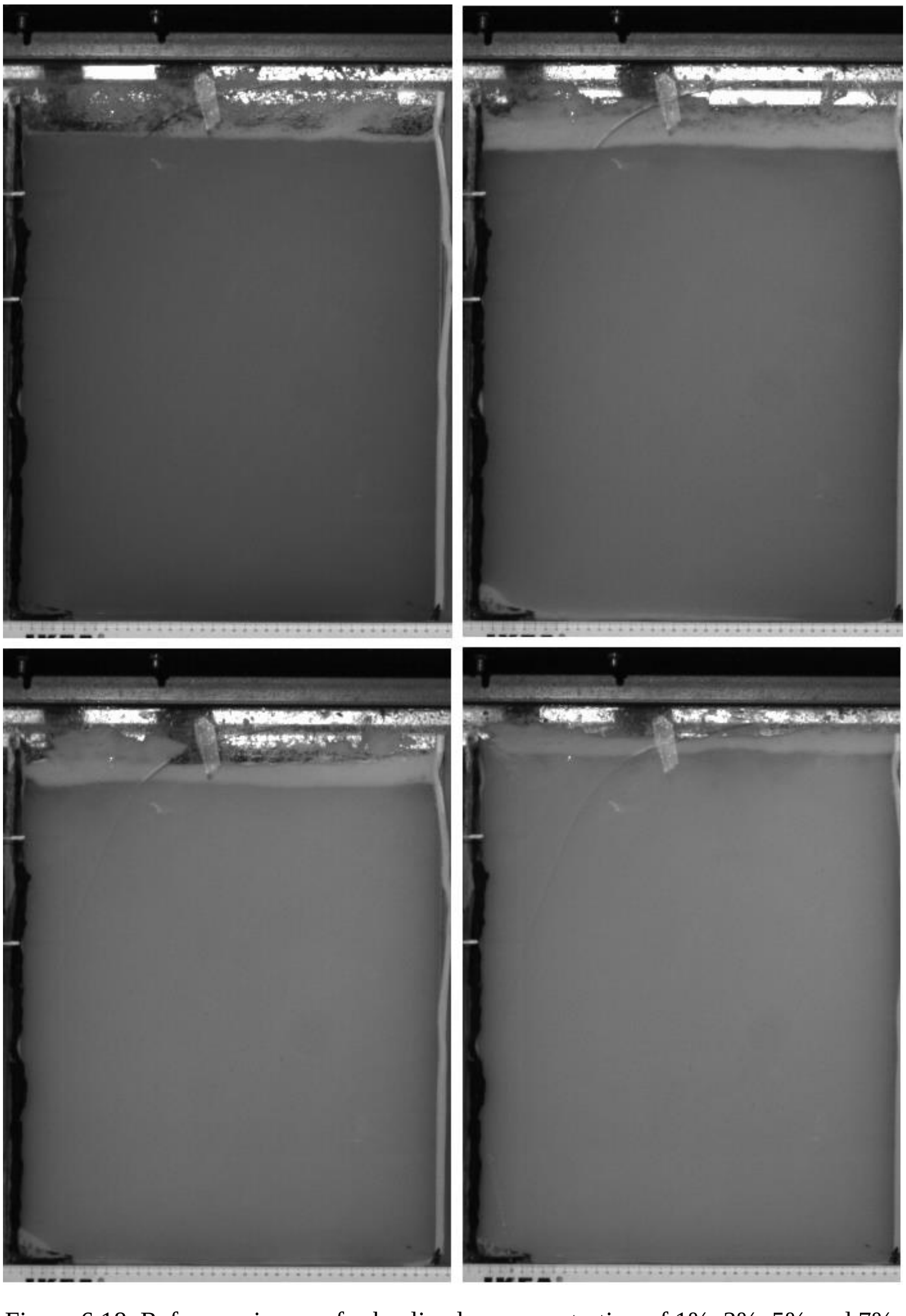

Figure 6.18. Reference images for kaolin clay concentration of 1%, 3%, 5% and 7%.

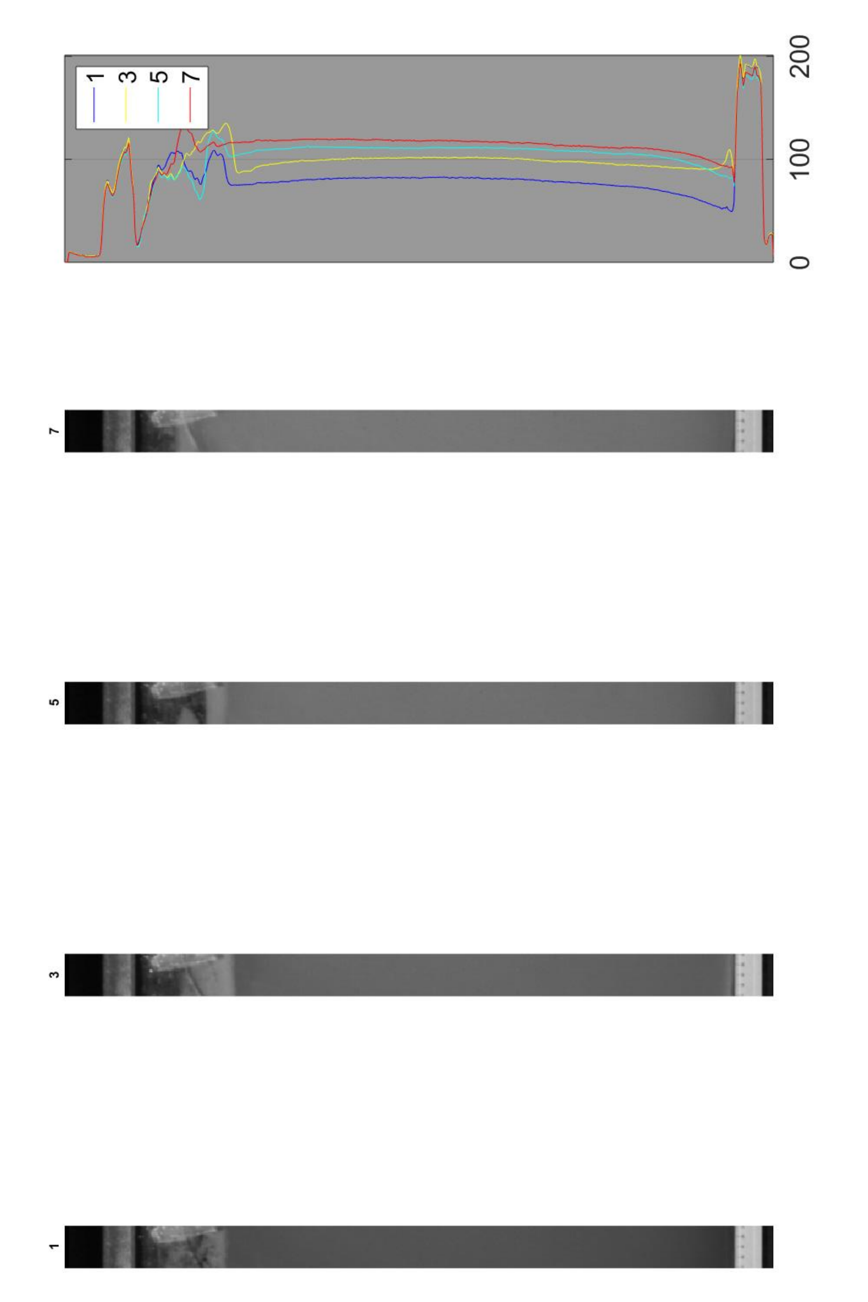

Figure 6.19. Part of the reference image for each slurry used for the calculation of the brightness distribution over depth.

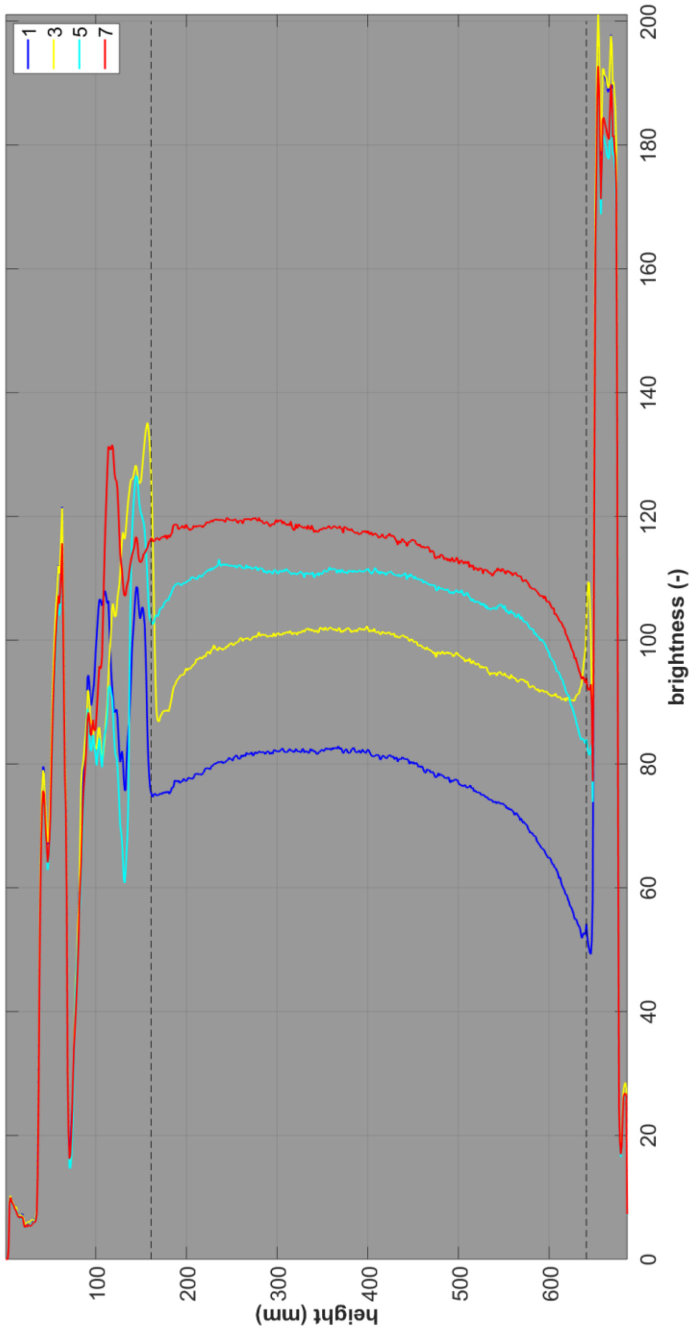

Figure 6.20. Brightness distribution over depth. Dotted lines define the net flow field

After careful preparation of the mixture adopting the procedure explained above, the case with sediment concentration of 10% and 20% of the small grain size d_{50} = 84 μm failed to reproduce a high-density current. The behavior of the resulted flow looked more like a plume and is captured in the pictures of Figure 6.21.

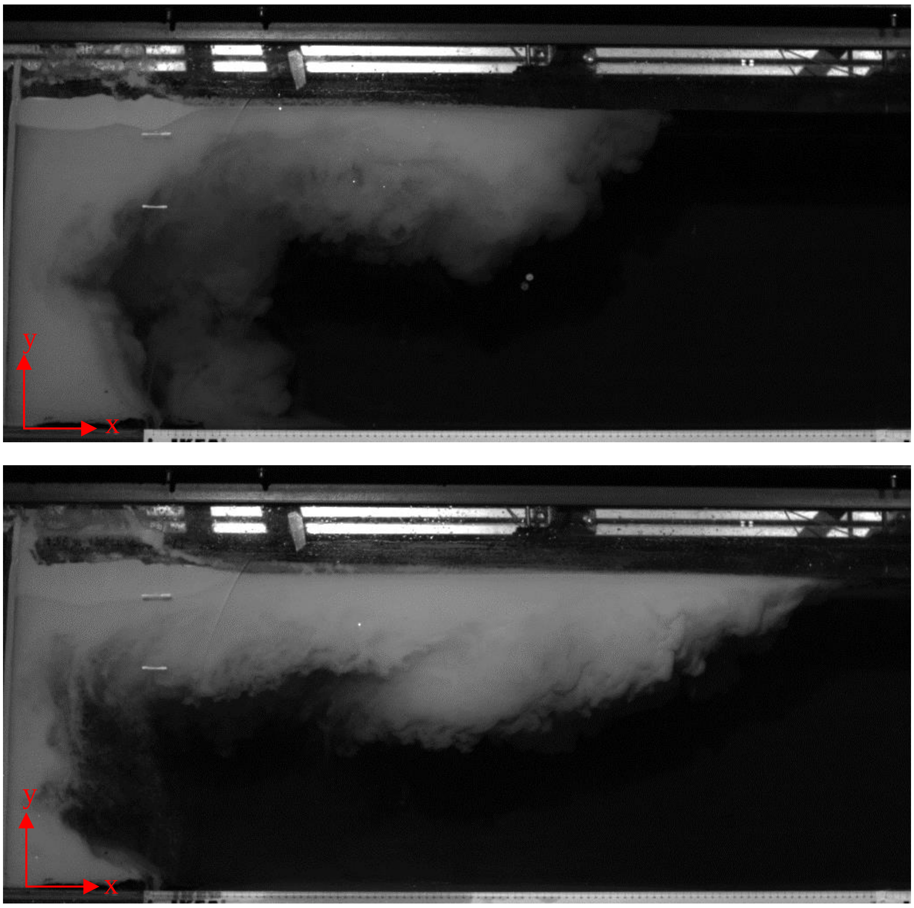

Figure 6.21. Snapshots from the experiments with sediment volumetric concentration of 10% (top) and 20% (bottom) and characteristic diameter of 84 μm.

As the small size of plastic polyurethane does not seem to work for this lock-exchange type of experiment, the larger grain size with a characteristic diameter of 169 μm has been tested in the same configuration. Figure 6.22 presents the time evolution of front velocity and position at the first 1000 mm after the release location. The velocity of the head of the current increases linearly until it reaches the value of 180 mm/s and then remains almost constant. In Figure 6.23, the downstream velocity profile of the flow at the location of the second transducer is presented for various time instances. The time instance t = 5.6 s, corresponds to the time in which the front of the current passes from the transducer's location. The measured velocity of the front, given by the UVP measurement, matches with the value obtained after image processing (see Figure 6.23). The velocity profiles at later time instances that correspond to the main body of the current, are decreasing as the current continues its propagation. As no external seeding occurs, the oscillations in the profiles near the top can be explained by the lack of particles in this region which prevents the transmitted ultrasound to be echoed back to the transducer.

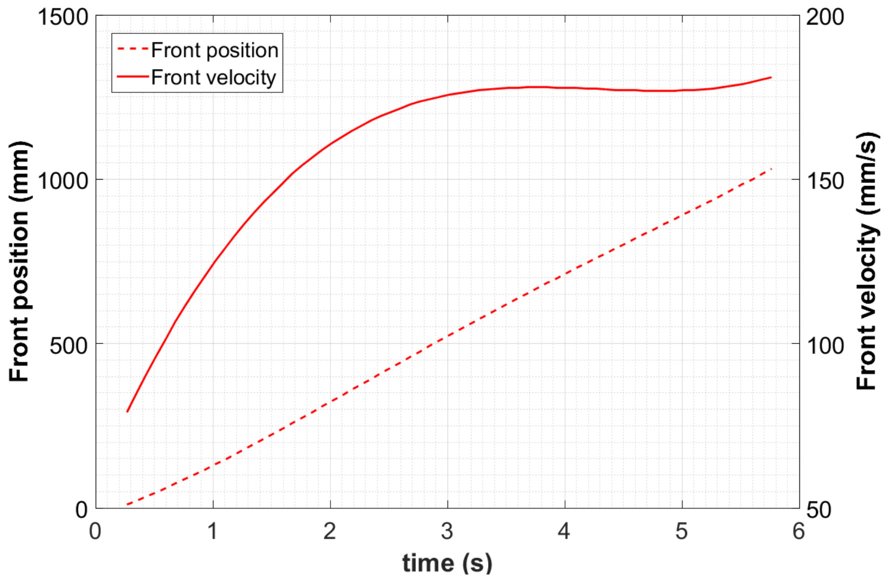

Figure 6.22. Time evolution of the front position (dashed line, left axis) and front velocity (dotted line, right axis).

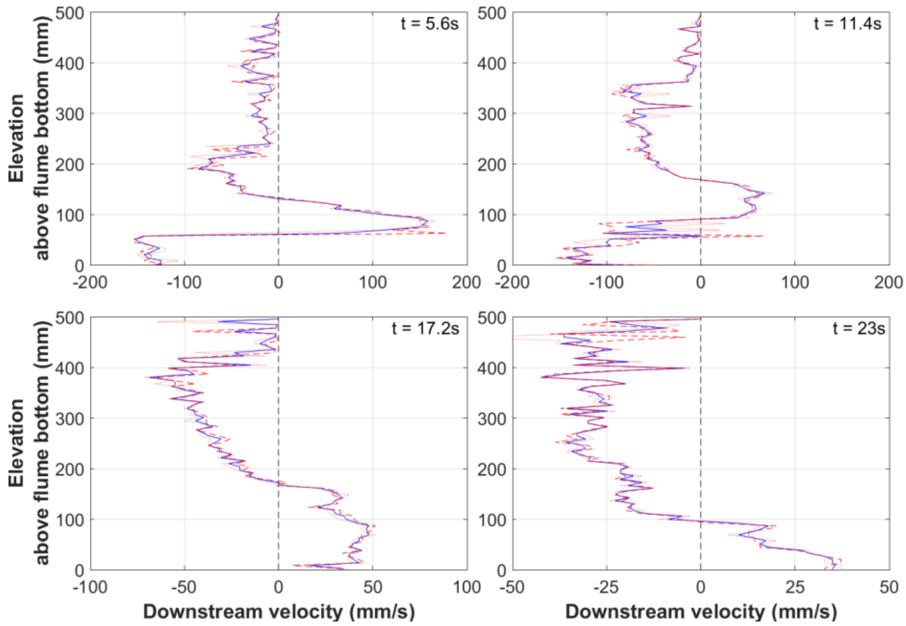

Figure 6.23. Downstream velocity profile at position x = 1000 mm.

Figure 6.24 and Figure 6.25 depict the comparison of the time evolution of the front position and velocity between the experiment with an initial polyurethane sediment concentration of 15% and the experiment with the same percentage of kaolin clay sediment along the first 1000 mm of the flume (see Section 6.6.1). The current generated from the slurry of kaolin clay develops almost double frontal velocity than the corresponding slurry of plastic sediment does. When the kaolin clay current reaches at the location x = 1000 mm keeps accelerating, while the one with the polyurethane sediment has stabilized its velocity. As it has been commented for Figure 6.9, in the experiment with kaolin clay a high velocity for fractions of a second immediately after the lowering of the gate is observed, which drops when the current is fully formed. Then, the front starts to accelerate.

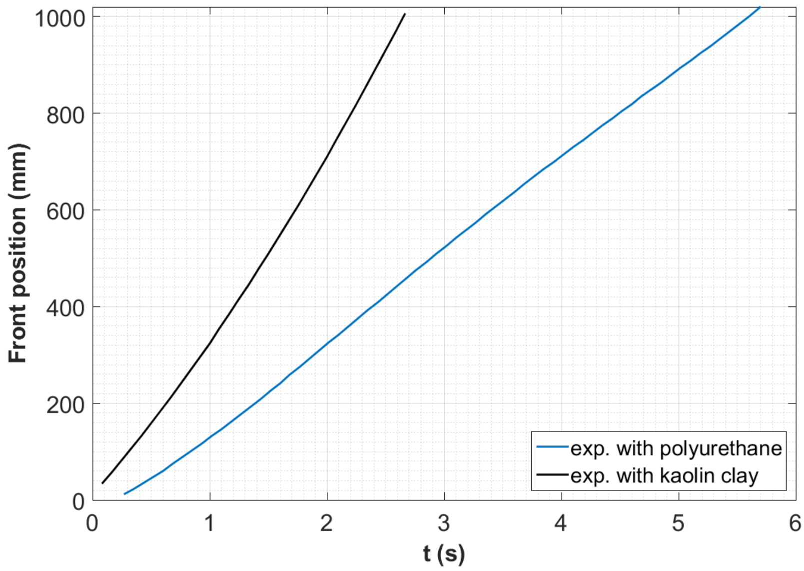

Figure 6.24. Comparison of the time evolution of the front position between the experiments with plastic polyurethane (blue line) and kaolin clay (black line).

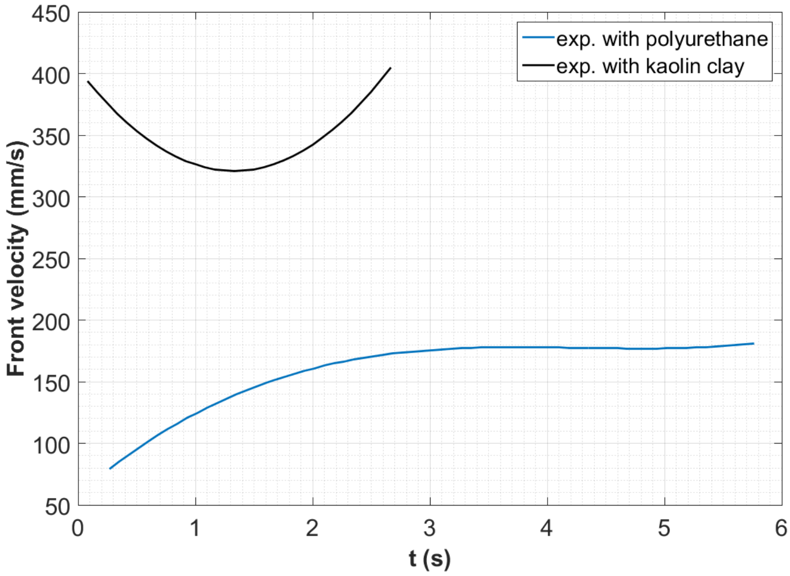

Figure 6.25. Comparison of the time evolution of the front velocity between the experiments with plastic polyurethane (blue line) and kaolin clay (black line).

6.7 Comparison of model SWBI2D and experiments

The two-layer computational model has been validated against analytical solutions for two different cases of idealized dam-break configurations in Section 3.5. In this section, the numerical results will be compared with the results obtained from the experiments with kaolin clay slurries.

The numerical model was tested in the same lock-exchange configuration as the experiments with kaolin clay slurries. Four simulations were set up in all of which the imposed debris flow density matched the initial density of the slurries with kaolin clay volumetric concentration of 1%, 2%, 3% and 15%, used for the experiments. The densities of the released volume of each numerical simulation are given in Table 6.1. The ambient fluid density ϱ_w is set to 1000 kg/m^3, which is a good approximation of pure water density that was used in the experiments.

The choice of the rheological properties of the released material that could better simulate the behavior of the kaolin clay-water slurry, was based on the combination of values, which resulted from rheological tests found in literature (e.g. Ilstad *et al.* (2004), Zakeri (2010)), and adjustments made on the parameters relying on the already obtained results from the experiments (see Table 6.1). Rheological tests of clay-rich submarine debris flows of high densities are usually presented in literature using mixtures of clay-water but also adding sand, while the presented experiments are ranging in lower density values.

Table 6.1. Rheological properties of the numerical simulations.

kaolin clay concentration	ρ_{DF}	τ_y	**K**	**n**
(%)	(kg/m^3)	(Pa)	(Pa·s^n)	(-)
1.0	1016	8.0	0.35	0.4
2.0	1032	10.0	0.35	0.4
3.0	1048	12.0	0.35	0.4
15.0	1242	12.0	0.35	0.4

The program SWBI2D is created to simulate dense debris flows transitioning to dilute turbidity currents. It manages well the case of the complete transformation of the debris flow and switches to a single turbidity current propagation mode, but with the initial condition of a released volume behaving as a debris flow.

Clay-water mixtures with clay concentration of 1%, 2% and 3%, correspond to densities of 1016, 1032 and 1048 kg/m^3 respectively. These values are better representing a turbidity current density. This fact can explain the weakness of the model to simulate precisely the cases of low initial sediment concentration. For the case of initial clay concentration of 15%, the comparison between the numerical and experimental results is more satisfying.

Snapshots of the comparison of the numerical simulation and kaolin clay experiment results are given in Figure 6.26-Figure 6.29.

In Figure 6.26, snapshots of the numerical simulation are compared with the corresponding experimental results in which the initial slurry had clay concentration of 1%. The total flow thickness could not be precisely predicted by the model. Despite the fact that the total flow thickness of the simulation did not match the one obtained by the experiment for all time instances, the front velocity was reproduced correctly by the model. At t = 3.6 s, the debris flow layer has been deposited, while the turbidity current layer is almost eliminated. This behavior is not representative of the reality. The produced current was very dilute and was propagating slowly until the end of the flume. This significant difference can be explained by the fact that the model reproduced the release of this dilute mixture using the debris flows equation, while its composition refers more to a turbidity current.

The behavior of the flow starts to be differentiated with the increase of clay content. In Figure 6.27, the simulated total flow thickness for the case of 2% of sediment concentration approaches the corresponding values of the real current. There is an overestimation of the front velocity which starts to reduce as the current propagates away from the gate. At t = 2.0 s, the front position of the numerical and experimental results matches.

The case with 3% of initial clay concentration depicted in Figure 6.28 failed to reproduce the behavior of the current at the first time instances after the release of the slurry. It is interesting to notice that when the current starts to be fully developed and is not affected by the release shock, the prediction by the model is significantly improved. The front velocity for both cases matches well, while the total flow thickness is comparable.

The density of 1242 kg/m^3 for the slurry of 15% clay concentration, is significantly higher than those of the other cases which are ranging between 1010 and 1050 kg/m^3. After choosing the proper rheological parameters (τ_y, K, n) , the slurry could be considered as representative of a debris flow. This can explain that the comparison of the numerical simulation and the laboratory test results is quite satisfying. The reproduction of front velocities and total flow thickness matches with the corresponding values of the experiment. The main difference is observed downstream the gate where the model shows the occurrence of a thin layer of debris flow deposited (see Figure 6.29), while the entire initial volume was incorporated in the propagating current in the physical test.

The UVP method used in the experiments provided longitudinal velocity profiles along depth at three locations of the flume. The model calculates depth-averaged velocities in the streamwise and spanwise direction. A comparison between the two is not considered efficient enough in order to lead to precise conclusions.

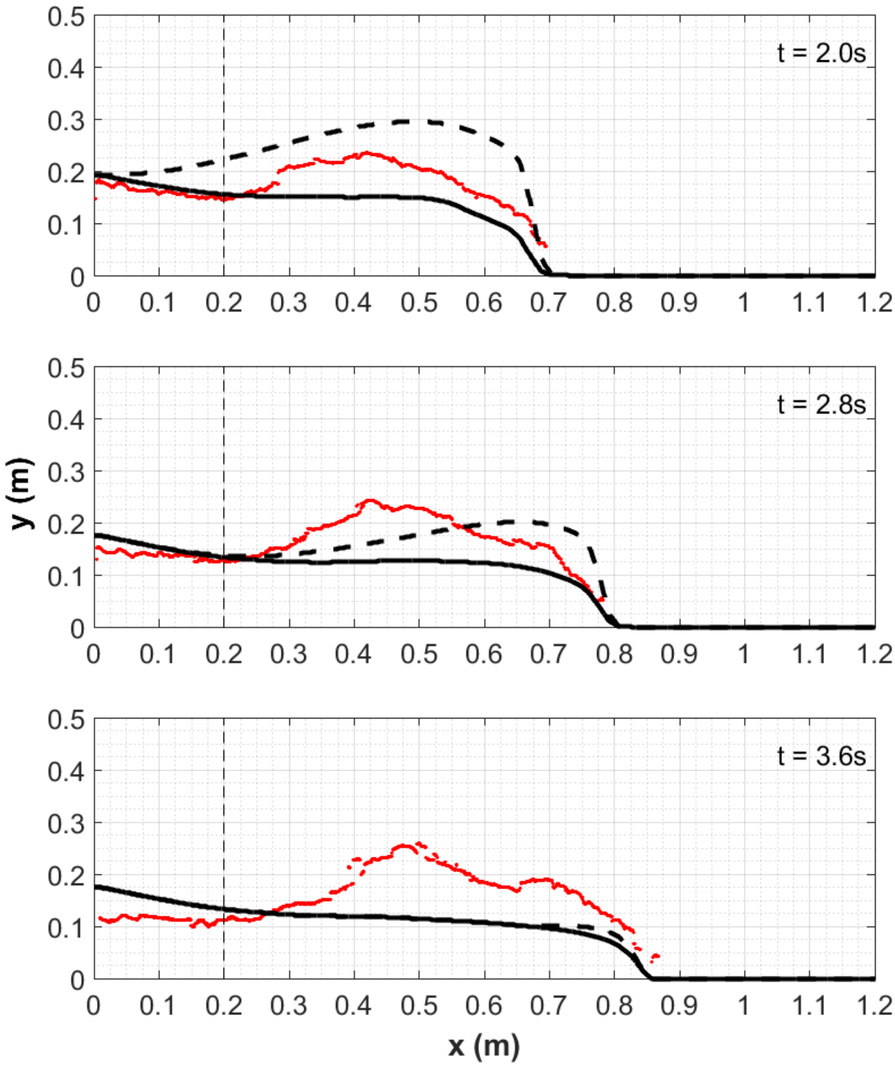

Figure 6.26. Comparison of numerical results with the experiments with kaolin clay concentration of 1% at selected time instances. Black solid line corresponds to the dense basal layer, black dashed line corresponds to the upper turbidity current layer and red dots correspond to the experiment results after image processing.

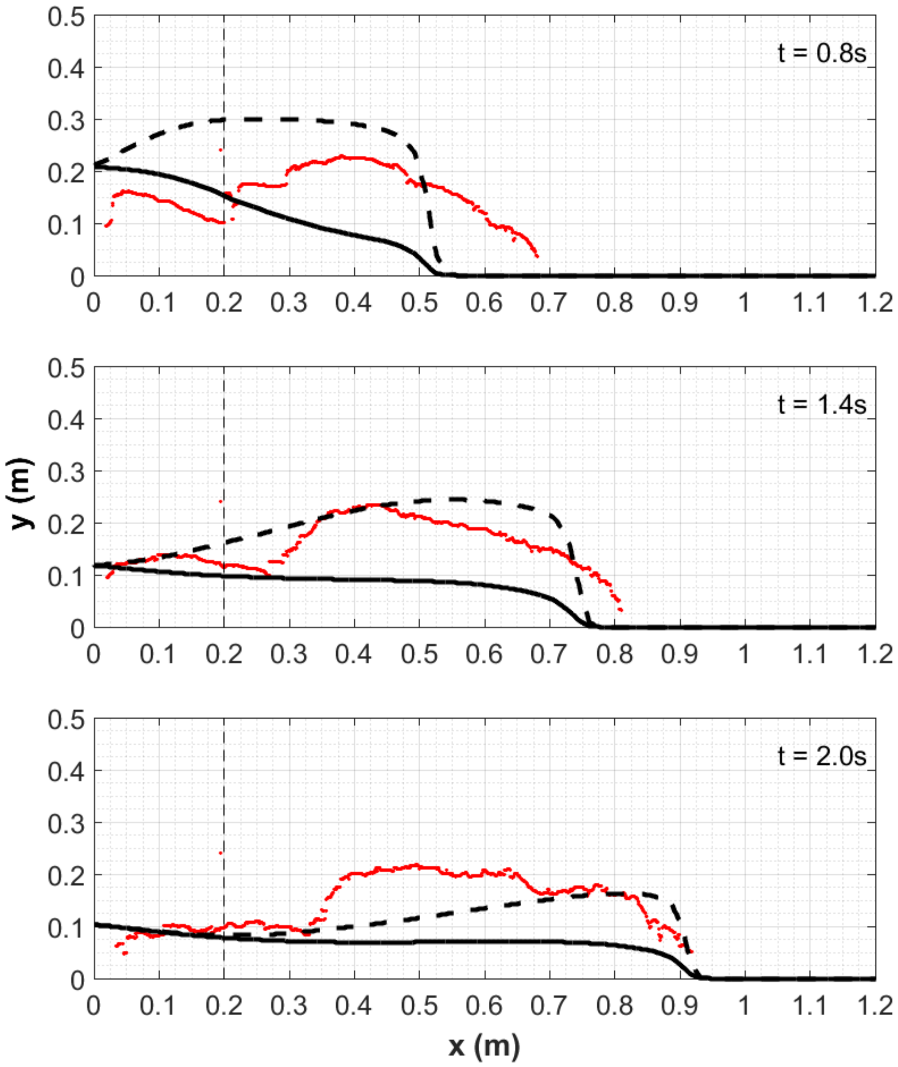

Figure 6.27. Comparison of numerical results with the experiments with kaolin clay concentration of 2% at selected time instances. Black solid line corresponds to the dense basal layer, black dashed line corresponds to the upper turbidity current layer and red dots correspond to the experiment results after image processing.

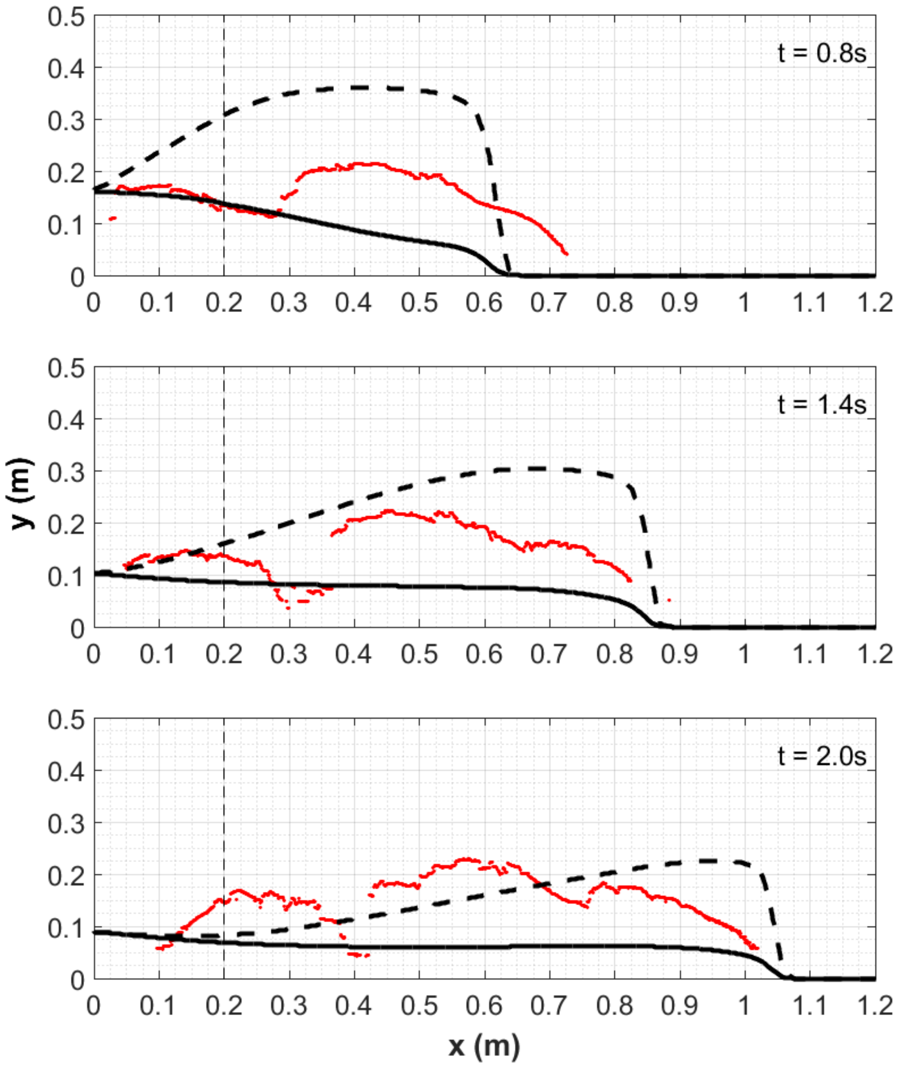

Figure 6.28. Comparison of numerical results with the experiments with kaolin clay concentration of 3% at selected time instances. Black solid line corresponds to the dense basal layer, black dashed line corresponds to the upper turbidity current layer and red dots correspond to the experiment results after image processing.

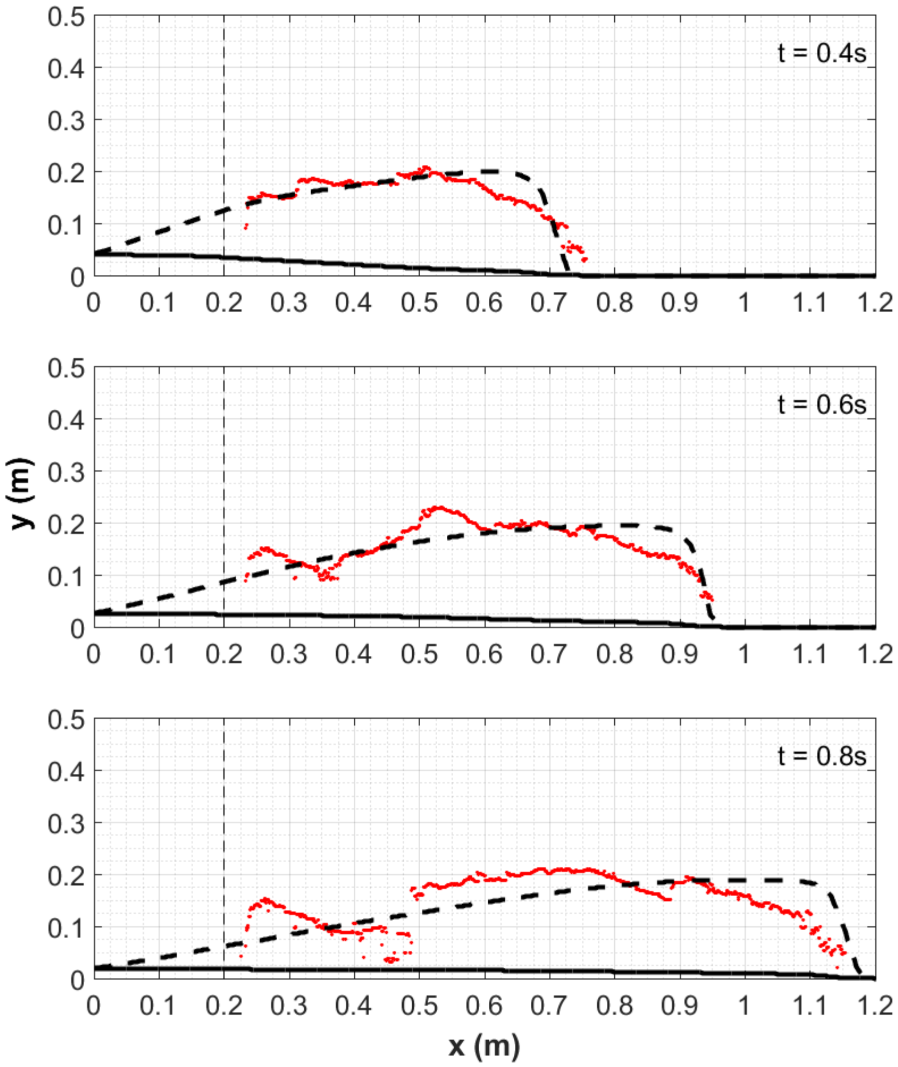

Figure 6.29. Comparison of numerical results with the experiments with kaolin clay concentration of 15% at selected time instances. Black solid line corresponds to the dense basal layer, black dashed line corresponds to the upper turbidity current layer and red dots correspond to the experiment results after image processing.

6.8 Summary

A series of lock-exchange experiments were conducted to investigate the behavior of kaolin clay-water slurries for sediment volumetric concentrations of 1%, 2%, 3% and 15%. The flow was observed using two cameras located at different distance and two UVP transducers that measured velocity profiles in the vertical axis in a distance of 0.5 m and 1m from the gate, respectively.

Results suggest that the addition of sediment mass in the released material leads to higher velocities of the front and the body of the flow. This increase seems to follow a parabolic distribution depending on the sediment volumetric concentration φ_i. UVP measurement indicated maximum velocities at the location positions, ranging from 100 mm/s to 200 mm/s from the slurries with φ_i equal to 1%, 2% and 3%. The UVP measurement for the 15% slurry was not satisfactorily as the ultrasonic waves did not manage to penetrate in the whole depth of the current as it was much denser than in the other tests. According to image processing, the head of the slurry with φ_i of 15% reached the maximum velocity of 600 mm/s and the total propagation time after the release was 5 s.

The lock-exchange type of experiment has been chosen as its idealized-design of initial conditions provide clear-cut situations ideally suited for the validation and testing of numerical models. Results were satisfactorily compared with a numerical simulation of the corresponding lock-exchange case using SWBI2D. This work could also provide sufficient information that can be used as a benchmark for comparison and validation, by future modellers.

Chapter 7 Runout of submarine landslide on real bathymetry

7.1 Introduction

The two-layer numerical model developed in this work, aims to simulate a large scale event in which the subaqueous mass movement leads to the development of a debris flow followed by the partial or total transition to a turbidity current that occurs in deep-sea environments.

The model is validated by comparison to known solutions in Chapter 3 and tested in an idealized bathymetry for a small scale event in Chapter 4. In Chapter 7 the behaviour of the depth-averaged two-layer model is tested in a more complex case of a large scale event. For this scenario, a location was selected on the edge of the Australian continental shelf, approximately 130 km north-west of Perth, near the vast Perth Canyon. At this location, the shelf break is characterized by evidence of massive failures of the canyon head region. Following these canyon-forming failures, there are indications of retrogressive, slab-like failures of the top soils situated on top of the escarpment. Even these latter failures, however, remain massive, characterized by thicknesses of several tens to a few hundred meters. Water depths vary from around 1600 m at the shelf break through to 3900 m at the base of the escarpment over a horizontal distance of only around 15 km.

7.2 Initial conditions

For this analysis, one of the smaller slope failures was reconstructed by extrapolating surrounding topography contours, and the resulting volume of soil (around 0.5 km^3) was used as the source volume for the simulation. This resulted in a variable initial thickness, varying to a maximum of about 25 m (Figure 7.1).

Downslope of the source region, the remnants of a larger failure are apparent, followed by a gradual slope towards the bottom of the escarpment.

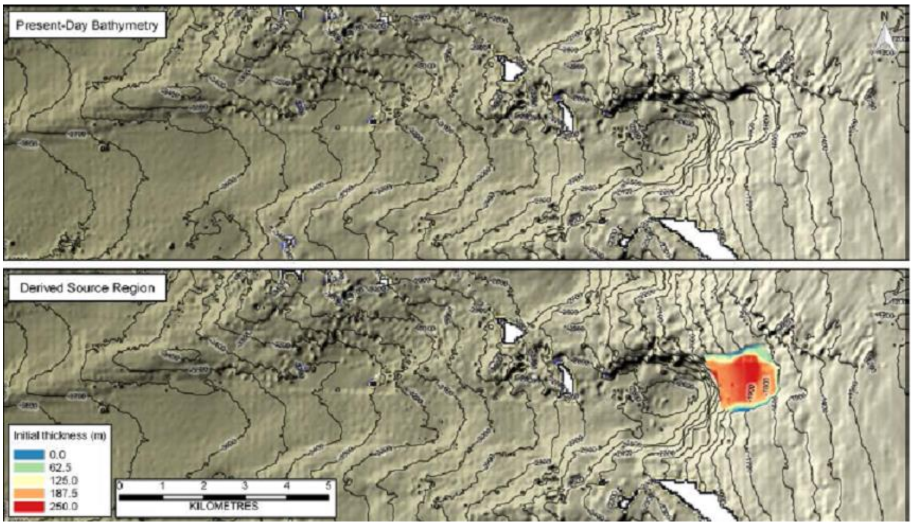

Figure 7.1. Large scale event situation.

7.3 Rheological model

Due to the velocities likely to be achieved during submarine mass movements in the Australian shelf area, these slides will occur in an undrained manner - the density of the slide material will remain constant and the slide material can be treated as a single phase. The most appropriate soil rheology model for slides with these characteristics is the non-linear Herschel-Bulkley soil model (Herschel and Bulkley, 1926). The governing equations of this model are given in Chapter 2.

In the absence of rheology testing on soil samples taken from this region, the viscosity parameters were assumed to follow viscoplastic behavior. The rheological parameters used for this simulation are given in Table 7.1.

The detrainment coefficient e_d was set to 0.001 and the friction coefficient C_d was set to 0.005.

Table 7.1. Rheological parameters.

Input parameters	
ρ_{DF}	1400 kg/m^3
ρ_w	1025 kg/m^3
ρ_{sed}	2650 kg/m^3
d_{50}	80 μm
τ_y	1200 Pa
K	90 Pa·s^n
n	0.3

7.4 Computational mesh

The model relies on an unstructured mesh for the presentation of the bathymetry. The computational mesh is generated using mesh generator GMSH. This generator provides capability for local mesh refinement in the area of the anticipated runout and along steeper slopes and/or channelised areas, so as to achieve best accuracy in the area of interest. The cell size is decreasing until it reaches the area around the source and the estimated runout area.

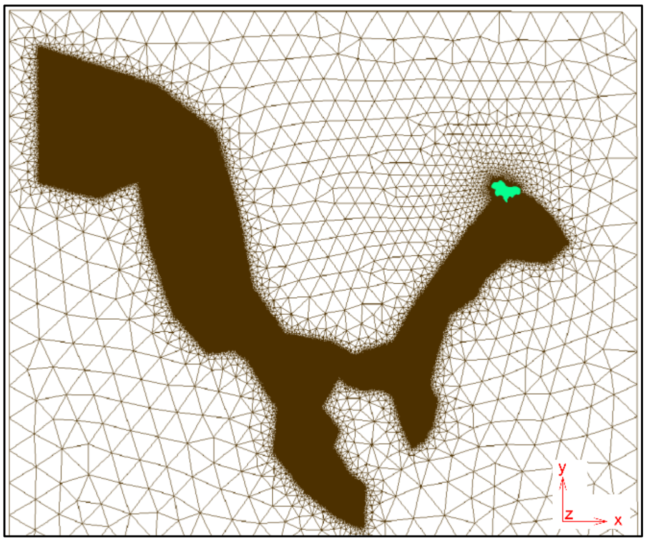

Figure 7.2. Mesh of the computational domain.

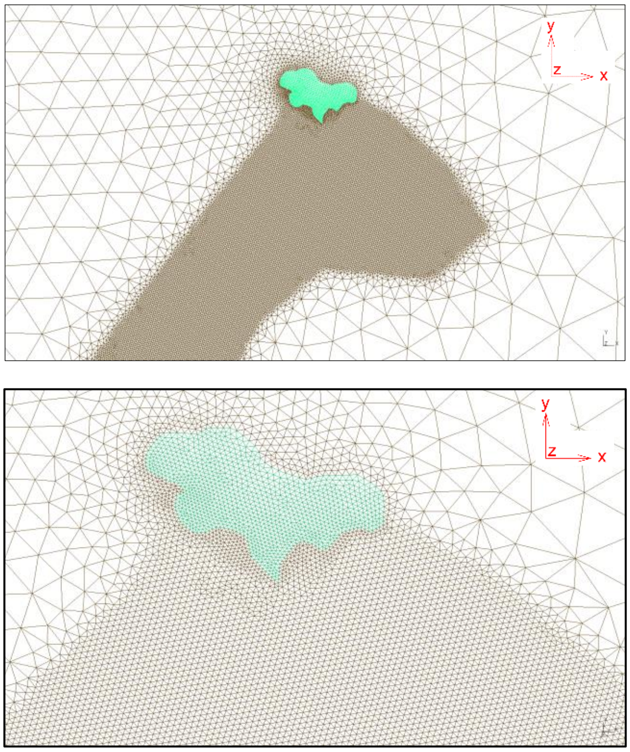

Figure 7.3. Details of the mesh around source and runout area.

7.5 Results

The different flow dynamics illustrated on the idealized scenario of Chapter 4, were also illustrated in a more complex case. The source has an irregular profile, suggesting a complex side topology. The failure is considered as a single event.

Eight cross-sections have been selected for the presentation of the time evolution of the flow thickness of the debris flow layer and the developed turbidity current layer. The location of the selected cross-sections is depicted in Figure 7.4.

From Figure 7.5 to Figure 7.11, the flow thickness profiles of the two layers are illustrated on the bathymetry of each cross-section. At the bottom of each figure, the top view of the flow is given for the corresponding time instance. At t = 500 s, the turbidity is already generated on top of the debris flow due to detrainment. At later time instances, the turbidity current is detached from the basal layer and is expanding its propagation in all directions. At the end of the simulation at t = 3000 s, only a thin layer of debris flow has remained and deposited in cross-sections T3 and L2, as it is constant from previous time instances. The maximum height observed for the turbidity current is around 180 m.

Figure 7.12 to Figure 7.14 show the sediment concentration distribution of the turbidity current along each selected cross-section at various time instances. It is observed that that the sediment concentration of the generated turbidity current ranges from 2 to 3%.

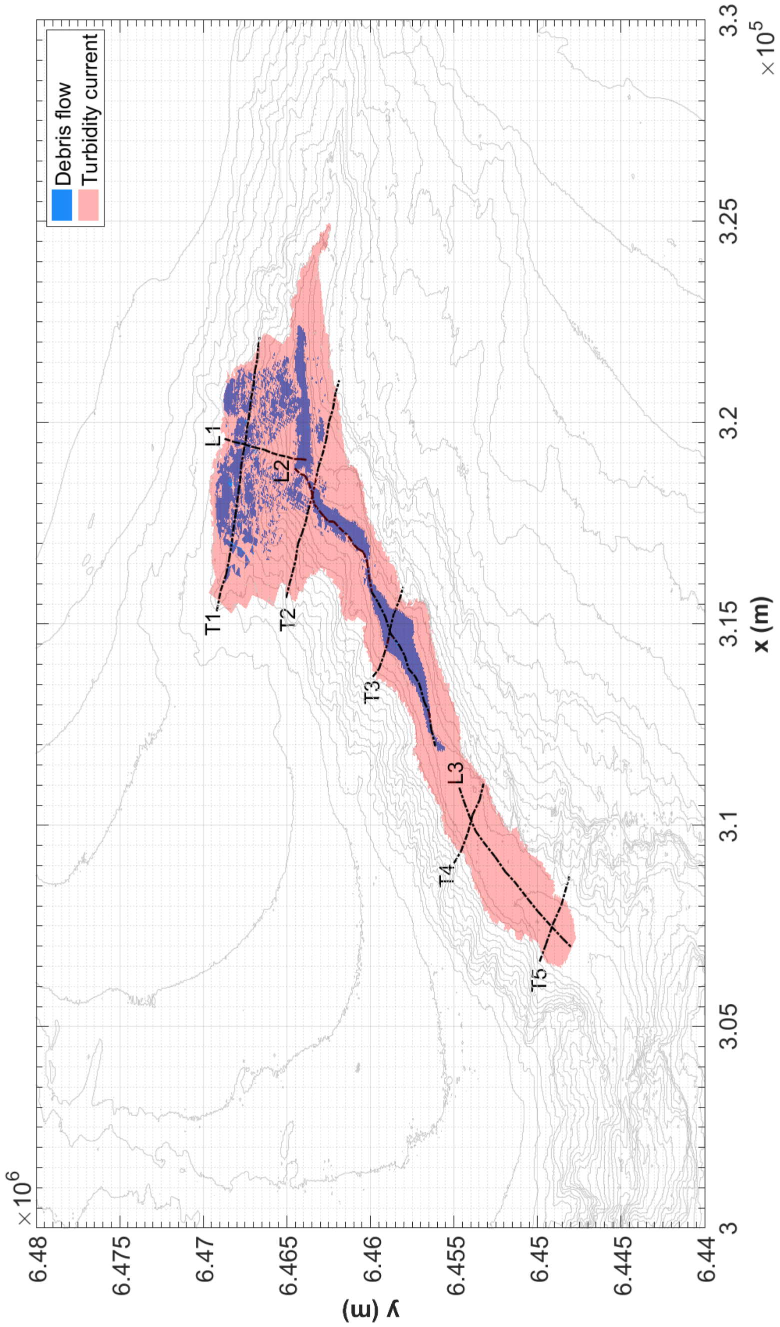

Figure 7.4. Location of the selected cross-sections.

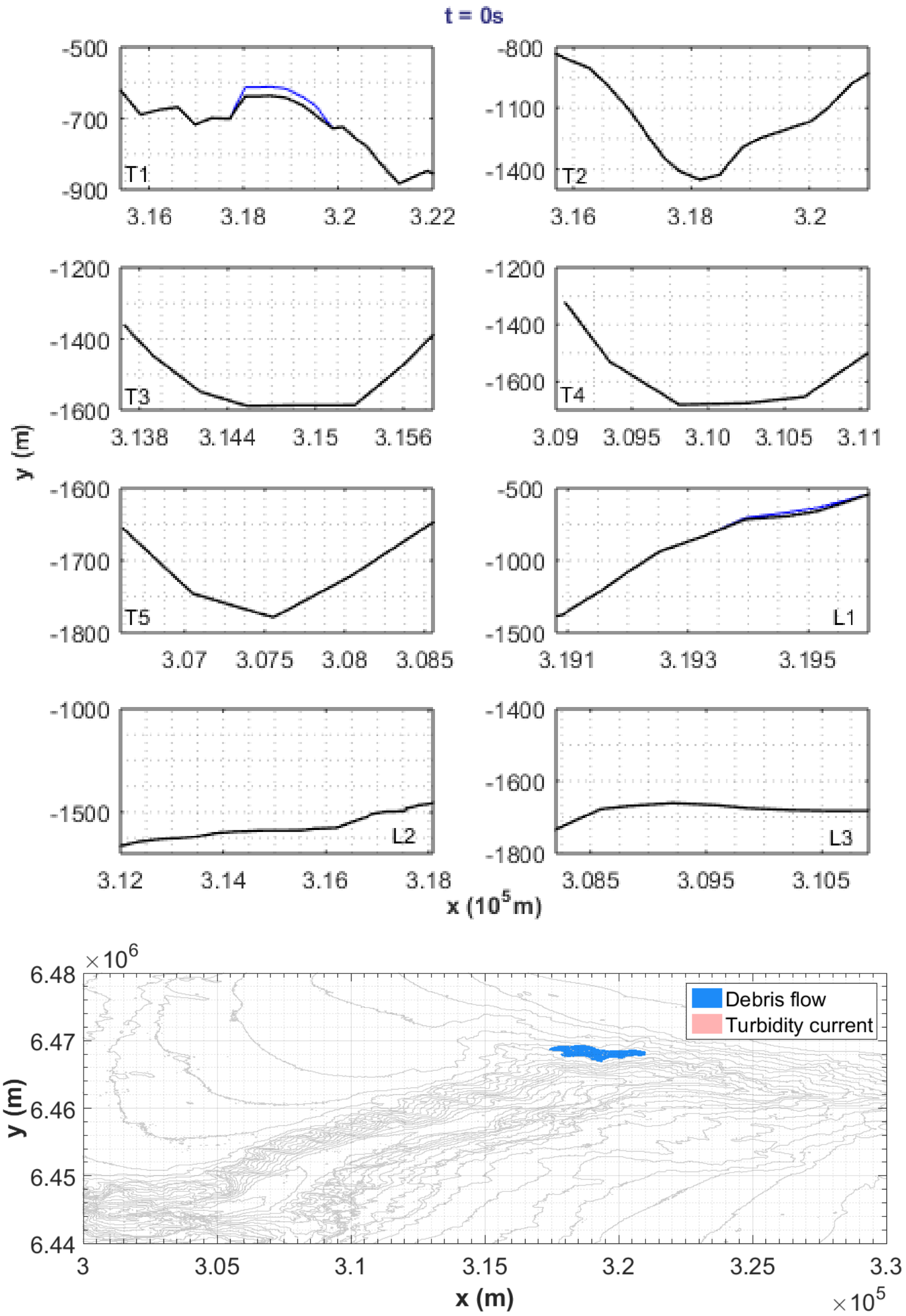

Figure 7.5. Flow thickness at selected cross sections at instant t = 0 s. Blue line corresponds to the debris-flow layer and red line to turbidity current layer.

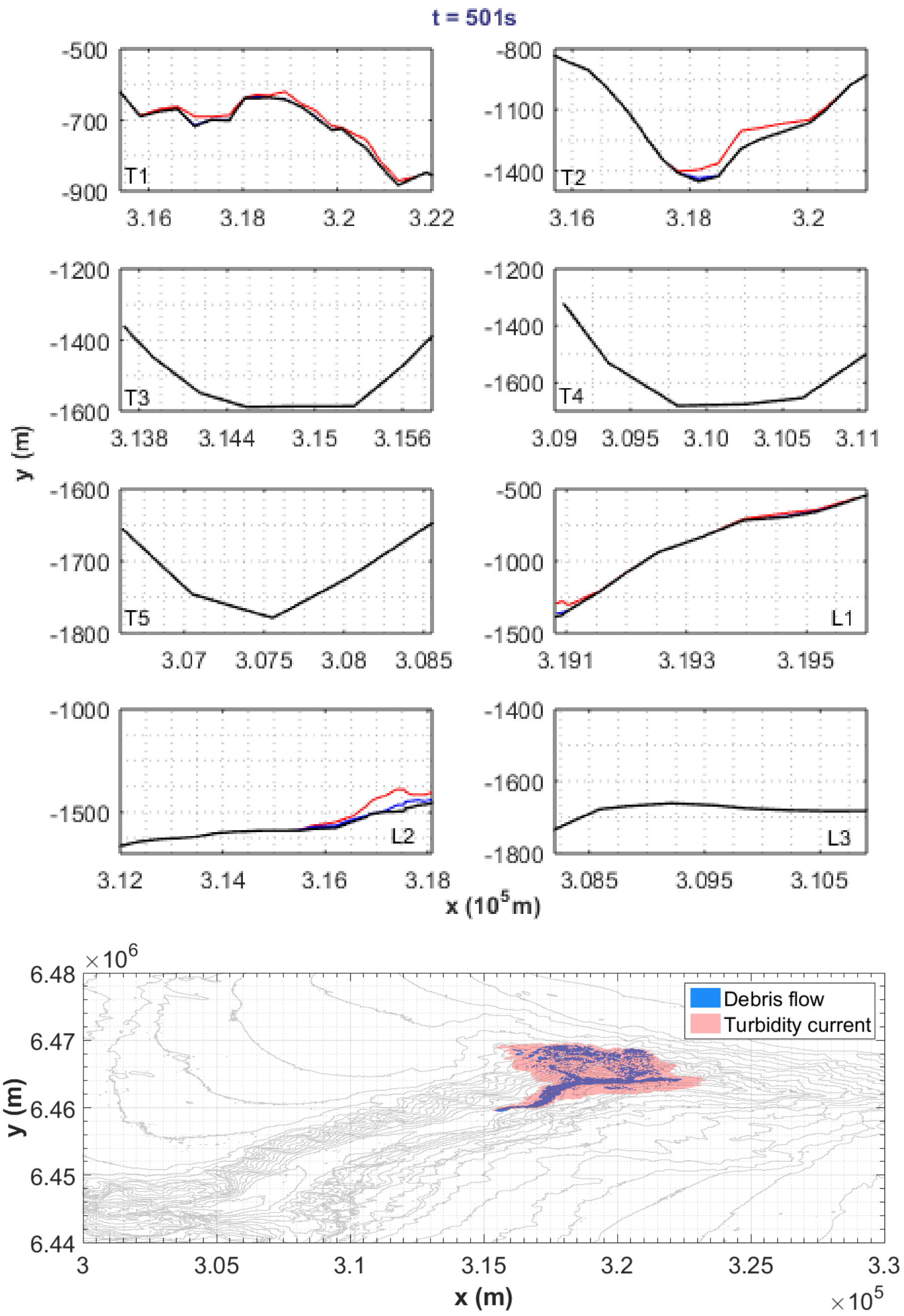

Figure 7.6. Flow thickness at selected cross sections at instant t = 501 s. Blue line corresponds to the debris-flow layer and red line to turbidity current layer.

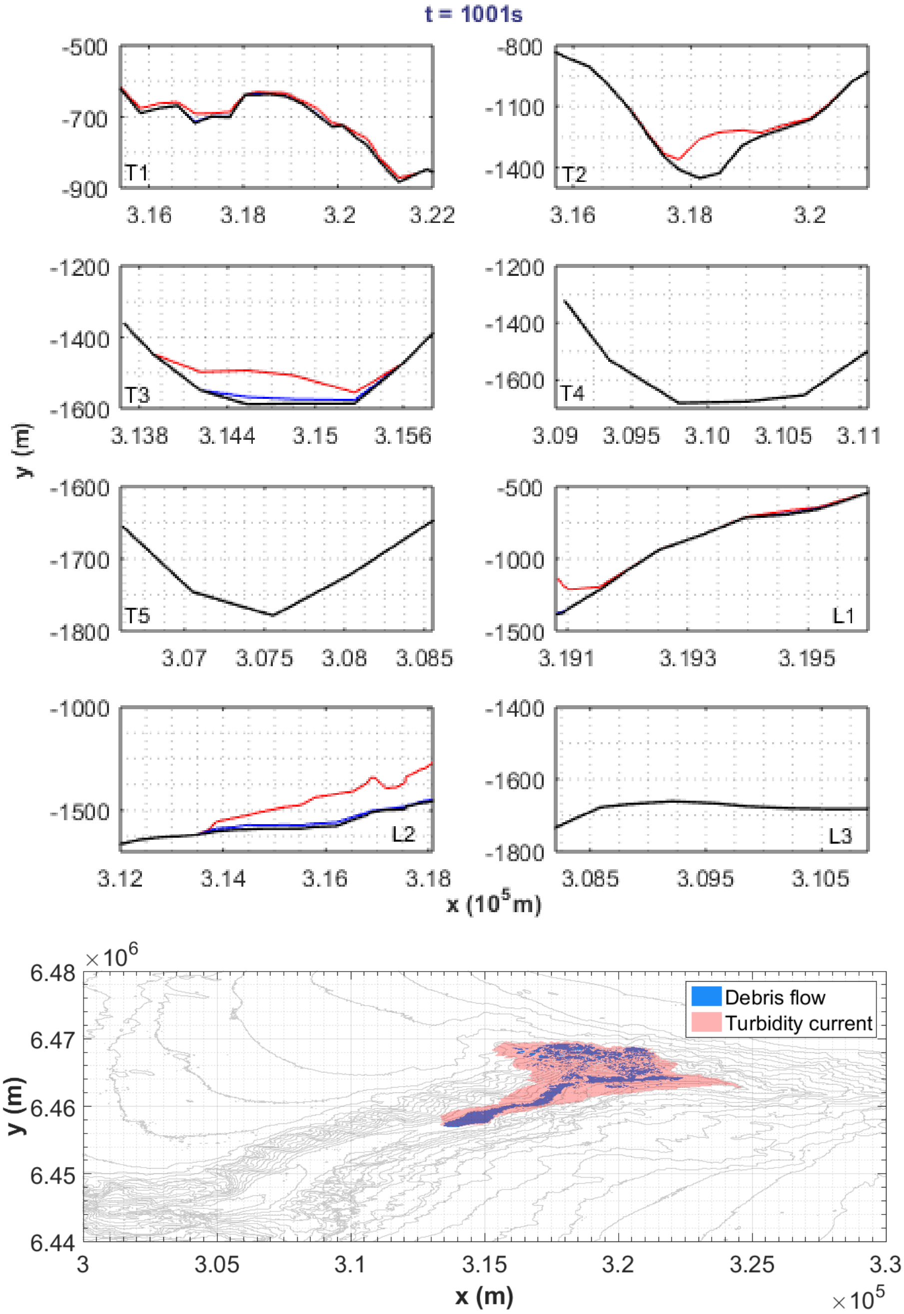

Figure 7.7. Flow thickness at selected cross sections at instant t = 1001 s. Blue line corresponds to the debris-flow layer and red line to turbidity current layer.

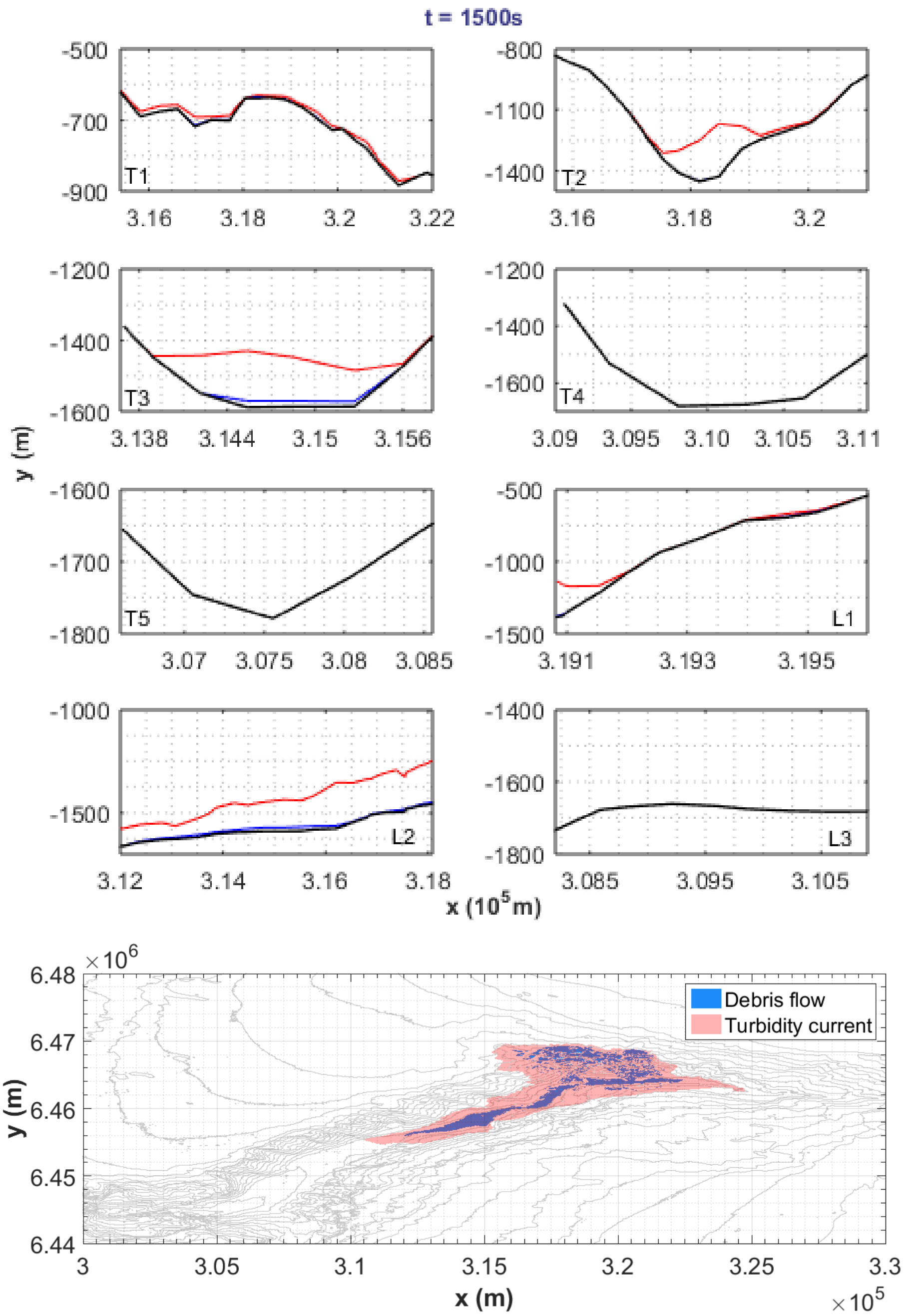

Figure 7.8. Flow thickness at selected cross sections at instant t = 1500 s. Blue line corresponds to the debris-flow layer and red line to turbidity current layer.

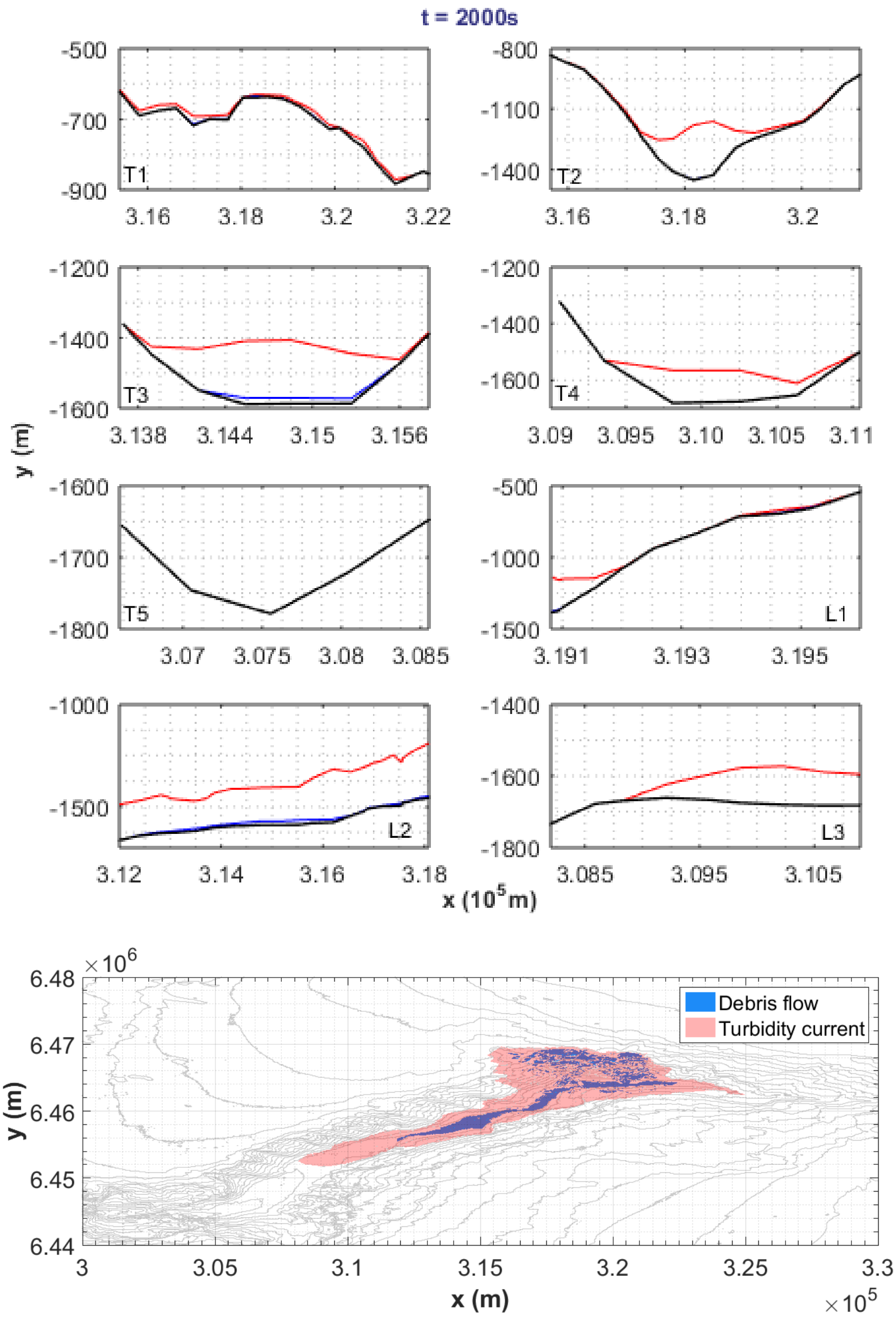

Figure 7.9. Flow thickness at selected cross sections at instant t = 2000 s. Blue line corresponds to the debris-flow layer and red line to turbidity current layer.

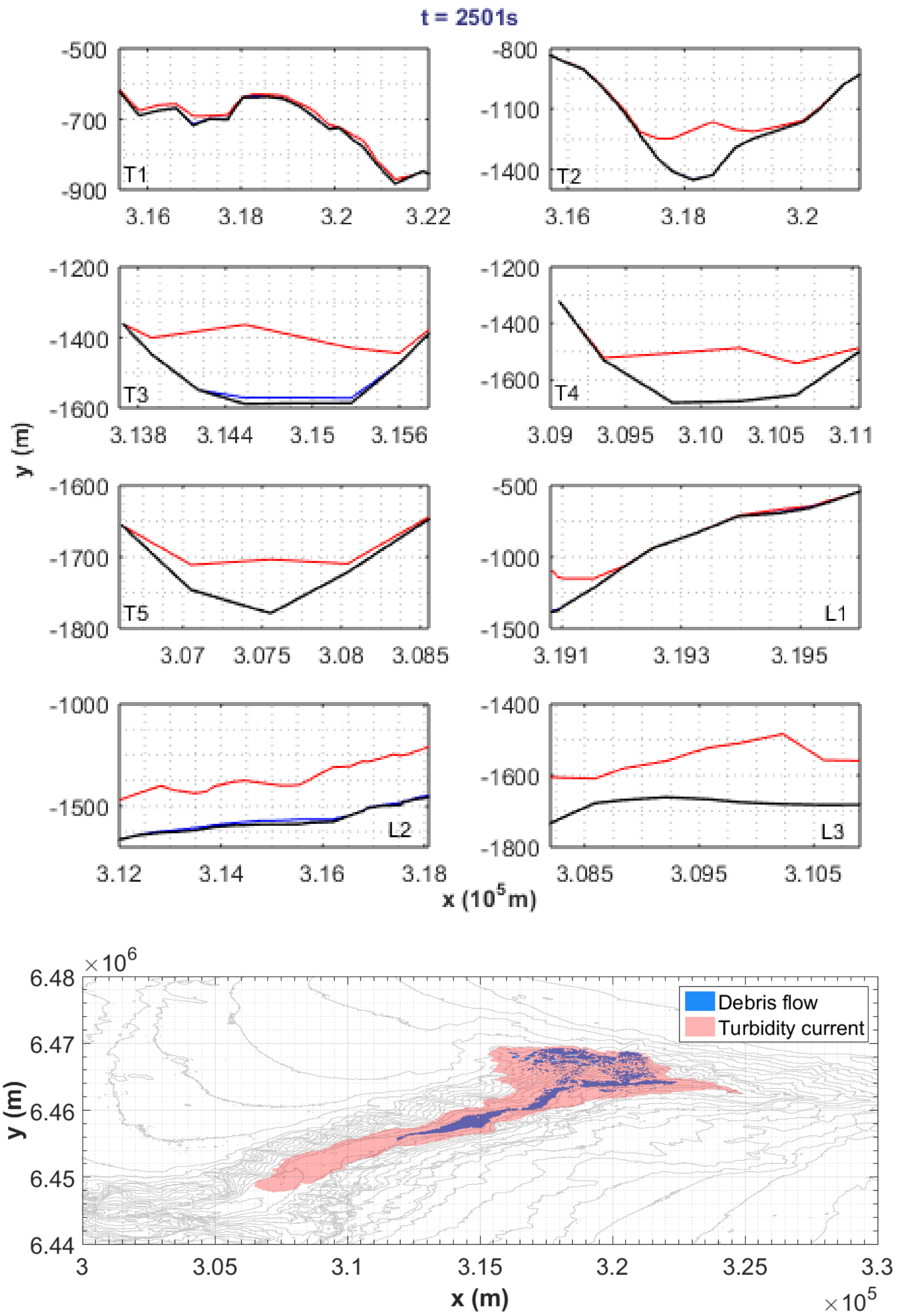

Figure 7.10. Flow thickness at selected cross sections at instant t = 2501 s. Blue line corresponds to the debris-flow layer and red line to turbidity current layer.

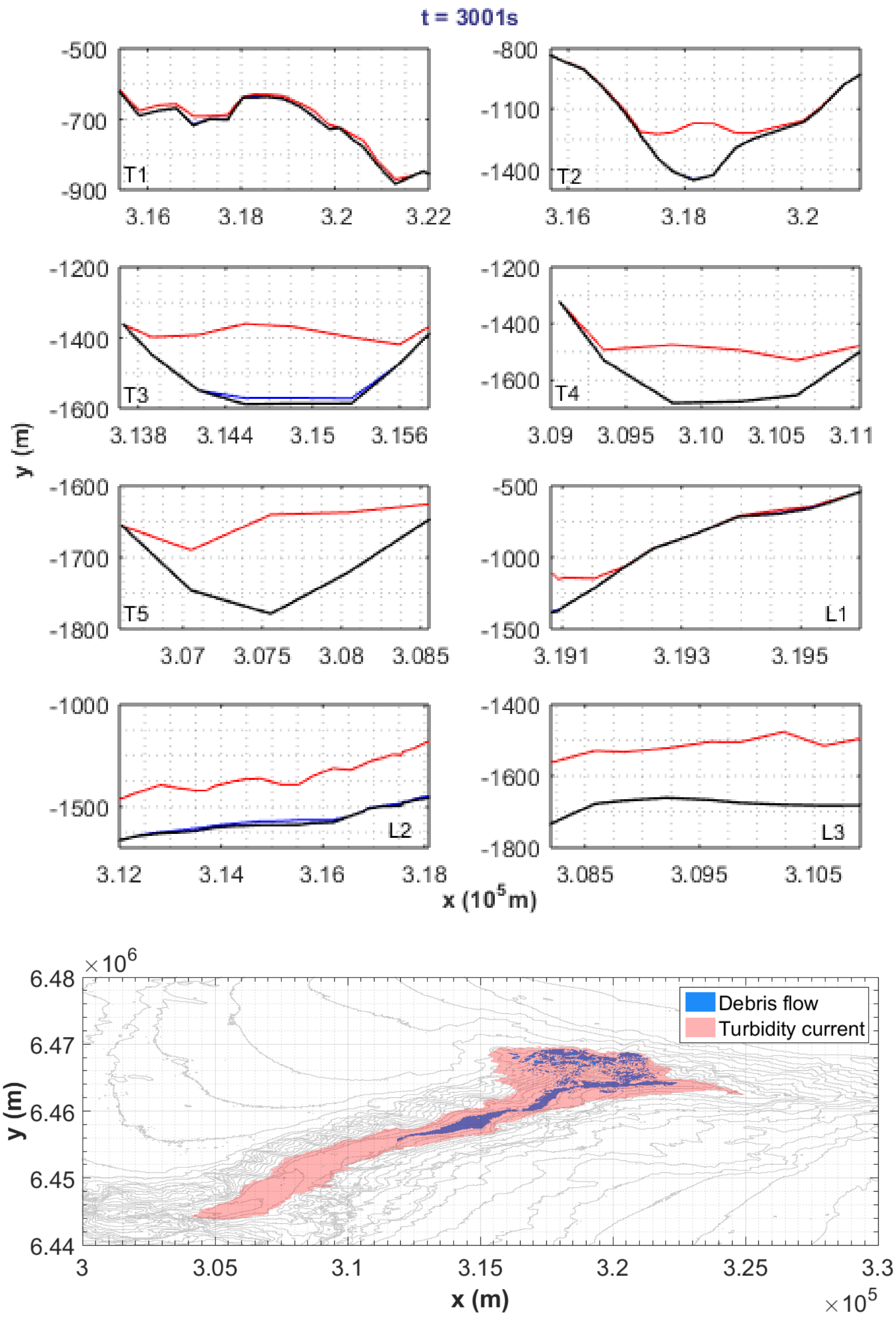

Figure 7.11. Flow thickness at selected cross sections at instant t = 3001 s. Blue line corresponds to the debris-flow layer and red line to turbidity current layer.

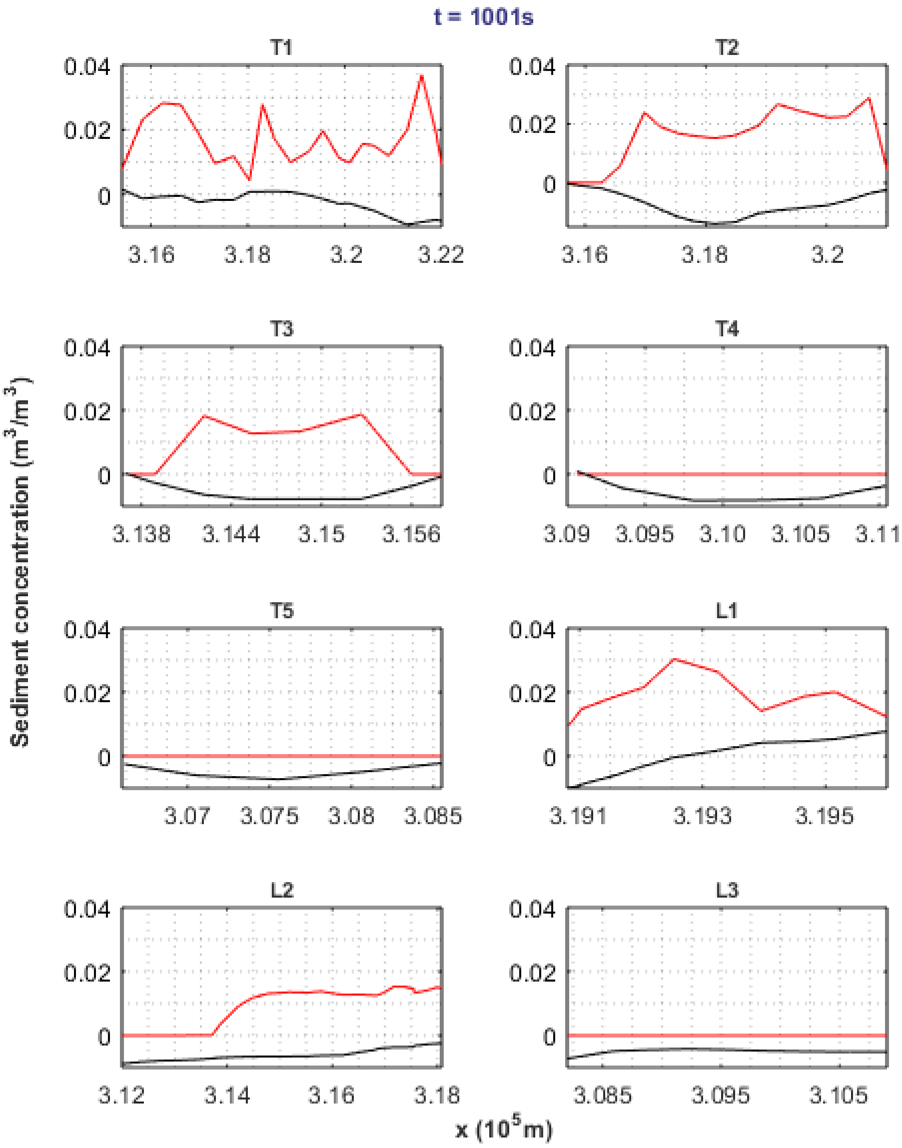

Figure 7.12. Sediment concentration of the turbidity current layer (red line) at selected cross-sections at instant t = 1001 s.

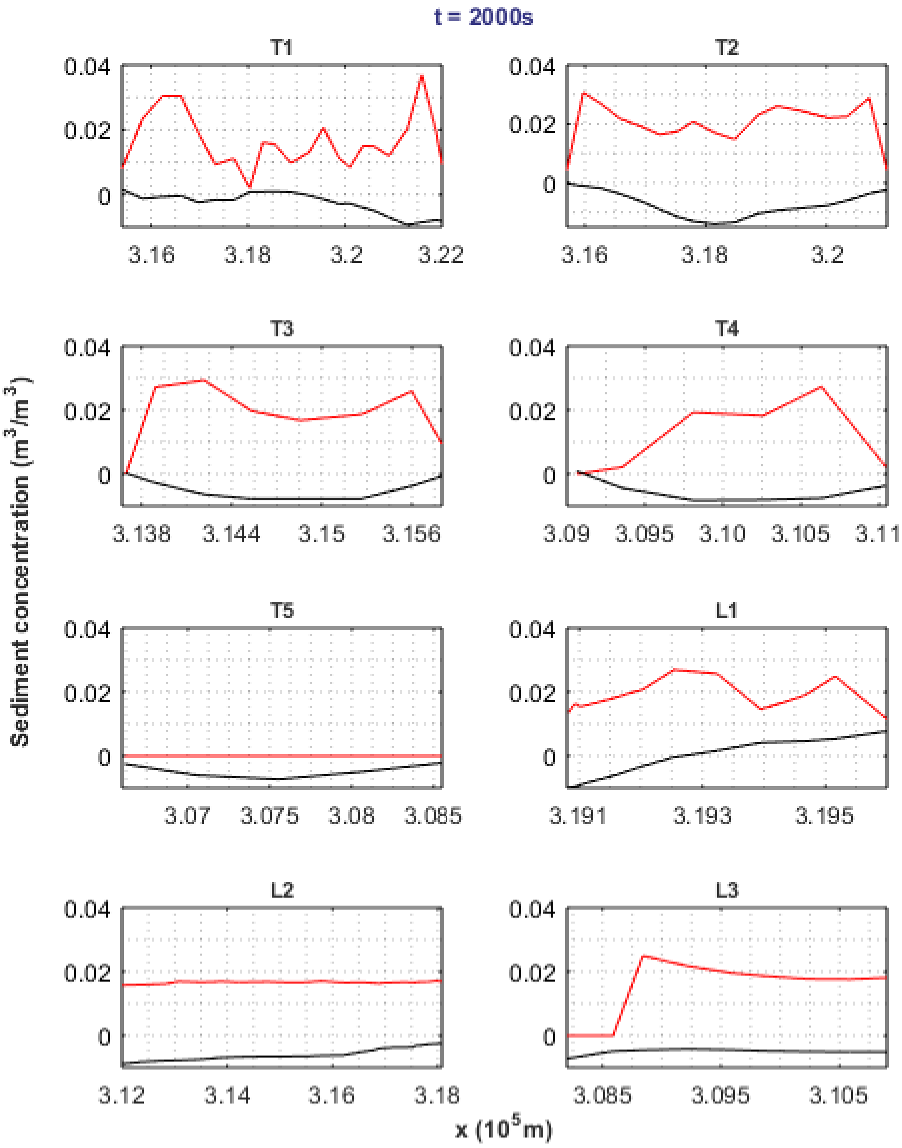

Figure 7.13. Sediment concentration of the turbidity current layer (red line) at selected cross-sections at instant t = 2000 s.

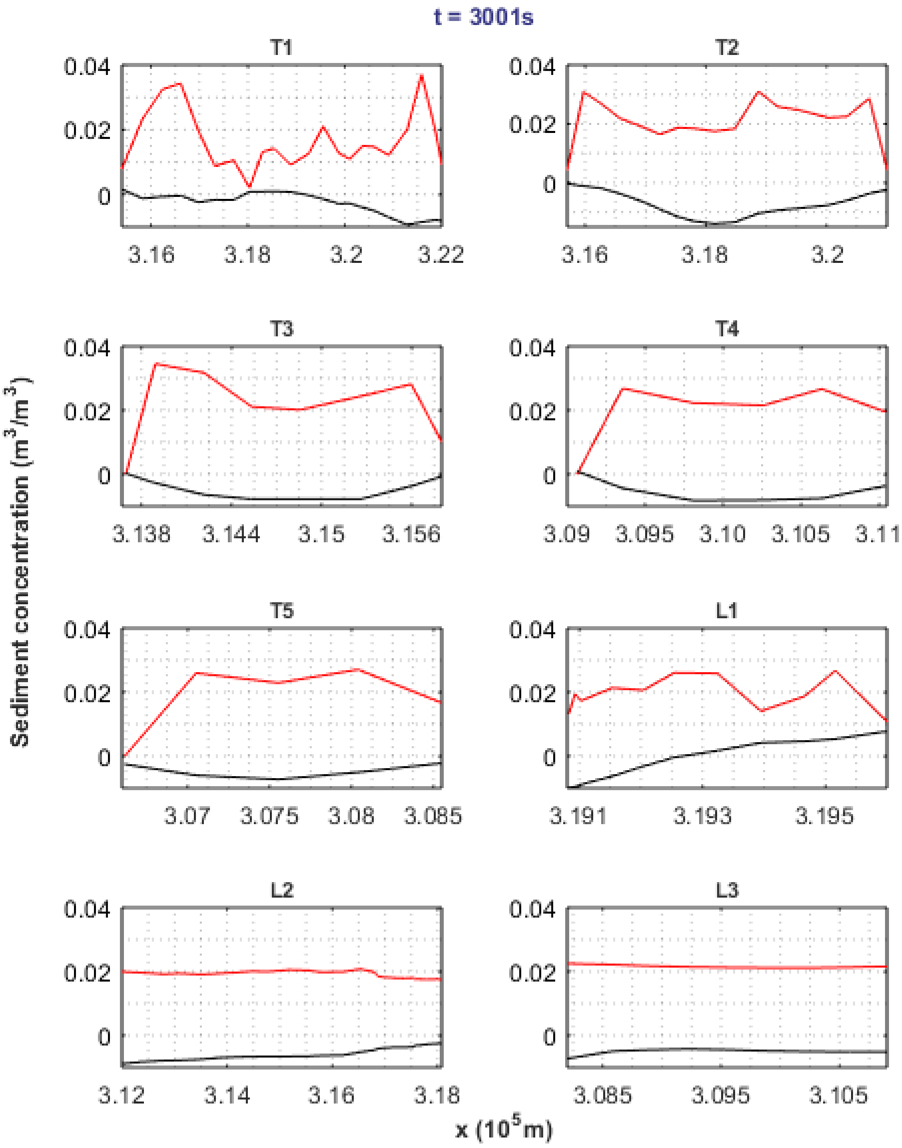

Figure 7.14. Sediment concentration of the turbidity current layer (red line) at selected cross-sections at instant t = 3001 s.

The velocity map of the debris flow layer at various simulation time instances is given in Figure 7.15 to Figure 7.20. As the initial volume flows downslope, velocities from 20 to 42 m/s are developed. When the slope begins to decrease, the debris flow decelerates and after propagating for around 8 km in the canyon, it has already stopped at t = 1200 s.

The velocity history of the turbidity current is presented from Figure 7.21 to Figure 7.26. At the first stage, the turbidity current is mainly confined to the debris flow area and propagates with much lower velocity. At t = 250 s, the maximum velocity observed is 14 m/s for the turbidity current, while the corresponding maximum velocity for the debris flow is 42 m/s. After t = 500 s, the behaviour of the two layers starts to significantly change. The debris flow starts to decelerate and stops, while the turbidity current continues its propagation down the canyon in both longitudinal and transversal directions, while simultaneously detraining the debris flow deposits (see Figure 7.8 Figure 7.11). At the end of simulation that is translated in 3000 s after the initial volume release, the turbidity current keeps propagating with maximum velocity ranging from 6 to 13 m/s.

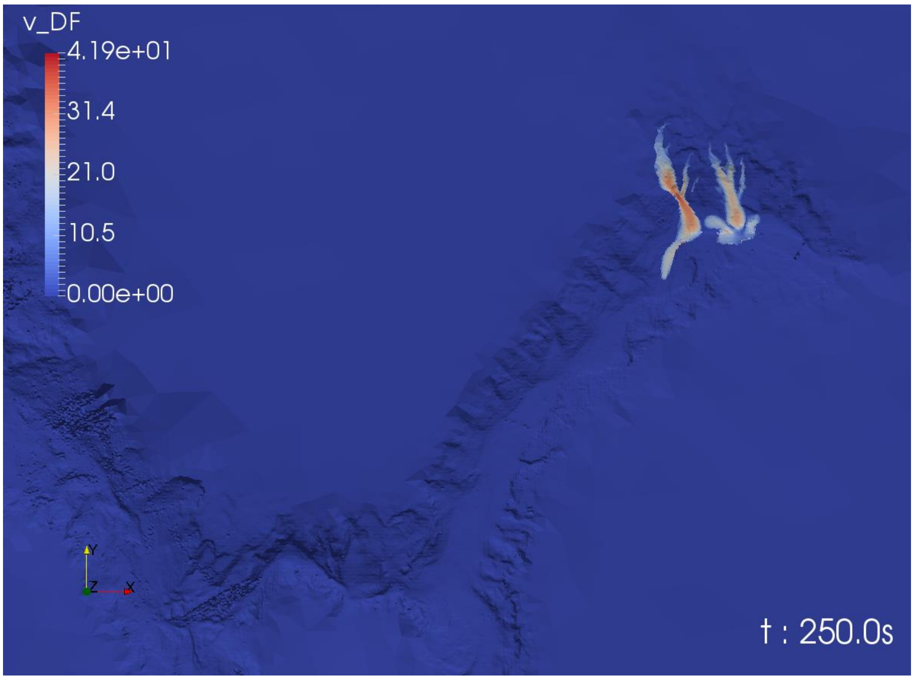

Figure 7.15. Velocity in m/s of the debris flow layer at instant t = 250 s.

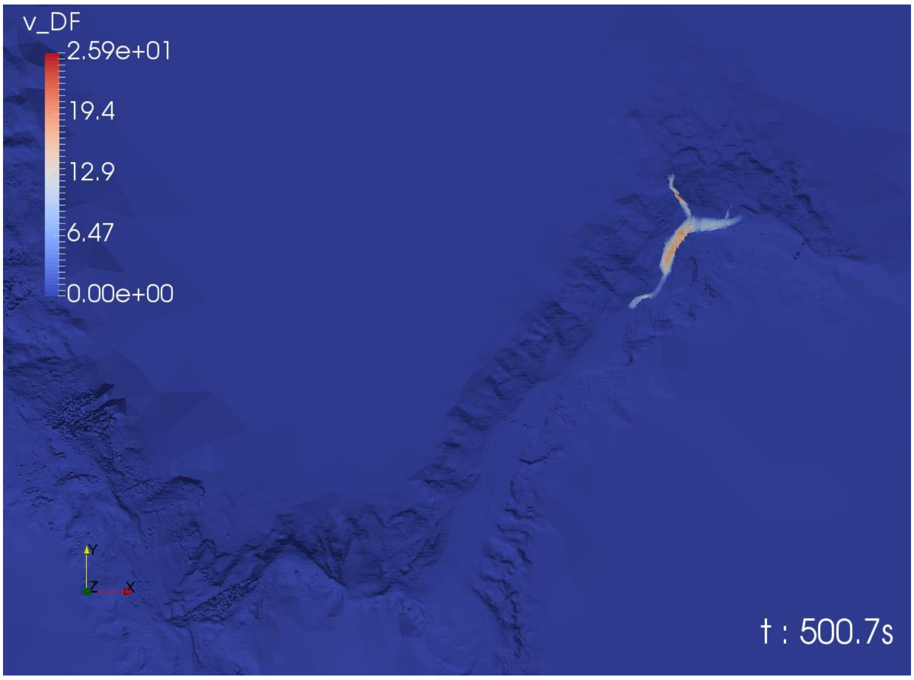

Figure 7.16. Velocity in m/s of the debris flow layer at instant t = 500 s.

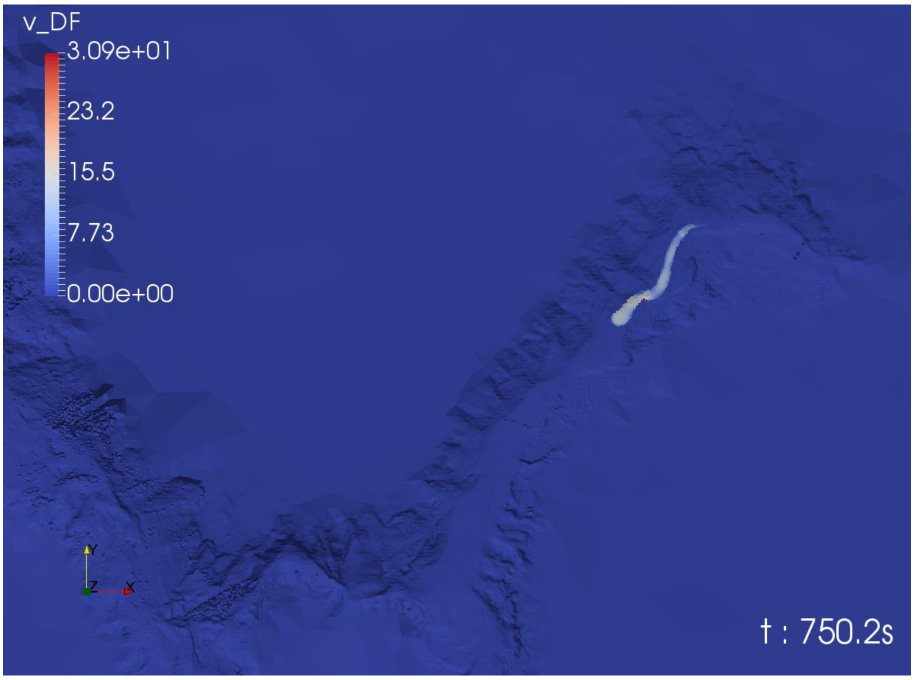

Figure 7.17. Velocity in m/s of the debris flow layer at instant t = 750 s.

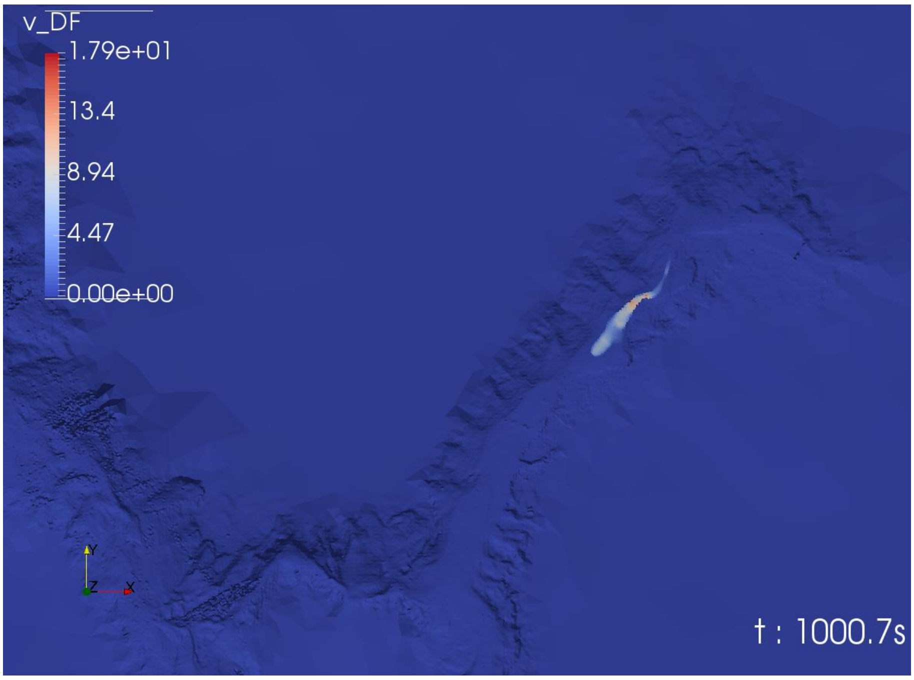

Figure 7.18. Velocity in m/s of the debris flow layer at instant t = 1000 s.

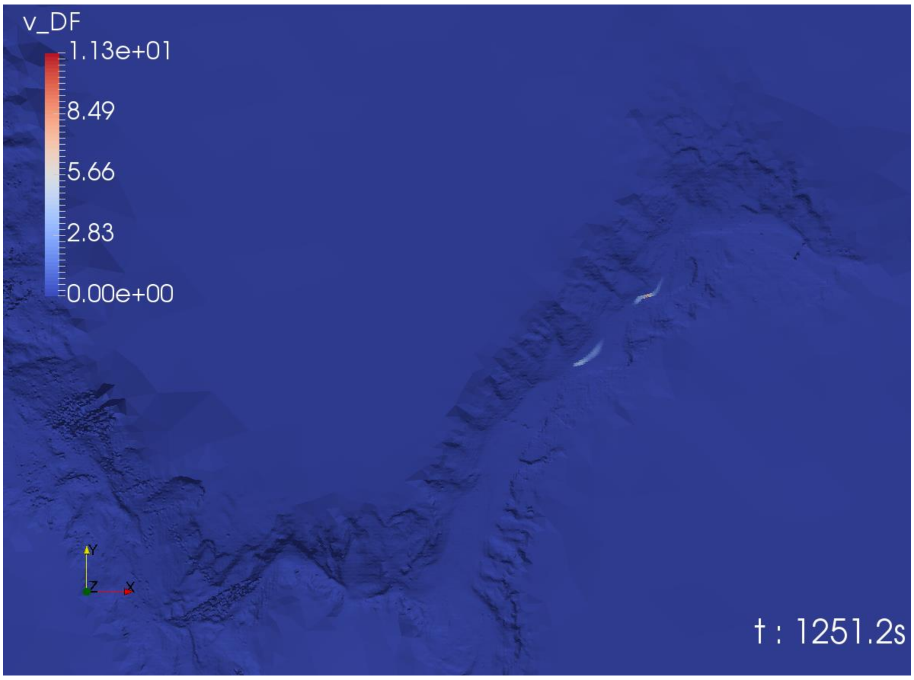

Figure 7.19. Velocity in m/s of the debris flow layer at instant t = 1250 s.

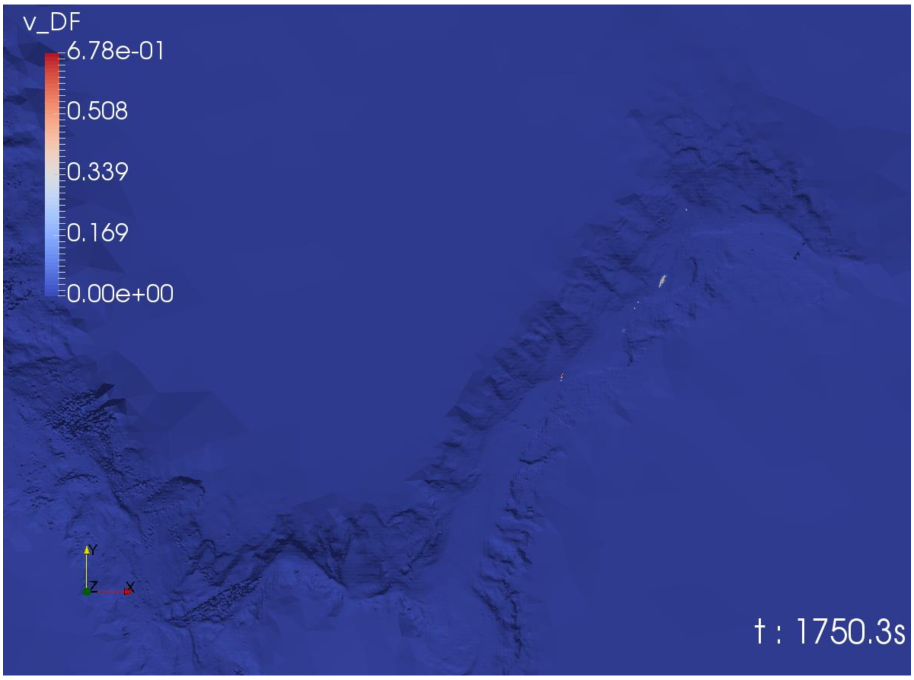

Figure 7.20. Velocity in m/s of the debris flow layer at instant t = 1750 s.

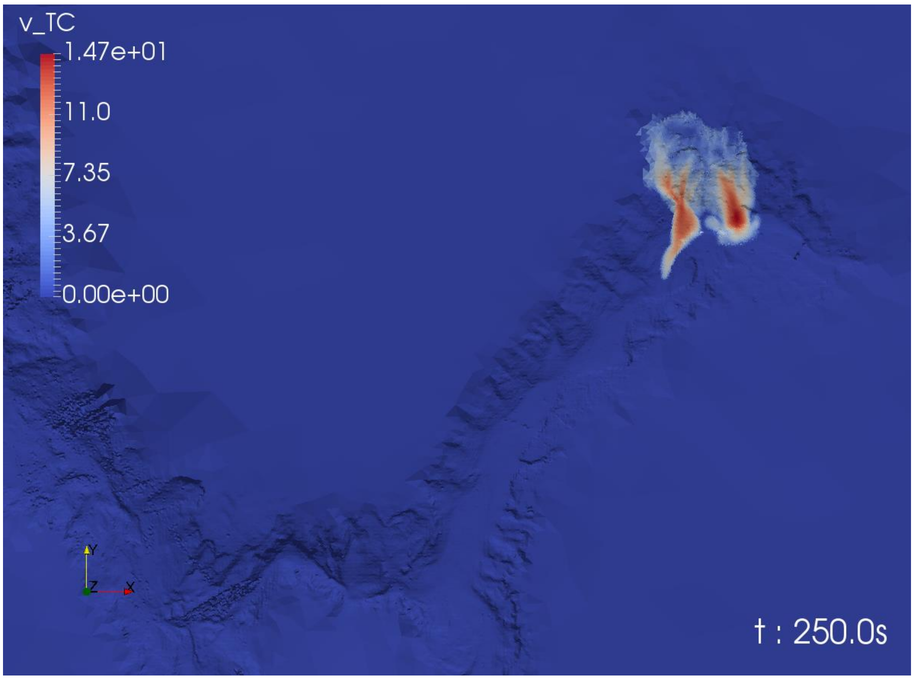

Figure 7.21. Velocity in m/s of the turbidity current layer at instant t = 250 s.

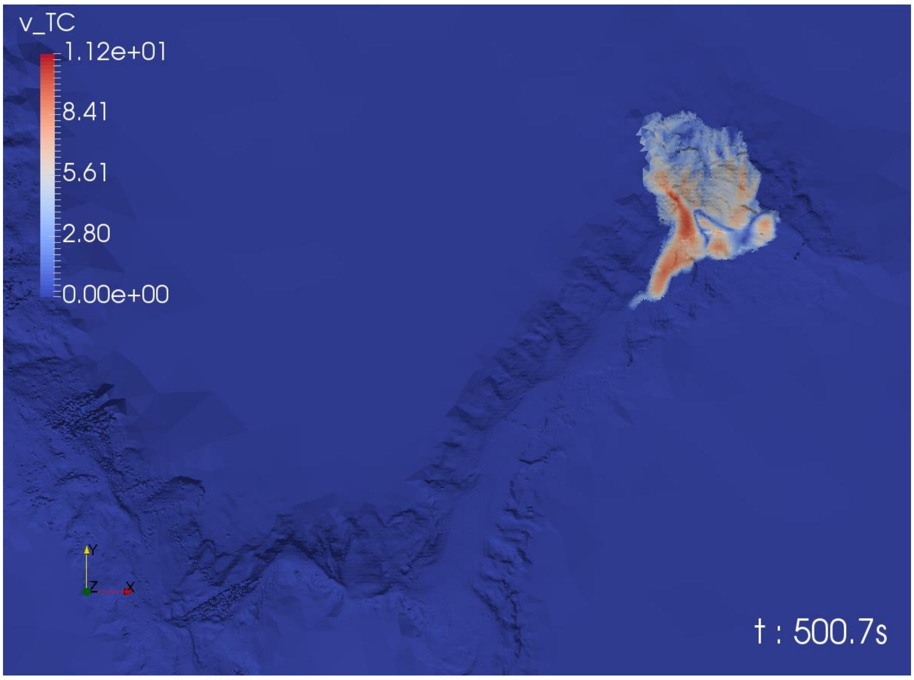

Figure 7.22. Velocity in m/s of the turbidity current layer at instant t = 500 s.

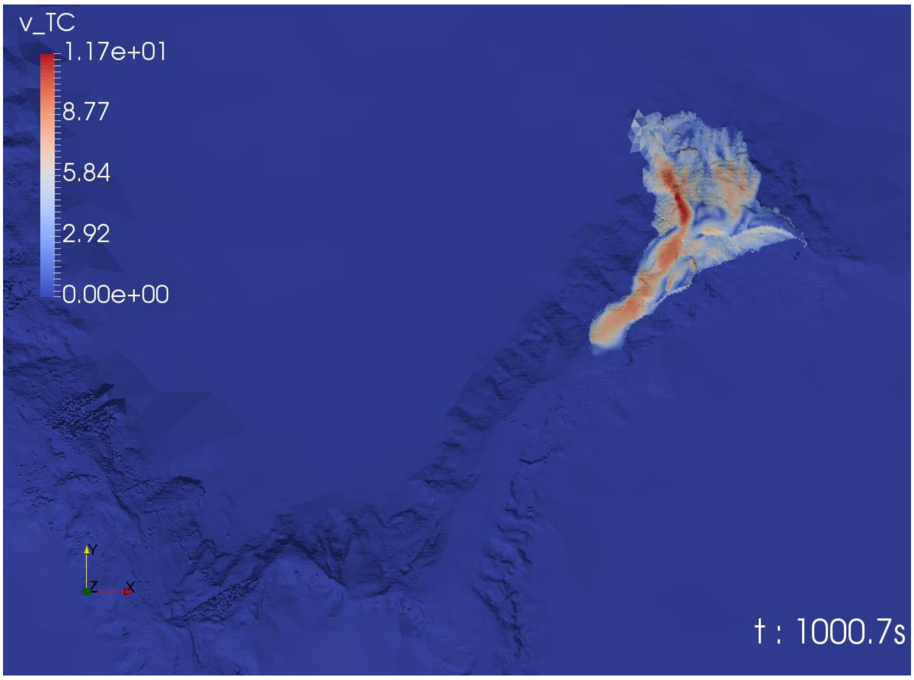

Figure 7.23. Velocity in m/s of the turbidity current layer at instant t = 1000 s.

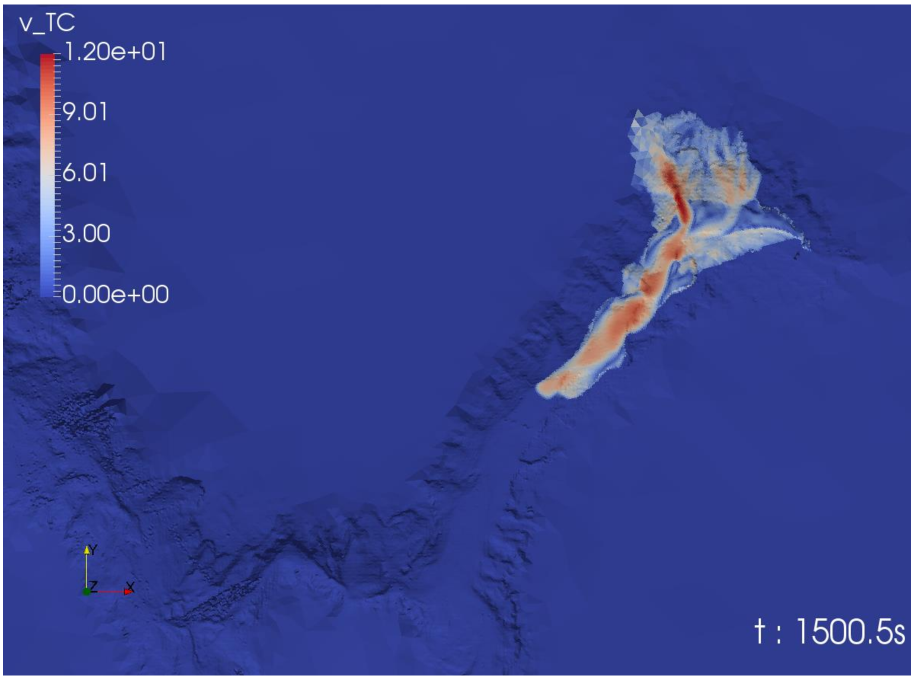

Figure 7.24. Velocity in m/s of the turbidity current layer at instant t = 1500 s

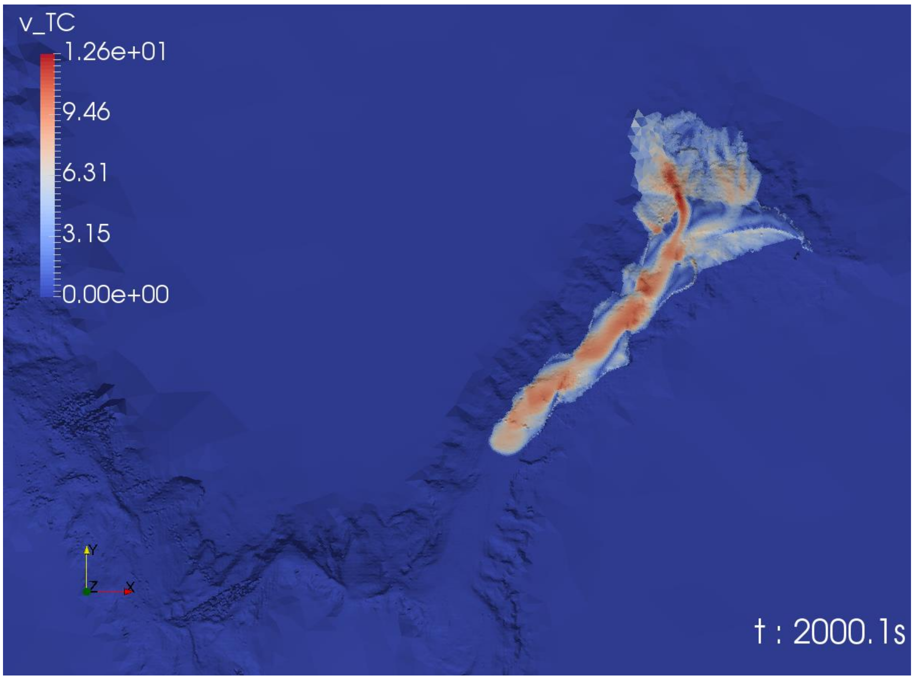

Figure 7.25. Velocity in m/s of the turbidity current layer at instant t = 2000 s.

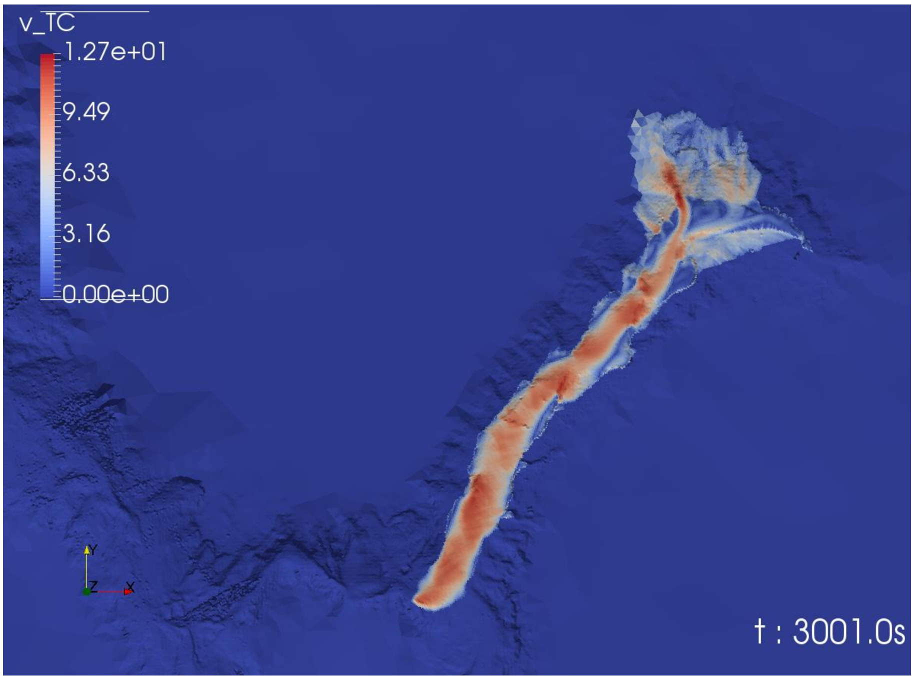

Figure 7.26. Velocity in m/s of the turbidity current layer at instant t = 3000 s.

The detrainment coefficient e_d is the main parameter that controls the generation of the turbidity current from the debris flow layer. Three simulations were run to investigate the effect of the detrainment coefficient on flow behaviour in real bathymetry case. The cases with detrainment coefficient e_d = 0 (practically a single debris flow layer), 0.001 and 0.01 were investigated.

Figure 7.27 shows the debris flow depth at simulation time t = 500 s. For all cases the propagation distance of the front is the same. As the detrainment increases the debris flow layer is more confined. For the case with no detrainment, debris flow of high thickness remained close to the source area. Maximum thickness is observed for the case with e_d = 0.001 but in a limited part of the flow.

Figure 7.28 shows the debris flow thickness at the end of the simulation (t = 3000 s). In the case where the flow is a single debris flow layer (e_d = 0), high flow thickness has been maintained along all the runout distance. The debris flow with low detrainment (e_d = 0.001) has travelled longer distance in the canyon, the debris flow with high detainment (e_d = 0.01) has been eliminated in the source area and intensively detrained in the canyon head region.

The developed turbidity current is faster for the case of e_d = 0.01, but the flow thickness is of the same order at simulation time t = 500 s (Figure 7.29). For the case of e_d = 0.0, there is no turbidity current as expected. From Figure 7.30 to Figure 7.32, it can be observed that higher detrainment coefficient results to a turbidity current that propagates faster and reaches higher maximum thickness.

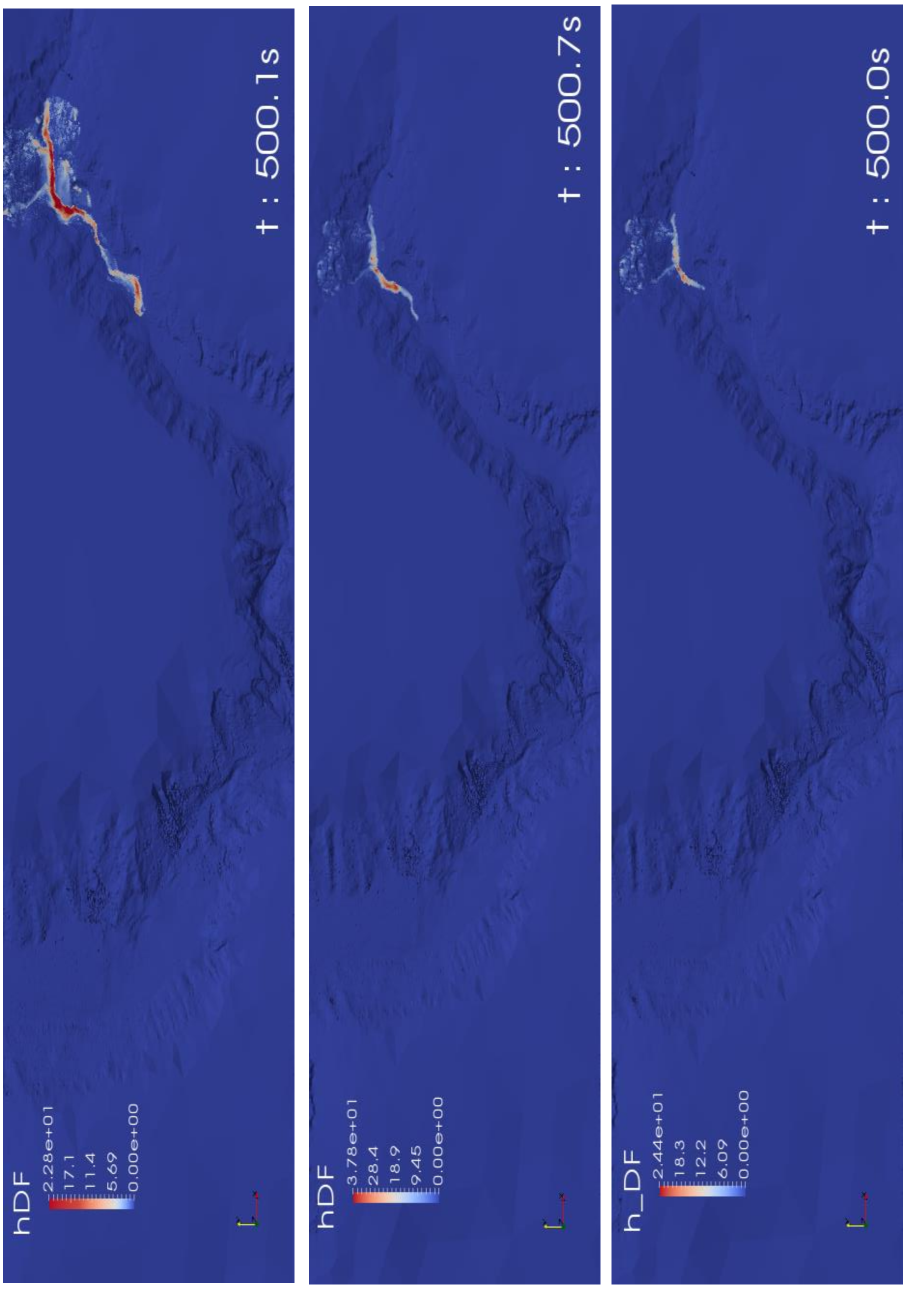

Figure 7.27. Flow thickness in m of the debris flow for the case of e_d = 0.0 (left), e_d = 0.001 (middle) and e_d = 0.01 (right) at t = 500 s.

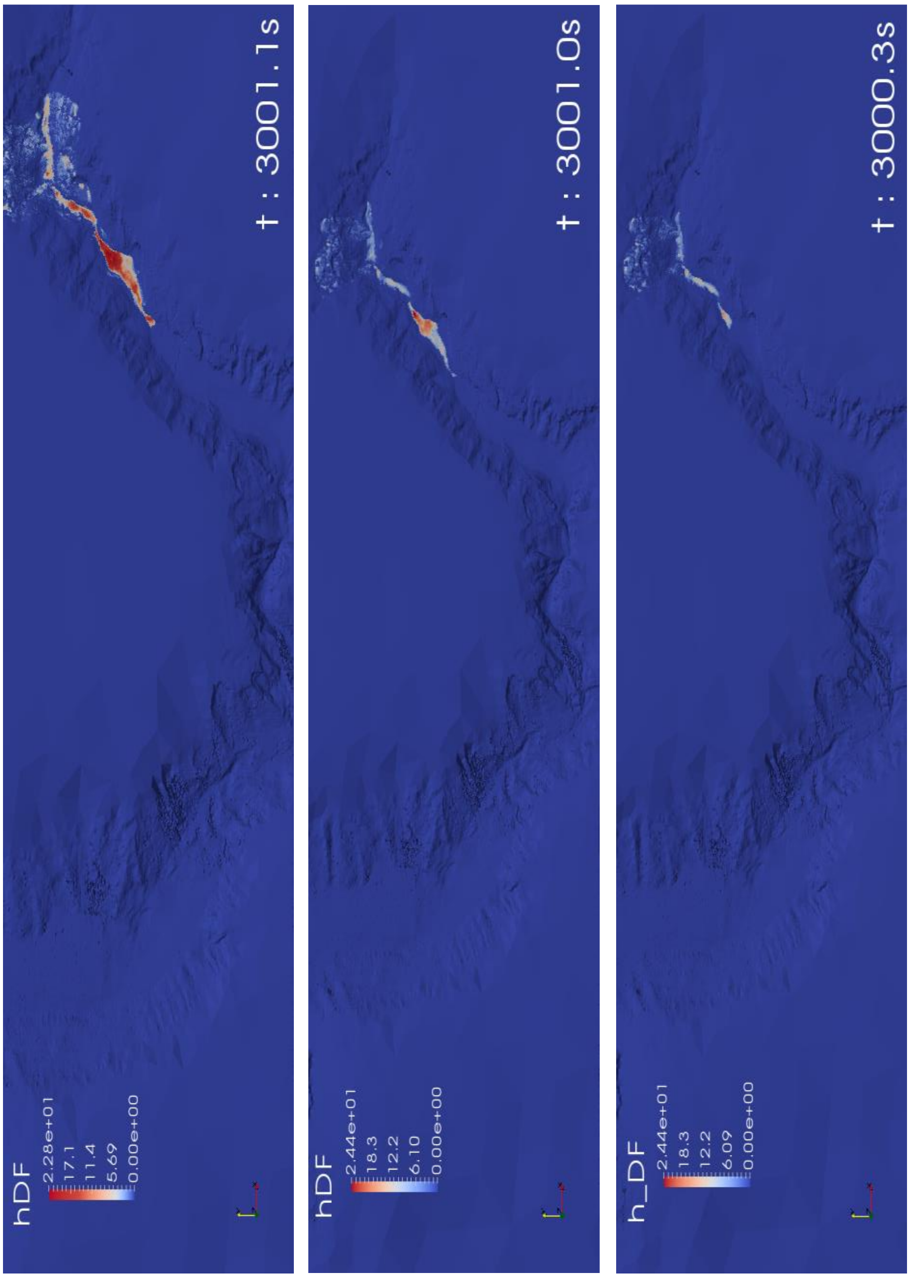

Figure 7.28. Flow thickness in m of the debris flow for the case of e_d = 0.0 (left), e_d = 0.001 (middle) and e_d = 0.01 (right) at the end of the simulation at t = 3000 s.

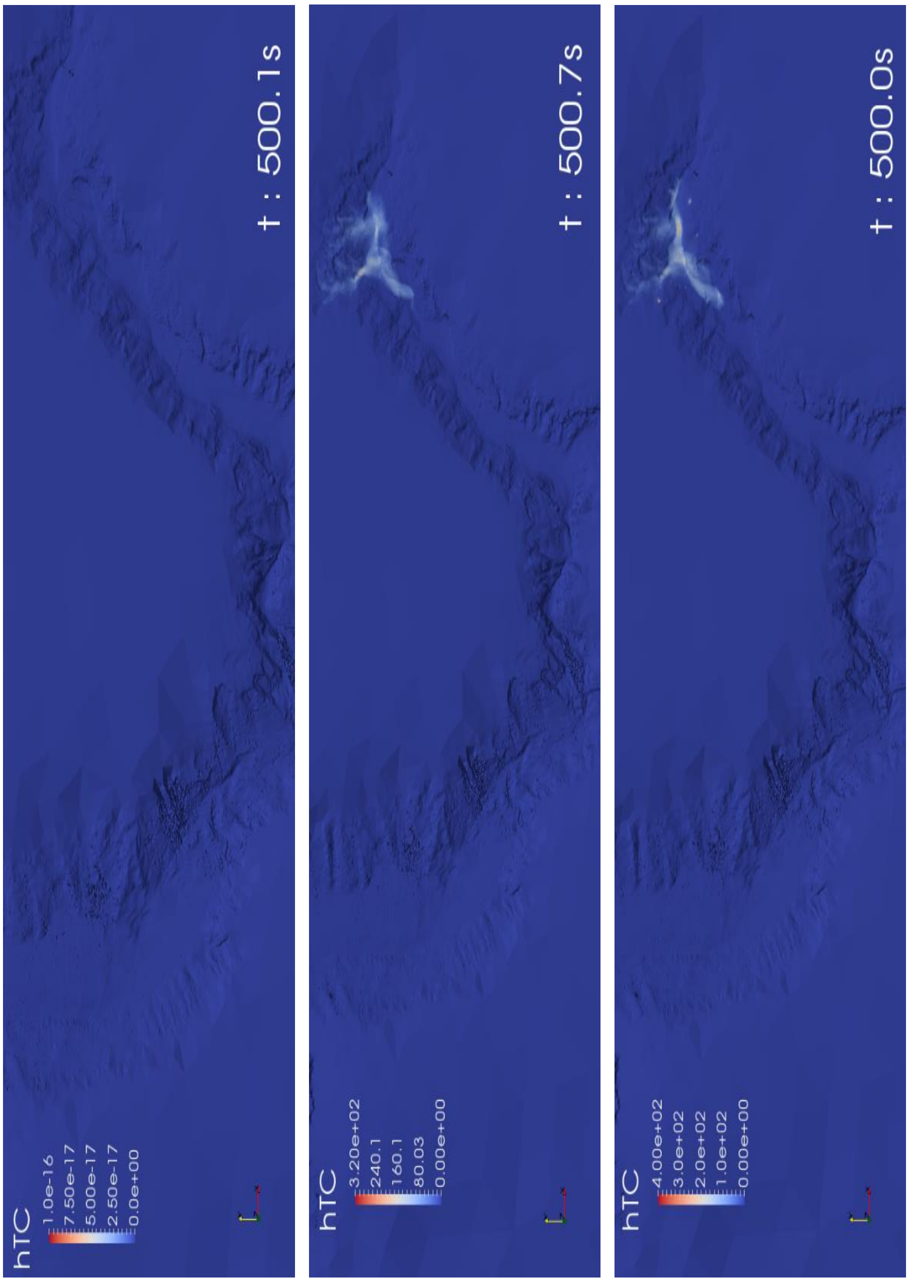

Figure 7.29. Flow thickness in m of the turbidity current for the case of e_d = 0.0 (left), e_d = 0.001 (middle) and e_d = 0.01 (right) at t = 500 s.

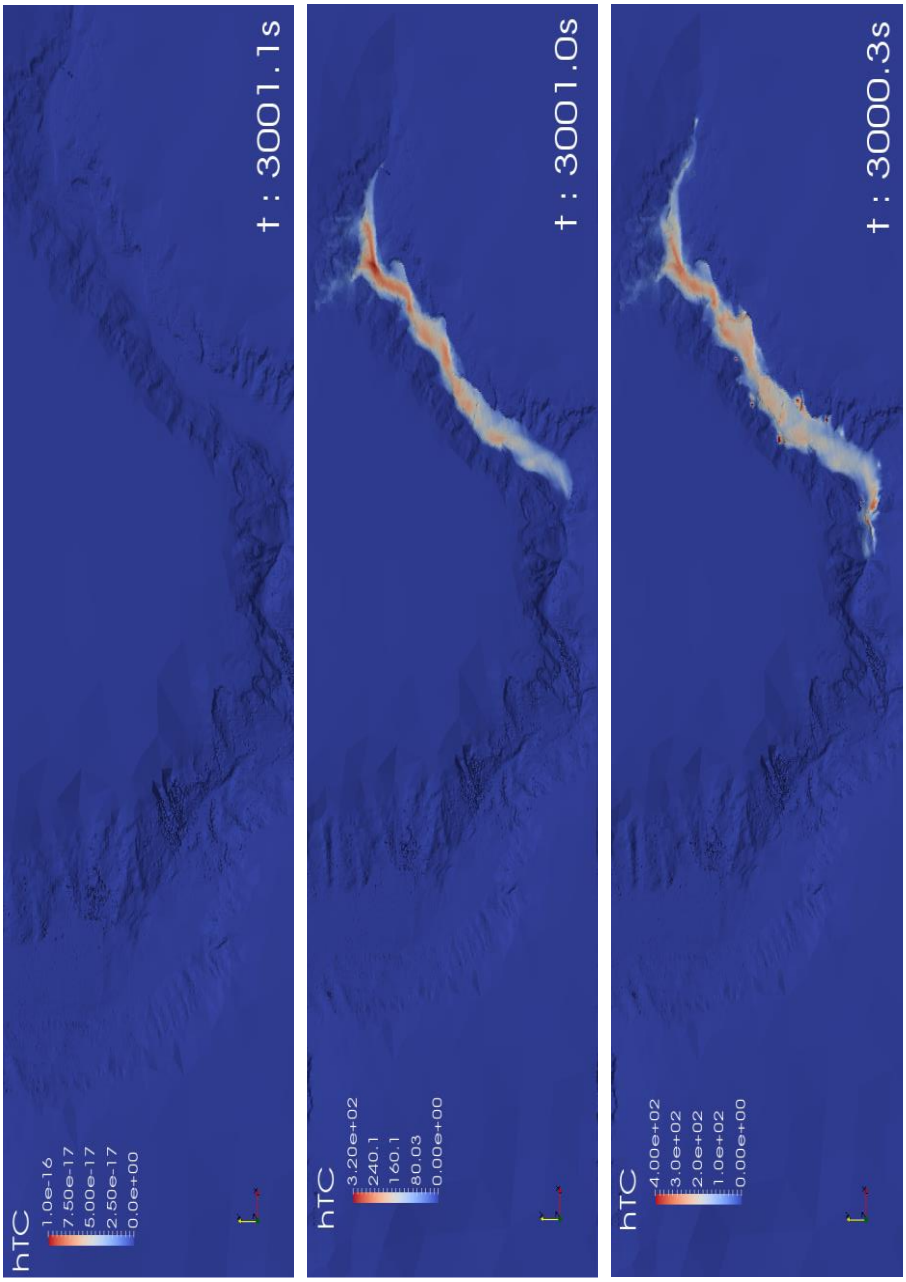

Figure 7.30. Flow thickness in m of the turbidity current for the case of e_d = 0.0 (left), e_d = 0.001 (middle) and e_d = 0.01 (right) at the end of the simulation at t = 3000 s.

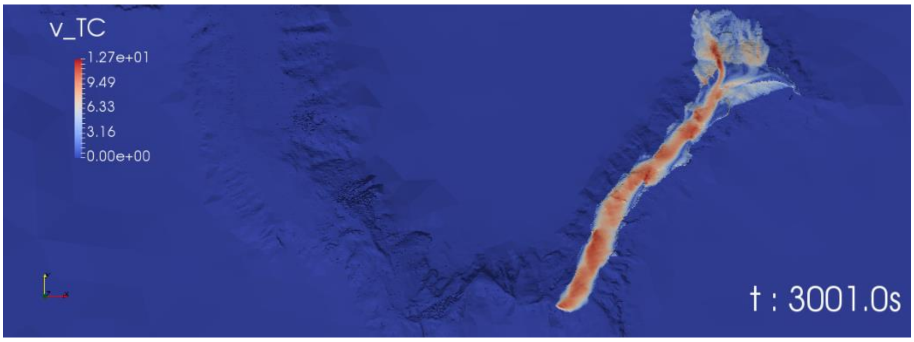

Figure 7.31. Flow velocity in m/s of the turbidity current for the case of e_d = 0.001 at instance t = 3000 s.

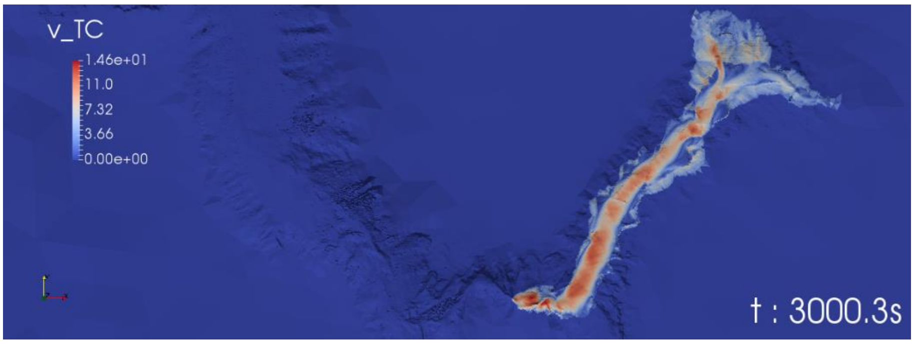

Figure 7.32. Flow velocity in m/s of the turbidity current for the case of e_d = 0.01 at instance t = 3000 s.

7.6 Summary

The flow dynamics of a debris flow transitioning into a turbidity current have been illustrated for a case in a real location on the edge of the Australian continental shelf which is characterized by evidence of massive failures. Water depths vary from around 1600 m at the shelf break through to 3900 m at the base of the escarpment over a horizontal distance of only around 15 km. One of the smaller slope failures was reconstructed by surrounding topography extrapolation and was used as the source volume for the simulation.

The introduced two-layer model performed well in this 2-D complex case in which the landslide occurs in very steep slopes and the flow propagates in both longitudinal and transversal direction.

Three simulations were run for detrainment coefficients e_d= 0, 0.001 and 0.01. For no detrainment, the model managed well in the case of a single debris flow. In such large scale event, it was concluded that effect of the detrainment coefficient remains important.

The performance of the model in this case, is promising enough to proceed to simulation of landslide events of the past where data about developed velocities and deposits are available. The dependence of the flow dynamics on the input rheological parameters would be interesting to investigate.

Chapter 8 Conclusions

Subaqueous mass movements, including debris flows and turbidity currents, have had catastrophic impacts as they are connected with the transport of vast quantities of soil down channels and escarpments at significant velocities. The destruction of seabed infrastructure, the collapse of coastal areas into the sea and in some cases the generation of tsunamis highlight the importance of being able to accurately assess the risk in the case of important submarine landslide events. The analysis of flow deposits, which resulted from subaqueous mass movements of the past, indicated the co-existence of both debris flows and turbidity currents during a single event. Laboratory studies suggest that depending on the nature of the material that forms the slide, on the triggering mechanism and on the available energy, the initial mass can form a debris flow with specific flow properties, which as it interacts with the sea floor and ambient water may evolve to a dilute turbidity current. The two layers can co-exist at first and then the debris flow may stop and be deposited while the turbidity current continues its propagation. A numerical model that predicts their dynamic behavior from inception to runout could ascertain the risks of such potential flow event.

An extensive and in-depth literature review was the stepping stone for this research. Chapter 2 was devoted to previous research on submarine landslide events and provided information about the morphology and dynamics of submarine gravity flows, involving debris flows and turbidity currents. The theoretical background of shallow water equations and the closure relations for the source terms suggested by researchers in the past, constituted the basis for the formation of the constitutive equations of the introduced model. Previous experimental studies provided significant information that was used for setting up the two experimental campaigns conducted for this study. The review of numerical models provided knowledge about suitable numerical tools, application fields but also their limitations. The modeling of the transition of a debris flow to a turbidity current was poorly investigated and this fact led to the introduction of the present model after exploiting the knowledge of the past.

A two-layer framework is proposed for the simulation of a slide-induced debris flow gradually transforming into a turbidity current through sediment mixing and detrainment with a shallow-water approach in Chapter 3. This work seems to open a new path for the specific area of research, as previous attempts were limited in the coupling of two separate models for the debris flow and the turbidity current layer (Drago, 2002).

The model describes the co-existence and transition from a basal debris flows layer to an upper turbidity current layer. A non-Newtonian Herschel-Bulkley rheology is adopted for the lower layer which is assumed to retain a constant density, while the upper layer is endowed with a variable density, depending on the rate of sediment transferred from the parent debris flow and the amount of ambient seawater entrained through mixing. Two superimposed shallow moving layers were assumed to flow under reduced gravity in an ambient seawater body. Without any interaction mechanisms between the layers other than gravity, the system could be described by the well-known two-layer shallow water equations. In order to consider the exchanges of mass and momentum between the layers, the two-layer model was supplemented with a vertical flow structure. The choice of the proper exchange mechanisms constitute the most challenging part of the formation of the equations. Sediment detrainment directed from the debris-flow layer to the turbidity current layer, water entrainment into the turbidity current layer, interfacial friction between the two layers and sediment erosion/deposition for the case of a single layer of turbidity current, were the selected exchange mechanisms for this model. After incorporating the closure equations obtained based on the exchange mechanisms, the description has been formalised into a set of governing equations.

Model simulations were validated against known analytical solutions for cases with equal layer densities or distinct layer densities. The model's performance was examined in an idealized 1-D case, in which an initial debris flow mass is released on a sloped profile that features a sudden reduction in seabed slope at some distance downstream of the initial release point. The effect of the sediment detrainment of the debris flows and the interfacial friction between the two layers, was studied in a sensitivity analysis through the detrainment coefficient e_d and friction coefficient C_d in Chapter 4.

Upon studying the behaviour of the model and the influence of its parameters in various simulations, it is concluded that: (i) model simulations converge well towards analytical solutions available for degenerate cases with equal layer densities $\rho_1 = \rho_2$, with a contact discontinuity marking the point at which the two distinct fluids are in contact with each other; (ii) the model was validated against general case of dam- break flow of a light fluid of density ρ_1 over dense fluid of density ρ_2 showing that as the ratio ρ_1/ρ_2 decreases, the mobility of the lower layer decreases and the initially sharp discontinuity evolves into a smoother profile. The mixing of the two layers of different density at the front region was enhanced by the decrease of the density ratio; (iii) the model is robust to the emergence or disappearance of any of the two layers by vanishing thickness, and downgrades to known solutions for pure debris flows or turbidity currents when any of the two layers vanishes; (iv) the increase of detrainment coefficient of the debris flow is connected with the development of a turbidity current which propagates faster and has higher sediment concentration than for cases with low detrainment, and is able to remobilize or eliminate the debris flow deposits; (v) high friction at the interface of the two layers leads to a behavior where the two layers propagate with almost same velocity as single mass but for shorter runout distances and the generated turbidity current is much weaker in comparison with low friction coefficient cases where the turbidity current is quickly detached and continues its propagation as a single layer.

In Chapter 5, the behavior of subaqueous sediment density flows was investigated. Plastic sediment-water mixtures of different grain sizes were tested in a series of flume experiments with varying bed slopes. A combination of digital imaging through the flume transparent sidewall with velocity field measurements using UVP method ensured a detailed monitoring of the flow.

After experimental observation and performing a quantitative analysis of the acquired data, it was concluded that: (i) the partition of the flow into a basal layer, which remains dense throughout the current propagation, and a dilute turbidity current resulting from mixing with ambient water at the rear of the current head, was observed; (ii) the brightness thresholds used for the definition of each layer, were obtained after a correlation of the brightness profiles with the velocity profiles acquired with the UVPs. The height of the bottom layer as defined by the brightness threshold coincided well with the height of the flow region characterized by streamwise velocity, indicating rapid propagation of the dense basal layer and much slower, or even reverse, velocity for the dilute turbidity cloud; (iii) the space-time evolution of depth-integrated quantities reveals that the front of the flow remains dense throughout the experiment, suggesting that near the front, the sediment lost to turbidity trailing behind at the top of the current is balanced by additional dense current fed from the basal layer. The formation of mixing billows results in “ejection” events with a distinctive curved path on the space-time plots.

These experiments are quite unique in the sense that they allow simultaneous measurements of velocity and density within the density currents, and allow investigating their internal stratification. Parametrization of the vertical stratification and water entrainment relations will be important for predictive numerical models for slide-induced debris flows transitioning to turbidity currents. These experiments could also provide a validation case for the introduced two-layer model if a modification on initial boundary conditions will be implemented.

In Chapter 6 a series of lock-exchange experiments have been conducted for reproducing small scale subaqueous landslides. The behavior of sediment-water slurries was investigated for cases of different types of sediments and different initial sediment volumetric concentrations. A high speed camera was used for capturing the propagation of the flow along the first meter after the gate and a digital camera monitored the total runout domain. Velocity field measurements were obtained using UVP method. Kaolin clay-water slurries and thermoplastic polyurethane-water slurries were utilized as the released material of the lock exchange.

A simple correction technique was suggested for improving the quality of the results in terms of even illumination. A liquid with natural colour similar to the one of the resulted mixtures (shades of white and grey) was mixed with water along the total length of the flume. This condition was captured in a reference picture that was used to obtain a correction matrix. Every image of the experiments was then multiplied by this matrix as a correction of uneven illumination along the horizontal direction of the flume.

For the experiments using kaolin clay, the effect of the increase of the sediment was clearly captured by the measurements of the slurry flow characteristics (e.g. slurry head and body velocities, flow thickness). Results suggest that the addition of sediment mass in the released material leads to higher velocities of the front and the body of the flow. This increase seems to follow a parabolic distribution depending on the initial sediment volumetric concentration.

The behavior of thermoplastic polyurethane proved to be challenging in a lock-exchange type of experiment. The preparation of the material before the final mixing with water demanded sieving and air-removal procedures. The small grain size with a characteristic diameter of 84 μm in the slurries of initial sediment concentration above 10%, was defeated by surface tension that did not allow the flow to start. The large grain size with a characteristic diameter of 169 μm had a more foreseeable behaviour. The propagation of the current generated by an initial slurry of 15% sediment concentration was compared with the corresponding experiment using kaolin clay sediment. It was concluded that a slurry of kaolin clay develops almost double frontal velocity than the corresponding slurry of plastic sediment.

While the treatment of the plastic sediment was very demanding and time-consuming, it appears to have an important potential for quantifying the sediment distribution and provide information about the exchange mechanisms between the layers developed in a high-density flow. The preparation of mixtures with kaolin clay and water was simpler and its behavior can support clear-cut initial conditions that are the desideratum for experiments. Despite this it was very difficult to investigate the layering of the flow based on image processing. Potentially a siphoning device obtaining samples at different elevations may prove to be more effective (e.g. Sequeiros *et al*., 2010).

This experimental work provided a basis for comparison with the introduced numerical model SWBI2D, as it guarantees the initial boundary condition of a sudden release in contrast with the experiments presented in Chapter 5. Simulations obtained with this two-layer model are in a relatively good agreement with the case of the lock-exchange experiment in which the initial released volume of sediment concentration was 15%, while the comparison with experiments of low sediment concentration of the initial volume was much poorer. It is concluded that the model performs better when imposing a soil volume of such density that is representative of a debris flow. These experimental results could also highlight the key points that are crucial for modelling such flows, while they can also be used as a benchmark for comparison and validation, by future modellers.

The satisfactory behavior of the model on a simple 1-D case, as well as the good agreement of the numerical with the experimental results, allowed the illustration of the behavior of the model on a more complex 2-D case. A large-scale scenario in a location on the Australian continental shelf was presented in Chapter 7. Real bathymetric data were used to define the source and runout area of the simulation. The model performed well in this 2-D complex case and managed to reproduce the behaviour of the landslide in very steep slopes with the flow propagating in both longitudinal and transversal direction.

The present work was formed within the framework of the European Union's Seventh Framework Programme, SEDITRANS, which targets the study of the sediment transport and its impacts in the fluvial, estuarine and costal environment. This study took place in both academic and industrial environment and the results were oriented to combine both academic and industrial interest.

Although the potential of the introduced two-layer model has been demonstrated through 1-D and 2-D case studies and the original objectives have been met, there are still directions that could be explored for further research. Some recommendations for future work could be: (i) the extension of the model for including flows generated by a continuous sediment source. The application range of the model will be extended and the experimental results presented in Chapter 5 can be used for validation; (ii) the addition of a term to include the possible sediment deposition of the turbidity current on top of the debris flow layer, as now the sediment detrainment is directed only from the debris flow to the turbidity current layer; (iii) the parametrization of the detrainment coefficient e_d defined in terms of interface shear gradient and not set as a constant value. This could be achieved by repeating the experiments of Chapter 6 ensuring the measurements of vertical sediment stratification; (iv) the introduction of the strain softening phenomenon to the model (Appendix A).

Appendices

Appendix A

Incorporation of the strain softening effect for debris flows in the numerical model SWBI2D

Rheological properties of debris flows

The rheology of debris flows can be described by either linear Bingham or nonlinear viscoplastic Herschel-Bulkley model. In Herschel-Bulkley model, the viscosity of the flow decreases with the shear rate and in such a model, there is a yield strength τ_y under which there is no movement. The mathematical form of the above can be summarised for the Herschel-Bulkley rheological model, in the expression (Imran *et al.* 2, 2001)

$$\tau = K\,\mathrm{sgn}(\dot{\gamma}) = \begin{cases} 0 & if \quad |\tau| < \tau_y \\ \tau_y\,\mathrm{sgn}(\dot{\gamma}) - K|\dot{\gamma}|^n\,\mathrm{sgn}(\dot{\gamma}) & if \quad |\tau| \geq \tau_y \end{cases} \tag{A.1}$$

where n is the flow index which is generally less than 1, and K is a coefficient determined by rheological tests that has the dimensions of dynamic viscosity only in the limiting case n = 1. The equation (1) can be similarly expressed by the relation (Imran *et al.* 2)

$$\tau = \begin{cases} 0 & if \quad |\tau| < \tau_y \\ \tau_y\,\mathrm{sgn}(\dot{\gamma})\left(\left|\dfrac{\dot{\gamma}}{\dot{\gamma}_{ref}}\right|^n + 1\right) & if \quad |\tau| \geq \tau_y \end{cases} \tag{A.2}$$

considering that the reference strain rate is

$$\dot{\gamma}_{ref} = \left(\frac{\tau_y}{\mu}\right)^{1/n}$$

where μ is the dynamic viscosity (only for the case of Bingham fluid at n=1). The γ_{ref} can be considered only in case where it can actually be a reference strain rate, depending on parameters that remain constant. In cases where the yield shear stress is time-dependent, the rheological model has to be defined by the former definition.

The Strain-Softening phenomenon

In cases of decrease in soil strength due to remoulding, like in marine clays, the fixed values of the yield strength and consistency in the simple Bingham or Herschel-Bulkley models are inadequate to account this effect. The marine clays when subject to large strains demonstrate contractive behaviour causing pore pressure development and reduction in strength, i.e. strain-softening behaviour. The glacial debris layers are typically dilatant and thus ductile. However, at large strains limited strain-softening occurs and the residual strength can be assumed to be equal to the remoulded strength of the materials. As the material weakens on shear, further shear takes place preferentially in zones which have previously been sheared. Thus, failure can occur with shear being confined to a few failure zones. A major challenge is to model the transition from an initially intact soil with high strength to a mobile slide with a considerable lower strength.

Soil strength degradation from intact to remoulded strength due to the accumulated shear strains is represented using an exponential decay law

$$\tau_y = \tau_{rem} + (\tau_{\text{int}} - \tau_{rem}) e^{-\frac{3\gamma_{acc}}{\gamma_{95}}} \tag{A.3}$$

where τ_{int} is the intact shear strength of the soil and τ_{rem} is the remoulded shear strength, γ_{acc} is the accumulated shear strain rate and γ_{95} is the cumulative shear strain at which 95% of the strength reduction has occurred. The values of τ_{int}, τ_{rem} and γ_{95} are available after soil testing. Thus, the expression of the shear stress in the Herschel-Bulkley model can be written as

$$\tau = \left(\tau_{rem} + (\tau_{\text{int}} - \tau_{rem}) e^{-\frac{3\gamma_{acc}}{\gamma_{95}}} \right) \text{sgn}(\dot{\gamma}) + K |\gamma|^n \, \text{sgn}(\dot{\gamma}) \qquad \mathit{for} \quad |\tau| \geq \tau_y \tag{A.4}$$

For the definition of the cumulative absolute (plastic) shear strain γ_{acc} according to Einav and Randolph (2005) is given by the relation

$$\gamma_{acc} = \int_0^t |\dot{\gamma}_{\max}| dt \tag{A.5}$$

where $|\dot{\gamma}_{\max}|$ was originally defined according to the Tresca failure criterion but to accommodate the Von Mises criterion the two alternative definitions are

$$\begin{aligned} |\dot{\gamma}_{\max}| &= 2|\dot{\varepsilon}_{\max}| \quad (Tresca) \\ |\dot{\gamma}_{\max}| &= \sqrt{2\dot{\varepsilon}_{ij}\dot{\varepsilon}_{ij}} \quad (Von\,Mises) \end{aligned} \tag{A.6}$$

in which $|\dot{\varepsilon}_{\max}|$ represents the absolutely largest principal strain rate component.

However, in a depth integrated model, where the wall-normal direction z has been integrated and thus, not resolved but a posteriori the vertical distribution is computed through a prescribed profile given by

$$V(z) = V_p \left[1 - \left(1 - \frac{z}{h_s} \right)^{1+1/n} \right] \quad for \quad z < h_s \tag{A.7}$$

where $V = (U, V))$ is the velocity vector in the two horizontal directions, $V_p = (u_p, v_p)$ is the velocity vector that occurs as the solution of the equations for the debris flow in the two horizontal directions and h_s is the thickness of the shear layer. Given that consideration, the only region in the vertical column that the maximum rate of shear strain is non-zero is in the shear layer thickness due to the fact that the vertical velocity derivative is non-zero.

Hence, it can be written

$$\gamma_{acc} = \int_0^t \left(\frac{1}{h_s} \int_0^{h_s} \frac{\partial V}{\partial z} \right) dt \tag{A.8}$$

And by substituting the profile shape in the integral, it can be finally concluded that

$$\Gamma = \gamma_{acc} = \int_0^t \left(-\frac{V_p(t)}{h_s(t)} \right) dt \tag{A.9}$$

Then Equation (2) can be written for the present formulation as

$$\tau = \left(\tau_{rem} + (\tau_{\text{int}} - \tau_{rem}) e^{-b\Gamma} \right) \text{sgn}(\dot{\gamma}) + K|\gamma|^n \, \text{sgn}(\dot{\gamma}) \tag{A.10}$$

Implementation of the Strain-Softening in the code SWBI2D

Within the numerical code SWBI2D the strain-Softening module has been introduced for both the Bingham and the Herschel-Bulkley rheological models. Based on the definition concerning the debris flows given in Figure 1 (for simplification purposes subscript 2 will from now on, denote turbidity current properties and 1 the debris flow) the shear stress is computed by

$$\tau = \tau_b(1-\eta), \quad \eta = \frac{z}{h} \tag{A.11}$$

where τ_b is the bed shear stress, which is equal to $\tau_b = \tau_y/\xi$. The parameter $\xi = h_p/h$ and by geometric similarity we can get $\xi = \tau_y/\tau_b$. This parameter ξ is the one required for the computation of the instant shear S_r given by the expression

$$S_r = \frac{\tau_b h}{\mu}\frac{(1-\xi)^2}{2} \tag{A.12}$$

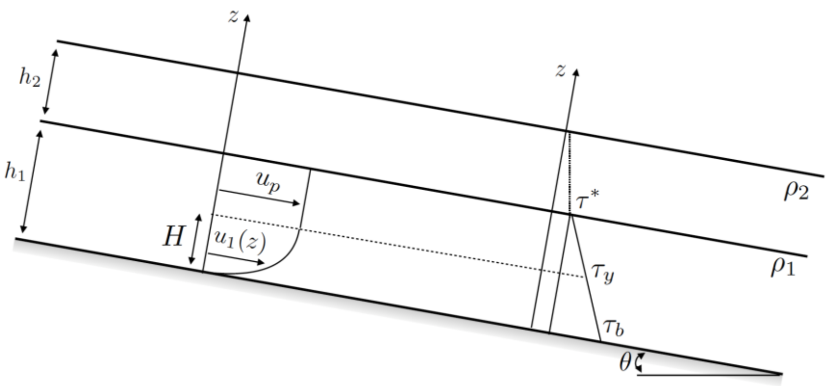

Figure 1. Sketch of a two-layer flow.

The parameter ξ can be computed by means of iterations from each of the expressions

$$\frac{\mu}{\tau_y}\left(\frac{U}{h}\right)^n = \left[\frac{n(n+1+n\xi)}{(n+1)(2n+1)}\right]^n \frac{(1-\xi)^{n+1}}{\xi} \tag{A.13}$$

For each of the rheological models, the only unknown is the $0 < \xi < 1$ parameter, which is computed through an iterative procedure. For Herschel-Bulkley rheology we get

$$\xi = \operatorname{int}erp\left[lo\,g_{10}\left(\frac{\mu}{\tau_y}\left(\frac{U}{h} \right)^n \right), \log_{10}\left(\left[\frac{n(n+1+n\xi)}{(n+1)(2n+1)} \right]^n \frac{(1-\xi)^{n+1}}{\xi} \right); \xi \right] \quad \text{(A.14)}$$

whereas for Bingham rheology the above relation can be written as:

$$\xi = \operatorname{int}erp\left[lo\,g_{10}\left(\frac{\mu}{\tau_y}\frac{U}{h} \right), \log_{10}\left(\frac{1}{6\xi}\left(1-\xi^2\right)\left(2+\xi\right) \right); \xi \right] \quad \text{(A.15)}$$

For considering strain softening in the simulations, the above procedure has to be repeated for every timestep, where the yield shear stress τ_y and the debris flow viscosity μ (or K) will be gradually weakened.

Appendix B
Example of SWBI2D data input file

; SWBI2D - Shallow Water Bilayer Model

; --

; Basic Parameters

; --

; Start time

t0 0

; End time

tend 500

; CFL constraint

cfl 0.7

; Sub-time stepping for source terms

n_source 10

; Limiter

; 1: Minmod

; 2: Superbee (not implemented in this version)

limiter 1

; Order of accurancy

; 1 : first

; 2 : second (not implemented in this version) order 1

; Number of threads

num_threads 4

; --

; Soil Parameters

; --

; Ambient fluid density

rho_ambient 1025

soil_porosity 0.4

layer {

; lower level is zero

level 0

; Soil/Fluid density (for Debris flow layer)

rho_fluid 1400 ;

; **Rheology model**. Parameters not required for specific models are ignored

; 1: Manning (Parameters: n) (not implemented in this version)

; 2: Chezy(Parameters: cs) (not implemented in this version)

; 3: Bingham(Parameters: tau_y,mu)

; 4: Herschel-Bulkley(tau_y,mu,n)

; 5: Frictionless

; 6: constant strength

; 7: constant factor (Parameter: Cd)

friction_type 4

friction_p1 400

friction_p2 90

```
	friction_p3	0.3
	initial {
		tag Left
		thickness 4
		sediment_concentration 0
		thickness_transition_width 0
		excavated n
		max_thickness_tag
		downstream_excavation_limit_tag
		}
}

layer {
	; lower level is zero
	level 1
	; Sediment particles density (for Turbidity currents layer)
	rho_particles   2650
	TC_has_entrainment y
	TC_has_erosion_deposition y
	particles_diameter 80e-6
	deposition_rate 1.6
	factor_erosion 1

	; 1: Akiyama&Fukushima
	; 2: = Garcia&Parker
	erosion_method 1
```

; Friction model. Parameters not required for specific models are ignored

; 1: Manning (Parameters: n) (not implemented in this version)

; 2: Chezy(Parameters: cs) (not implemented in this version)

; 3: Bingham(Parameters: tau_y,mu)

; 4: Herschel-Bulkley(tau_y,mu,n)

; 5: Frictionless

; 6: constant strength

; 7: constant factor (Parameter: Cd)

friction_type 7

friction_p1 .005

; Interface friction (between layers)

; 1: Manning (Parameters: n)

; 2: Chezy(Parameters: cs)

; 5: Frictionless

; 7: constant factor (Parameter: Cd)

lower_interface_friction_type 7

lower_interface_friction_p1 .005

has_lower_layer_detrainment y

lower_layer_detrainment_coefficient 0.001

lower_layer_detrainment_Rig_condition y

}

couple_layers y

enable_gauges n

gauge_file gauges.csv

; --

; Input/Outputs

; --

; Simulation mesh (GMSH)

gmsh_file A.msh

; Snapshot frequency (secs)

output_frequency 1

; Fields to export (leave blank for default)

output_fields "h_0, c_1, h_1, v_0, v_1, qx_0, qx_1, qy_0, qy_1, hc_0, hc_1, v_max_0, v_max_1, absolute_level_change, rate_level_change"

; Output filename (for both HDF5 and XDMF files)

output_name A

References

Akiyama, J and Fukushima, Y. (1984). Entrainment of non cohesive bed sediment into suspension. *External Memorandum No.195,* St. Anthony Falls Hydraulic Lab., Univ. of Minnesota.

Ancey, C. and Cochard, S. (2009). The dam-break problem for Herschel-Bulkley viscoplastic fluids down steep flumes. *Journal of Non-Newtonian Fuid Mechanics*,158, 18-35.

Armanini, A., and Di Silvio, G. (1988). A one-dimensional model for the transport of a sediment mixture in non-equilibrium conditions. *Journal of Hydraulic Research*, *26*(3), 275-292.

Armanini, A., Fraccarollo, L. and Rosatti, G. (2009). Two-dimensional simulation of debris flows in erodible channels. *Computational Geoscience* 35(5), 993–1006.

Assier-Rzadkiewiez, S., Heinrich, P., Sabatier, P.C., Savoye, B., Bourillet, J.F. (2000). Numerical modelling of a landslide-generated tsunami: the 1979 Nice-event. *Pageoph*, 157, 1707-1727.

Bagnold, R.A. (1966). An approach to the sediment transport problem from general physics. *U.S. Geol. Surv. Prof. Pap.*, 422(1), 37.

Beghin, P., Hopfinger, E.J. and Britter, R.E. (1981). Gravitational convection from instantaneous sources on inclined boundaries. *Journal of Fluid Mechanics*, 107, 407-422.

Benkhaldoun, F., Sari, S. and Seaid, M. (2014). A simple multi-layer finite volume solver for density-driven shallow water flows. *Mathematics and Computers in Simulation*, 99, 170-189.

Bingham, E.C., (1922). *Fluidity and Plasticity*, McGraw-Hill, New York.

Bradford, S.F. and Katopodes, N.D. (1999). Hydrodynamics of turbid underflows. I: Formulation and numerical analysis. *Journal of Hydraulic Engineering*, 1006-1015.

Boukpeti, N., White, D.J., Randolph, M.F. and Low, H.E. (2012). Strength of fine-grained soils at the solid-fluid transition. *Geotechnique*, 62(3), 213-226.

Bryn, P., Berg, K., Stoker, M.S., Solheim, A. (2005). Contouritic deposition and its relevance for the mass wasting record along the Mid-Norwegian Margin. *Marine and Petroleum Geology*, this issue, doi:10.1016/j.marpetgeo.2004.10.012

Capart, H., and Young, D. L. (1998). Formation of a jump by the dam-break wave over a granular bed. *Journal of Fluid Mechanics*, 372, 165–187.

Capart, H., Bellal, M., Boxus, L., De Roover C., Zech, Y. (1998). Approach to morphological equilibrium for steep-sloped river beds. River sedimentation - Theory and Applications, *Proceedings of the seventh International Symposium on River Sedimentation*, Hong-Kong, Japan, 231–237.

Capart, H. (2000). Dam-break induced geomorphic flows and the transition from solid- to fluid-like behaviour across evolving interfaces. PhD thesis, Université catholique de Louvain, Louvain-la-Neuve, Belgium.

Capart, H. and Young, D.L. (2002). A Q-scheme for a class of systems of coupled conservation laws with source term. Application to a two-layer 1-D shallow water system. *Math. Model. And Num. An.*, 35(1), 107-127.

Capart, H., Spinewine, B., Young, D.L., Zech, Y., Brooks, G.R., Leclerc, M. Secretan, Y. (2007) The 1996 Lake Ha! Ha! breakout flood, Québec: Test data for geomorphic flood routing methods. *J. Hydraul. Res*., 45 Extra Issue, 97–109.

Castro, M.J., Macias, J. and Pares, C. (2001). A Q-scheme for a class of systems of coupled conservation laws with source term. Application to a two-layer 1-D shallow water system. *Math. Model. And Num. An.*, 35(1), 107-127.

Chen, S.C. and Peng, S.H. (2006). Two-dimensional numerical model of two-layer shallow water equations for confluence simulation. *Advances in Water Resources,* 29, 1608–1617.

Chen, S.C., Peng, S.H. and Capart, H. (2007). Two-layer shallow water computation of mud flow intrusions into quiescent water. *Journal of Hydraulic Research*, Vol. 45(1), 13-25.

Coussot, P. (1997). Mudflow rheology and dynamics. *Balkema*, Rotterdam, 255 pp.

Dai, A. and Garcia, M.H. (2010). Gravity currents down a slope in deceleration phase. *Dynamics of Atmospheres and Oceans,* 49, 75-82.

Dangeard, L., Larsonneur, C. and Migniot, C. (1965). Les courants de turbidite, les coulees boueuses et les glissements: resultats d'experiences. *CR Acad. Sci. Paris,* 261, 2123-2126.

Davis, S. F. (1988). Simplified second-order Godunov-type methods. *SIAM J. Sci. Stat. Comput*., 9, 445–473.

De Blasio, F. V., Issler, D., Elverhøi, A., Harbitz, C. B., Ilstad, T.,Bryn, P.,Lien, R., and Løvholt, F. (2003). Dynamics, velocity and runout of the giant Storegga slide, in: Submarine Mass Movements and Their Consequences, edited by: Locat, J. and Mienert, J., Adv. Natural Technol. Hazards Res., 19, 223–230, 2003.

De Blasio, F. V., Elverhøi, A., Issler, D., Harbitz, C. B., Bryn, P., Lien, R. (2004a). Flow models of natural debris flows originating from overconsolidated clay materials, Marine Geol., 213, 439–455.

De Blasio, F. V., Engvik, L., Harbitz, C. B., and Elverhøi, A. (2004b). Hydroplaning and submarine debris flows. *J. Geophys. Res*.,109.

Dietrich, W.E. (1982). Settling velocity of natural particles. *Water Resources Research,* 18(6), 1615-1626.

Drago, M. (2002). A coupled debris flow – turbidity current model. *Ocean Enginnering,* 29, 1769-1780.

Edgers, L. and Karlsrud, K. (1981). Viscous analysis of submarine flows, Report 52207. *Norwegian Geotechnical Institute,* Norway.

Egashira, S. (1980). Basic research on the flow and mechanism of mixing of density-stratified fields. Ph.D. thesis, Kyoto University, Japan.

Ellison, T.H. and Turner, J.S. (1959). Turbidity entrainment in stratified flows. *J. Fluid Mech*., 6, 423-448.

Elverhoi, A., De Blasio, F.V., Ilstad, T., Harbitz, C.B. and Gauer, P. (2005). Emerging insights into the dynamics of submarine debris flows. *Nat Haz Earth Sys Sci*, 5, 633-648.

Elverhoi, A., Breien, H., De Blasio, F.V., Harbitz, C.B. and Pagliardi, M. (2010). Submarine landslides and the importance of the initial sediment composition for run-out length and final deposit. *Ocean Dynamics*, 60, 1027-1046.

Felix, M. and Peakall, J. (2006). Transformation of debris flows into turbidity currents: mechanisms inferred from laboratory experiments. *Sedimentology*, 53, 107-123.

Fraccarollo L., Capart H. (2002). Riemann wave description of erosional dam-break flows. *Journal of Fluid Mechanics*, 461, 183 – 228.

Fraccarollo, L., Capart, H., Zech, Y. (2003). A Godunov method for the computation of erosional shallow water transient. *International Journal for Numerical Methods in Fluids* 41(9), 951–976.

Fukushima, Y. (1981). Basic study on the density current into a stratified reservoir. PhD thesis, Tokyo University.

Fukushima, Y., Parker, G., Pantin, H. M.(1985). Prediction of ignitive turbidity currents in Scripps Submarine Canyon. *Marine Geology*, 67, 55-81.

Ganni, M. (2004). From turbid to lucid, a straightforward approach to sediment flows and their deposits. *The sedimentary Record, 2*, 4-11.

Garcia, M.H. (1985). Experimental study of turbidity currents. *M.S. thesis, Dept. of Civil and Mineral Engineering*, University of Minnesota, USA.

Garcia, M. and Parker, G. (1991), Entrainment of bed sediment into suspension, *J. Hydraul. Eng*., 117(4), 414 – 435.

Garcia, M. and Parker, G. (1993). Experiments on the entrainment of the sediment into suspension by a dense bottom current. *J. Geophys. Res*., 98(c3), p. 4793-4807.

Godunov, S. K. (1959). A Difference Scheme for Numerical Solution of Discontinuous Solution of Hydrodynamic Equations. *Math. Sbornik, 47, 271–306, translated US Joint Publ. Res. Service*, JPRS 7226, 1969.

Haflidason, H., Sejrup, H., Nygård, A., Mienert, J., Bryn, P., Lien, R., Forsberg, C.F., Berg, K., Masson, M. (2008). The Storegga Slide: architecture, geometry and slide development. *J. Marine geology*, 213(1-4), 201-234.

Hampton, M.A.., Karl. H.A., Murray, C.J. (2002). Accoustic profiles and images of the Palos Verdes margin: Implications concerning deposition from the White's Point outfall. *Continental Shelf Research*, 22, 841-858.

Hampton, M.A.., Lee, H.J., Locat , J. (1996). Submarine landslides. *Rev. Geoiphys.*, 34, 33-59.

Hampton, M.A. (1972). The role of subaqueous debris flows in generating turbidity currents. *Journal of Sedimentary Petrology*, 42, 775- 793.

Harten, A, Lax, PD and Van Leer, B (1983). "On upstream differencing and Godunov-type schemes for hyperbolic conversations laws." *SIAM Review 25,* 35-61.

Heezen, B.C., Ericson, D.B. and Ewing, M. (1954). Further evidence for a turbidity current following the 1929 Grand-Banks earthquake. *Reviews of Geophysics*, 35, 245-296.

Herschel, W.H., Bulkley, T. (1926). Measurement of consistency as applied to rubber-benzene solutions. *Am. Soc. Test Proc*., 26, 621-633.

Hsu, S.K., Kuo, J., Lo, C.L., Tsai, C.H., Doo, W.B., Ku, C.Y., Sibuet, J.C. (2008). Turbidity currents, submarine landslides and the 2006 Pingtung earthquake off Sedimentological Characteristics and Seafloor Failure 75 SW Taiwan. *Terr. Atmos. Ocean. Sci*., 19, 767-772.

Huang, X. and Garcia, M.H. (1997). A perturbation solution for Bingham-Plastic mudflows. *Journal of Hydraulic Engineering*, 123, 986-994.

Huang, X. and Garcia, M.H. (1998). A Herschel-Bulkley model for mud flow down a slope. *Journal of Fluid Mechanics*, 374, 305-333.

Huang, X. and Garcia, M. H. (1999). Modeling of non-hydroplaning mud flows on continental slopes. *Marine Geology*, 154, 132–142.

Ilstad, T., Elverhoi, A., Issler, D., Marr, J.G. (2004), Subaqueous debris flow behaviour and its dependence on the sand/clay ratio: a laboratory study using particle tracking. *Marine Geology*, 213, 415-438.

Imran, J, Parker, G, Katopodes, N. (1998). A numerical model of channel inception on submarine fans. *J. Geophy. Res*., 103(c1), 1219-1238.

Imran, J, Parker, G, Locat, J and Lee, H (2001). 1D Numerical model of muddy subaqueous and subaerial debris flows. *Journal of Hydraulic Engineering,* 127(11), 959-968.

Iverson, R.M. (1997). The physics of debris flows. *Deep-Sea Res*, 1, 193-202.

Jiang, L. and Leblond, P.H. (1992). The coupling of a submarine slide and the surface water waves which it generates. *Journal of Geophysical Research*, 971(C8), 12731-12744.

Johnson, A.M. (1970). Physical processes in geology. *Freeman, Cooper and Co,* 577.

Kuenen, P.H.. and Migliorini, C.I. (1950). Turbidity currents as a cause of graded bedding. *Journal of Geol*, 58, 91-127.

Kuenen, P.H. (1937). Experiments in connection with Daly’s hypothesis on the formation of submarine canyons. *Leidse Geol. Mededel*., 8, 327–335.

Lee, S. (2004). Soil erosion assessment and its verification using the universal soil loss equation and geographic information system: A casestudy at Boun, Korea. *Environmental Geology*, 45: 457-465.

Lin, J. and Leblond, H.J. (1993). Numerical modelling of an underwater Bingham plastic mudslide and the waves which it generates. *Journal of Geophysical Research*, 981(C6), 10303-10317.

Locat, J. and Demers, D. (1988). Viscosity, yield stress, remolded shear strength and liquidity index relationships for sensitive clays. *Canadian Geotechnical Journal*, 25, 799-806.

Locat, J. and Lee, P.H. (2005). Chapter 9: Subaqueous debris flows. *Debris-flow Hazards and Related Phenomena,* Springer, Berlin, 205-245.

Marr, J.G., Elverhoi, A., Harbitz, C., Imran, J. and Harff, P. (2002). Numerical simulation of mud-rich subaqueous debris flows on the glacially active margins of the Svalbard-Barents Sea. *Marine Geology*, 188:351-364.

Masson, D.G., Harbitz, C.B., Wynn, R.B., Pedersen, G. and Lovholt, F. (2006). Submarine landslides: processes, triggers and hazard prediction. *Phil. Trans. R. Soc. A.,* 364, 2009-2039.

Meiburg, E. and Kneller, B. (2010). Turbidity currents and their deposits. *Annual Review of Fluid Mechanics*, 42, 135-156.

Middleton, G.V. and Hampton, M.A. (1976). Subaqueous sediment transport and deposition by sediment gravity flows. *Marine Sediment Transport and Environmental Management*, New York, Wiley, 197-218.

Mohrig, D., Whipple, M., Hondzo, M., Ellis, C., Parker, G. (1998). Hydroplaning of subaqueous debris flows. *Bulletin of the Geological Society of America*, 110(3), 387-394.

Mohrig, D., Elverhoi, A., Parker, G. (1999). Experiments on the relative mobility of muddy subaqueous and subaerial debris flows, and their capacity to remobilize antecedent deposits. *Marine Geology*, 154(1-4), 117-129.

Mohrig, D., and Marr, J.G. (2003). Constraining the efficiency of turbidity current generation from submarine debris flows and slides using laboratory experiments. *Marine and Petroleum Geology,* 20, 883- 899.

Moresi, L.N, Dufour, F., Muhlhaus, H.. (2003). A Lagrangian Integration Point Finite Element Method for Large Deformation Modeling of Viscoelastic Geomaterials. *Journal Of Computational Physics*, 184(2) 476-497.

Niedoroda, A.W., Reed, C.W., Das H.S., Hatchett, J.L. and Perlet, A.B. (2006). Controls of the behaviour of marine debris flows. *Norwegian Journal of Geology*, 86, 265-274

Niedoroda, A.W., Reed, C.W., Hatchett, J.L. and Das H.S. (2003). Developing engineering design criteria for mass gravity flows in deep ocean and continental slope environments. *In Locat, J. & Mienert, J. (Eds.), Submarine Mass Movements and Their Consequences,* Kluwer Academic Press, Dordrecht, 85 – 94.

O'Brien, J.S. and Julien, P.Y. (1988). Laboratory analysis of mudflow properties. *Journal of Hydraulic Engineering,* 114, 877-887.

O'Neil, C., Moresi, L., Muller, D., Albert, R., Dufour, F. (2006). Ellipsis 3D: A particle-in-cell finite-element hybrid code for modelling mantle convection and lithospheric deformation. *Computers and Geoscience,* 32, 1769-1779.

Parker, G. (1982). Conditions for the ignition of catastrophically erosive turbidity currents. *Mar. Geol*., 46, 307-327.

Parker, G., Fukushima,Y. and Pantin, H.M. (1986). Self accelerating turbidity currents. *Journal of Fluids Mechanics,* Vol. 171, 145-181.

Pastor, M., Quecedo, M., Gonzalez, E., Herreros, M. I., Fernandez Merodo, J. A., and Mira, P. (2004). Simple approximation to bottom friction for Bingham fluid depth integrated models. *Journal of Hydraulic Engineering*, 330(2), 149–155.

Pratson, L.F., Imran, J., Parker, G., Syvitski, J.P.M. and Hutton, P.M. (2000). Debris flows versus turbidity currents: a modeling comparison of their dynamics and deposits. *Fine-grained turbidite systems, AAPG Memoir* 72/SEPM Special Publication 68, 57-72.

Randolph, M.F., (2004). Characterisation of soft sediments for offshore applications, Keynote Lecture. In: Proceedings of the Second International Conference on Site Characterisation, vol. 1, Porto, 209–231.

Randolph, M.F., Gaudin, C., Gourvenec, S.M., White, D.J., Boylan, N., Cassidy, M.J. (2011). Recent advances in offshore geotechnics for deep water oil and gas developments. *Ocean Engineering*. 38. 818-834.

Seed, H.B., Seed R.B., Schlosser, F., Blondeau, F., Juran, I. (1998). The landslide at the port Nice on October 16, 1979. EarthquakeEngineering Research Center, University of California Berkley, 68.

Sequeiros, O.E., Spinewine, B., Beaubouef, R.T., Sun, T., Garcia, M.H., Parker, G. (2010). Bedload transport and bed resistance associated with density and turbidity currents. *Sedimentology*, 57, 1463-1490.

Soares-Frazão, S. (2002) Dam-break induced flows in complex topographies. Theoretical, numerical and experimental approaches. Phd Thesis, Université catholique de Louvain, Belgium.

Soares-Frazão, S., and Zech, Y. (2002). Dam-break in channels with 90◦ bend. *J. Hydraul. Eng.*, ASCE, 128(11), 956–968.

Soares-Frazão, S., and Zech, Y. (2010). HLLC scheme with appropriate wave-speed estimators for two-dimensional shallow-water flow on erodible bed. *Intl J. Numer. Meth. Fluids,* published online, DOI: 10.1002/fld.2300.

Soares-Frazão S., Canelas R., Cao Z., Cea L., Chaudhry H.M., Die Moran A., El Kadi K., Ferreira R., Fraga Cadórniga I., Gonzalez-Ramirez N., Greco M., Huang W., Imran J., Le Coz J., Marsooli R., Paquier A., Pender G., Pontillo M., Puertas J., Spinewine B., Swartenbroekx C., Tsubaki R., Villaret C., Wu W., Yue Z., Zech Y. (2012). Dam-break flows over mobile beds: experiments and benchmark tests for numerical models. *J. Hydraul. Res.*, 50(4), 364–375.

Spinewine B., Capart H., le Grelle N., Soares Frazão S., Zech Y. (2002). Experiments and computations of bankline retreat due to geomorphic dambreak floods. *Proc. River Flow 2002* (1), 651–661, Louvain-la-Neuve, Belgium.

Spinewine, B. (2005). Two-layer flow behaviour and the effects of granular dilatancy in dam-break induced sheet-flow. PhD Thesis, Université catholique de Louvain, Belgium.

Spinewine, B., Aleixo, R., and Capart, H. (2011). Intense bedload associated with unsteady dam-break surges. *Proc. River, Coastal and Estuarine Morphodynamics: RCEM 2011*, Beijing, China.

Spinewine, B. and Capart, H. (2013). Intense bed-load due to a sudden dam-break. *Journal of Fluid Mechanics*, 731, 579–614.

Spinewine, B. and Zech, Y. (2007). Small-scale laboratory dam-break waves on movable beds. *Journal of Hydraulic Research*, 45(sup1), 73-86.

Stoker, J.J. (1957). Analysis of the Navier-Stokes Equations. ater Waves, the Mathematical Theory with Applications. Interscience Publishers Inc., New York.

Talling, P.J., Clare. M., Urlaub, M., Hunt, J. and Watt, S. (2014). Large submarine landslides on continental slopes: geohazards, methane release, and climate change. *Oceanography*, 27(2), 32–45.

Talling P.J., Paull, C.K., Piper, D.J.W. (2002). Experimental constraints on shear mixing rates and processes ; implications for the dilution of submarine debris flows, in Glacier-influenced Sedimentation on High-latitude Continental Margins, Eds. J.A. Dowdeswell and C. O'Cofaigh. *Geol. Soc. Spec. Publ.*, 203, 89-103.

Toro, E.F. and Spruce, M. (1994). Restoration for the contact surface in the HLL-Riemann solver. *Shock Waves*, 4, 25–34.

Toro, E.F. (1997). *Riemann solvers and numerical methods for fluid dynamics: a practical introduction*. Springer, Berlin, Germany.

Toro, E. (2001). *Shock-Capturing Methods for Free-Surface Shallow Flows,* Wiley, New-York.

Wan, Z. (1982). Bed material movement in hyperconcentrated flow. *Ser. Par. 31 Inst. Of Hydrodyn. And Hydraul. Engrg.* Technical University of Denmark, Lyngby.

Zakeri, A. (2008). Conceptual mitigative and control measures for protecting submarine pipelines against debris flows. *Oil & Gas Review* 2008, 6(11), 148-150.

Zakeri, A. (2010). Conceptual mitigative and control measures for protecting submarine pipelines against debris flows. *Oil & Gas Review 2008,* 6(11), 148-150.

Zakeri, A., Si, G., Marr, J.G. and Hoeg, K. (2010). Experimental investigation of subaqueous clay-rich debris flows, turbidity generation and sediment deposition. *Advances in Natural and Technological Hazards Research,* 28, 105-115.

Zech, Y., Soares-Frazão, S., Spinewine, B., Le Grelle, N. (2008). Dam-break induced sediment movement: Experimental approaches and numerical modelling. *J. Hydraul. Res*., 46(2), 176–190.